Compressive Techniques for Sub-Nyquist Data Acquisition & Processing in Vibration-based Structural Health Monitoring of Engineering Structures

Thesis by

KYRIAKI GKOKTSI

In partial fulfilment for the degree of

Doctor of Philosophy

CITY, UNIVERSITY OF LONDON

School of Mathematics, Computer Science & Engineering

Department of Civil Engineering

Research Centre for Civil Engineering Structures

JANUARY 2018

CITY, UNIVERSITY OF LONDON
School of Mathematics,
Computer Science & Engineering
Department of Civil Engineering
Research Centre for Civil Engineering Structures

Compressive Techniques for Sub-Nyquist Data Acquisition & Processing in Vibration-based Structural Health Monitoring of Engineering Structures

Doctoral Candidate: *Kyriaki Gkoktsi*

Supervisor: *Dr Agathoklis Giaralis*

Doctoral Committee: *Dr Stana Zivanovic*
Dr Iasonas Triantis

London, January 2018

Contents

Acknowledgements

First and foremost, I would like to thank my supervisor, *Dr Agathoklis Giaralis* for his mentorship, guidance, and continual support throughout my Ph.D studies. Over the last four years, *Dr Giaralis* has offered me unique opportunities that substantially contributed towards my academic and professional development, which I gratefully acknowledge. He has inspired me in various ways, and instilled great confidence in both myself and my research, being the most determining factors in making this work possible.

I am also particularly grateful to my research fellow, *Dr Bamrung Tau Siesakul*, for his valuable contribution in the initial stages of this research. He has introduced me to the electrical engineering discipline and helped me explore the world of signal processing. He has been a great colleague and friend, I cherish the days we were collaborating on a research project funded by EPSRC.

My sincere gratitude and appreciation is extended to *Prof. Pol D. Spanos*. It is difficult to express how honoured I feel for having been a visiting scholar in his research group. *Prof. Spanos* and his dedication to science have been an inspiration to me – thanks to him, I re-appreciated the beauty of maths. He has been a great mentor; his advice has always been invaluable to me.

I wish further to express my gratitude to *Prof. Eleni Chatzi* and to *Dr Vasileios Dertimanis* for our collaboration and for providing the field-recorded data used in *Chapter 5* and *Chapter 6* of this thesis. Special thanks are extended to my Ph.D committee members, *Dr. Stana Zivanovic* and *Dr Iasonas Triantis* for their insightful comments. My special gratitude goes to my supervisors on my diploma and MSc theses, *Prof. Christos Ignatakis* and *Prof. Kyriazis Pitilakis*, for assisting and encouraging my decision to pursue a Ph.D *at City, University of London.*

I would like also to thank my friends and my family, especially my parents, for their unconditional love. Special thanks are extended to *Angelina Damianou* and *Konstantinos Gkatzogias* for their extremely valuable support and for being my closest companion over the last few years.

This research has been supported by *City, University of London* thought a Ph.D scholarship and partially funded by EPSRC in UK, under grant No EP/K023047/1. I am grateful and honoured to have received this funding.

Declaration

I grant powers of discretion to the University Librarian to allow the thesis to be copied in whole or in part without further reference to the author. This permission covers only single copies made for study purposes, subject to normal conditions of acknowledgement.

Abstract

Vibration-based structural health monitoring (VSHM) is an automated method for assessing the integrity and performance of dynamically excited structures through processing of structural vibration response signals acquired by arrays of sensors. From a technological viewpoint, *wireless sensor networks* (WSNs) offer less obtrusive, more economical, and rapid VSHM deployments in civil structures compared to their tethered counterparts, especially in monitoring large-scale and geometrically complex structures. However, WSNs are constrained by certain practical issues related to local power supply at sensors and restrictions to the amount of wirelessly transmitted data due to increased power consumptions and bandwidth limitations in wireless communications.

The primary objective of this thesis is to resolve the above issues by considering *sub-Nyquist data acquisition and processing techniques* that involve simultaneous signal acquisition and compression before transmission. This drastically reduces the sampling and transmission requirements leading to reduced power consumptions up to 85-90% compared to conventional approaches at Nyquist rate. Within this context, the current state-of-the-art VSHM approaches exploits the theory of *compressive sensing* (CS) to acquire structural responses at non-uniform random sub-Nyquist sampling schemes. By exploiting the *sparse* structure of the analysed signals in a known vector basis (*i.e.*, non-zero signal coefficients), the original time-domain signals are reconstructed at the uniform Nyquist grid by solving an *underdetermined* optimisation problem subject to signal sparsity constraints. However, the CS sparse recovery is a computationally intensive problem that strongly depends on and is limited by the sparsity attributes of the measured signals on a pre-defined expansion basis. This sparsity information, though, is unknown in real-time VSHM deployments while it is adversely affected by noisy environments encountered in practice.

To efficiently address the above limitations encountered in CS-based VSHM methods, this research study proposes three alternative approaches for energy-efficient VSHM using compressed structural response signals under ambient vibrations. The first approach aims to enhance the sparsity information of vibrating structural responses by considering their representation on the wavelet transform domain using various oscillatory functions with different frequency domain attributes. In this respect, a novel *data-driven* damage detection algorithm is developed herein, emerged as a fusion of the CS framework with the *Relative Wavelet Entropy* (RWE) damage index. By processing sparse signal coefficients on the harmonic wavelet transform for two comparative structural states (*i.e.*, damage versus healthy state), CS-based RWE

damage indices are retrieved from a significantly reduced number of wavelet coefficients without reconstructing structural responses in time-domain.

The second approach involves a novel signal-agnostic *sub-Nyquist spectral estimation method* free from sparsity constraints, which is proposed herein as a viable alternative for power-efficient WSNs in VSHM applications. The developed method relies on *Power Spectrum Blind Sampling* (PSBS) techniques together with a *deterministic multi-coset sampling pattern*, capable to acquire stationary structural responses at sub-Nyquist rates without imposing sparsity conditions. Based on a network of wireless sensors operating on the same sampling pattern, auto/cross power-spectral density estimates are computed directly from compressed data by solving an *overdetermined* optimisation problem; thus, by-passing the computationally intensive signal reconstruction operations in time-domain. This innovative approach can be fused with standard operational modal analysis algorithms to estimate the inherent resonant frequencies and modal deflected shapes of structures under low-amplitude ambient vibrations with the minimum power, computational and memory requirements at the sensor, while outperforming pertinent CS-based approaches. Based on the extracted modal information, numerous data-driven damage detection strategies can be further employed to evaluate the condition of the monitored structures.

The third approach of this thesis proposes a noise-immune damage detection method capable to capture small shifts in structural natural frequencies before and after a seismic event of low intensity using compressed acceleration data contaminated with broadband noise. This novel approach relies on a recently established sub-Nyquist pseudo-spectral estimation method which combines the deterministic *co-prime sub-Nyquist sampling technique* with the *multiple signal classification* (MUSIC) pseudo-spectrum estimator. This is also a signal-agnostic and signal reconstruction-free method that treats structural response signals as wide-sense stationary stochastic processes to retrieve, with very high resolution, auto-power spectral densities and structural natural frequency estimates directly from compressed data while filtering out additive broadband noise.

List of Figures

List of Tables

List of Symbols

$\mathbf{C}_{\hat{\mathbf{r}}_y}$	covariance estimator matrix of output signal $y[k]$
$\mathbf{\Phi}$	mode shape matrix
$\mathbf{R}_c$	pattern cross correlation matrix $(\mathbf{R}_c \in \mathbb{R}^{\bar{M}^2 \times \bar{N}})$
σ_x^2	variance of input signal $x[n]$
$\mathbf{O}$	zero matrix
$f_{\text{WMSE}}(\mathbf{s})$	cost-function of weighted mean square error criterion for the design of the multi- coset sampling pattern
$\mathbf{\Lambda}(\boldsymbol{\alpha})$	Diagonal matrix $\left(\mathbf{\Lambda}(\boldsymbol{\alpha}) \in \mathbb{Z}^{\bar{N} \times \bar{N}}\right)$
$\mathbf{F}_{(2L+1)\bar{N}}$	Discrete Fourier Transform $\left(\mathbf{F}_{(2L+1)\bar{N}} \in \mathbb{C}^{\bar{N}(2L+1) \times \bar{N}(2L+1)}\right)$
$\hat{\mathbf{r}}_{y^a y^b}$	estimated output cross-correlation matrix
$c_i[n]$	filter coefficients of multi-coset sampling pattern
$\hat{\mathbf{r}}_{x^a x^b}$	input cross-correlation estimate of signals $x^a[n],\ x^b[n]$
$r_{x^a x^b}[k]$	input cross-correlation function between the input signals $x^a[n],\ x^b[n]$
$\mathbf{r}_{x^a x^b}$	input cross-correlation matrix $(\mathbf{r}_{x^a x^b} \in \mathbb{R}^{\bar{N} \times D})$
$\mathbf{G}_{x^a x^b}$	input cross-power spectrum matrix of the input signals $x^a[n], x^b[n]$
$\hat{\mathbf{G}}_{x^a x^b}$	input cross-spectrum estimate of signals $x^a[n],\ x^b[n]$
$\mathbf{F}_{N \times N}^{-1}$	inverse discrete Fourier transform
$\hat{\mathbf{s}}_{\text{WMSE}}$	optimum design of the multi-coset sampling pattern, $\mathbf{s}$
$\hat{\mathbf{W}}_{\text{MMSE}}$	optimum design of weighting matrix, $\mathbf{W}$
$r_{y_i^a, y_j^b}[k]$	output cross-correlation function of the compressed signals $y_i^a[k],\ y_j^b[k]$
$\mathbf{r}_{y^a y^b}$	output cross-correlation matrix $(\mathbf{r}_{y^a y^b} \in \mathbb{R}^{\bar{M}^2 \times D})$
$y_i[k]$	output/acquired compressed discrete-time signal from the i-th channel of the multi-coset sampler

$r_{c_i,c_j}[p]$	pattern cross-correlation function
$\alpha_n(\mathbf{s})$	scalar value associated with the multi-coset sampling pattern
$\hat{r}_{y_i^a,y_j^b}[\ell]$	unbiased estimator of $r_{y_i^a,y_j^b}[k]$
$1/T_s$	Nyquist sampling rate (in Hz)
$\mathbf{A}$	CS partial measurement matrix of size $M \times N$, $\mathbf{A}=\mathbf{\Theta\Psi}$
A_{J+1-j}	"approximation" sequence of wavelet coefficients
A_r	amplitude value related to mode shapes and modal participation factors
b	time index/translational parameter in the wavelet transform
B_r	sinusoidal amplitude
C	constant within the CoSaMP algorithm
CR	compression ratio
D	number of sensors in a WSN (d=a=b=1,2,…,D)
d_{bl}	diameter of the longitudinal reinforcement
D_{J+1-j}	"detail" sequence of wavelet coefficients
E	signal's energy
e	upper error bound in noisy CS reconstruction
$\mathbf{e}(f)$	signal's vector
$f_{\max}$	highest frequency component in signal $x(t)$
f_r	natural frequency at the r^{th} mode of vibration (in Hz)
F_s	sampling frequency
f_{uk}	characteristic steel ultimate strength
f_{yk}	characteristic steel yielding strength
$g[p]$	low-pass filter in multi-resolution analysis
$G_{\text{MUSIC}}(f)$	pseudo-spectrum MUSIC estimator
$\mathbf{G}_q$	diagonal spectrum density matrix of the modal coordinates $\mathbf{q}(t)$
$G_x(\omega)$	power spectrum of $x(t)$
$h[p]$	high-pass filter in multi-resolution analysis
$\mathbf{I}$	identity matrix
j	level of multi-resolution analysis – scale-related parameter of wavelet transform
K	number of blocks the reference signal is divided within the multi-coset sampling pattern
k	translational-related parameter in the discrete wavelet transform
L	parameter related to correlation support
L_o	shear span
L_{pl}	plastic hinge length
M	length of compressed signal

$\bar{M}$	number of acquired multi-coset samples
$\bar{M}$	number of channels in multi-coset samplers ($i, j = 1,2,\ldots,\bar{M}$)
M_y	bending moment at yielding
M-φ	Moment-curvature pair
$\bar{N}$	down-sampling parameter in multi-coset samplers
$\bar{N}$	number of uniform samples in each K block in the multi-coset sampling pattern
N	length of original/reference/uncompressed signal
N_1, N_2	co-prime numbers
N_R	number of realizations
Q	ratio of effective frequency over the effective bandwidth at each analysis level
$\mathbf{q}(t)$	modal coordinate matrix
$q_r(t)$	modal coordinates at the r-th mode of vibration
R	number of structural modes of vibration ($r = \{1,2,\ldots,R\}$)
$\mathbf{R}_{ss}$	spatially-smoothed correlation matrix
$\mathbf{r}_y$	correlation matrix
R_{yy}	auto-correlation function of $y[k]$
$\mathbf{s}$	sequence of multi-coset sampling pattern
S	signal sparsity
s_i, s_j	coset/ delay parameter at the m-th channel of the multi-coset sampler
S_T	target sparsity in reconstructed time-domain signals
SWE	Shannon wavelet entropy
T_s	sampling rate
$\mathbf{U}$	unitary singular matrices holding the left singular vectors
$u(\alpha,b)$	wavelet coefficients
$u[n]$	discrete Fourier transform coefficients
$\hat{u}[n]$	recovered signal coefficients on the DFT domain
$\mathbf{V}$	unitary singular matrices holding the right singular vectors
$v(u)$	auxiliary smoothing function in Meyer wavelet functions
$\mathbf{W}$	weighting matrix
w_j	energy ratio at scale j for a potentially damaged structure
$x(t)$	real-valued signal in time domain
$X(\omega)$	Fourier transform of signal $x(t)$ in frequency domain
$x[n]$	input full-length discrete-time signal
$\hat{x}[n]$	time-domain reconstructed input signal
$y[k]$	compressed signal in time domain
$y[m]$	compressed signal

z_j	energy ratio at scale j for a "healthy" structure
α	scaling parameter in wavelet transform
δ_S	restricted isometry constant
$\boldsymbol{\varepsilon}$	measurement error vector
$\varepsilon[k]$	zero-mean complex Gaussian white noise sequences; noise sequence component
η	tolerance parameter in CoSaMP algorithm
$\boldsymbol{\Theta}$	measurement matrix in compressive sensing of size $M \times N$
θ_r	random phase
μ_φ	curvature ductility
$\boldsymbol{\Sigma}$	diagonal positive semi-definite matrix comprising the singular values, Σ_{rr}, at the r-th mode of vibration
σ^2	variance, signal's power
T_o	total length (duration) of the time interval
φ	structural mode shapes/eigenvectors
$\varphi(t)$	scaling function in wavelet transform
$\boldsymbol{\varphi}_r$	structural mode shapes/eigenvectors at the r-th mode of vibration
φ_y	curvature at yielding
$\boldsymbol{\Psi}$	Basis matrix of size $N \times N$
$\psi(t)$	wavelet function
ω	circular frequency (in rad/s)
Ω	set of numbers
ω_c	central or the dominant frequency of the (unscaled) mother wavelet
ω_{eff}	effective frequency of wavelet function
$\mathcal{E}I$	flexural rigidity

List of Operations

$\left\|\cdot\right\|_p$	ℓ_p norm
$\left\|\cdot\right\|$	absolute value
$*$	discrete-time convolution operator
$\overline{x}$	complex conjugate of x
$\delta_{n,m}$	Dirac delta function
$\hat{x}$	estimated value of x
$\mathrm{E}_{\mathrm{a}}\{\cdot\}$	expectation operator with respect to a
$\lfloor\cdot\rfloor$	floor operator
$(\cdot)^{\mathrm{H}}$	Hermitian transpose
$\Im$	Imaginary part of complex number
$\otimes$	Kronecker product operator
$(\cdot)^{-1}$	matrix inverse
$(\cdot)^{\mathrm{T}}$	matrix transpose
$vec(\cdot)$	matrix vectorisation
$(\cdot)^{\dagger}$	Moore-Penrose pseudo-inverse
$\Re$	Real part of complex number

Glossary of Acronyms

ADC	Analog-to-Digital Converter
ARMA	Auto-Regressive Moving Average
CoSaMP	Compressive Sampling Matching Pursuit; signal recovery algorithm
CR	Compression ratio
CS	Compressive Sensing
DFT	Discrete Fourier Transform
D*P*	Daubechies wavelet of an *P*-length finite impulse response
DS	Damage State
FDD	Frequency Domain Decomposition
FE	Finite Element
FFT	Fast Fourier Transform
FRF	Frequency Response Function
IDFT	Inverse Discrete Fourier Transform
MAC	Modal Assurance Criterion
MSE	Mean Square Error
MSEI	Modal Strain Energy Index
MUSIC	Multiple Signal Classification
OMA	Operational Modal Analysis
PGA	Peak Ground Acceleration
PSBS	Power Spectrum Blind Sampling
PSD	Power Spectrum Density
RMSE	Root Mean Square Error
RWE	Relative Wavelet Entropy
SHM	Structural Health Monitoring
SNR	Signal-to-Noise Ratio
SVD	Singular Value Decomposition
VSHM	Vibration-based Structural Health Monitoring
WMSE	Weighted Mean Square Error
WSN	Wireless Sensor Network
MDOF	Multi-degree of freedom

Chapter 1
Introduction

1.1. Structural Health Monitoring

Structural Health Monitoring (SHM) of civil engineering structures such as buildings, bridges, dams, masts, etc., aims to assess their structural integrity and performance either periodically or following extreme events/actions (*i.e.*, floods, earthquakes, structural upgrades, blast loading) (*e.g.*, *Brownjohn* (2007)). Periodic structural assessment is pursued by long term SHM seeking to capture the gradual structural changes due to operational and environmental conditions (aging, degradation, thermal loading, etc.) and to provide useful information for structural maintenance and retrofitting, as well as validation of design models (*e.g.*, *Brownjohn* (2007)). In the occurrence of extreme events, short term SHM involves rapid and real-time monitoring to provide information for intermediate structural integrity. Ideally, SHM should extract the maximum information at minimum time without interrupting the structure's normal functionality.

For most of the existing structures, apart from visual inspections which tend to be qualitative and non-continuous, vibration-based SHM (VSHM) is arguably the most commonly used method for global condition assessment (*e.g.*, *Lynch & Loh* (2006); *Lynch* (2007); *Nagayama & Spencer* (2007); *Spencer & Yun* (2010)). It relies on acquisition and processing of structural dynamic response signals (*e.g.*, acceleration responses) measured by sensors placed on structures exposed to time-varying loads, for the purpose of (i) estimating the inherent dynamic/modal properties of linearly vibrating structures under operational conditions, and (ii) detecting potential structural damage from vibration measurements.

The first purpose above concerns the so-called modal identification problem, which is divided into experimental and operational modal analysis depending on the type of the excitation force, *i.e.*, measured-deterministic signals or unmeasured-stochastic processes, respectively (*e.g.*, *Reynders* (2012)). Traditional Experimental Modal Analysis (EMA) measures both input (excitation) and output (response) signals to infer structural vibration characteristics (*i.e.*, natural frequencies ω_r, damping ratio ζ_r, mode shapes $\boldsymbol{\varphi}_r$). It is mainly applicable to laboratory experiments where controllable excitation forces (*e.g.*, impact testing, harmonic excitations) are applied to sub-structures and structural components (*e.g.*, *Zhang et al.* (2005); *Reynders* (2012)).

On the antipode, Operational Modal Analysis (OMA) – also known as ambient, natural excitation or output-only modal analysis – utilises unmeasured ambient/natural excitation forces (*e.g.*, wind, vehicle, and pedestrian traffic), assumed to be wide-sense stationary stochastic processes observing a sufficiently flat spectrum across a wide frequency band that can be approximated as Gaussian white noise (*i.e.*, stochastic quantities with unknown parameters but with known behaviour) (*e.g., Zhang et al.* (2005); *Reynders* (2012)). OMA is suitable for real-time monitoring of large-scale and complex structures with the minimum cost and network disruption, being particularly useful in cases where it is difficult or unaffordable to measure the input forces, and/or when controllable excitation of structures is not possible in practice (*e.g., Amezquita-Sanchez & Adeli* (2016)). However, OMA may encounter bias errors, measurement noise, and other un-modelled effects and thus validation criteria are employed to assess the quality of the extracted modal estimates (*e.g., Zhang et al.* (2005)).

Moving next to the structural damage detection problem in the VSHM framework, four different aims are normally set, *i.e.*, (1) identification of the existence of structural damage; (2) detection of its location; (3) damage classification, and (4) quantification of damage severity in terms of structural serviceability/durability (*e.g., Ewins* (2000); *Humar et al.* (2006)). A plethora of damage detection algorithms have been proposed, capable to derive damage-sensitive indices by processing dynamic response signals, measured between the current (potentially damaged) and a past baseline ("healthy") structural state (*e.g., Sohn & Farrar* (2001); *Worden et al.* (2007)).

Traditional *model-based* damage indices can infer damage by measuring changes in physically meaningful properties, such as natural frequencies, mode shapes, mode shape curvature, etc., that describe the global structural response (*e.g., Humar et al.* (2006)). However, these quantities are adversely affected by environmental noise while they are not very sensitive to local damage (*e.g., Doebling et al.* (1988)). In fact, damage is a local phenomenon mainly captured by higher frequency modes that are not adequately excited in most cases, and thus rarely measured with sufficient accuracy (*e.g., Doebling et al.* (1988)). Further, these global features show little changes due to stress re-distribution in damaged structures, rendering the damage localisation problem a difficult task. On the contrary, the above limitations can be efficiently addressed by considering *data-driven* non-physical damage indices, derived from signal processing techniques on vibration signals (*e.g., Humar et al.* (2006)). Notably, these techniques enable direct operations on real-time monitored structural responses to optimally extract the carrier information. Among others, transformation operations can be particularly useful in VSHM deployments, allowing the signal representation in various domains and co-domains (*e.g.*, time, space, frequency domain). Examples include the Wavelet Transform in the joint time-frequency or space-frequency domain (plane) (*e.g., Goswami & Chan* (1999)), being a powerful signal analysis tool capable to identify abrupt and cumulative damages (*e.g., Sun & Chang* (2004); *Taha* (2006)).

1.2. Conventional Wireless Sensor Networks (WSN) in VSHM

Over the last two decades, the consideration of wireless sensor networks (WSNs) has been an important development in VSHM of civil structures (*e.g.*, *Lynch & Loh* (2006); *Lynch* (2007); *Nagayama & Spencer* (2007); *Spencer & Yun* (2010)). It has emerged as a viable alternative to cabled sensor networks which are restricted by costly and labour-intensive installations of long coaxial wires. Specifically, WSNs enable dense structural instrumentation and access to remote locations on structures, offering less obtrusive, rapid, and more economical VSHM implementations, especially in monitoring large-scale and geometrically complex civil engineering structures. Compared to arrays of wired sensors, the reduction in cost is reported to be one to two orders of magnitude per sensing channel in real life applications (*e.g.*, *Spencer & Yun* (2010)). Thus, WSNs are particularly suited for periodic VSHM of the large stocks of existing structures and for VSHM in the aftermath of natural disasters in densely populated areas.

Nonetheless, wireless sensors are mainly powered by batteries in need of frequent replacement (*e.g.*, from few weeks to few months depending on the application and the sampling considerations). Apart from the environmental impact, this has a direct impact on the maintenance cost of "permanent" VSHM in large-scale deployments and poses constraints to the rapid assessment of large number of structures. Alternatively, energy harvesting solutions can be used to power WSNs by exploiting environmental energy sources (*e.g.*, wind, solar, thermal, etc.) – however, such solutions increase the overall cost for sensor deployment and pose restrictions in sensors placement. Thus, the consensus is that WSNs will become the preferred way for low-cost VSHM in civil structures once its major limitation – energy supply and power consumption – is addressed in a cost-effective manner (*e.g.*, *Lynch & Loh* (2006); *Lynch* (2007)).

A typical WSN used for VSHM is composed of *wireless sensors* – equipped with a sensing interface, computational core, and wireless transceiver – and a *server* (*base station)* that collects the transmitted measurements for further processing. In each component, the following operations are performed (see also Figure 1.1(a) and *Lynch & Loh* (2006); *Lynch* (2007); *Nagayama & Spencer* (2007); *Novakovic et al.* (2009); *Spencer & Yun* (2010)):

- *Sensing interface (wireless sensor)*: Traditional analog-to-digital converters (ADCs) are utilised to acquire structural responses at the uniform Nyquist rate, which is defined as twice the highest frequency component in the measured signals (*i.e.*, twice the signal's bandwidth, *e.g.*, *Jerri* (1977)). In practical applications, though, faster sampling rates are employed followed by low-pass filtering to eliminate any potential aliasing and to increase resolution.

- *Computational core (wireless sensor)*: The acquired measurements are then stored at the sensor and locally processed by on-board micro-processors that typically perform *off-line*

lossy or lossless data compression (*e.g., Duarte et al.* (2012)). The main goal of this operation is to address the increased power demands and bandwidth limitations in wireless transceivers.

- *Wireless Transceiver (wireless sensor)*: This building block is responsible for the wireless communication between sensors and server by wirelessly transmitting and receiving the measured data. Notably, wireless data transmission is by far the most power consuming operation in WSNs ((*e.g., Lynch* (2007)), being inextricably linked with the local energy harvesting and/or battery replacement requirements in wireless sensors. The wireless transceivers are also constrained by the limited available wireless transmission bandwidth, posing limitations on the amount of data that can be reliably transmitted within WSNs.
- *Server (base station)*: After wireless data transmission to the server, the encoded measurements (*i.e.*, compressed data) are *de-compressed* to retrieve the originally acquired signals, or an estimate of them in case of lossy compression schemes. The recovered measurements can be further processed by standard VSHM algorithms to retrieve the salient features of the monitored structures.

Despite these efforts, the power resources of current WSNs are limited by the technical specifications of conventional wireless sensors, associated with the power consumption in the above operations (*i.e.*, sampling and analog-to-digital conversion; computational and memory requirements; wireless communications among sensors and server, *e.g., Lynch & Loh* (2006); *Lynch* (2007); *Nagayama & Spencer* (2007); *Novakovic et al.* (2009); *Spencer & Yun* (2010)). Within this context, the most important factors are:

- the *sampling considerations, i.e.*, the sampling rate and resolution, continuous or periodic sampling and the pertinent duration of each monitoring interval, the length of the acquired dataset and the number of transmitted data;
- the *computational efficiency, i.e.*, the on-board hardware and software to be executed;
- the *network size, i.e.*, the number of wireless sensors within the network;
- the *network topology* and the *wireless communication* protocol, controlling the power consumption by minimising the wireless transmission range and increasing the communication reliability by addressing the problem of information loss (*i.e.*, due to missing data packets and/or multipath fading when radio waves are masked by obstacles, etc.);
- the *power supply and resources, i.e.* the battery type, capacity, and drainage ratio due to ageing, or the energy harvesting requirements; and

- other issues related to errors due to inherent measurement noise in sensors, as well as spatial issues associated with the positioning of sensors.

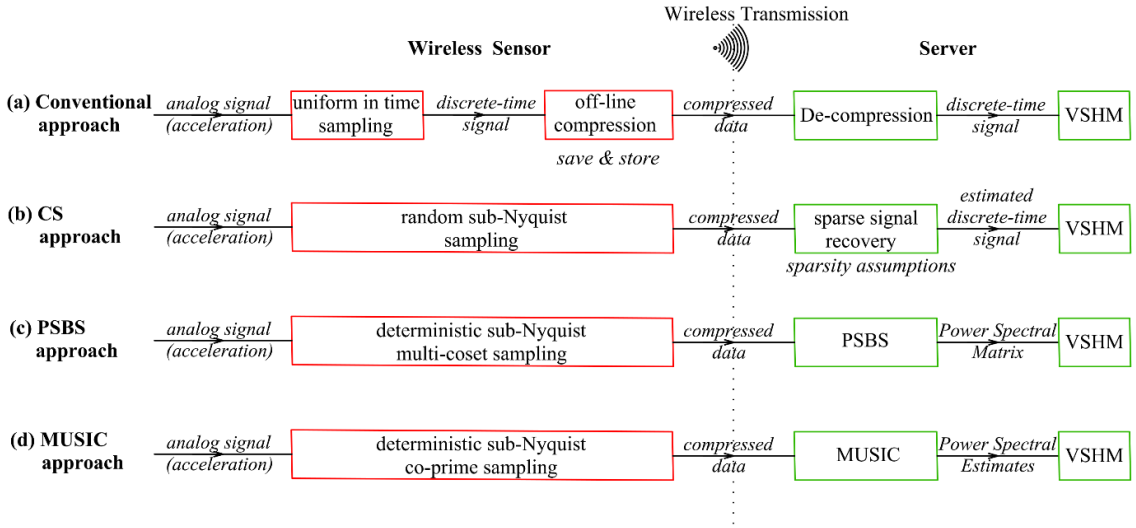

Figure 1.1: *Comparison of four different data acquisition schemes in wireless sensors for VSHM: (a) conventional; (b) CS-based; (c) PSBS-based; and (d) co-prime based approach*

1.3. Sub-Nyquist Data Acquisition Schemes for Low-Power WSNs in VSHM

Recent advances in *sub-Nyquist* sampling schemes have paved the way for the development of *Analog-to-Information Converters* that involve simultaneous signal acquisition and compression at the sensor front-end prior to wireless transmission (*e.g.*, *Tropp et al.* (2006), (2010); *Bajwa et al.* (2007); *Mishali & Eldar* (2010); *Baraniuk et al.* (2011); *Jingchao et al.* (2015); *Moon et al.* (2015)). Arguably, this technological breakthrough can offer viable alternatives for low-power WSNs in VSHM deployments, leading to significant savings in wireless communications (*e.g.*, *O'Connor et al.* (2014)). The latter is accomplished by considering low-rate non-uniform sampling strategies (below the Nyquist rate) capable to:

- Reduce the sampling and power requirements in the sensing interface;
- Minimise the dimensions of transmitted data, yielding drastic reductions in the consumed power during wireless communications while efficiently addressing the pertinent bandwidth limitations;
- By-pass the computational requirements for on-sensor data storage and local on-board data processing before wireless transmission; and
- Transfer most of the data post-processing and the associated computational burden from the sensors to the server (*e.g.*, *Duarte et al.* (2012)).

Motivated by the above advances, this thesis focuses on the development of novel algorithmic approaches based on compressive/sub-Nyquist data acquisition and processing techniques to address the power constraints in WSNs used for operational modal analysis and data-driven damage detection in civil engineering structures.

This line of research has been primarily triggered by developments in the field of *Compressive Sensing* (CS) (*e.g., Candès et al.* (2006); *Donoho* (2006); *Baraniuk* (2007)) – a recently proposed sub-Nyquist sampling scheme that exploits the signal's *sparsity* (*i.e.*, the non-zero signal coefficients) on an orthonormal basis to achieve dimensionality reduction. Based on *random* non-uniform in time data acquisition techniques at average sampling rates below Nyquist, *Candès* proved that any sparse signal can be reconstructed, with high probability, at the uniform Nyquist grid from a relatively small number of random measurements by solving an underdetermined system of linear equations subject to sparsity constraints (*e.g., Candès* (2008)).

Interestingly, the CS theory is valid within the VSHM framework since structural vibration responses preserve a *compressible* (*i.e.*, nearly sparse) structure in various domains and co-domains (*e.g.*, noiseless response acceleration signals from linear vibrating structures tend to be appreciably sparse in the frequency domain, since their Fourier coefficients with non-negligible magnitudes are clustered around their natural frequencies). These important findings have motivated numerous VSHM research studies in the literature over the last decade, aiming to provide quality structural estimates from compressed data while efficiently addressing the WSN challenges related to bandwidth constraints, limited power resources, and loss of information due to wireless data transmissions. In this respect, *O'Connor et al.* (2014) developed the CS-based approach shown in Figure 1.1 (b), which was implemented in the first long-term VSHM field deployment using customised *Analog-to-Information Converters*. Given its successful implementation, the approach of *O'Connor et al.* is treated herein as a paradigm of CS-based VSHM using low-rate randomly sampled measurements; thus, it is adopted in this study for comparative purposes. *Nonetheless, the CS sparse recovery is a computationally intensive problem that strongly depends on the sparsity attributes of the measured signals on a pre-defined vector basis. This sparsity information, though, is unknown in real-time VSHM deployments while it is adversely affected by noisy environments encountered in practice* (*e.g., Bao et al.* (2011); *O'Connor et al.* (2014); *Huang et al.* (2016)).

1.4. Aims and Objectives

The current research study aims to circumvent the above CS limitations by setting three goals. The first goal is to improve the CS-based VSHM approaches by examining the sparsest representation of vibrating responses on the wavelet transform domain using various oscillatory functions with different frequency domain attributes. In this respect, a novel CS-based damage

detection algorithm is developed herein, capable to retrieve *data-driven* damage indices directly from compressive data without reconstructing structural responses in time-domain. The proposed method couples the CS framework with the Relative Wavelet Entropy (RWE), a well-established in the literature damage-sensitive index (*e.g., Ren & Sun* (2008); *Yun et al.* (2011); *Lee et al.* (2014)) derived by wavelet transforming response acceleration signals obtained from a healthy/reference and a damaged state of a given (linear) structure subject to broadband excitations.

The second goal is to develop a novel signal-agnostic *sub-Nyquist spectral estimation strategy* (Figure 1.1 (c)) free from sparsity constraints, which is proposed herein as a viable alternative for power-efficient WSNs in VSHM applications. The developed strategy relies on *Power Spectrum Blind Sampling* (PSBS) techniques (see also *Leus & Arianandа* (2011)) together with a *deterministic* non-uniform-in-time sampling scheme, known as *multi-coset sampling (e.g.., Venkataramani & Bresler* (2001)), which can be implemented by utilising $\bar{M}$ interleaved ADCs each operating $\bar{N}$ times slower than the Nyquist rate $\left(\bar{M} < \bar{N}\right)$. Ultimately, this novel approach in Figure 1.1 (c) can retrieve auto/cross power spectral estimates of non-sparse wide-sense stationary random signals (*i.e.*, stochastic processes) directly from compressed measurements, by-passing the computationally demanding signal reconstruction operations in time-domain. This is achieved based on a weighted least-squares optimisation criterion (*e.g., Tausiesakul & Gonzalez-Prelcic* (2013)) which mathematically defines an *overdetermined* system of linear equations that can be easily solved.

The third goal is to introduce a *sub-Nyquist pseudo-spectral estimation* method (Figure 1.1 (d)) for structural natural frequency estimation and/or damage detection using compressed signals contaminated with broadband noise. This approach couples the *deterministic sub-Nyquist co-prime sampling* scheme proposed by *Vaidyanathan & Pal* (2011) with the *multiple signal classification* (MUSIC) algorithm for spectral estimation (*e.g., Marple* (1987)) – a framework that was originally developed in radar applications to address the bandwidth limitations in wireless communications and detect unoccupied bands in telecommunication signals buried in high level noise. Similar to the developed approach in Figure 1.1 (c), the adopted sub-Nyquist MUSIC-based approach does not rely on signal sparsity conditions while it treats structural response signals as wide-sense stationary stochastic processes. However, co-prime sampling is significantly different from the multi-coset sampling as it considers two sensors per acceleration channel operating at different sub-Nyquist rates and accumulating collectively in time a much smaller number of measurements than a single sensor operating at the Nyquist rate. With the aid of the spatial smoothing technique (*e.g., Pal & Vaidyanathan* (2011)), the method in Figure 1.1(d) can extract structural resonant frequencies (*i.e.*, locations of pseudo-spectral peaks) from a

significantly reduced number of measurements with super-high resolution while filtering out additive broadband noise.

1.5. List of Referred Papers

Parts of this thesis, indicated in the next sub-sections, have already been published, or submitted for publication, in the following peer-reviewed journal papers and conference proceedings.

1.5.1. Journal papers

[J1] Gkoktsi, K. & Giaralis, A., 2015. Effect of frequency domain attributes of wavelet analysis filter banks for structural damage localization using the relative wavelet entropy index. *International Journal of Sustainable Materials and Structural Systems (IJSMSS)*, 2(1/2), pp.134–160.

[J2] Gkoktsi, K. & Giaralis, A., 2017. Assessment of sub-Nyquist deterministic and random data sampling techniques for operational modal analysis. *Structural Health Monitoring: An International Journal*, 16(5), pp.630–646.

[J3] Gkoktsi, K. & Giaralis, A., 2018. A multi-sensor sub-Nyquist power spectrum blind sampling approach for low-power wireless sensors in operational modal analysis applications. *Mech. Syst. Signal Process.* (under review, submitted September 2017).

1.5.2. Conference proceedings

[C1] Gkoktsi, K. & Giaralis, A., 2014. On the influence of frequency selectivity of wavelet bases for relative wavelet entropy-based structural damage localization. In *6th World Conference on Structural Control and Monitoring (6WCSCM)*. pp. 1366–1378.

[C2] Tausiesakul, B., Gkoktsi, K. & Giaralis, A., 2014. Compressive Sensing Spectral Estimation For Output-Only Structural System Identidication. In *7th International Conference on Computational Stochastic Mechanics*. pp. 1–12.

[C3] TauSiesakul, B., Gkoktsi, K. & Giaralis, A., 2015. Compressive power spectrum sensing for vibration-based output-only system identification of structural systems in the presence of noise. In *SPIE Sensing Technology + Applications*.

[C4] Gkoktsi, K., TauSiesakul, B. & Giaralis, A., 2015. Multi-channel sub-Nyquist cross-Spectral Estimation for Modal Analysis of Vibrating Structures. In *International Conference on Systems, Signals and Image Processing (IWSSIP 2015)*.

[C5] Gkoktsi, K., Giaralis, A. & TauSiesakul, B., 2016. Sub-Nyquist signal-reconstruction-free operational modal analysis and damage detection in the presence of noise. In J. P. Lynch, ed. *SPIE Smart Structures and Materials + Nondestructive Evaluation and Health Monitoring*. International Society for Optics and Photonics, p. 980312.

[C6] Gkoktsi, K. & Giaralis, A., 2016. Assessment of sub-Nyquist deterministic and random data sampling techniques for operational modal analysis. In *8th European Workshop On Structural Health Monitoring (EWSHM 2016)*. Bilbao, Spain.

[C7] Gkoktsi, K., Giaralis, A., Klis, R.P., Dertimanis, V. & Chatzi E., 2017. Vibration-based structural performance assessment via output-only sub-Nyquist / compressive wireless sensor data. In *4th International Conference on Smart Monitoring, Assessment and Rehabilitation of Civil Structures (SMAR).*

[C8] Gkoktsi, K., Giaralis, A. & Tausiesakul, B., 2017. A reconstruction-free sub-Nyquist sensing approach for earthquake damage detection using the MUSIC algorithm. In *16th World Conference on Earthquake Engineering*.

1.6. Thesis Organisation

This thesis is divided into eight chapters. The current introductory chapter (§*1. Introduction*) gives a general overview of the notion of the vibration-based structural health monitoring (VSHM) in civil engineering structures using wireless sensor networks (WSN) and reports the limitations encountered in conventional and advanced approaches, concluding with the scope of this thesis and the aims and objectives set. *Chapter 2* (§*2. Compressive Sensing: Basic Concepts & Applications in VSHM*) presents the basic principles of the Compressive Sensing (CS) theory and reviews the state-of-the-art in CS-based VSHM approaches for civil structures, underlying the main factors that limit their performance. Recognising that CS is constrained by signal sparsity requirements on a pre-defined vector basis, a comprehensive numerical study is undertaken in *Chapter 3* (§*3. CS-based Damage Detection Using the Relative Wavelet Entropy*) to define the "sparsest" representation of structural responses on the wavelet transform domain using various wavelet analysis filter banks with different frequency domain attributes. From these findings, a novel CS-based RWE damage detection algorithm is further proposed for data-driven VSHM deployments using dense arrays of wireless sensors with reduced power demands. (*Parts of Chapter 3 have been published in the journal paper [J1] of §1.5.1, and in the conference proceedings [C1] of §1.5.2*).

Chapter 4 (§*4. Proposed Multi-Sensor Power Spectrum Blind Sampling Approach for OMA: Theory*) provides the theoretical development of the *multi-sensor PSBS-based strategy* –a signal-agnostic compressive auto/cross power spectrum estimation approach that enjoys numerous advantages over the state-of-the-art CS-based approaches used for low-power WSNs in OMA applications. The effectiveness of the proposed strategy is numerically evaluated in *Chapter 5* (§*5. Proposed Multi-Sensor Power Spectrum Blind Sampling Approach for OMA: Applications*) using four examples. Firstly, the recovery performance of the PSBS-based approach is numerically assessed under the influence of signal compression and noise levels, which is further verified with field-recorded data obtained from an operational wind turbine. Next, the modal identification and damage detection capabilities of the developed method are examined with simulated compressed (multi-coset sampled) data originating from finite element models of benchmark structures. In *Chapter 6* (§ *6. Assessment of the Proposed PSBS Approach vis-à-vis CS-Based Approachfor OMA*), the proposed multi-sensor PSBS-based approach is comparatively assessed vis-à-vis the Compressive Sensing (CS) based approach developed by *O'Connor et al.* (2014) for OMA. Comparative numerical results are presented for both synthetic (*i.e.*, computer-

generated signals with different sparsity levels) and field-recorded (*i.e.*, from an operational bridge in Zurich, Switzerland) wide-sense stationary structural acceleration response datasets. Estimates of the anticipated energy savings achieved by the proposed approach are further provided using the second dataset (*i.e.*, real data), assuming a battery-operated wireless multi-coset sampler. (P*arts of Chapters 4 – 6 have been published, or submitted for publication, in the journal papers [J2, J3] of §1.5.1, and in the conference proceedings [C2 – C7] of §1.5.2).*

Next, *Chapter 7* (§ *7. A Novel MUSIC-Based Approach for Structural Damage Detection from Sub-Nyquist Measurements*) reviews the theoretical background of the *co-prime MUSIC strategy* proposed by *Pal & Vaidyanathan* (2011) and explores its applicability and usefulness in VSHM of civil engineering structures. Special focus is given in OMA applications susceptible to the modal coupling effect in the presence of noise. A significant contribution of this chapter is the development of a novel damage detection approach aiming to infer structural damage due to low-intensity earthquake excitations by monitoring small shifts to the resonant frequencies directly from compressed (co-prime sampled) response acceleration data contaminated with noise. *(Parts of Chapter 7 have been published in the conference proceedings [C8] of §1.5.2*).

Finally, *Chapter 8* (§ *8. Conclusions*) summarises the contributions achieved by this doctoral thesis and highlights areas for future research.

Chapter 2
Compressive Sensing:
Basic Concepts & Applications in VSHM

2.1. Preliminary Remarks

This chapter presents the rudiments of *Compressive Sensing* (CS) (*e.g.*, *Candès et al.* (2006); *Donoho* (2006); *Baraniuk* (2007)) – a recently emerged sub-Nyquist random sampling scheme that offers reliable and low-power wireless data transmissions, gaining increasing popularity in various research fields (*e.g.*, *Qaisar et al.* (2013)), including the VSHM framework for civil engineering structures.

In a nutshell, the CS theory asserts that a discrete-time finite length signal (*e.g.*, an analog response acceleration signal uniformly sampled in time) can be recovered, with high probability, from a relatively small number of randomly acquired samples/measurements in time, by solving an underdetermined system of linear equations. Importantly, the number of random (compressed) measurements required for a faithful signal recovery is governed by the "*sparsity*" information of the acquired signal on some known pre-specified vector basis rather than the signal's bandwidth as dictated by the Nyquist/Shannon sampling theorem (*e.g.*, *Jerri* (1977)). The above CS theoretical developments have been widely used for structural modal identification and damage detection purposes (*e.g.*, *Bao et al.* (2014)), and also fused with other signal processing tools (*e.g.*, *Nagarajaiah & Yang* (2017)) to efficiently address various VSHM challenges.

In this respect, an extended literature review of the CS-based VSHM approaches for civil structures is presented herein, classified into three categories depending on the application at hand (*i.e.*, sub-sections §*2.4.1. CS-based operational modal analysis*, §*2.4.2. CS-based damage detection*, and §*2.4.3. CS for recovery of missing data in WSNs for VSHM applications*). It will be recognised that the efficiency of the CS-based approaches is limited by the *sparsity* level of the monitored signals, which is practically unknown and adversely affected in noisy environments, while it strongly depends on the suitability of the adopted expansion basis. These observations are discussed at the end of this chapter, raising some open issues to be addressed in the succeeding chapters.

In this chapter, the mathematical background of the CS theory is briefly reviewed in section §2.2 (§*2.2. Overview of Basic Theoretical Aspects of Compressive Sensing*). The next section (§*2.3. CoSaMP - CS Sparse Signal Reconstruction Algorithm*) presents a CS sparse recovery algorithm for noisy signals (*i.e.*, the CoSaMP algorithm developed by *Needell & Tropp* (2009)) that has been adopted in the numerical work undertaken in Chapter 3 (§*3. CS-based Damage Detection Using the Relative Wavelet Entropy*) and Chapter 6 (§*6. Assessment of the Proposed PSBS Approach vis-à-vis CS-based Approach for OMA*). The current state-of-the art in CS-based VSHM applications is next reviewed in section 2.4 (§*2.4. Overview of Compressive Sensing in Structural Health Monitoring*), while their limitations are discussed in section 2.5 (§*2.5. CS Limitations & Conclusions*) followed by concluding remarks.

2.2. Overview of Basic Theoretical Aspects of Compressive Sensing

2.2.1. Signal sparsity on a given basis matrix

Consider a deterministic N-long discrete-time (response acceleration) signal $x[n] \in \mathbb{R}^N$ having a "sparse" structure on a given vector basis $\mathbf{\Psi} \in \mathbb{C}^{N \times N}$. Examples of such a basis include the discrete Fourier transform (DFT) basis used for representation of vectors in the Fourier/frequency domain, a wavelet transform basis for the time-frequency analysis of signals, or, more generally, a "dictionary" of vectors basis (*e.g.*, *Rubinstein et al.* (2010)). The signal expansion on the adopted basis $\mathbf{\Psi}$ is written in the form

$$x[n] = \mathbf{\Psi}\, u[n], \tag{2.1}$$

where $u[n] \in \mathbb{C}^N$ is the vector collecting the signal coefficients on the considered basis, having S entries with significant magnitude, where $S \ll N$.

By definition, an *S-sparse* signal has only S non-zero expansion coefficients on some vector basis/dictionary. For illustration, consider a discrete-time multi-tone signal $x[n]$ of length N=256, comprising 2 harmonic components at f_1=121 Hz and f_2=223 Hz, which is sampled from a continuous signal, $x(t)= \sin(2\pi f_1 t)+ \sin(2\pi f_2 t)$, at a sampling rate F_s=1000 Hz (T=0.001s). Figure 2.1 plots the considered multi-tone signal $x[n]$ both in time (Figure 2.1(a)) and frequency domain (Figure 2.1(b)– single-sided Fourier spectrum). It is readily observed that the adopted discrete-time signal has a sparse structure on the Fourier/frequency domain attaining only S=2 non-zero spectral peaks at f_1=121 Hz and f_2=223 Hz in the frequency range [0, 500] Hz. Assuming next that the multi-tone signal $x[n]$ is corrupted with a zero-mean additive Gaussian white noise with a signal-to-noise ratio (*SNR*) at 0dB (*i.e.*, $SNR = 10 \cdot \log_{10}\left(\sigma_x^2 / \sigma_\varepsilon^2\right)$, where σ_x^2 and σ_ε^2 are the

signal and the noise variance, respectively; the extreme noise case of *SNR*= 0dB pertains to $\sigma_e^2 \approx \sigma_x^2$). The time and frequency representation of the generated noisy signal is illustrated in Figure 2.2. Note that the Fourier spectrum exhibits *S*=2 significant spectral peaks at the same frequencies as in the noiseless case; however, the remaining peaks are not exactly zero, but they yield considerably smaller values compared to the dominant spectral peaks.

In practical applications, though, real signals are not purely sparse on a given domain (*i.e.*, due to damping in structural systems and/or due to signal acquisition in inherently noisy environments, etc); instead, they are often *compressible*, meaning that they have certain expansion coefficients on a given basis/dictionary with values larger than a relatively low threshold so that their entries decay rapidly when sorted by magnitude. Under these circumstances, an *S-compressible* signal can be well-represented by the associated *S-sparse* signal; therefore, these two terms are used interchangeably hereafter. Notably, the signals' sparsity/compressibility is a key property that can lead to dimensionality reduction, enabling the simultaneous signal acquisition and compression within the CS framework in an efficient manner. Apparently, the higher sparsity level of the underlying signal (*i.e.*, the fewer number of *S* values it comprises), the higher signal compression can be achieved, requiring the acquisition of fewer random measurements for its *sparse recovery* (*i.e.*, estimation of the *S* non-zero expansion coefficients) as explained in what follows next.

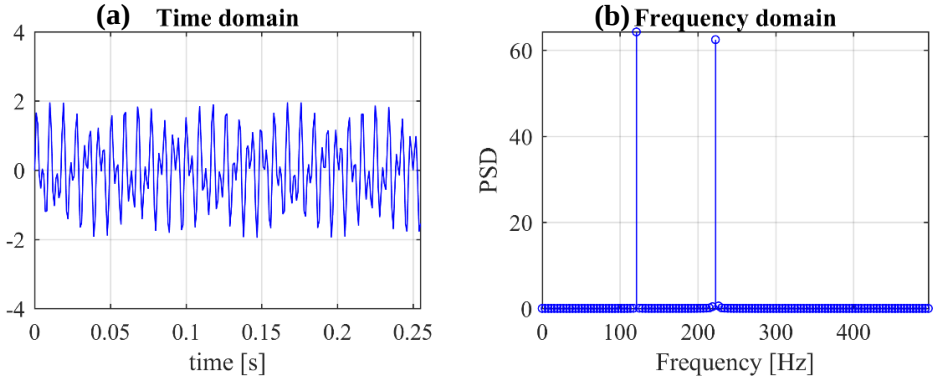

Figure 2.1:*Noiseless multi-tone signal in (a) time domain and (b) single-sided Fourier spectrum in frequency domain*

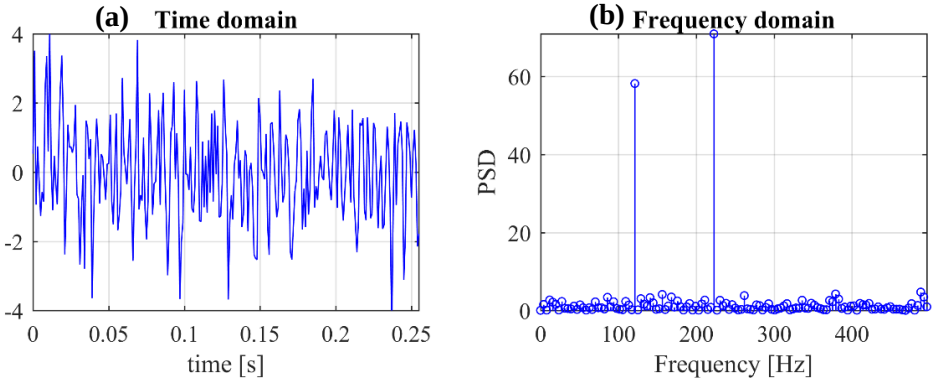

Figure 2.2: *Noisy multi-tone signal with SNR=0dB in (a) time domain and (b) single-sided Fourier spectrum in frequency domain*

*2.2.2. Random measurement matrix **Θ** and the restricted isometry property*

As illustrated in Figure 2.3, the CS theory (*e.g.*, *Candès et al.* (2006); *Donoho* (2006); *Baraniuk* (2007)) asserts that the information contained in the *S*-sparse signal $x[n]$ in eq. (2.1) can be retrieved in a robust manner from *M* non-uniform random measurements $y[m] \in \mathbb{R}^M$

$$y[m] = \mathbf{\Theta}\, x[n] \;= \mathbf{\Theta}\, \mathbf{\Psi}\, u[n] \tag{2.2}$$

for $S<M \ll N$, and M/N defining the *compression ratio* (*CR*). The above can be achieved by considering a random measurement matrix $\mathbf{\Theta} \in \mathbb{C}^{M \times N}$ during sampling that satisfies the so-called restricted isometry property (RIP) (*i.e.*, *Candès* (2008))

$$(1-\delta_S)\|x\|_2^2 \le \|\mathbf{\Theta} x\|_2^2 \le (1+\delta_S)\|x\|_2^2 \tag{2.3}$$

with δ_S being the *S*-restricted isometry constant, and $\|\mathrm{a}\|_p$ denoting the ℓ_p norm of the vector a, *i.e.*

$$\|\mathrm{a}\|_p = \left(\sum_i \mathrm{a}_i^p \right)^{1/p}, \quad p \in [1, \infty]. \tag{2.4}$$

The RIP in eq. (2.3) is associated with the orthonormality level of the columns of **Θ**, which enables the exact recovery of an *S*-sparse signal $x[n]$ from only *M* measurements in $y[m]$ provided that δ_S yields very small values (*i.e.*, δ_S <1) (*i.e.*, *Candès* (2008).

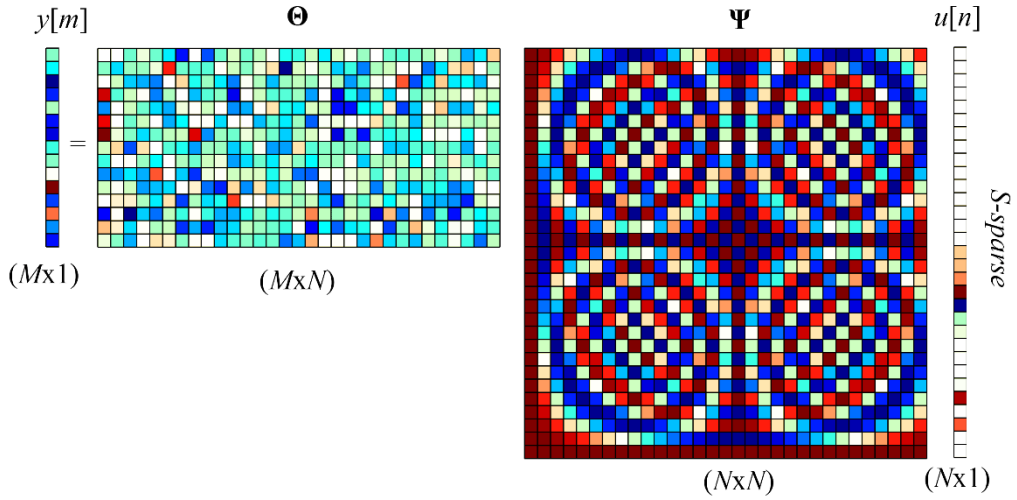

Figure 2.3: *Compressive sensing measurement process with a random Gaussian measurement matrix* **Θ** *and the Inverse Discrete Fourier Transform IDFT matrix* **Ψ**. *The vector of coefficients u[n] is S-sparse (figure adapted from Baraniuk* (2007)*).*

Conveniently, the RIP holds with high probability for several matrices $\mathbf{\Theta} \in \mathbb{C}^{M\times N}$ (*e.g.*, *Candès* (2006)). Examples include random matrices populated with independent and identically distributed entries sampled from a normal distribution with zero mean and variance 1/*M* (*i.e.*, Gaussian measurements) or from a symmetric Bernoulli distribution (*i.e.*, binary measurements) for which the RIP is satisfied for *M* of the order of *S*·log(*N*/*M*),(symbolically $M = O\left(S\log\left(N/M\right)\right)$). Other examples include measurement matrices $\mathbf{\Theta} \in \mathbb{C}^{M\times N}$ populated with incoherent measurements of zero-one entries that randomly selects *M* rows from an orthonormal matrix $\mathbf{\Psi} \in \mathbb{C}^{N\times N}$. In this manner, a "partial" sampling matrix $\mathbf{A} = \mathbf{\Theta\Psi}$, $\mathbf{A} \in \mathbb{C}^{M\times N}$ is defined, which satisfies the RIP in eq. (2.3) with high probability (*i.e.*, $(1-\delta_S)\|u\|_2^2 \le \|\mathbf{A}u\|_2^2 \le (1+\delta_S)\|u\|_2^2$) on condition that

$$M = O\left(S \cdot \mu_{\mathbf{A}}^2 \cdot \log^4(N)\right). \tag{2.5}$$

In the above equation, $\mu_{\mathbf{A}}$ is derived from

$$\mu_{\mathbf{A}} = \sqrt{N}\max_{i\ge 1, j\le N}\left|\mathbf{\Theta}_i\mathbf{\Psi}_j\right| \tag{2.6}$$

and represents the mutual coherence between the *i*-rows of $\mathbf{\Theta}$ and the *j*-columns of $\mathbf{\Psi}$, taking values within the range $1 \le \mu_{\mathbf{A}} \le \sqrt{N}$, with the limiting cases of $\mu_{\mathbf{A}} = 1$ and $\mu_{\mathbf{A}} = \sqrt{N}$ pertaining to the maximum and minimum incoherence, respectively. Eq. (2.5) and eq. (2.6) suggest that the higher the incoherence between the selected pair of matrices ($\mathbf{\Theta}$,$\mathbf{\Psi}$) is (*i.e.*, at smaller $\mu_{\mathbf{A}}$ values), the fewer number of measurements, *M*, need be acquired for a faithful reconstruction of the unknown signal *x*[*n*] (*e.g.*, *Candès* (2006)). A special case of a "partial" sampling matrix with incoherent measurements is the "partial" Fourier matrix, or equivalently, the partial inverse Fourier matrix, $\mathbf{A} = \mathbf{F}_{M\times N}^{-1} \in \mathbb{C}^{M\times N}$ illustrated in Figure 2.4, which is defined by randomly selecting *M* rows from the standard orthonormal inverse discrete Fourier transform (IDFT) matrix $\mathbf{\Psi} = \mathbf{F}_{N\times N}^{-1} \in \mathbb{C}^{N\times N}$ in

$$\mathbf{F}_{N\times N}^{-1} = \frac{1}{\sqrt{N}}\exp(-i\ 2\pi nk/N), \quad n,k = [0,1,\cdots,N-1] \tag{2.7}$$

to construct the re-normalised to unit-norm "partial" matrix $\mathbf{A} = \mathbf{F}_{M\times N}^{-1} \in \mathbb{C}^{M\times N}$

$$\mathbf{F}_{M\times N}^{-1} = \sqrt{\frac{N}{M}}\exp(-i\ 2\pi mk/N), \quad \begin{matrix} m = [0,1,\cdots,M-1] \\ k = [0,1,\cdots,N-1]. \end{matrix} \tag{2.8}$$

Notably, eq. (2.8) satisfies the RIP with high probability (*i.e.*, 99%) yielding $\mu_{\mathbf{A}} = 1$ and $M = O(S \cdot \log^4 N)$ (*e.g.*, *Rudelson & Vershynin* (2008)) (see also eq. (2.5) and eq. (2.6)). *Candès* (2006) reported that the above theoretical bound derives from sophisticated techniques and may be too stringent, suggesting that M should be of the order of $O(S \cdot \log N)$. The latter has also been adopted in a CS-based VSHM study by *O'Connor et al.* (2014), providing reasonably accurate sparse approximations of the signal coefficients (on the DFT basis) of field-recorded response acceleration signals, leading to acceptable structural modal estimates. The above theoretical advances combined with the ease of implementation of the "partial" Fourier matrix in practice (*e.g.*, *Needell & Tropp* (2010)) has rendered the latter as the preferred sampling considerations in various CS-based VSHM applications as discussed in section §2.4.

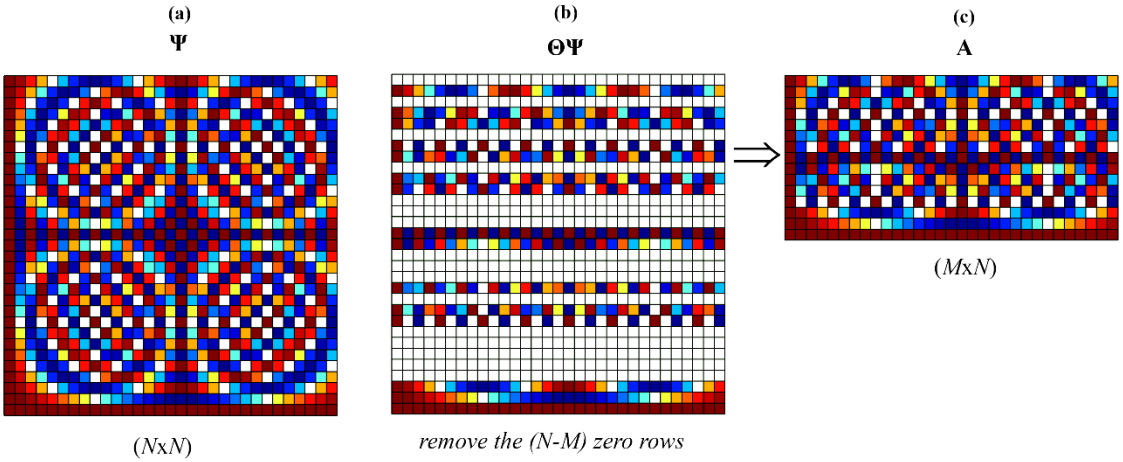

***Figure 2.4**: (a) Orthonormal IDFT basis $\mathbf{\Psi} \in \mathbb{C}^{N \times N}$, (b) selection of M random rows from $\mathbf{\Psi} \in \mathbb{C}^{N \times N}$ to derive (c) the partial IDFT matrix $\mathbf{A} \in \mathbb{C}^{M \times N}$*

Recent developments in hardware architecture of sensors paved the way for the design of *Analog-to-Information Converters* prototypes that support random acquisitions of compressed measurements in real-time. Among the most well-known CS-based *Analog-to-Information Converters* are the *random demodulator* (*e.g.*, *Tropp et al.* (2010)), the *random filtering* (*e.g.*, *Tropp et al.* (2006)), the *random convolution* (*e.g.*, *Bajwa et al.* (2007); *Romberg* (2009)), the *compressive multiplexer* (*e.g.*, *Slavinsky et al.* (2011)), and the *random modulator pre-integrators* (*e.g.*, *Becker* (2011)). It is important to note that the above architectures typically pertain to reduced level of randomness using more structured matrices that satisfy the RIP (*e.g.*, partial Fourier matrix) compared to a fully random matrix, since the latter is not physically realisable in hardware design (see also *Baraniuk et al.* (2011)). Despite the above advances, such *Analog-to-Information Converters* are not commercially available yet.

2.2.3. Time-domain reconstruction of noisy measurements

To account for the inherent noisy sensor measurements encountered in practical applications, eq. (2.2) can be cast in the form

$$y[m] = \boldsymbol{\Theta}\,\boldsymbol{\Psi}\,u[n] + \boldsymbol{\varepsilon} = \mathbf{A}\,u[n] + \boldsymbol{\varepsilon}\,, \tag{2.9}$$

where $\boldsymbol{\varepsilon}$ is the error vector added to compressed data $y[m]$. Such errors do not influence the sparsity level S of the signal $x[n]$ and they are treated by numerous practical CS sparse recovery algorithms by solving the so-called "noisy" sparse recovery problem. Notably, the problem in eq. (2.9) defines an underdetermined system of linear equations, which yields a unique solution when subjected to signal's sparsity constraint. Assuming no prior knowledge on the location and amplitude of the signal coefficients $u[n]$ on a given basis, or, equivalently, in the transform domain, *Candès* proved that the dominant S coefficients in $u[n]$ can be recovered from the compressed noisy measurements $y[m]$ by solving the ℓ_1 convex optimisation problem (*e.g.*, *Candès* (2008)), that is

$$\min_{\hat{u}\in\mathbb{R}^N} \left\|\hat{u}\right\|_1 \quad \text{subject to} \quad \left\|y - \mathbf{A}\hat{u}\right\|_2 \le e\,, \tag{2.10}$$

where e pertains to the upper bound of the noise energy $\left\|\boldsymbol{\varepsilon}\right\|_2$. Eq. (2.10) defines a complex problem with increased computational demands. To overcome this issue, several faster and computationally more efficient sparse signal reconstruction algorithms have been developed (*e.g.*, *Bruckstein et al.* (2009); *Vaswani & Zhan* (2016)) to approximate a signal $x[n]$ and/or its coefficients $u[n]$ on $\boldsymbol{\Psi}$ from the acquisition of only few noisy measurements in $y[m]$. Among the numerous sparse recovery alternatives (*e.g.*, *Vaswani & Zhan* (2016)), the next sub-section presents the iterative matching pursuit algorithm CoSaMP developed by *Needell & Tropp* (2009), which has been adopted in the ensuing numerical work presented in Chapter 3 and Chapter 6.

2.3. CoSaMP - CS Sparse Signal Reconstruction Algorithm

CoSaMP is an acrostic standing from *Compressive Sampling Matching Pursuit* and it represents an iterative CS sparse recovery algorithm for noisy signals, being extremely efficient in practical applications while providing rigorous and fast implementations with relatively low computational burden and storage requirements (*e.g.*, *Needell & Tropp* (2009)). CoSaMP takes as input the compressed observation vector $y[m]$ and the sampling matrix $\mathbf{A} \in \mathbb{C}^{M\times N}$ in eq. (2.9) together with a target sparsity level S_T, which should be less than $M/3$, (*i.e.*, $S_T < M/3$), and a

tolerance parameter η. It returns an S_T-sparse estimate $\hat{u}[n]$ of the S-sparse signal coefficients $u[n]$ that satisfies the condition

$$\left\|u[n]-\hat{u}[n]\right\|_2 \le C\cdot\max\left\{\eta,\frac{1}{\sqrt{S_T}}\left\|u[n]-u_{S_T/2}[n]\right\|_1+\left\|\boldsymbol{\varepsilon}\right\|_2\right\}, \tag{2.11}$$

where $u_{S_T/2}[n]$ is the optimal $S_T/2$-sparse approximation of $u[n]$ – obtained by retaining the $S_T/2$ largest entries of $u[n]$ and setting the remaining entries to zero – C is a positive constant, and $\|\cdot\|_p$ is the ℓ_p norm given in eq. (2.4). In each iteration, CoSaMP captures part of the energy of the target signal by solving a least-squares problem involving the pseudoinverse of the matrix $\mathbf{A} \in \mathbb{C}^{M\times N}$ in eq. (2.9), given in $\mathbf{A}^{\dagger}=(\mathbf{A}^{\mathrm{H}}\mathbf{A})^{-1}\mathbf{A}^{\mathrm{H}}$, where the superscript "H" denotes the Hermitian transpose while the superscript "-1" designates matrix inversion (*e.g.*, *Needell & Tropp* (2009)). The extracted energy is subtracted from the target signal and in the next iteration the residual signal becomes the target signal. This iterative process continues until any of the following three stoppage criteria is met: (i) the relative residual signal energy between two iterations is less than the tolerance η, or (ii) the total residual energy in the last iteration is smaller than η, or (iii) a predefined maximum number of iterations is reached.

2.4. Overview of Compressive Sensing in Structural Health Monitoring

Over the last decade, the vibration-based SHM community has begun to consider CS techniques in WSNs used for modal identification and damage detection in civil engineering structures, with the scope of providing quality structural estimates while efficiently addressing various VSHM challenges related to bandwidth constraints, limited power resources, and loss of information due to wireless data transmissions.

In this context, *Bao et al.* (2011) were the first to examine the potential of using sub-Nyquist random sampling schemes in acceleration response data acquired from an operational cable-stayed bridge in China, which was dynamically vibrating under environmental and traffic loading. The underlying signal sparsity was assessed in both the Fourier and the Haar wavelet transform domain, while signal reconstruction was achieved by solving the noisy sparse recovery optimisation problem in eq. (2.10). This successful implementation has triggered the development of a plethora of CS-based VSHM approaches, which are divided, herein, into three categories and reviewed in the ensuing sub-sections, that is CS-based Operational Modal Analysis (§2.4.1), CS-based damage detection (§2.4.2), and CS for recovery of missing data (§2.4.3).

2.4.1. CS-based operational modal analysis

O'Connor et al. (2013), (2014) were the first to deploy customized CS-based wireless sensors in a long-term monitoring field application. By randomly triggering in time conventional Analog-to-Digital Converters (ADC), they managed to acquire non-uniform in time compressed acceleration responses from an overpass in Michigan, USA, attaining some level of sparsity on the DFT basis. The compressed measurements were wirelessly transmitted to a server and treated by the CoSaMP sparse signal recovery algorithm by *Needell & Tropp* (2009) (see also §2.3) to retrieve the DFT coefficients of the response acceleration signals in the uniform grid and perform a frequency domain-based OMA. Accurate mode shapes estimation as well as appreciable savings in battery energy consumption were achieved using a Wireless Sensor Network (WSN) of five CS-based sensor nodes operating at up to 80% slower average rate compared to a concurrently operating network of conventional wireless sensors sampling uniformly in time at twice an assumed Nyquist rate.

A different sparse recovery algorithm was considered by *Klis & Chatzi* (2015) which enables efficient and more accurate sparse signal recovery by relying on pertinent *a priori* knowledge of the signal sparse structure on the DFT basis. This knowledge is gained from a relatively small network of wired sensors judicially placed onto structures which operates concurrently with the CS-based WSN and samples in the conventional manner (*i.e.*, uniformly-in-time at the Nyquist rate or above). The sparsity of the structural response acceleration signals acquired by the auxiliary wired sensors and its support in the DFT domain are estimated by Fourier transforming the signals at the server. This information is both wirelessly communicated to the CS-based sensors to inform the rate of the random sampling, and stored at the server for the sparse recovery operation.

More recently, a *group sparse optimisation algorithm* was developed by *Bao et al.* (2017) to reconstruct structural response data by exploiting their joint sparsity on the Fourier domain. Using nine commercial wireless sensors on the *Xiamen Haicang Bridge*, velocity response time-series were conventionally acquired at a uniform sampling rate, sub-Nyquist sampled using a non-uniform low-rate random scheme, and reconstructed back in time-domain using the *group sparse optimisation algorithm*. The reconstructed signals were further processed with standard OMA algorithms to retrieve the underlying structural modal properties at the first two dominant modes of vibration. It was shown that smaller signal reconstruction errors occur in larger networks of wireless arrays compared to a single-sensor case, yielding modal estimates of higher accuracy. The latter was verified for compression ratios up to 10% and the processing of 90% less data.

Compared to the previously reviewed approaches, two significantly different methods were proposed by *Yang & Nagarajaiah* (2015) and *Park et al.* (2014), respectively, for mode shape estimation from non-uniform in time random sampling of structural vibration time-histories at

sub-Nyquist rates. Mode shape estimated were retrieved by *Yang & Nagarajaiah* (2015) based on modal structural responses obtained by application of blind source separation directly to compressed measurements of structural response signals. Sparse signal recovery in the time-domain is next applied to each compressed modal response vector to retrieve the underlying structural natural frequencies and modal damping ratios. *Park et al.* (2014) extracted mode shapes based on a novel singular value decomposition algorithm which was applied directly to response acceleration compressed measurements, without taking any signal sparse recovery step. Interestingly, although the theoretical development of *Park et al.* (2014) assumes noiseless undamped free vibration structural response signals (*i.e.*, multi-tone signals), which are different from the typical response time-histories recorded in civil engineering structures under operational conditions, their algorithm performed well when applied to field recorded data from an overpass open to traffic.

Parenthetically, it is noted that CS-based OMA approaches have also been proposed for *lossy off-line signal compression in conventional wireless sensor networks* (*e.g., Klis & Chatzi* (2017)). As opposed to the above-reviewed approaches, data acquisition and data compression are two distinct processes in such applications. In fact, conventional uniform-in-time sampling is first undertaken, while low-rate CS-based random sampling is conducted off-line, locally on each sensor, before wireless transmission. This off-line data compression step is informed by knowledge on the signal sparsity structure, gained via extensive on-sensor processing of the conventionally sampled data. The latter processing involves, at minimum, projection of the uniformly sampled data onto an adopted sparsifying basis and estimation of signal sparsity/compressibility and its support, leading to increased power, memory, and computational requirements onboard (see also §1.2).

2.4.2. CS-based damage detection

A two-stage CS-based damage classification framework was developed by *Mascarenas et al.* (2013) for low-power WSNs, aiming to detect structural damage from compressed measurements. The developed method relies on compressed matched filtering techniques – known as smashed filter – together with training sets of structural data originating from both healthy and damaged structural states. Assuming a user-defined threshold, this application-dependent damage detection method statistically tests the correlation between known sub-sampled structural responses in the training sets with unknown compressed measurements to classify the pertinent observations under the two defined structural states (*i.e.*, healthy or damaged state). The effectiveness of the proposed method was experimentally tested in a lab specimen of a 3-storey frame subjected to harmonic excitations, using a digital prototype of a compressed sensor which first acquires structural responses at fast sampling rates and next performs on-board post-processing operations to

generate compressed data. The latter was accomplished by utilising a random measuring matrix $\boldsymbol{\Theta}$ populated with independent and identically distributed ±1 entries.

In a recent study by *Jayawardhana et al.* (2017), the applicability of the CS theory for structural damage localisation was experimentally tested in a laboratory test specimen pertaining to a reinforced concrete slab with two spans. Static load testing was first performed at various intensity levels to induce structural damage of increasing severity. Impact testing was further undertaken at three different structural damage states and acceleration responses were recorded from six sensors using conventional sampling schemes. De-noising techniques were considered to enhance signal sparsity on the wavelet transform domain using a Daubechies wavelet family, while various compression levels were adopted for signal compression and reconstruction as in (2.10). The reconstructed signals were further treated by two well-established in the literature damage detection algorithms, yielding highly accurate results for *CR* at approximately 40% (*i.e.*, reduced data by a factor of 2.48).

It is noted in passing that local structural damage has also been regarded in the literature as a *spatially sparse* phenomenon (*e.g.*, *Bao et al.* (2014); *Yao et al.* (2016); *Ganesan et al.* (2017)), which can be treated by various well-established CS reconstruction techniques, to identify the location of structural damage from a limited number of sensors placed at random location along a structure. This concept can be viewed as compression in the space domain which lies beyond the scope of this research study. The theory of CS has also inspired various research studied within the pattern recognition and damage classification framework (*e.g.*, *Yang & Nagarajaiah* (2014); *Wang & Hao* (2015)), by considering sparse signal representation on a pre-defined and application-dependent dictionary of structural features linked with various damage scenarios – a considerably different damage detection approach that does not rely on sub-Nyquist sampling of structural responses in time domain.

2.4.3. CS for recovery of missing data in WSNs for VSHM applications

CS-based approaches have also been considered to rectify the problem of data loss in WSNs for structural health monitoring of civil engineering structures (*e.g.*, *Bao et al.* (2013); *Zou et al.* (2015); *Huang et al.* (2016)). This challenging issue is associated with loss of information in wireless VSHM communications due to various factors including sensors failure, insufficient power resources, bandwidth and transmission limitations, radio interference, harsh weather conditions, that adversely affect the communication reliability (*e.g.*, *Nagayama et al.* (2007)). In such cases, the received signals observe gaps either at random or continuous time intervals that occur accidentally and, thus, they are not known in advance in real-time monitoring deployments. Further, the missing data are not necessarily uniformly distributed over the entire observation window which poses restrictions on the required amount of data for faithful CS-based

reconstruction operations *Comerford et al.* (2015). *Note that these applications have a clearly distinguishable aim from what was reviewed in the previous cases, since the CS theory is not used for data compression to reduce wireless transmission costs.*

Instead, the CS-based missing data recovery problem (*e.g.*, *Bao et al.* (2013), (2014); *Zou et al.* (2015); *Huang et al.* (2016)) relies on conventional uniform-in-time sampling schemes to acquire full-length structural response signals. The latter are further modulated on-sensor by adopting a (rectangular) random matrix capable to spread the underlying signal information across the entire spectrum, and subsequently stored in sequentially numbered data packets. Assuming data packet loss during the wireless transmission of the (full-length) modulated signal towards the server, the received data can be treated as compressed measurements, observing gaps in certain time intervals that can be easily inferred by the out-of-sequence received data packets. Based on the assumption of sparse structural responses on an expansion basis, CS reconstrunction algorithms are then employed to retrieve the original full-length signal at the uniform time-grid.

Along these lines, the CS-based approach developed by *Bao et al.* (2013) relies on the Haar wavelet basis for the sparse representation of structural data originating from actual monitoring campaigns, showing promising results in rectifying up to 20% missing data (*i.e.*, by processing the available 80% of the data samples) for both random and continuous packet loss, yielding more accurate results when de-noising operations are employed. The above CS-based approach was also adopted by *Zou et al.* (2015) and efficiently embedded in a wireless smart sensor – the Imote2. This was achieved based on the random demodulator method (*i.e.*, a widely known approach within the CS community), incorporating appropriate modifications to address the limited power, memory, and computational resources onboard due to increasing requirements in performing the above operations (*i.e.*, fast uniform sampling, signal modulation, and wireless transmission of complete datasets).

2.5. CS Limitations & Conclusions

This chapter outlined the current state-of-the-art in novel VSHM approaches relying on random sub-Nyquist data acquisition schemes for low-cost and reliable WSNs. To this end, the basic principles of the Compressive Sensing (CS) theory were summarised and an extensive review of the newly surfaced CS-based VSHM approaches was provided.

Overall, it can be concluded that the required number of compressed measurements, *M*, and the minimum average random sampling rate for which quality CS-based signal recovery can be achieved *depend strongly on and are limited by the sparsity/compressibility level of the monitored response acceleration signals on a sparsifying basis*. The latter is judicially selected and has a key role in the efficient implementation of the CS strategy.

In this respect, the DFT basis has been widely used in most of the CS-based VSHM approaches review in the previous section. Despite the fact that the energy of linear structural response acceleration signals is clustered in the frequency domain around the structural natural frequencies, discrete- time versions of these signals, as recorded in the field, are not significantly sparse on the DFT basis (*e.g., Bao et al.* (2011); *O'Connor et al.* (2014); *Huang et al.* (2016)). This lack of sparsity can be attributed partly to unknown environmental excitation added to the compressively sensed signals and causing detrimental noise folding (*e.g., Axell et al.* (2012); *Davenport et al.* (2012); *Huang et al.* (2016)), and partly to spectral leakage (*e.g., Davenport & Wakin* (2012); *Duarte & Baraniuk* (2013)). The latter phenomenon is due to the fact that the grid points defined by the DFT basis on the frequency axis may not coincide with the (unknown) resonant structural natural frequencies.

Nonetheless, the consideration of alternative expansion bases, such as the discrete Haar wavelet basis, does not significantly improve the sparsity of response acceleration signals (*e.g., Bao et al.* (2011)). Arguably, enhanced structural response signal sparsity can be achieved by considering either compactly supported in the frequency domain generalised harmonic wavelet bases as discussed by *Gkoktsi & Giaralis* (2015), or over-complete dictionaries as discussed by *Mascarenas et al.* (2013). However, the fine-tuning of harmonic wavelet bases properties and the composition of redundant dictionaries are strongly application-dependent. More importantly, in any case, low levels of signal sparsity requires a larger number of compressed measurements for faithful signal reconstruction and, therefore, reduced gains in terms of energy savings in wireless data transmission (see also *O'Connor et al.* (2014)).

Further, the actual sparsity/compressibility level, S, of real-time monitored signals is not known in advance, unless *a priori* knowledge becomes available through probabilistic approaches (*e.g., Huang et al.* (2016)), or conventional uniform-in-time sampling and signal processing (*e.g., Davenport et al.* (2012); *Klis & Chatzi* (2015), (2017)) at the cost of increased computational, power, and storage/memory requirements. In the absence of such information, a target sparsity level S_T is assumed in the CS sparse signal recovery step. Nonetheless, the optimal selection of the S_T value is not trivial, since it is associated with a trade-off between reconstruction accuracy and computation complexity. In particular, choosing a relatively large value of S_T ($>>S$) leads to unnecessarily high computational cost, as the latter is bounded by $O(S_T \cdot M \cdot N + \log(||x||_2/\eta) \cdot S_T \cdot M)$ (*e.g., Needell & Tropp* (2009)). On the antipode, a relatively small value of S_T ($<<S$) may lead to poor approximation of the vibration measurements and, therefore, to low quality structural estimation. In practice, a range of different S_T values should be tested (off-line) to strike a good balance between accuracy and computational complexity.

Finally, it is recognised that the CS framework is a potent tool for low-cost and dependable wireless communications that can be successfully applied to VSHM deployments once its sparsity limitations are addressed in cost-effective manner. Further experimental research in field-

implementations is warranted to attest the CS-based VSHM approaches in actual wireless systems, which is a challenging task due to the lack of commercially available sensing units with embedded compressive random sampling schemes.

Chapter 3
CS-based Damage Detection Using the Relative Wavelet Entropy

3.1. Preliminary Remarks

The primary objective of this chapter is to propose a novel compressive sensing-based damage detection approach for low-cost and power-efficient WSNs in VSHM applications. The proposed method originates from the theory of *Compressive Sensing* (CS) in Chapter 2 (§*2. Compressive Sensing: Basic Concepts & Applications in VSHM*) fused with the *Relative Wavelet Entropy* (RWE). The latter is a well-established in the literature damage-sensitive index (*e.g., Ren & Sun* (2008); *Yun et al.* (2011); *Lee et al.* (2014)), derived by wavelet transforming response acceleration signals obtained from a healthy/reference and a damaged state of a given (linear) structure subject to broadband excitations.

In brief, the *wavelet transform* represents any given signal on the time-scale plane by projecting it onto a collection of double-indexed localised in time oscillatory functions (wavelets) generated by scaling and translating in time a single "mother" wavelet function (*e.g., Daubechies* (1992)). Depending on the properties of the mother wavelet, each scale considered in the *wavelet transform* can be assigned an effective (central) frequency and an effective bandwidth. In this regard, if an energy-preserving analysing wavelet basis is used, the squared magnitude of the *wavelet transform* maps the energy of a signal on the time-frequency plane (see also *Cohen* (1995)). Under this condition, the damage detection capability of the RWE relies on detecting changes to the energy distribution of (or to the information carried by) response acceleration signals between the healthy and the damaged state across the different scales considered in the *wavelet transform* spanning certain frequency bands. Indeed, the definition of the RWE is closely related to the Shannon wavelet entropy introduced by *Blanco et al.* (1998) for signal characterisation in certain biomedical applications, based on the information carried by the *wavelet transform* in time and in frequency.

Ren & Sun (2008) verified the potential of the RWE to serve as a damage-sensitive index by considering experimental data pertaining to a beam and to a composite bridge excited by impulsive/hammer force. In computing the RWE, the authors considered a non-smooth

Daubechies (or Haar) wavelet basis implemented in a wavelet analysis digital filter bank yielding a quite efficient to compute discretised version of the *wavelet transform*, the so-called *discrete wavelet transform* (*e.g.*, *Daubechies* (1992); *Goswami & Chan* (1999)). The RWE damage index was adopted by *Lee et al.* (2014) to detect faulty/damaged connections in pin-jointed truss structures by considering healthy connections as a reference (healthy state), and processing signals recorded at all healthy and faulty connections acquired from a single vibration test. Recognising the potential of the RWE for damage detection in practical VSHM applications, *Yun et al.* (2011) considered arrays of battery operated wireless sensors computing locally on on-board micro-processors the *discrete wavelet transform* and, thus, being able to derive the RWE in a decentralised computationally-efficient manner aiming to reduce the power consumption of sensors and, therefore, to prolong their battery life: a very important practical consideration in cost-effective VSHM using wireless sensor networks *Lynch* (2007). In fact, as detailed in Chapter 1 (§*1. Introduction*), current wireless sensors (*e.g.*, Figure 1.1(a)) require battery replacement at intervals of few weeks to few months, depending on various factors such as the sampling frequency, the duration of each monitoring interval, the on-board hardware and software to be executed, while the amount of data that can be reliably transmitted within WSNs is subjected to bandwidth limitations (*e.g.*, *Lynch & Loh* (2006); *Lynch* (2007)). Despite the above efforts, *Yun et al.* (2011) derived the RWE from *full-length structural response acceleration signals, conventionally-sampled at Nyquist rate (or above)*, which increases the power demands due to wireless transmission of a large number of data, while keeping the memory and storage requirements at the sensor high.

Motivated by recent advances in the field of Compressive Sensing (*e.g.*, *Bao et al.* (2013); *O'Connor et al.* (2014); *Park et al.* (2014); *Klis & Chatzi* (2015); *Yang & Nagarajaiah* (2015)), the problem of increased power requirements during wireless transmission is addressed herein by considering a random non-uniform in time sub-Nyquist sampling scheme (*e.g.*, *Candès* (2006); *Donoho* (2006); *R. G. Baraniuk* (2007); *Duarte et al.* (2012)) to acquire *compressed structural response datasets* at the sensor front-end. In this respect, wireless sensors cost and energy consumption can be significantly reduced, while the on-sensor data storage and local on-board data processing before wireless transmission can be considerably reduced, or even by-passed. A key issue is the derivation of a wavelet basis matrix in which the structural acceleration response data are sufficiently sparse (*i.e.*, attaining only few non-zero wavelet coefficients on the adopted wavelet transform domain). Thus, any standard CS reconstruction algorithm can be further used to retrieve the underlying wavelet coefficients directly from the acquired compressed measurements, without reconstructing the acceleration responses in time domain. The latter enables the computation of the RWE and the detection of structural damage directly from the acquisition and processing of much fewer data compared to conventional approaches at Nyquist rate (*e.g.*, *Ren & Sun* (2008); *Yun et al.* (2011); *Lee et al.* (2014)).

In the remainder of this chapter, the mathematical framework of the wavelet transform and the RWE are briefly reviewed in section 3.2 (§*3.2. Theoretical Background of Relative Wavelet Entropy*). Four orthogonal (energy-preserving) wavelet filter banks are further presented in section 3.3 (§*3.3. On Frequency Selectivity of Wavelet Basis Functions*), used to assess the influence of the wavelets' frequency domain attributes within the RWE damage index and to determine the sparsest representation of structural responses on the wavelet transform domain. The efficiency of the proposed method is compared against the conventional approach with computer-simulated structural response data, while comparative numerical results are presented and discussed in section 3.4 (§*3.4. Numerical Assessment of Relative Wavelet Entropy–based damage Detection for Various Wavelet Bases*) and section 3.5 (§*3.5. Proposed Compressive Relative Harmonic Wavelet Entropy Approach for Damage Detection*), followed by concluding remarks in section 3.6 (§*3.6. Concluding Remarks*).

Note that sections §3.2, §3.3, have appeared in [J1] and [C1] of section §1.5 (list of publications), parts of section §3.4 appeared in [J1], while section §3.5 presents novel contributions not being disseminated yet in the public domain.

3.2. Theoretical Background of Relative Wavelet Entropy

3.2.1. The continuous wavelet transform

Consider a real signal $x(t)$ of finite energy E in the axis of time t, or in time domain, expressed by

$$E = \int_{-\infty}^{\infty} |x(t)|^2 \, dt = \frac{1}{2\pi} \int_{-\infty}^{\infty} |X(\omega)|^2 \, d\omega \, . \tag{3.1}$$

In the above equation, $X(\omega)$ is the complex-valued *Continuous-Time Fourier Transform* defined by

$$X(\omega) = \int_{-\infty}^{\infty} x(t) \, \overline{e^{i \omega t}} dt \, , \tag{3.2}$$

in which i is the imaginary unit and the bar over a function denotes complex conjugation. The *Fourier Amplitude Spectrum* $|X(\omega)|$ maps/projects the signal $x(t)$ onto the frequency domain, ω, with the sharpest possible resolution, since the non-decaying in time sinusoidal (harmonic) function $e^{i\omega_0 t}$ with frequency ω_0 becomes a "delta function" at ω_0 in the frequency domain. Moreover, the relation eq. (3.1) implies that the transformation in eq. (3.2) preserves the signal energy and, therefore, the square of the *Fourier Amplitude Spectrum* normalised by the signal energy, $|X(\omega)|^2/E$, can be interpreted as the energy distribution carried by the signal $x(t)$ on the frequency domain, averaged at all times (see *e.g.*, *Cohen* (1995)).

Further, consider the *Continuous Wavelet Transform* defined as (*e.g.*, *Daubechies* (1992); *Goswami & Chan* (1999))

$$u(a,b) = \frac{1}{\sqrt{a}} \int_{-\infty}^{\infty} x(t)\ \overline{\psi\left(\frac{t-b}{a}\right)}\, dt\,, \tag{3.3}$$

which projects the signal $x(t)$ onto a collection of localised in time oscillatory waveform functions ("wavelets") generated by scaling in time, via the positive scale parameter α, and by translating in time, via the time position parameter b, a single finite energy function $\psi(t)$, the so-called "mother wavelet" (see also Figure 3.1).

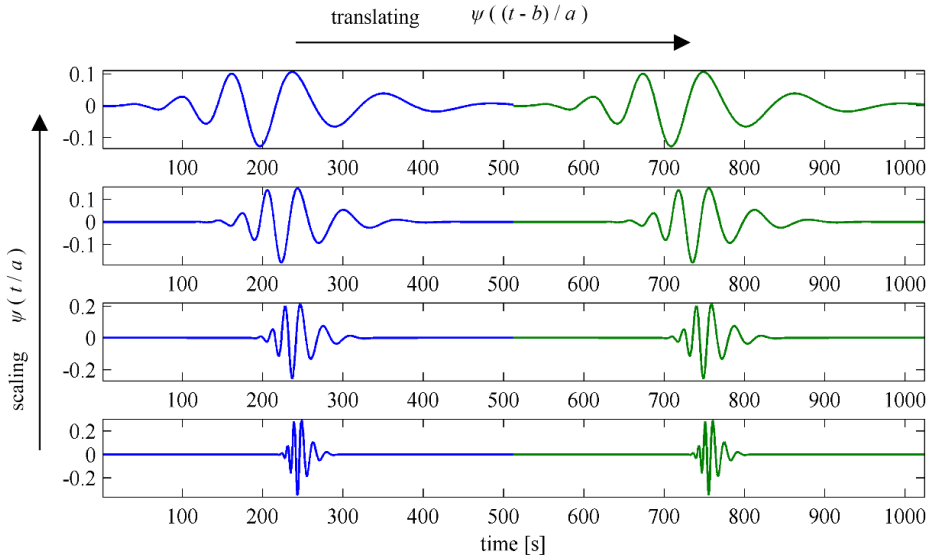

Figure 3.1: *Generation of a family of wavelet functions by scaling and translating in time the mother wavelet $\psi(t)$*

For the purposes of this work, it is important to note that the square of the magnitude of the *Continuous Wavelet Transform* normalised by the signal energy, $|u(\alpha,b)|^2/E$, can be interpreted as an estimator of the signal energy distribution on the joint time-frequency plane (see *e.g.*, *Cohen* (1995)). This is because: firstly, the *Continuous Wavelet Transform* in eq. (3.3) preserves the energy of the original signal; secondly, the parameter b is a time-related index defining the origin in time of each wavelet considered in the analysis for a fixed scale a; and, thirdly, the scale parameter a can be related to an effective frequency via the equation

$$\omega_{eff} = \frac{\omega_c}{a}\,, \tag{3.4}$$

where ω_c is the central or the dominant frequency of the (unscaled) mother wavelet *Fourier Amplitude Spectrum*, $|\Psi(\omega)|$. Therefore, the *Continuous Wavelet Transform* in eq. (3.3) "scans" the signal $x(t)$ in the time domain by varying the parameter b to detect frequency components that pertain to a specific effective frequency and bandwidth. The latter two frequency domain

attributes of *Continuous Wavelet Transform* depend on the scale α and on the properties of the mother wavelet.

3.2.2. The discrete wavelet transform and wavelet filter banks

In many practical numerical applications, the *Continuous Wavelet Transform* in eq. (3.3) is computed by considering a set of particular values for the parameters *a* and *b* following a dyadic discretization scheme. According to this scheme, the scaling parameter is expressed by $\alpha=2^{-j}$ while the time position parameter is expressed $b = ka = k2^{-j}$ where *j* and *k* are integer numbers *j*, $k \in \mathbb{Z}$. The convolution integral in eq. (3.3) becomes (*e.g.*, *Daubechies* (1992); *Goswami & Chan* (1999))

$$u\left(\frac{1}{2^j},\frac{k}{2^j}\right)=u_j[k]=2^{j/2}\int_{-\infty}^{\infty}x(t)\overline{\psi\left(2^j t-k\right)}\,dt\,. \tag{3.5}$$

A further time discretization of the integral in eq. (3.5) to accommodate finite duration discrete-time *N*-length signals $x[n]=x(n/F_s)$; $n=0,1,\ldots,N-1$, where F_s is the sampling rate, yields the so-called *discrete wavelet transform*. Notably, the latter can be efficiently computed by means of a digital filter bank comprising a sufficient number of the (same) "building block" repeated in series as shown in Figure 3.2 in a multi-resolution analysis framework (*Daubechies* (1992); *Vetterli & Herley* (1992), *Goswami & Chan* (1999)).

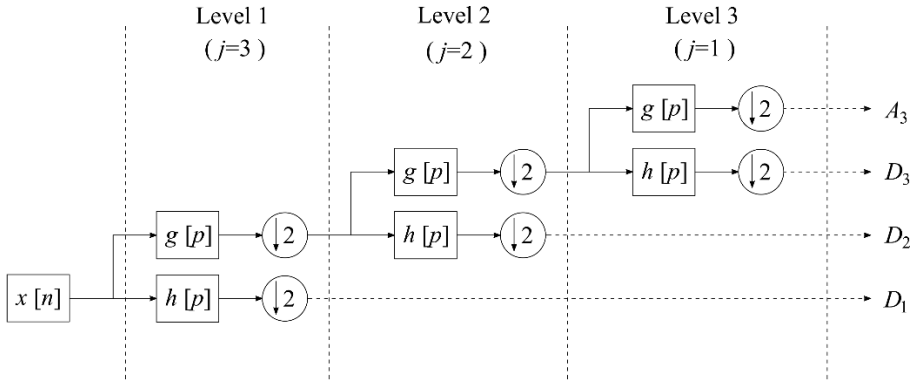

Figure 3.2: *Typical dyadic discrete wavelet transform analysis filter bank with J=3 scales for processing N=8 long discrete-time signals*

Each building block corresponds to a particular scale or analysis "level" and consists of a high-pass filter with coefficients $h[p]$; $p=1,2,\ldots,P$, a low-pass filter with coefficients $g[p]$; $p=1,2,\ldots,P$, and a dyadic down-sampler (*i.e.*, a mechanism of reducing the sampling rate by retaining every other sample of the input discrete-time signal) applied to the output of each of the previous filters. These filters are designed such that no energy is lost during transformation/processing of the input signal. At each level corresponding to the scale $a=2^{-j}$ the spectrum of the input discrete-time signal is split into two parts separating the high frequency

components, represented by the "detail" sequence of wavelet coefficients D_{J+1-j} upon down-sampling, from the low frequency components, represented by the "approximation" sequence of coefficients A_{J+1-j} upon down-sampling (see *e.g.*, *Vetterli & Herley* (1992)). The full *discrete wavelet transform* requires $J=\log_2 N$ total number of levels to be considered and at each level the number of coefficients in the output sequences upon down-sampling is $N/2^{(J+1-j)}$. Therefore, the *discrete wavelet transform* is non-redundant: it produces exactly N coefficients given an N-long discrete-time signal which preserve the signal energy E.

In this respect, the processing of a given signal by a *discrete wavelet transform* filter bank begins by extracting, first, the highest frequency components at the lowest scale (*i.e.*, for the largest j value) and proceeds at each level by extracting lower and lower frequencies, that is, the values of j follow a descending order: $j=J, J-1,\ldots,1$ (see also Figure 3.2). The detail (or wavelet) coefficients at each scale capture only the part E_j of the total signal energy defined as

$$E_j = \sum_k \left| u_j[k] \right|^2 , \tag{3.6}$$

where it is understood that summation is over all coefficients D_{J+1-j} at scale j. Then, the total energy of the signal is retrieved by summing the energy over all J scales, that is,

$$E = \sum_j E_j = \sum_j \sum_k \left| u_j[k] \right|^2 , \tag{3.7}$$

under the assumption that the energy of the approximation coefficient at the final analysis level is negligible. Note that the ratio

$$w_j = \frac{E_j}{E} , \tag{3.8}$$

gives the fraction of the total signal energy, contained within a particular frequency band corresponding to the j scale of the *discrete wavelet transform* analysis filter bank. It, therefore, characterises a discretised version of the Fourier transform-based function $|X(\omega)|^2/E$ within this band. Notably, the width and location on the frequency axis of the frequency band corresponding to a scale j does not only depend on the value of j, but also on the frequency domain attributes of the filter $h[p]$ or, equivalently, on the frequency domain attributes of the underlying analysis mother wavelet. In the following section, a structural damage sensitive index, introduced by *Ren & Sun* (2008), is briefly presented which relies on computing the ratio in eq. (3.8) of acceleration response signals from dynamically excited linear structures. Further, in sub-section §3.3, the frequency domain attributes of *discrete wavelet transform* filter banks using different analysing mother wavelets are presented, while the influence of these attributes for vibration-based structural damage detection is numerically demonstrated in section §3.3.

3.2.3. The relative wavelet entropy for structural damage detection

Introduced by *Blanco et al.* (1998), the Shannon wavelet entropy is defined as

$$\mathrm{SWE} = -\sum_j w_j \ln(w_j)\,, \tag{3.9}$$

where w_j is the positive ratio in eq. (3.8) with $0 \le w_j \le 1$ (*i.e.*, w_j qualifies as a probability distribution) and the summation involves all scales considered in an energy preserving *discrete wavelet transform* filter bank to transform a given signal $x(t)$. The Shannon wavelet entropy was proved to be an effective quantitative measure to characterise the information carried by signals at different scales (or corresponding frequencies) and time instants in certain biomedical applications (*e.g.*, *Blanco et al.* (1998); *Rosso et al.* (2006)). Interpreted from a structural dynamics viewpoint, the Shannon wavelet entropy of the acceleration response signal of a white noise-excited lightly-damped linear single-degree-of-freedom structural system will attain a relatively small value compared to the Shannon wavelet entropy of the response signal of a white noise excited structure with multiple degrees of freedom. This is because the energy of the former signal will be well-localised in the frequency domain around the natural frequency of the system and, ideally, will be captured by a single w_j corresponding to the scale containing this frequency. The value of this particular w_j will be close to unity and, therefore, its contribution to the sum in eq. (3.9) will be almost zero as the term $\ln(w_j)$ will be almost zero, and so will be the contributions of the ratios from all other scales whose value will be close to zero. However, the energy of the response signal of a multi-degree of freedom structure will be spread around the various different natural frequencies of the structure. Consequently, there will be several non-zero contributions to the sum in eq. (3.9) and the overall value of Shannon wavelet entropy will be large. Clearly, the Shannon wavelet entropy is maximised for a white noise signal implying a highly "disordered" process, while the Shannon wavelet entropy of a very narrowband signal (close to a pure sinusoid) will be almost zero implying an "ordered" process.

To this end, note that structural damage causes a shift to the natural frequencies of a structure and this should reflect in changes to the values of the scale-dependent energy ratios in eq. (3.8) obtained from linear structural response acceleration signals commonly considered in VSHM. In this regard, *Ren & Sun* (2008) proposed the use of the relative wavelet entropy defined by

$$\mathrm{RWE} = \sum_j w_j \ln\left(\frac{w_j}{z_j}\right), \tag{3.10}$$

as a structural damage-sensitive index. In the last equation, w_j is the scale dependent energy ratio in eq. (3.8) obtained from a response acceleration signal measured at a particular location of the damaged-state structure and z_j is the scale dependent energy ratio in eq. (3.8) from a response

acceleration signal measured at the same point of the healthy-state structure. For structures with negligible damage close to the measurement location, it is expected that $w_j \approx z_j$ for all considered j scales and thus RWE attains a negligible value, corresponding to an ordered process. For damaged structures, it is expected that the two ratios will differ across some of the scales due to a shift to the natural frequencies of the system yielding a large RWE value, corresponding to a "disordered" process. Larger values of RWE are expected at measurements points close to the damage and, therefore, comparing the RWE values computed from an array of sensors may achieve damage localisation (*Ren & Sun* (2008); *Yun et al.* (2011).

Note that the RWE index in eq. (3.10) is independent of time aiming to detect stationary structural damage. Since the underlying information for the detection of such kind of damage is associated with signal energy distribution in the frequency domain, it is intuitive to expect that the RWE is strongly dependent on the frequency domain properties of the wavelet filter bank used to compute the energy ratios appearing in eq. (3.10) and the quality of frequency domain resolution. The frequency domain properties of four different wavelet filter banks are discussed in the next sub-section focusing on the frequency resolution and selectivity across different scales. The influence of using different wavelet filter banks to the effectiveness of the RWE as a damage detection index for stationary damage is numerically assessed in the following sub-sections.

3.3. On Frequency Selectivity of Wavelet Basis Functions

3.3.1. Daubechies wavelet analysis filter banks

Unlike the *Continuous Wavelet Transform* in eq. (3.3), the *discrete wavelet transform* discussed in sub-section §3.2.2 does not require an analytical definition for the mother wavelet $\psi(t)$. Instead, it allows for different families of analysing wavelet functions to be indirectly defined by means of appropriately constructed filters $g[p]$ and $h[p]$; $p=1,2,\ldots,P$ in Figure 3.2. This is the case of the Daubechies family of wavelets, denoted by DP, which are defined via a single P-length finite impulse response filter construction due to Daubechies (*e.g.*, *Daubechies* (1992)), and are widely used within the *discrete wavelet transform* multi-resolution analysis framework. Daubechies wavelets are constructed to be compactly supported in the time domain forming orthogonal analysis bases within each scale and across all dyadic scales. Consequently, they achieve sharp localisation of signal energy in time domain and preserve the input signal energy.

Nevertheless, the enhanced time domain localisation capabilities of Daubechies wavelets, comes at the cost of relatively poor frequency domain localisation and discrimination across scales in typical Daubechies *discrete wavelet transform* filter banks. These issues are illustrated in Figure 3.3(a) which plots the *Fourier Amplitude Spectrum*, $|\Psi(\omega/2^j)|$, of D2 Daubechies wavelets (defined using an P=2-long finite impulse response filter reported in *Daubechies* (1992)

for four adjacent scales. These FASs have been obtained by Fourier transforming D2 wavelets at different scales (Figure 3.3(b) and Figure 3.3(c) plot two such wavelets). The wavelets are obtained by means of a standard algorithm which constructs recursively the so-called scaling function, $\varphi(t)$, at first, and, then, the associated wavelet function at each considered scale j by relying on the following two-scale equations (see *Goswami & Chan* (1999))

$$\varphi(2^j t) = \sum_p g_1[p]\, \varphi(2^{j+1} t - p)\,, \tag{3.11}$$

$$\psi(2^j t) = \sum_p h_1[p]\, \varphi(2^{j+1} t - p)\,. \tag{3.12}$$

The sequence $g_1[p]$ in eq. (3.11) are the P coefficients of the finite impulse response filter defining the DP wavelets. Further, in eq. (3.12), $h_1[p]=(-1)^p g_1[1-p]$. Note that the signal analysis finite impulse response filters appearing in Figure 3.2 for the DP wavelets are defined as $g[p]=0.5 \cdot g_1[-p]$ and $h[p]=0.5 \cdot (-1)^p g_1[p+1]$ (quadrature mirror construction).

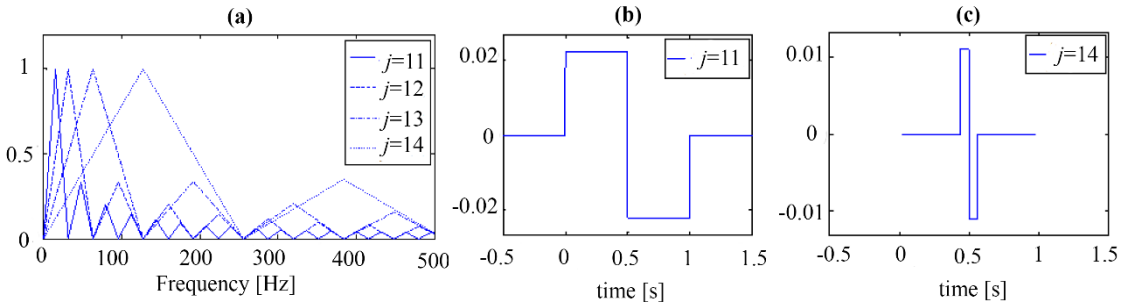

Figure 3.3: *Daubechies D2 (or Haar) wavelets for four different scales* j *from a filter bank with* J*=16 total number of scales and Q= 0.49: (a) Normalised to the peak value Fourier Amplitude Spectrum, $|\Psi(\omega/2j)|$; (b) wavelet in time domain at scale* j*=11; and (c) wavelet in time domain at scale* j*=14*

Figure 3.3(a) shows clearly that the FASs of a Daubechies wavelet basis, as implemented in a dyadic *discrete wavelet transform* filter bank, exhibit significant overlapping among the different scales and have a relatively poor frequency selectivity among scales j especially in the lower frequencies (see also *Vetterli & Herley* (1992)). In fact, being compactly supported in the time domain, Daubechies wavelets are infinitely supported in the frequency domain: their *Fourier Amplitude Spectrum* comprises one main dominant lobe and several lower periodic side-lobs at higher frequencies. This is a consequence of the so-called uncertainty principle which holds for any Fourier pair: enhancing the energy localisation of a function in the time domain deteriorates its frequency resolution (*i.e.*, widens its effective bandwidth) and vice versa (*e.g.*, *Cohen* (1995)). Note that the wavelets shown in Figure 3.3 attain the lowest possible order of Daubechies wavelets, D2, which are also known in the literature as "Haar" wavelets. Figure 3.4 provides similar plots as Figure 3.3 for higher-order Daubechies wavelets, D20. The latter support a rather

smooth structure and the side lobs of their FASs at higher frequencies are minimised (Figure 3.4(a)). However, severe overlapping occurs between adjacent scales, especially in the lower frequencies where the frequency selectivity among scales is rather poor. Consequently, the use of such filter banks renders the task of assigning any single frequency band to the signal energy captured at a particular scale in eq. (3.6), E_j, a rather challenging task.

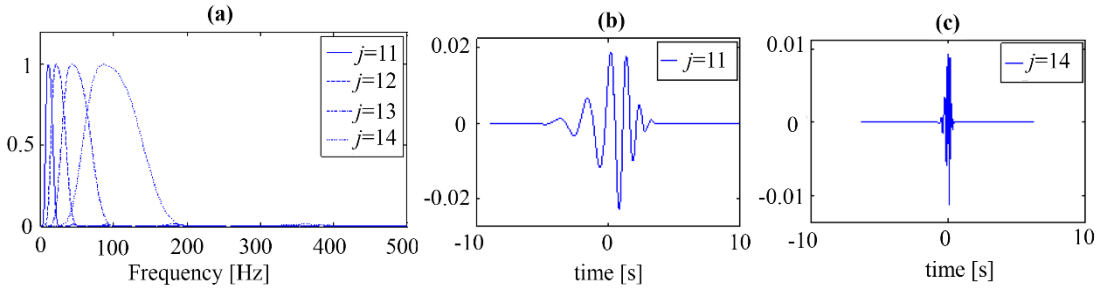

Figure 3.4: *Daubechies D20 wavelets for four different scales* j *from a filter bank with* J*=16 total number of scales and Q= 0.46: (a) Normalised to the peak value Fourier Amplitude Spectrum, |Ψ(ω/2j)|; (b) wavelet in time domain at scale* j*=11; and (c) wavelet in time domain at scale* j*=14.*

3.3.2. Meyer wavelet filter banks

Unlike the Daubechies wavelets which are compactly supported in the time domain, the Meyer (mother) wavelet is compactly supported in the frequency domain defined as (*e.g.*, *Daubechies* (1992))

$$\Psi(\omega)=\begin{cases}\exp(i\omega/2)\sin\left[\frac{\pi}{2}v\left(\frac{3}{2\pi}|\omega|-1\right)\right] & ; \quad \frac{2\pi}{3}\le|\omega|\le\frac{4\pi}{3}\\ \exp(i\omega/2)\cos\left[\frac{\pi}{2}v\left(\frac{3}{2\pi}|\omega|-1\right)\right] & ; \quad \frac{4\pi}{3}\le|\omega|\le\frac{8\pi}{3}\\ 0 & ; \quad \textit{otherwise}\end{cases}, \tag{3.13}$$

In the last equation, the auxiliary function $v(u)$ controls the smoothness of the *Fourier Amplitude Spectrum* of Meyer wavelets and, therefore, their rate of decay in the time domain. A common smoothing function of choice is (*e.g.*, *Daubechies* (1992); *Misiti et al.* (1997))

$$v(u)=\begin{cases}u^4(35-84u+70u^2-20u^3) & ; \quad u\in[0,1]\\ 0 & ; \quad \textit{otherwise}\end{cases} \tag{3.14}$$

Orthogonal Meyer wavelet bases can be readily constructed and used to obtain energy preserving *Continuous Wavelet Transform* in eq. (3.3). In fact, *Lee et al.* (2014) considered the Meyer *Continuous Wavelet Transform* to identify the potentially damaged connections in trusses by relying on the RWE from signals measured at healthy and damaged connections from a single

excitation test. However, there exist *discrete wavelet transform* filter bank constructions comprising finite impulse response filters (as in Figure 3.2) that approximate the Meyer-based *Continuous Wavelet Transform* using a dyadic frequency domain discretisation scheme (*e.g.*, *Misiti et al.* (1997)). Such a Meyer *discrete wavelet transform* filter bank is used in the numerical applications of the next sub-section since it is much more efficient to compute and therefore more likely to be adopted in computing wavelet coefficients on on-board micro-processors for wireless sensors used in VSHM (*e.g.*, *Lynch* (2007); *Yun et al.* (2011)).

Figure 3.5(a) plots the *Fourier Amplitude Spectrum* of Meyer wavelets at four adjacent scales. Compared to the Daubechies wavelets of Figure 3.3(a) and Figure 3.4(a), overlapping in the frequency domain is observed only between neighbouring wavelet scales and there are no side lobs at high frequencies. Therefore, *discrete wavelet transform* filter banks of Meyer wavelets attain enhanced frequency selectivity among scales compared to Daubechies wavelets. However, as in the case of Daubechies wavelet filter banks, the frequency resolution deteriorates in higher frequencies as the wavelets becomes better localised in time domain at lower scales (larger values of *j*). This issue is further discussed in the following sub-section.

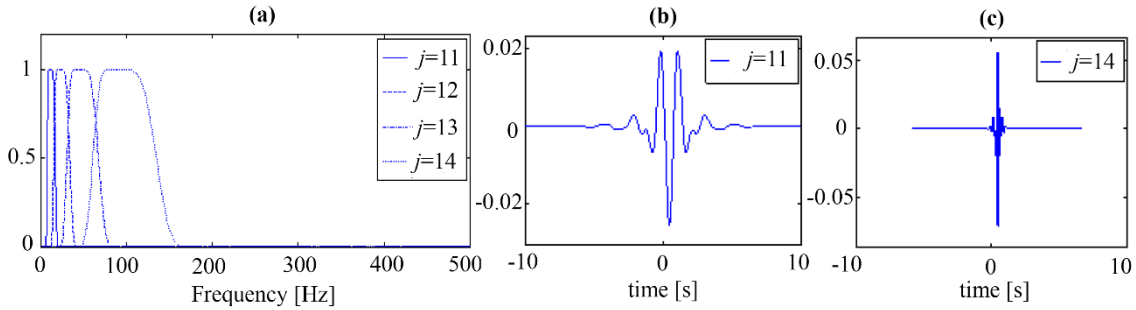

Figure 3.5: *Meyer wavelets for four different scales* j *from a filter bank with* J*=16 total number of scales and Q= 0.68: (a) Normalised to the peak value Fourier Amplitude Spectrum, $|\Psi(\omega/2j)|$; (b) wavelet in time domain at scale* j*=11; and (c) wavelet in time domain at scale* j*=14.*

3.3.3. Constant Q-analysis wavelet filter banks

The ability of the square magnitude of the *Continuous Wavelet Transform* and of the *discrete wavelet transform* (*i.e.*, of the $|u(\alpha,b)|^2$ and of the $|u_j[k]|^2$, respectively) to resolve the frequency components of any signal in time relies on the scaling operation and on the oscillatory form of the wavelets. Specifically, as the scaling parameter *a* takes on smaller values (or as *j* assumes higher values in the case of *discrete wavelet transform*) the wavelets are compressed in the time domain. However, the number of the wavelet zero-crossings (*i.e.*, oscillations) remain the same and, thus, the wavelet *Fourier Amplitude Spectrum* becomes wider, due to the uncertainty principle, while it shifts towards higher frequencies since the effective frequency in eq. (3.4) increases. The above points can be readily observed in Figure 3.3, Figure 3.4 and Figure 3.5: the width of the main lobe of the wavelet *Fourier Amplitude Spectrum* widens as the average

frequency content, characterised by the central or the peak frequency of the main lobe, increases. This well-known property of the standard *Continuous Wavelet Transform* in eq. (3.5) is called constant-Q analysis, where Q is defined as the ratio of the effective frequency over the effective bandwidth at each analysis level or scale (see also *Brown* (1991)). Consequently, the dyadic *discrete wavelet transform* filter banks assume a constant Q across scales or analysis levels (note that the value of Q is reported for the filter banks of Figure 3.3 toFigure 3.5).

In many signal analysis applications, a constant Q-analysis is favourable. This is because high-frequency components in time-series are usually well-localised in time, while low-frequency trends are well-spread in time. Nevertheless, this is not necessarily true in processing acceleration response signals from dynamically excited linear structures whose location of the dominant frequency components on the frequency domain depends on the structural natural frequencies. The natural frequencies of lightly damped linear structures are well-localised in the frequency domain and may lie anywhere on the frequency axis. In this regard, the use of non-constant Q wavelet analysis filter banks is a reasonable consideration in order to target natural frequencies related to higher modes of vibration effectively. The wavelet family presented in the next subsection can readily achieve custom-made non-constant Q wavelet analysis filter banks. These considerations have important practical implications to the effectiveness of the RWE in eq. (3.10) for structural damage localisation purposes as will be numerically illustrated in the following sub-section.

3.3.4. Harmonic wavelet filter banks

Introduced by *Newland* (1994), the *harmonic wavelet transform* proved to be a potent tool for structural damage detection of yielding multi-storey building structures under severe earthquake excitation (*e.g., Spanos et al.* (2007)). The *harmonic wavelet transform* incorporates a basis of complex-valued functions with compactly supported box-like *Fourier Amplitude Spectrum* (harmonic wavelets). A "general" harmonic wavelet at scale j centred at the $k/(n[j]-m[j])$ position in time can be written in the frequency domain as (see *e.g.*, *Giaralis & Spanos* (2009))

$$\begin{aligned} \Psi_{j,k}(\omega) &= \frac{T_o}{(n[j]-m[j])2\pi}\exp\left(\frac{-i\omega k T_o}{(n[j]-m[j])}\right); \\ & \quad m[j]\frac{2\pi}{T_o} \le \omega \le n[j]\frac{2\pi}{T_o} \quad , \\ \Psi_{j,k}(\omega) &= 0 \quad ; \quad \textit{otherwise.} \end{aligned} \tag{3.15}$$

where T_o is the total length (duration) of the time interval considered in the analysis. In the last equation, the sequences (vectors) $m[j]$ and $n[j]$ contain integer positive numbers. It was shown by *Newland* (1994), that a collection of harmonic wavelets spanning adjacent non-overlapping

intervals at different scales on the frequency domain forms a complete orthogonal basis. This can be achieved by proper definition of the $m[j]$ and $n[j]$ sequences. The inverse Fourier transform of eq. (3.15) expresses the time-domain representation of the harmonic wavelet

$$\psi_{j,k}(t) = \frac{\exp\left(i\, n[j] \frac{2\pi}{T_o}\left(t - \frac{kT_o}{n[j]-m[j]}\right)\right) - \exp\left(i\, m[j]\, \frac{2\pi}{T_o}\left(t - \frac{kT_o}{n[j]-m[j]}\right)\right)}{i\,\left(n[j]-m[j]\right)\, \frac{2\pi}{T_o}\left(t - \frac{kT_o}{n[j]-m[j]}\right)}. \tag{3.16}$$

The *harmonic wavelet transform* is defined in

$$u_{j,k} = \frac{n[j]-m[j]}{kT_o} \int_{-\infty}^{\infty} x(t)\, \overline{\psi_{j,k}(t)}\, dt \tag{3.17}$$

In which the harmonic wavelet coefficients $u_{j,k}[k]$ preserve the input signal energy.

Importantly, note that at scale j the effective bandwidth of the *harmonic wavelet transform* is $(n[j]-m[j])2\pi/T_o$ and the central frequency is $(n[j]+m[j])\pi/T_o$. In this respect, it can be readily seen that *harmonic wavelet transform* enables arbitrary frequency resolution within any given range of frequencies. Furthermore, the effective frequency band at each scale is defined directly in the frequency domain in a straightforward manner. Therefore, the *harmonic wavelet transform* provides for exceptional freedom in defining "frequency bins" of arbitrary width which, theoretically, do not overlap (note though that some overlapping does occur in practical computation of the *harmonic wavelet transform* since "ideal" band-pass filters cannot be numerically implemented). This is not the case for typical wavelet families (*e.g.*, Meyer and Daubechies families) whose frequency content at each scale is implicitly defined by means of a single scalar (*i.e.*, the scaling parameter). An example of four neighbouring scales as part of a basis with constant-width "frequency bins" is shown in Figure 3.6(a) where the central frequency of each scale is noted by a broken line. Such a basis leads to a non-constant Q-analysis. Still, constant Q-analysis with dyadic discretisation of the typical *discrete wavelet transform* can be accommodated by the *harmonic wavelet transform* by taking $m[j]=2^j$ and $n[j]=2^{j+1}$.

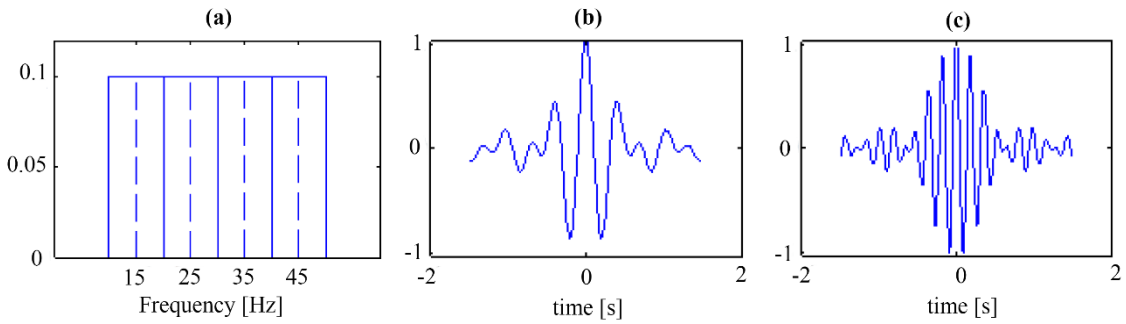

Figure 3.6: *Harmonic wavelets 10Hz constant bandwidth filter bank: (a) Fourier Amplitude Spectrum for 4 different scales with central frequencies denoted by broken lines, (b) real part harmonic wavelet with 15Hz central frequency, (c) real part harmonic wavelet with 35Hz central frequency.*

Nevertheless, the aforementioned "freedom of choice" of *harmonic wavelet transform* comes at the cost of relatively poor time localisation as evidenced by comparing the wavelets plotted in time domain in Figure 3.6 compared to those in Figure 3.3 to Figure 3.5. In fact, harmonic wavelets can be viewed as the complex counterpart of the so-called "Shannon wavelets" associated with the Littlewood-Paley basis (see for example *Daubechies* (1992) and *Vetterli & Herley* (1992)), which are well-known for their poor time localisation properties. Still, for stationary damage detection, poor time-localisation attributes are of secondary importance. From a computational viewpoint, robust fast Fourier transform (FFT)-based algorithms have been proposed by *Newland* (1994) and *Newland* (1999) for the efficient computation of non-redundant as well as for redundant *harmonic wavelet transform* on the frequency domain. A custom-made implementation of Newland's FFT-based algorithm is used to compute non-constant Q *harmonic wavelet transform* considered in the following section.

An orthonormal harmonic wavelet basis matrix $\mathbf{\Psi}_{N\times N} \in \mathbb{C}^{N\times N}$ can be constructed (*e.g.*, *Comerford et al.* (2015)) by defining first the number of wavelet scales, *j*, and the associated width of each frequency bin, ($n[j] - m[j]$), depending on the desired the time-frequency resolution of the problem at hand. Next, for each scale $j \in \left[0,1,...,N/\left(2\left(n[j]-m[j]\right)\right)\right]$, a discrete-time complex-valued harmonic wavelet $\psi_{j,k}[n] = \psi_{j,k}(nt)$ is computed from eq. (3.16) for n=[0, 1,…, N-1]. The obtained waveform is then separated in its real, $\Re$, and imaginary, $\Im$, components, each of which is translated in time by $kN/\left(n[j]-m[j]\right)$, with k taking values within the range $[0,\ n[j]-m[j]-1]$. The generated waveforms are then inserted as column vectors in $\mathbf{\Psi}_{N\times N}$ (see also *Comerford et al.* (2015)).

3.4. Numerical Assessment of Relative Wavelet Entropy–based Damage Detection for Various Wavelet Bases

3.4.1. Benchmark structural models

The RWE damage detection framework is applied herein to conventionally sampled acceleration response signals obtained from two finite element (FE) models corresponding to a healthy and a damaged state of an aluminum space truss, respectively. Lab specimens of similar structures have also been adopted by *Yun et al.* (2011) to attest the applicability of the RWE for damage detection from linear response acceleration signals obtained by tethered and wireless sensors.

In particular, the 8-bay simply supported aluminium truss of Figure 3.7 is considered, which is based on *Humar et al.* (2006), as a benchmark structure to assess the performance of various

vibration-based techniques for damage detection. The truss comprises 100 tubular members and each bay is a cube with 707mm long side. The members shown in blue in Figure 3.7 have 22mm diameter and 1mm wall thickness, while the members shown in grey are 30mm in diameter and 1.5mm wall thickness. The truss is modelled in SAP2000 FE commercial software using standard linear one-dimensional elements. Gravitational masses of 0.44kg are lumped at each of the 36 nodes of the FE model. Additional gravitational masses of 1.75kg are assigned to nodes 1,7,30, and 34, and of 2.75kg are assigned to nodes 20, 26, and 32 to produce FE models with well-separated modes of vibration (see also *Humar et al.* (2006)). A damaged state of the truss structure is further modelled by 50% reduction of the axial rigidity of the two truss members shown in red in Figure 3.7(b). For the first four vertical (gravitational) in-plane modes of vibration of the considered FE models, the structural natural frequencies obtained by means of standard modal analysis are reported in Table 3-1. In all the ensuing dynamic analyses, a critical damping ratio of 1% for all vibration modes is assumed.

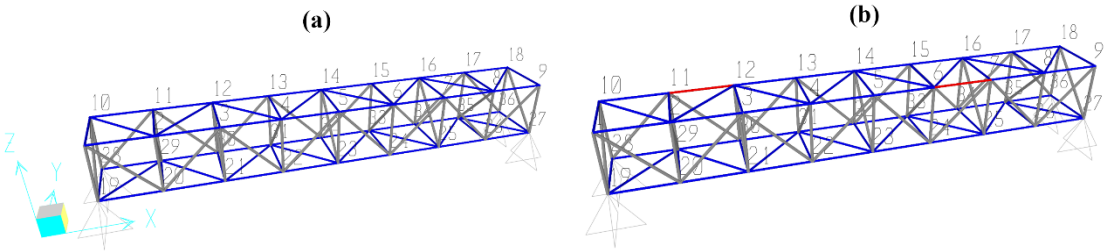

Figure 3.7: *Space truss FE models: (a) healthy state and (b) damaged state.*

Table 3-1: Natural frequencies corresponding to in-plane vertical bending mode shapes for the space truss FE models

Natural frequencies	Healthy State	Damaged State
f_1 [Hz]	73.6	68.9
f_2 [Hz]	165.4	163.9
f_3 [Hz]	294.5	291.6
f_4 [Hz]	424.3	419.0

3.4.2. Excitation forcing functions and response acceleration signals

Two different types of dynamic forcing functions are considered to excite the above FE models for reasons discussed later in the text: a 50s-long harmonic excitation with unit amplitude and linearly increasing frequency within the range of 0.1Hz to 320Hz (sine sweep), and a 40s-long realization of a zero-mean Gaussian white noise process with single-sided unit-amplitude power spectrum band-limited to 500Hz. Both functions are sampled at 1000Hz rate. Figure 3.8(a) plots the first 4s of the sine-sweep excitation and Figure 3.8(b) plots the white noise sample excitation normalised by its peak value. Further, Figure 3.8(c) plots the *Fourier Amplitude*

Spectrum of the sine-sweep normalised by its mean value and Figure 3.8(d) plots the *Fourier Amplitude Spectrum* of the white noise. It is seen that the considered forcing functions have a practically flat *Fourier Amplitude Spectrum* within a sufficiently wide frequency range to excite the structural natural frequencies of the considered FE models listed in Table 3-1. Therefore, both functions qualify for experimental forced vibration testing for damage detection using electromechanical shakers (*e.g.*, *Ewins* (2000)). However, in this study, forced vibration tests are simulated as described below.

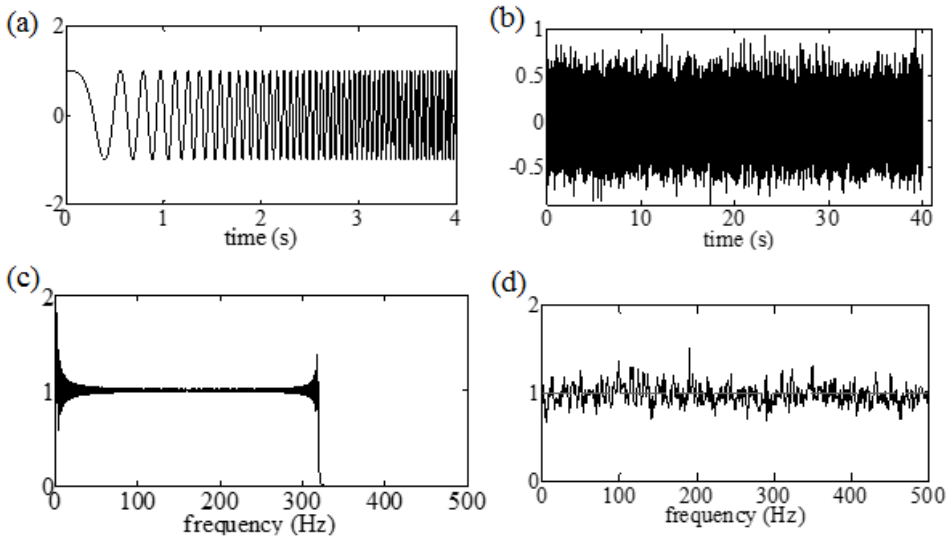

Figure 3.8: *Sine-sweep (only first 4s shown) and white noise forcing functions in the time domain, (a) and (b), and in the frequency domain, (c) and (d), respectively*

The above forcing functions are applied to 5th node of the space truss FE models along the z-axis (see Figure 3.7). For each individual forcing function, standard linear response history analyses are undertaken in SAP2000 FE software to obtain vertical acceleration response signals of the FE models in Figure 3.7 at 9 equidistant measurement points coinciding with the nodes 1 to 9 of the FE model in Figure 3.7. The obtained acceleration time-histories are treated as structural response signals corresponding to standard forced vibration experimental testing in a noise-free environment and are wavelet transformed by different filter banks introduced in the following section. It is important to note that the two forcing functions of Figure 3.8 differ in both time and frequency domain. Specifically, the white noise excitation is a *quasi-stationary* signal in the time domain (*i.e.*, a finite duration signal whose frequency and amplitude properties do not change in time), while the sine-sweep excitation is *non-stationary* in the time domain having a frequency content that evolves in time. Considering next the representation of these signal in the frequency domain, it is noted that the white noise excitation has a higher cut-off frequency at 500Hz compared to the sine-sweep excitation which is bandlimited by a maximum frequency at

320Hz. Consequently, the properties of the response acceleration signals will also be different in the two domains (*i.e.*, time and frequency domain) for the adopted excitations.

Along these lines, Figure 3.9 plots the acceleration time-series obtained from the 4th node of the damaged space truss model under the sine-sweep and white noise excitations, respectively. The pertinent FASs normalised to their peak value are illustrated in Figure 3.10. Note that the response signal to the sine-sweep excitation is non-stationary in time, observing three prominent "bursts" which are located at the time instants when resonance occurs. The latter phenomenon happens when the frequency of the sine-sweep input coincides with the truss resonant frequencies of Table 3-1 (*i.e.*, the first three natural frequencies are excited by the bandlimited sine-sweep input in the frequency range [0.1, 320] Hz). On the antipode, the response signal to the white noise excitation is stationary in time, exciting additional higher order mode shapes whose natural frequencies lie outside the bandwidth of the sine-sweep excitation. This additional broadband high frequency content may affect the interpretation of RWE values derived from different wavelet filter banks; the latter is examined and discussed in subsequent sections. *The reason for considering both sets of response signals (stationary and non-stationary) is to test whether the above differences in the time domain might influence the potential of the RWE for damage detection depending on the wavelet filter bank used, given that the poor time localisation capabilities of certain wavelet families considered in this study (i.e., the harmonic wavelets in Figure 3.6).*

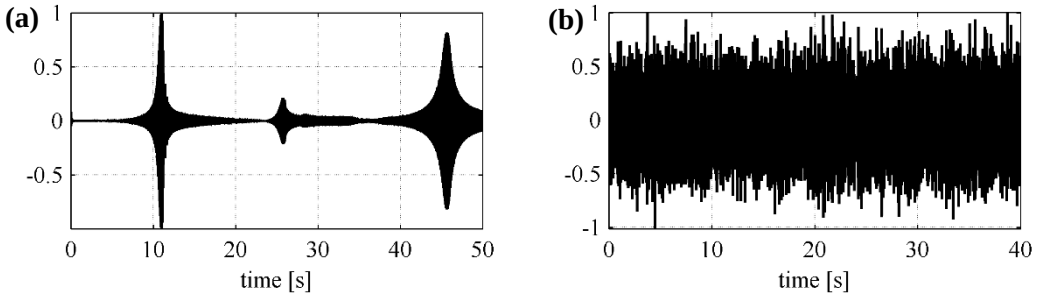

Figure 3.9: *Time domain representation of the normalised to unit amplitude response acceleration signals recorded at node 4 of the damaged space truss in Figure 7 under (a) sine-sweep and (b) white noise excitation.*

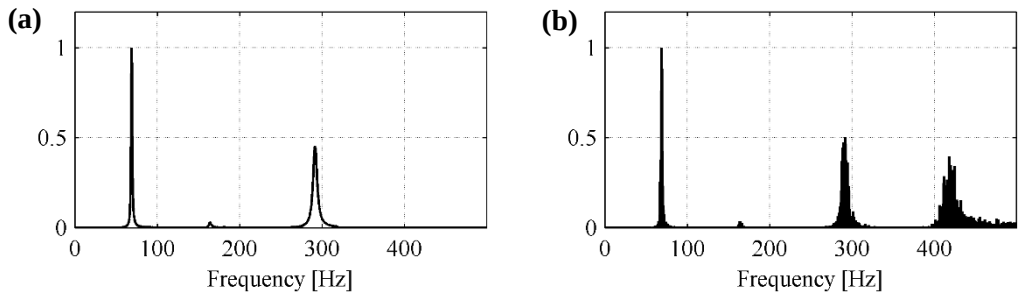

Figure 3.10: *Frequency domain representation of the normalised to unit amplitude response acceleration signals recorded at node 4 of the damaged space truss in Figure 7 under (a) sine-sweep and (b) white noise excitation.*

3.4.3. Wavelet analysis filter banks and scale-dependent relative wavelet entropy

Prior to the implementation of the wavelet analysis, signal pre-processing operations are applied to the considered acceleration response datasets of the truss FE models in Figure 3.7. Firstly, the structural responses are zero-padded to generate N-length time-sequences, where N is a power of 2. In this respect, time-sequences of $N=2^{16}$ data-samples are generated for both excitation cases considered (*i.e.*, sine-sweep and white noise). The generated signals are further normalised by the energy of the corresponding forcing functions, their potential non-zero mean value is then subtracted, and they are wavelet transformed using various different energy preserving wavelet filter banks. Specifically, two 16-scale dyadic *discrete wavelet transform* filter banks are considered implementing non-smooth Daubechies D2 (or Haar) and smooth Daubechies D20 wavelets, attaining almost the same (constant) Q value: Q≈0.49 for the Haar filter bank and Q≈0.46 for the D20. Furthermore, a Meyer wavelet basis approximated by a 16-scale dyadic finite impulse response *discrete wavelet transform* filter bank of approximately Q≈0.68 constant (*i.e.*, significantly higher that the two Daubechies filter banks) is also considered. Table 3-2 reports the effective bandwidth (accounting only for the main lobes of the *Fourier Amplitude Spectrum* for the Daubechies wavelets) and the characteristic frequency at which the wavelet *Fourier Amplitude Spectrum* is maximised for the first 10 *discrete wavelet transform* analysis levels of the above three filter banks. To facilitate the interpretation of the results presented in the following section, Table 3-2 indicates with bold fonts the 4 analysis scales corresponding to the FASs in Figure 3.3, Figure 3.4, and Figure 3.5, which pertain to the D2, D20, and Meyer wavelets, respectively. The *discrete wavelet transform* for all the above filter banks is carried out using the built-in functions of the MATLAB-based wavelet toolbox developed by *Misiti et al.* (1997). Notably, the natural frequencies of the truss in Table 3-1 are not uniquely defined within the effective range of a given scale j (or analysis level) for the three *discrete wavelet transform* presented in Table 3-2, due to overlapping between adjacent scales.

Additionally, the considered signals are also processed by means of a harmonic wavelet basis of 128 adjacent non-overlapping "frequency bins" (scales) of constant width equal to 3.91Hz spanning the range of 0-500 Hz on the frequency axis. Note that the consideration of constant effective bandwidth for all scales/analyses levels is a reasonable assumption in SHM cases where the structural natural frequencies are not known *a priori.* Table 3-3 reports the frequency domain attributes of the non-constant Q *harmonic wavelet transform* for 16 analysis levels, which include the first four truss resonant frequencies listed in Table 3-1 (both healthy and damaged states). Note that each natural frequency of the truss in Table 3-1 is uniquely located in a single frequency bin of the *harmonic wavelet transform*, which is rather beneficial in the computation of RWE index as discussed in §3.4.4. The non-constant Q *harmonic wavelet transform* analysis is carried

out by means of a custom-made code implementing the FFT-based algorithm described by *Newland* (1994) and *Newland* (1999).

Table 3-2: Frequency domain attributes of the first 10 analysis levels for the considered wavelet filter banks

Analysis Level (scale)	D2 Daubechies or Haar wavelet filter bank (Q≈0.49)		D20 Daubechies wavelet filter bank (Q≈0.46)		Meyer wavelet filter bank (Q≈0.68)	
	Effective range (Hz)*	Effective Frequency (Hz)*	Effective range (Hz)*	Effective Frequency (Hz)*	Effective range (Hz)	Effective Frequency (Hz)
Level 1 (j=16)	0-1024	498.05	70.62-812.14	342.11	179.2-674.13	331.68
Level 2 (j=15)	0-558	249.03	45.85-412.66	171.05	85.33-341.33	165.84
Level 3 (j=14)	**0-267**	**124.51**	**21.48-207.66**	**85.53**	**42.67-170.67**	**82.92**
Level 4 (j=13)	**0-130**	**62.26**	**10.41-100.66**	**42.76**	**22.4-85.33**	**41.46**
Level 5 (j=12)	**0-64**	**31.13**	**5.13-51.29**	**21.38**	**11.2-42.67**	**20.73**
Level 6 (j=11)	**0-32**	**15.56**	**2.55-25.45**	**10.69**	**5.33-21.33**	**10.37**
Level 7 (j=10)	0-16	7.78	1.27-12.68	5.35	2.8-10.67	5.18
Level 8 (j=9)	0-8	3.89	0.63-6.33	2.67	1.4-5.33	2.59
Level 9 (j=8)	0-4	1.95	0.32-3.16	1.34	0.67-2.67	1.30
Level 10 (j=7)	0-2	0.97	0.16-1.63	0.67	0.35-1.32	0.65

**Values accounting for only the main lobe of the Fourier Amplitude Spectrum of the scaled wavelets*

Table 3-3: Frequency domain attributes of the non-constant Q harmonic wavelet transform for 16 analysis levels (in non-consecutive order) which include the first four resonant frequencies of truss in its healthy and damaged state

Analysis Level (scale)	Harmonic wavelet analysis		Analysis Level (scale)	Harmonic wavelet analysis	
	Frequency Range (Hz)	Central Frequency (Hz)		Frequency Range (Hz)	Central Frequency (Hz)
Level 19	425.81 - 429.69	427.75	**Level 85**	168.00 - 171.88	169.94
Level 20	421.88 - 425.81	423.84	**Level 86**	164.06 - 168.00	166.03
Level 21	418.00 - 421.88	419.94	**Level 87**	160.19 - 164.06	162.12
Level 22	414.06 - 418.00	416.03	**Level 88**	156.25 - 160.19	158.22
Level 52	296.88 - 300.81	298.84	**Level 109**	74.25 - 78.13	76.19
Level 53	293.00 - 296.88	294.94	**Level 110**	70.31 - 74.25	72.28
Level 54	289.06 - 293.00	291.03	**Level 111**	66.44 - 70.31	68.37
Level 55	285.19 - 289.06	287.12	**Level 112**	62.50 - 66.44	64.47

For the sine-sweep excitation, the square magnitude of the wavelet coefficients, computed from the above wavelet filter banks (*i.e.*, D2, D20, Meyer, and Harmonic wavelets), is illustrated in Figure 3.11 for a typical truss acceleration response measured at the 4th node of the damaged FE model in Figure 3.7. It is readily observed from Figure 3.11 that the distribution of the signal's energy in the time-frequency plane depends strongly on the frequency attributes of the adopted wavelet filter banks. In all panels of Figure 3.11, the signal energy is time-limited at t_1=11.7s, t_2=26.8s and t_3=46.1s, *i.e.*, at the same time instants that the "bursts" in Figure 3.9 occur, pertaining to the first three resonant frequencies of the adopted structure (see also Figure 3.10). Note the considerably smaller signal energy around the 2nd resonance at t_2=26.8s for all cases in Figure 3.11 (compared to the other two resonances at t_1 and t_3) due to the consideration of the truss acceleration response at node #4 which is close to a zero node for the 2nd modal deflected shape of the truss.

For the D2, D20 and the Meyer wavelet filter banks in Figure 3.11 (a-c), it is seen that the signal's energy is mainly concentrated at t_1=11.7s, associated with the first natural frequency of the truss (see also Figure 3.10). At resonances, though, of higher frequency content (*i.e.*, at t_3=46.1s), the pertinent energy is not adequately retrieved by these three wavelets (D2, D20, Meyer) due to their poor frequency selectivity at higher frequencies. Further, significant energy leakage is observed in Figure 3.11 (a-c) for the D2, the D20 and the Meyer wavelet, caused by the significant overlapping of their frequency bands among scale (see also Figure 3.3-Figure 3.5 and Table 3-2). Note that the Haar *discrete wavelet transform* observes the poorest frequency resolution, which is also reflected in Figure 3.11(a) with the spread of the signal's energy over 5 scales (*i.e.*, j=10-15). However, the frequency resolution is improved in Figure 3.11(b) for the D20 wavelet, while it gets even better in Figure 3.11(c) for the Meyer wavelet. On the contrary, Figure 3.11 (d) reveals that the high-resolution harmonic wavelets can efficiently capture the signal energy at the two dominant resonances at t_1=11.7s and t_3=46.1s, despite their poor time-domain localisation properties, yielding two distinct peaks at the pertinent natural frequencies of the damaged truss (*i.e.*, at 68.9 Hz and 291.6 Hz in Table 3-1).

Similar remarks hold for the white noise excitation in Figure 3.12, which plots the square magnitude of the wavelet coefficients for the four considered wavelet filter banks (*i.e.*, D2, D20, Meyer and the *harmonic wavelet transform*) by employing the same truss acceleration signal as in Figure 3.11 for the sine-sweep excitation. Notably, the energy distribution of the truss acceleration response under the quasi-stationary white noise excitation (bandlimited to 500Hz) preserves the time and frequency domain attributes discussed in sub-section §3.4.2. The latter include the signal's stationarity property along the time axis (*i.e.*, the excited frequencies do not change in time) as well as the excitation of the higher modes of the vibrating truss, pertaining to resonant frequencies up to 500 Hz (*i.e.*, signal energy is also concentrated around the 4th natural frequency of the truss at f_4=419 Hz).

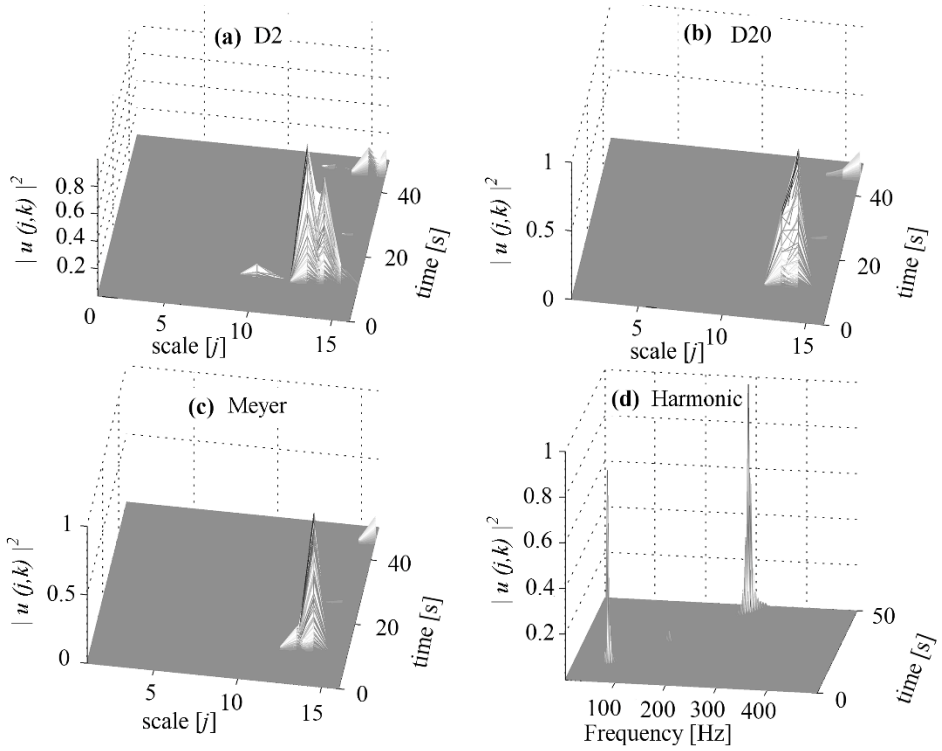

Figure 3.11*:Normalised squared magnitude of wavelet coefficients pertaining to the truss acceleration response at node #4 (damaged state) under the sine-sweep excitation; discrete wavelet transform analysis with (a) D2 (Haar), (b) D20, (c) Meyer; and (d) Harmonic wavelet transform*

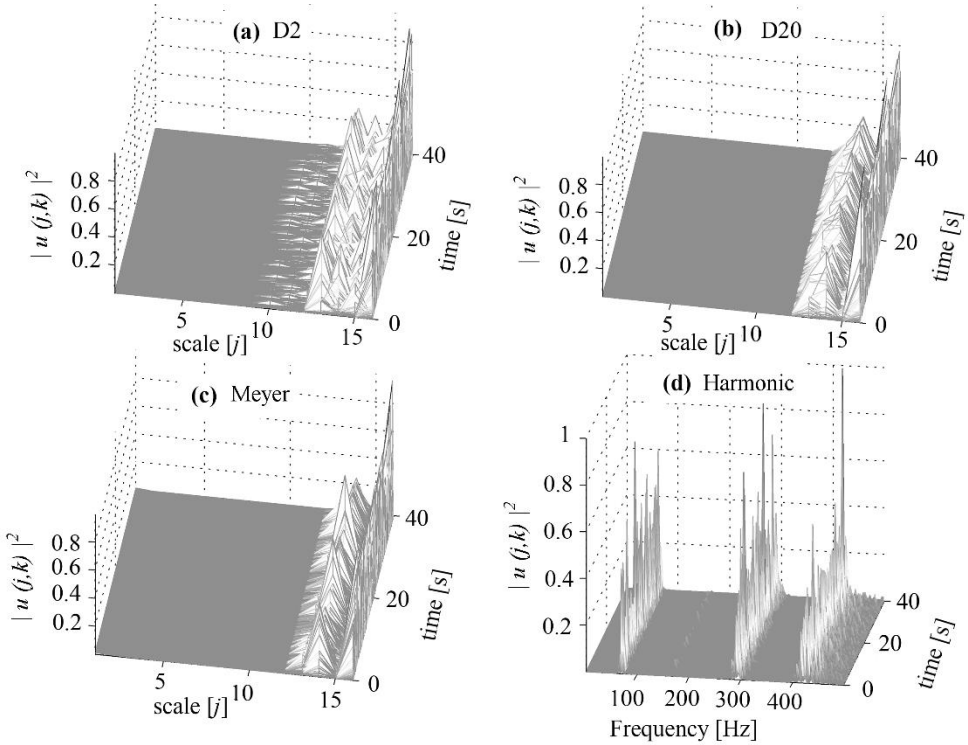

Figure 3.12*: Normalised squared magnitude of wavelet coefficients pertaining to the truss acceleration response at node #4 (damaged state) under the white noise excitation; discrete wavelet transform analysis with (a) D2 (Haar), (b) D20, (c) Meyer; and (d) Harmonic wavelet transform*

Next, the relative wavelet energy in eq. (3.8) is computed from the wavelet coefficients of the response acceleration signals (healthy and damaged states) at each scale of the 4 different wavelet filter banks. Subsequently, the following "scale-dependent" contributor to the overall RWE in eq. (3.10) is calculated for all measurement points of the damaged models

$$\mathrm{RWE}(j) = w_j \ln\left(\frac{w_j}{z_j}\right). \tag{3.18}$$

In the last equation, z_j is the relative wavelet energy at scale j computed from the simulated response signals of the "healthy" FE models, while w_j is the relative wavelet energy at scale j corresponding to response signals of the damaged state. The consideration of the above scale-dependent RWE(j) makes possible to discriminate the contributions to the overall RWE in eq. (3.10) from each wavelet analysis level. Therefore, it serves well the purpose of assessing the influence of the frequency domain attributes of the different wavelet filter banks considered (*i.e.*, frequency selectivity among scales and Q value) to the computed values of the RWE index. Finally, it is noted that no hard-thresholding is applied to the RWE as has been proposed by *Ren & Sun* (2008) to sharpen damage localisation by keeping only the values of the RWE above a certain threshold. *This is because this study focuses on gauging the influence of using different wavelet filter banks to the computation of the RWE across different scales, rather than the potential of RWE for damage localisation.* The latter issue is well-established in the literature (*Ren & Sun* (2008);*Yun et al.* (2011); *Lee et al.* (2014)). Therefore, the next sub-section presents and discusses "raw" scale-dependent RWE(j) data obtained from the various analyses undertaken without any further filtering or processing.

3.4.4. Numerical results and discussion

Considering the uniform-sampled N-length truss acceleration responses to the sine-sweep and the white noise excitations, the scale-dependent RWE(j) in eq. (3.18) is computed for the four different wavelet bases in §3.3, and plotted in the three-dimensional bar charts of Figure 3.13(a) to Figure 3.20 (a). The RWE(j) bars are stacked along a scale/frequency axis corresponding to the wavelet analysis levels in Table 3-2 and Table 3-3, and along a spatial axis, labelled after the points on the FE models in Figure 3.7 at which the response acceleration signals are recorded. A large *positive* value of the RWE(j) at a particular scale/frequency and measurement point indicates a potential local damage. This local damage is inferred from the *changes* in the signals energy around the *dominant resonant frequencies of the damaged* structure (in Table 3-1) by processing response accelerations recorded at the given location/point in two structural states (*i.e.*, a healthy and a damaged state). Further, Figure 3.13(b) to Figure 3.20(b) plot the RWE in (3.10), that is,

the sum of the scale dependent RWE(j) across all scales/frequencies as considered by *Ren & Sun* (2008).

The non-stationary sine-sweep excitation case (bandlimited to 320Hz in Figure 3.8(c)) is first considered and the set of RWE plots in Figure 3.13 - Figure 3.16 is examined. It is noted that acceptable damage localisation is achieved, for all four filter banks considered in this study, indicated by large RWE values around the 3rd and 7th measurement points. The latter is better visualised in Figure 3.13(b) - Figure 3.16(b), in which a red broken line is also plotted to indicate the value of an assumed hard thresholding criterion for efficient damage detection. In the case of the Haar wavelet basis (Figure 3.13), the smooth Daubechies D20 wavelets (Figure 3.14) and of the Meyer wavelets (Figure 3.15), the RWE values are primarily contributed from scale at $j=13$ (or analysis level 4), with effective ranges that contain the first damaged natural frequency of the damaged space truss (at 68.9 Hz), as shown in Table 3-2. The RWE derived from the Haar wavelet basis exhibits certain non-zero RWE values from scales j=9 to j=15, which can be attributed to the energy (spectral) leakage shown in Figure 3.11 (a) caused by the significant overlapping of the wavelet's frequency bands among scales (Figure 3.3, Table 3-2). For the same reasons, non-zero RWE values are also observed in Figure 3.14 for the Daubechies D20 wavelet, which, however, contribute only at scale j=15 (of higher frequency content) and at fewer measurements points compared to the Haar wavelet basis in Figure 3.13. Note that the Meyer wavelet case in Figure 3.15 exhibits spurious RWE values at lower scales (j=1,2), associated with very low effective frequencies below the range of interest. On the contrary, the computed RWE values from the *harmonic wavelet transform* in Figure 3.16 are confined within just two frequency bins, pertaining to the first and the third natural frequencies of the damaged truss. Further, it is clearly seen in Figure 3.16 that the structural damage is mainly attributed to the frequency shifts associated with the fundamental resonant frequency of the adopted structure - an observation that is not easily distinguished in the previous cases (Figure 3.13-Figure 3.15) due to the overlapping phenomenon. Therefore, the non-constant Q harmonic wavelet filter bank with, theoretically, zero overlapping among scales offers a more robust RWE-based damage detection compared to the other *discrete wavelet transform* filter banks as it draws information about the damage from both the excited mode shapes at all measurement points.

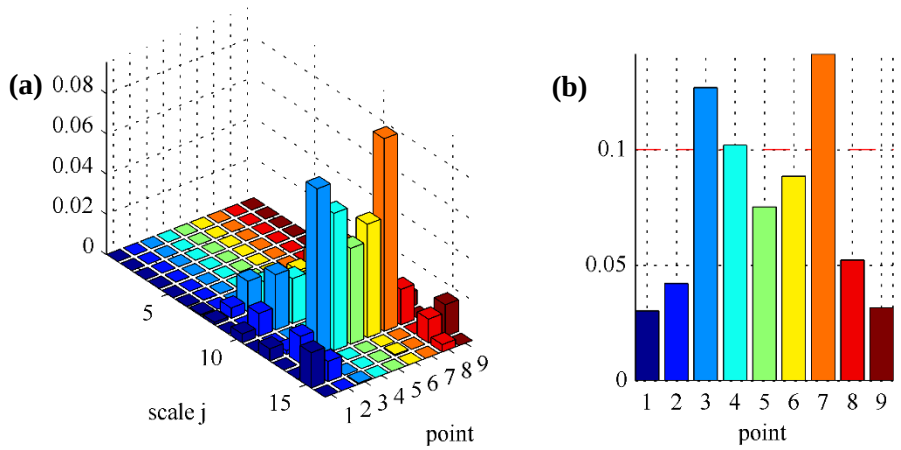

Figure 3.13: *(a) Scale-dependent RWE(j) in eq. (3.18) and (b) RWE in eq. (3.10) using the Daubechies D2 (or Haar) wavelet filter bank for the space truss subject to the sine-sweep excitation*

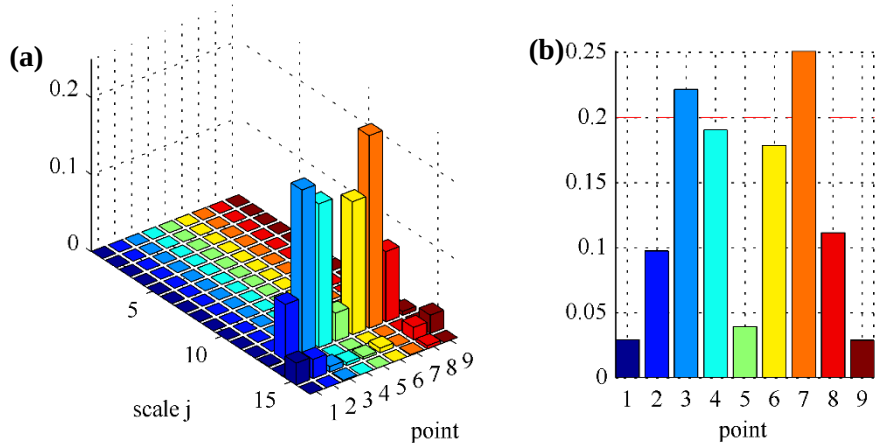

Figure 3.14*: (a) Scale-dependent RWE(j) in eq. (3.18) and (b) RWE in eq. (3.10) using the Daubechies D20 wavelet filter bank for the space truss subject to the sine-sweep excitation*

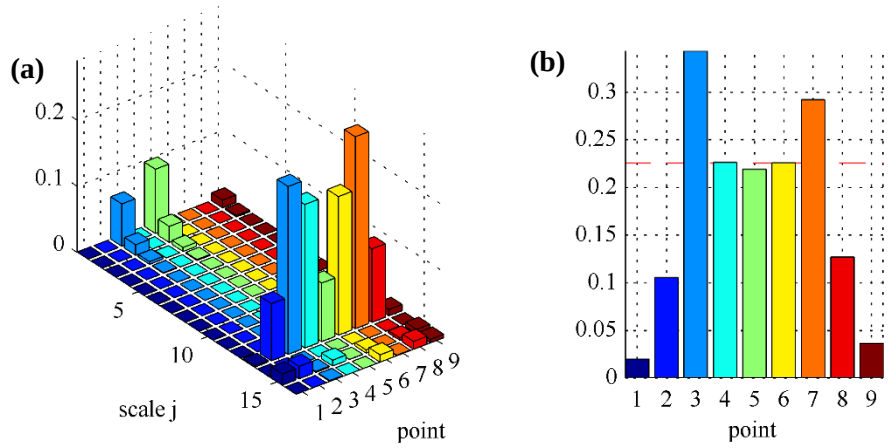

Figure 3.15*: (a) Scale-dependent RWE(j) in eq. (3.18) and (b) RWE in eq. (3.10) using the Meyer wavelet filter bank for the space truss subject to the sine-sweep excitation*

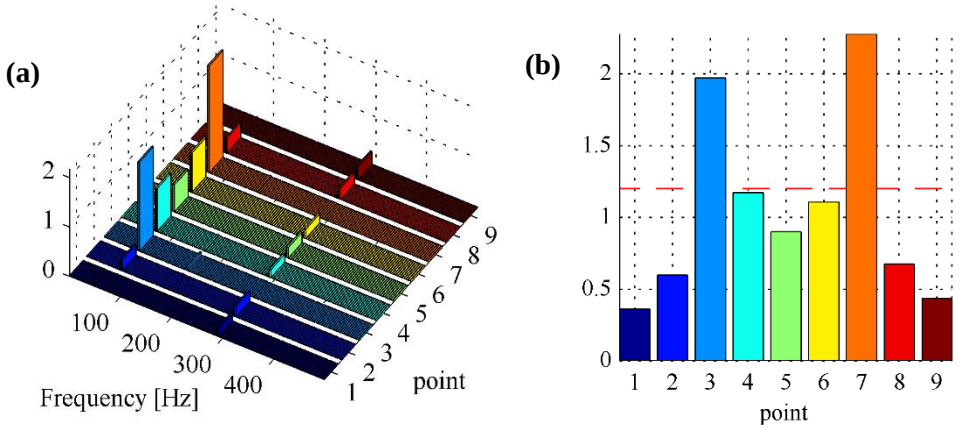

Figure 3.16: *(a) Scale-dependent RWE(j) in eq. (3.18) and (b) RWE in eq. (3.10) using a 128-scale harmonic wavelet filter bank (3.91Hz bandwidth per scale) for the space truss subject to the sine-sweep excitation*

Similar remarks hold for the set of RWE plots in Figure 3.17-Figure 3.20 pertaining to the stationary white noise excitation (bandlimited to 500Hz in Figure 3.8(d)). A marked difference, though, is the partial detection of structural damage around the 7th measurement point only, where the largest RWE values are observed. Exception to the latter is the Meyer wavelet case in Figure 3.19, which can also retrieve the structural damage close to the 3rd measurement point. Nonetheless, the RWE values derived from the Meyer *discrete wavelet transform* attain non-negligible values at low scales (below j=5) which are not related to the broadband high frequency content in the considered truss acceleration responses (see also Table 3-1). As in the case of response signals from the sine-sweep excitation, the harmonic wavelet filter bank in Figure 3.20 can resolve accurately the shifts of natural frequencies as they reflect to changes to the wavelet energy distribution captured by the RWE. Clearly, the fact that the two sets of response acceleration signals examined (*i.e.*, due to the sine-sweep and white noise excitations) have very different time-domain properties does not affect the ability of harmonic wavelets to represent correctly the frequency content even for the highly non-stationary signals despite their relatively poor time localisation capabilities.

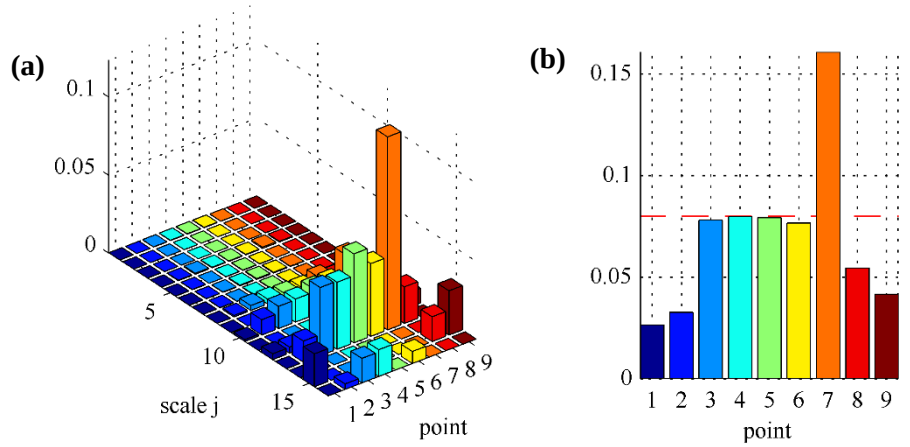

Figure 3.17: *(a) Scale-dependent RWE(j) in eq. (3.18) and (b) RWE in eq. (3.10) using the Daubechies D2 (or Haar) wavelet filter bank for the space truss subject to the white noise excitation.*

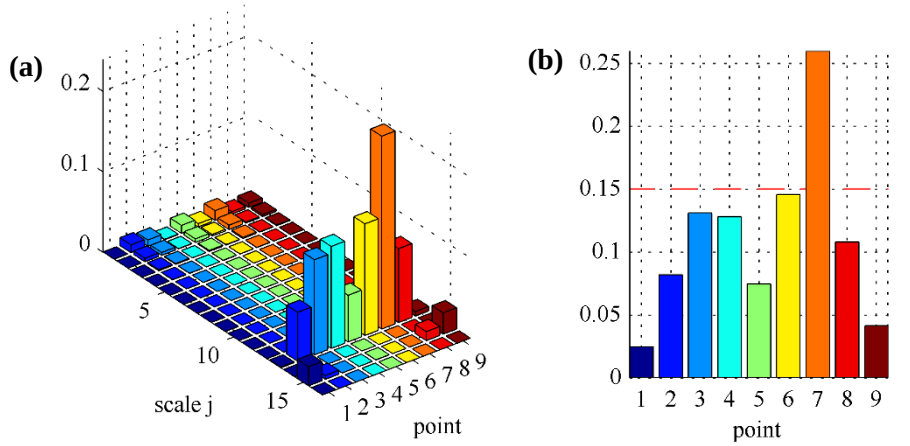

Figure 3.18: *(a) Scale-dependent RWE(j) in eq. (3.18) and (b) RWE in eq. (3.10) using the Daubechies D20 wavelet filter bank for the space truss subject to the white noise excitation.*

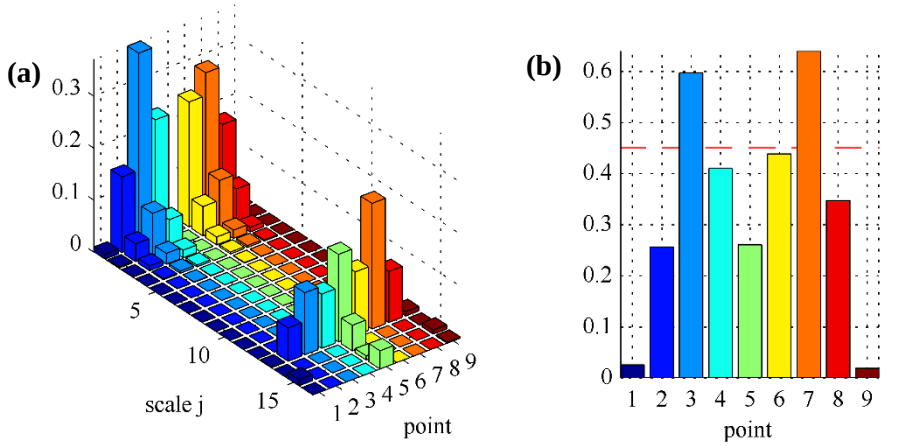

Figure 3.19: *(a) Scale-dependent RWE(j) in eq. (3.18) and (b) RWE in eq. (3.10) using the Meyer wavelet filter bank for the space truss subject to the white noise excitation.*

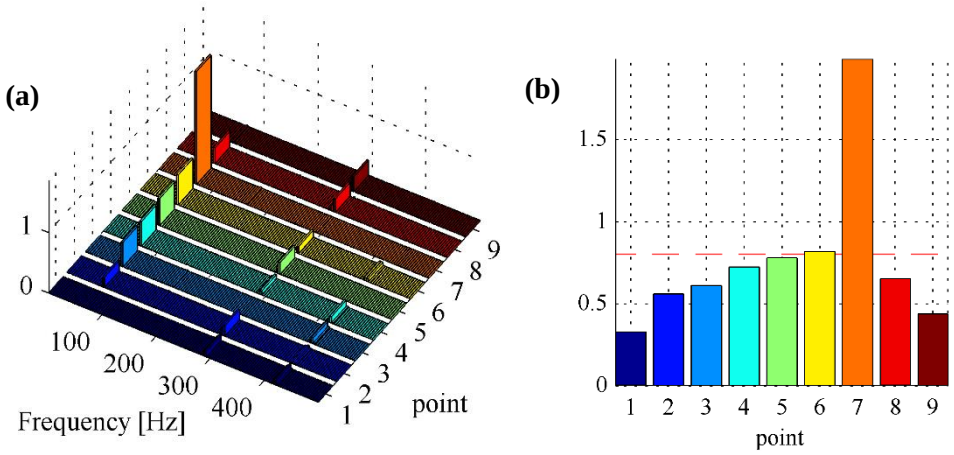

Figure 3.20: *(a) Scale-dependent RWE(j) in eq. (3.18) and (b) RWE in eq. (3.10) using a 128-scale harmonic wavelet filter bank (3.91Hz bandwidth per scale) for the space truss subject to the white noise excitation.*

Overall, the above numerical results show that the dyadic *discrete wavelet transform* bases capture structural damage from non-zero RWE(*j*) values manifested at various scales with effective/central frequencies that are not necessarily close to a structural natural frequency. Further, significant spectral leakage is seen across scales due to severe overlapping among various frequency bands, which does not facilitate the interpretation of the results. On the contrary, it is shown that the adopted harmonic wavelet basis, spanning non-overlapping frequency bands among scales and maintaining the same level of (high) resolution for the full range of frequencies of interest, is always able to discriminate changes to the distribution of the signal energy between the damaged and the healthy states caused by shifts in all excited structural natural frequencies. This is achieved no matter whether the recorded signals are stationary or non-stationary in the time domain and with negligible spectral leakage which renders the interpretation of the results a straightforward task.

These promising results suggest that the adopted energy-preserving harmonic wavelet basis can be fused with compressive sensing data acquisition techniques (*e.g.*, *Baraniuk* (2007)) to significantly reduce the computational cost and power consumption in wireless sensors for VSHM while providing quality estimates of structural damage using the RWE damage index. This issue is addressed in the next section.

3.5. Proposed Compressive Relative Harmonic Wavelet Entropy Approach for Damage Detection

3.5.1. Sparsity of truss acceleration responses on the harmonic wavelet basis

This section numerically assesses the potential of using the compressive sensing data acquisition and reconstruction technique (Chapter 2) within the RWE-based structural damage

detection framework detailed in §3.2.3. This evaluation is performed for the space truss model in Figure 3.7 subjected to the sine-sweep and white noise excitation forces in Figure 3.8. For these cases, the truss acceleration response datasets in both "healthy" and damaged structural states are considered, while their sparsity attributes are examined on the orthonormal *harmonic wavelet basis*. As opposed to the other wavelet families presented in this chapter (*i.e.*, non-smooth Daubechies/ Haar (D2), smooth Daubechies (D20) and Meyer wavelet), the high-resolution harmonic wavelets do not suffer for spectral leakage across scales, rendering this particular basis the most suitable (among the wavelet bases presented herein) for the sparsest representation of stationary structural responses.

To demonstrate the above, consider Figure 3.11(d) and Figure 3.12 (d), which present the square magnitude of the harmonic wavelet coefficients derived from the response acceleration at the 4th node of the damaged truss under the sine-sweep and white noise excitation, respectively. The magnitude of these coefficients is sorted in descending order and plotted in Figure 3.21 to obtain an estimate of the signal's sparsity on the harmonic wavelet basis. Commenting first on the deterministic and non-stationary sine-sweep excitation, it is seen in Figure 3.11(d) that the signal's energy is mainly clustered around the 1st and 3rd natural frequencies of the space truss (see also Table 3-1) at the time instants when the resonance phenomenon occurs (*i.e.*, when the frequency of the input excitation force coincides with the inherent resonant frequencies of the adopted structure). This highly sparse signal representation is also confirmed in Figure 3.21(a), in which the harmonic wavelet coefficients are shown to decay extremely fast when sorted by magnitude. Thus, it is confirmed that signal information can be captured from only $S \simeq 1000$ (complex-valued) harmonic wavelet coefficients out of a total number of 32768 coefficients, pertaining to just the 3% of the time-frequency plane.

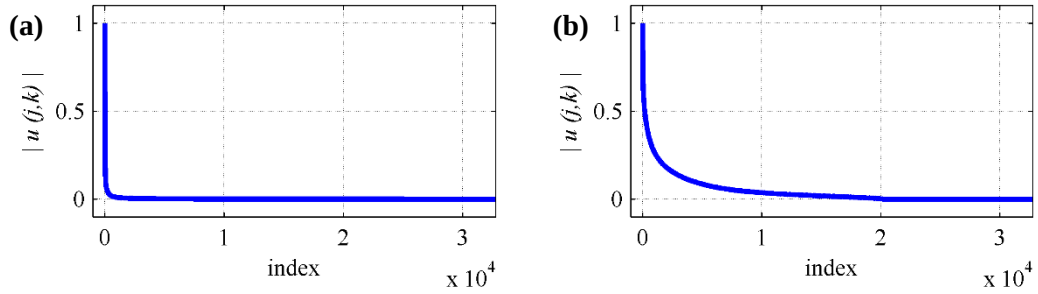

***Figure 3.21**: Normalised magnitude of harmonic wavelet coefficients sorted in descending order obtained from the truss acceleration response at node 4 for the (a) sine-sweep excitation and (b) white noise excitation.*

Moving next to the random stationary white noise excitation, a less sparse signal representation is observed in Figure 3.12 (d) and Figure 3.21 (a) compared to the previously discussed sine-sweep case. This is explained by the fact that the signal energy is also retrieved in higher modes of vibration along the entire time axis due to the time and frequency domain

attributes of the white noise excitation detailed in §3.4.2. However, Figure 3.21 confirms that the truss acceleration responses preserve a *compressible* structure on the considered harmonic wavelet transform domain, given the quick decay in the sorted magnitude of the pertinent coefficients (see *e.g.*, *Needell & Tropp* (2010); *O'Connor et al.* (2014)). Therefore, the significant signal information is retained in roughly $S \simeq 10000$ (complex-valued) harmonic coefficients which is still a small fraction of the total number of coefficients in the order of 30%.

From the above observations, it can be deduced that the excellent signal sparsity attributes of the truss acceleration responses on the orthonormal harmonic wavelet basis allows to couple CS with the RWE-based damage detection framework in §3.2.3 resulting in a novel CS-based damage detection approach supporting inexpensive data acquisition and transmission in WSNs. In this respect, the significant wavelet coefficients and the RWE damage-sensitive indices can be retrieved directly from much fewer acquired compressed measurements compared to conventional signal acquisition techniques (at Nyquist sampling rates or above) without recovering the time-domain acceleration responses in the uniform Nyquist grid. This CS-based approach can significantly reduce the computational cost and power consumption in wireless sensors, being extremely useful in vibration-based structural health monitoring applications.

3.5.2. Compressive sensing and partial harmonic wavelet basis

Following that mathematical framework of the Compressive Sensing theory in Chapter 2, a "partial" harmonic wavelet sampling matrix $\mathbf{\Psi}_{M\times N} \in \mathbb{C}^{M\times N}$ is defined by considering a measurement matrix $\mathbf{\Theta} \in \mathbb{C}^{M\times N}$ populated with incoherent measurements of zero-one entries that randomly selects *M* rows from an orthonormal harmonic wavelet matrix $\mathbf{\Psi}_{N\times N} \in \mathbb{C}^{N\times N}$ (*e.g.*, *Comerford et al.* (2015)). This is a standard technique to derive a "partial" orthonormal sampling matrix that satisfies the RIP in eq. (2.3) with high probability (*e.g.*, *Candès* (2008)). Examples include the *"partial" Fourier matrix* detailed in Chapter 2, the *partial Haar wavelet basis* used in pertinent CS-based VSHM applications in the literature (*e.g.*, *Bao et al.* (2011), (2013), (2014)). The "*partial" harmonic wavelet basis* $\mathbf{\Psi}_{M\times N} \in \mathbb{C}^{M\times N}$ was employed by *Comerford et al.* (2015) to address the missing data problem in environmental stochastic processes, demonstrating its efficacy in accurately solving the sparsity-constrained ℓ_1 minimisation problem in eq. (2.10) and reconstructing sparse signals with 65% missing measurements.

In this numerical study, an orthonormal harmonic wavelet basis $\mathbf{\Psi}_{N\times N} \in \mathbb{C}^{N\times N}$ is first formulated, consisting of 128 adjacent non-overlapping "frequency bins" (scales) of constant width equal to 3.91Hz spanning the range of 0–500 Hz on the frequency axis (*i.e.*, the same assumptions were also made in §3.4.3). To efficiently compute the "fat" basis matrix of size

$N \times N$ and to facilitate the fast implementation of the CoSaMP sparse recovery algorithm* by *Needell & Tropp* (2010) used in subsequent sub-sections, the truss acceleration response signals are divided in 256 segments of length N=256.

For all considered datasets, random signal compression is then performed by considering three *CRs* at 10%, 20%, and 30%. In this respect, compressive-sampled truss acceleration responses, $y[m]$, $m=\{1,2,\ldots,M\}$, are simulated in MATLAB, by randomly acquiring M entries from each segment of the reference signal $x[n]$, $n=\{1,2,\ldots,256\}$ with $M=\{25, 51, 76\}$ for the three *CRs*, respectively. The position of the M random measurements is associated with the unit entries in $\boldsymbol{\Theta} \in \mathbb{C}^{M\times N}$ that determines the selection of the M rows in $\boldsymbol{\Psi}_{N\times N} \in \mathbb{C}^{N\times N}$. For illustration, Figure 3.22 depicts the random signal compression at CR=30% for a typical truss acceleration response (at node #4 of the damaged truss model in Figure 3.7) in the sine-sweep (Figure 3.22 (a)) and the white noise (Figure 3.22 (b)) forcing cases. In these figures, the compressive-sampled measurements $y[m]$ (red) are plotted against the uniform-sampled data $x[n]$ (blue), and results are presented within a time-window of 0.2s.

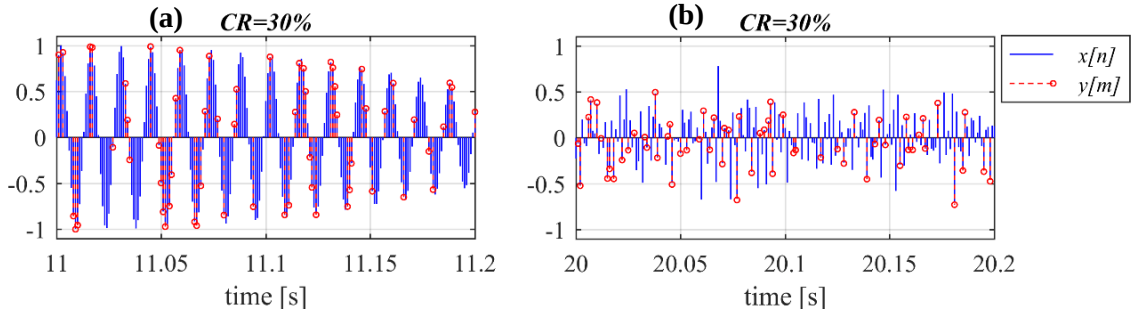

Figure 3.22: *Compressive sensing at CR=30% and the acquisition of M=60 samples from acceleration response signal at node #4 within a time-window of 0.2sec duration with N=200 Nyquist samples; (a) sine-sweep excitation and (b) white noise excitation*

3.5.3. Reconstruction of harmonic wavelet coefficients

The CoSaMP sparse recovery algorithm (see also §2.2) is further employed, to recover the harmonic wavelet coefficients directly from the obtained compressed measurements $y[m]$, without reconstructing the time-domain acceleration responses. The CoSaMP algorithm takes as input the compressed accelerations $y[m]$, the partial harmonic wavelet sampling matrix $\boldsymbol{\Psi}_{M\times N} \in \mathbb{C}^{M\times N}$ together with an assumed value for target sparsity S_T, and returns the harmonic wavelet coefficients for all j-scales and k-translations (*i.e.*, $\hat{u}_{j,k}[n] = \text{CoSaMP}\ (y[m],\ \boldsymbol{\Psi}_{M\times N},\ S_T)$). Recall from Chapter 2 that the selection of the S_T plays a crucial role in the reconstruction performance of the CoSaMP algorithm, while an upper bound

* *The sparse recovery in CoSaMP entails the pseudo-inverse of the considered sampling matrix - a process that has increased computational cost depending on the size of the matrix to be "pseudo"-inverted (see also section §2.2)*

is set at $M/3$ (*e.g.*, *Needell & Tropp* (2010)). For the needs of this study, the maximum possible target sparsity is assumed, *i.e.*, $S_T = M/3$.

For the case of CR=30% and for the two considered excitation cases, Figure 3.23 illustrates the square magnitude of the CS-reconstructed harmonic wavelet coefficients, obtained by application of the CoSaMP algorithm to compressed truss acceleration time-sequences at node #4. The two panels in Figure 3.23 are further compared against Figure 3.11(d) and Figure 3.12(d), respectively, to assess the reconstruction quality of the CS-based harmonic wavelet coefficients. For the sine-sweep excitation case, it is easily observed that the CS-based spectrum in Figure 3.23 (a) closely approximates the pertinent spectrum in the non-compressive case of Figure 3.11(d). For this case, the time-frequency localisation of the spectral peaks is retrieved with high accuracy. This is not confirmed, though, for the white-noise excitation case shown in Figure 3.23(b), where significant energy leakage occurs in the entire time-frequency plane in contrast to Figure 3.12(d). Nonetheless, the maximum spectral peaks are accurately resolved around the resonant frequencies of truss. Notably, the quality of the CS-recovered coefficients depends strongly on the signal sparsity level on the considered basis, which differs in two forcing cases. As explained in §3.5.1, the sine-sweep case pertains to response acceleration signals that attain a sparser structure on the harmonic wavelet transform domain compared to the white noise excitation case. The latter suggests that the sine-sweep case can support higher signal compression levels (*i.e.*, lower *CRs*) than the white noise case for the same level of accuracy on the obtained results.

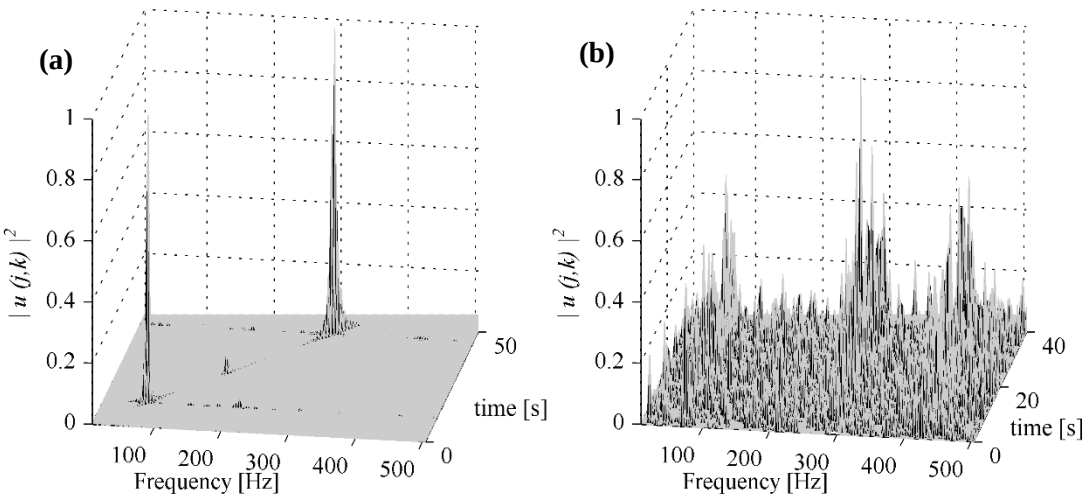

***Figure 3.23**: Normalised square magnitude of the reconstructed harmonic wavelet coefficients derived from the CR=30% compressed truss acceleration response (at node 4) for the (a) sine-sweep and (b) the white noise excitation.*

3.5.4. CS-based RWE for damage detection

Having obtained the CS-reconstructed harmonic wavelet coefficients at the three considered *CRs* (*i.e.*, 10%, 20%, 30%), the scale-dependent CS-based RWE(j) is then computed from (3.18)

and plotted in the three-dimensional bar charts of Figure 3.24(a)-Figure 3.29(a) for the two considered forcing cases. The CS-based RWE in (3.10) is further illustrated in Figure 3.24(b)-Figure 3.29(b), observing roughly equal RWE amplitudes along measurement points as in Figure 3.16 and Figure 3.20 for the conventional RWE approach in the sine-sweep and white noise excitation, respectively.

More importantly, it is easily noticed in Figure 3.24-Figure 3.26 that the generated CS-based RWE values are not significantly affected by the signal's compression level in the non-stationary sine-sweep excitation case, yielding almost identical RWE distribution in the space-frequency plane for all considered *CRs* (*i.e.*, 10%, 20%, 30%). These exceptional results in the sine-sweep case, can be attributed to the highly sparse structure of truss acceleration responses on the harmonic wavelet basis (see also Figure 3.21 (a)), enabling the accurate CS recovery of the wavelet coefficients even for the limiting case of *CR*=10% and the processing of 90% fewer measurements (Figure 3.26) compared to the full-length uniform-sampled signals (at Nyquist rate or above) used in the conventional RWE approach presented in §3.4. This is not confirmed, though, in Figure 3.27-Figure 3.29 for the white noise excitation case at the three adopted *CRs*, respectively. In fact, this case pertains to less-sparse acceleration datasets, exhibiting lower accuracy in the reconstruction of harmonic wavelet coefficient compared to the sine-sweep case, as confirmed in Figure 3.23. In this respect, the generated CS-based RWE values are more sensitive to signal compression at lower *CRs*. For example, in the limiting case of *CR*=10% illustrated in Figure 3.29, certain non-zero RWE values are contributing to frequencies that are not related to the resonances of the damaged truss which may hinder the interpretation of the obtained results. Nonetheless, this rather poor performance of the CS-based RWE approach is significantly improved at *CR*=20% (Figure 3.28).

Thus, it is confirmed that the CS-based RWE method can identify the location of structural damage equally well with the conventional RWE case, by acquiring and processing a significantly smaller number of structural data, reduced by 90% for the sine-sweep excitation and by 80% for the white noise case in the herein numerical study.

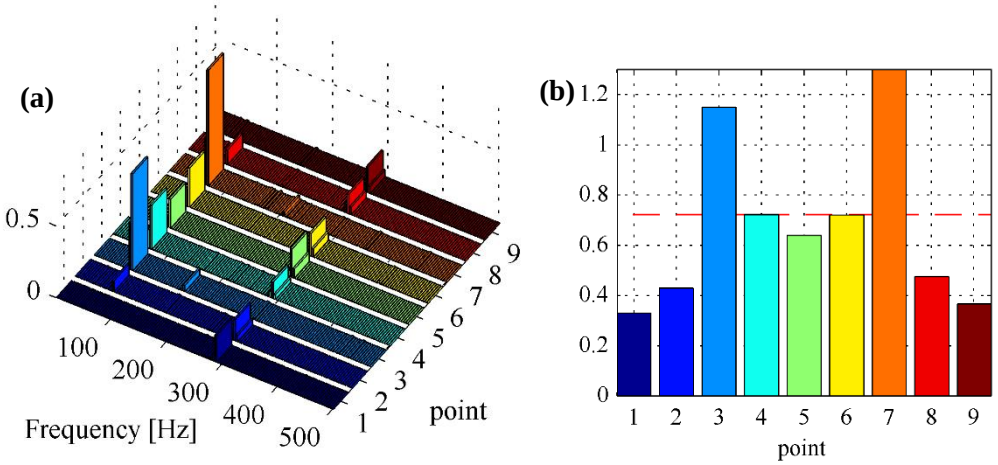

***Figure 3.24**: (a) Scale-dependent CS-based RWE(j) in eq. (3.18) and (b) CS-based RWE in eq. (3.10) using reconstructed harmonic wavelet coefficients at CR=30% for the space truss subject to the sine-sweep excitation*

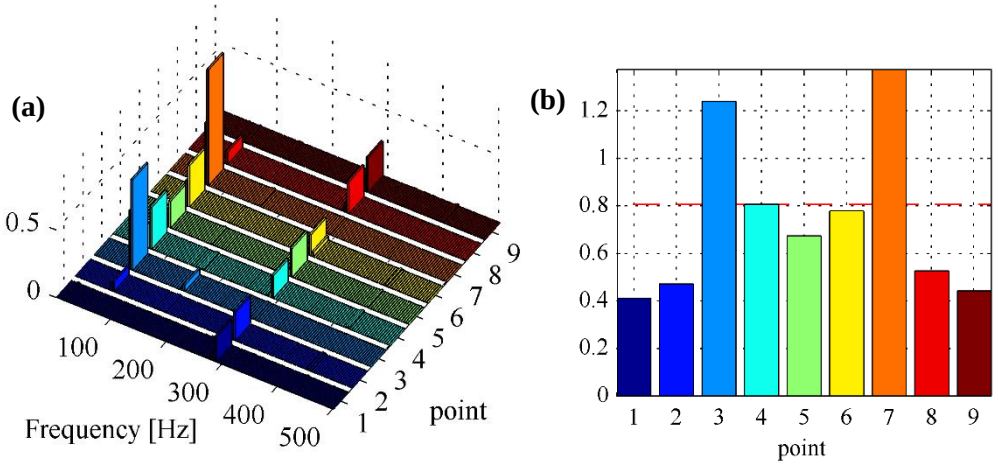

***Figure 3.25**: (a) Scale-dependent CS-based RWE(j) in eq. (3.18) and (b) CS-based RWE in eq. (3.10) using reconstructed harmonic wavelet coefficients at CR=20% for the space truss subject to the sine-sweep excitation*

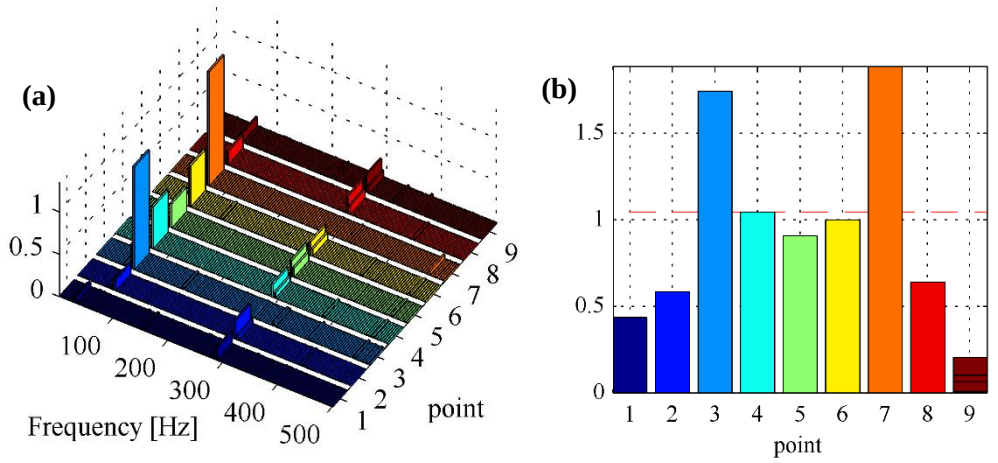

***Figure 3.26**: (a) Scale-dependent CS-based RWE(j) in eq. (3.18) and (b) CS-based RWE in eq. (3.10) using reconstructed harmonic wavelet coefficients at CR=10% for the space truss subject to the sine-sweep excitation*

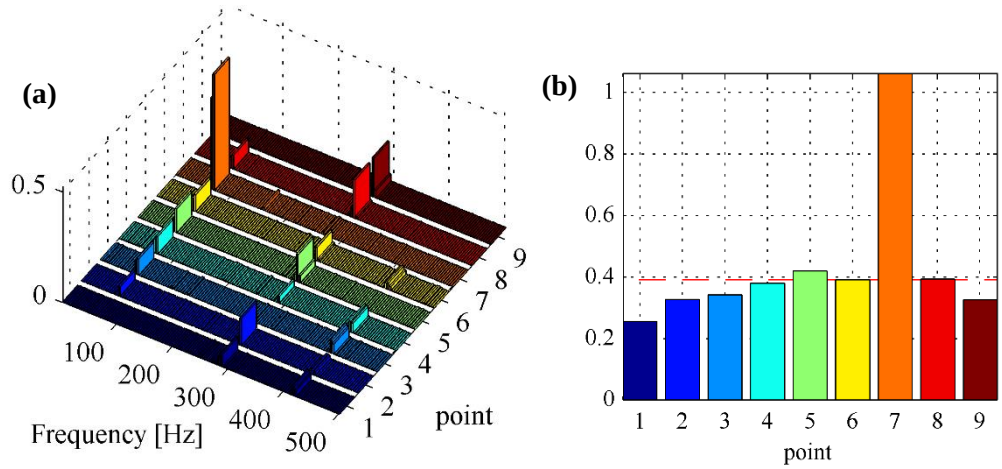

***Figure 3.27**: (a) Scale-dependent CS-based RWE(j) in eq. (3.18) and (b) CS-based RWE in eq. (3.10) using reconstructed harmonic wavelet coefficients at CR=30% for the space truss subject to the white noise excitation*

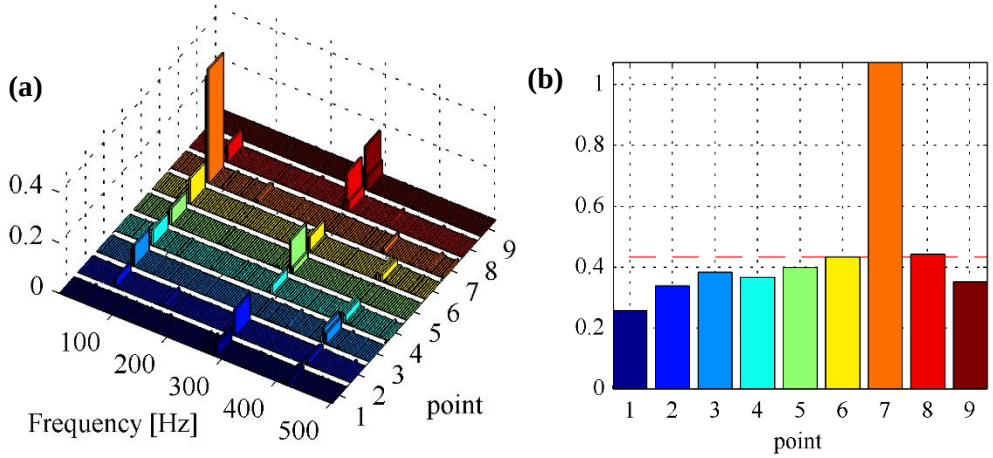

***Figure 3.28**: (a) Scale-dependent CS-based RWE(j) in eq. (3.18) and (b) CS-based RWE in eq. (3.10) using reconstructed harmonic wavelet coefficients at CR=20% for the space truss subject to the white noise excitation*

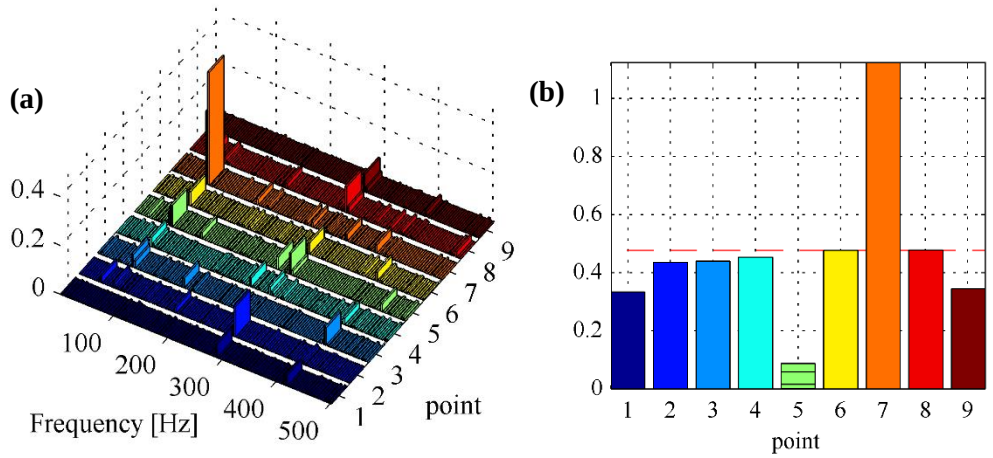

***Figure 3.29**: (a) Scale-dependent CS-based RWE(j) in eq. (3.18) and (b) CS-based RWE in eq. (3.10) using reconstructed harmonic wavelet coefficients at CR=10% for the space truss subject to the white noise excitation*

3.6. Concluding Remarks

A novel CS-based damage detection approach is developed herein for low-cost and energy efficient WSNs in VSHM applications. The proposed method originates from the theory of Compressive Sensing (in Chapter 2) fused with the relative wavelet entropy (RWE) index. The latter is a well-established in the literature damage-sensitive index derived by wavelet transforming linear response acceleration signals obtained from a healthy/reference and a damaged state of a given structure subject to broadband excitations. To this end, a comprehensive numerical study was first undertaken to define the "sparsest" representation of structural acceleration responses on various wavelet analysis filter banks by assessing the frequency domain attributes of the adopted wavelets – a key factor that was found to significantly affect the computation of the RWE.

For the numerical evaluation, two finite element (FE) models were developed, pertaining to a space truss benchmark structure in healthy and damage states, respectively. The adopted FE models were further excited by two different broadband forcing functions, *i.e.*, a non-stationary sine-sweep and a stationary finite duration sample of Gaussian white noise process. Linear response history analyses were conducted to obtain response acceleration signals at equidistant locations, which were treated as the reference/full-length datasets. Four energy-preserving wavelet analysis filter banks with different frequency domain attributes were employed to wavelet transform the response acceleration signals. These operations rely on algorithms that can efficiently run on wireless sensors used for decentralised vibration-based structural health monitoring.

Considering the conventional RWE approach using the full-length response acceleration datasets, RWE values were reported vis-à-vis for the four different wavelet filter banks. Focus was given on the scale-dependent contributors to the total RWE values to examine the ability of the different wavelet filter banks to resolve changes to the response signals' energy distribution on the frequency domain indicative of structural damage. The reported numerical data suggest that frequency selectivity and resolution across the scales of the wavelet analysis filter bank, which are strongly dependent on the frequency domain properties of the underlying wavelet basis, are the key for achieving enhanced RWE-based stationary damage detection/localisation drawing information about damage from multiple mode shapes. It was shown that the extensively used in the literature Haar wavelets (or non-smooth Daubechies wavelets) in conjunction with the standard dyadic *discrete wavelet transform* suffer from significant energy leakage across scales. Thus, these wavelets may not be able to detect damage based on information carried at relatively high frequencies (or higher modes of vibration). Wavelet filter banks with enhanced frequency selectivity among scales (*i.e.*, minimum overlapping of the frequency bands corresponding to adjacent scales), reduce spectral leakage of the signal energy, and facilitate the results

interpretation as the non-zero contributors to the RWE values can be clearly associated with different natural frequencies/ modes of vibration.

Hence, the compactly supported in the frequency domain harmonic wavelets that achieve non-constant Q analysis were found to be the most effective for RWE-based stationary damage detection as they are not limited by the dyadic *discrete wavelet transform* discretisation and can achieve any level of frequency resolution anywhere on the frequency domain, as deemed appropriate.

Thus, the harmonic wavelet basis was found the most suitable for the sparsest representation of stationary structural responses, and it was further employed in the numerical evaluation of the proposed CS-based RWE approach. To this end, simulated randomly-sampled compressed acceleration response datasets were generated at the three *CRs* ={10%, 20%, 30%}. The latter were treated by a standard CS-reconstruction algorithm along with a "partial" harmonic wavelet basis matrix to retrieve the underlying harmonic wavelet coefficients directly from the compressed measurements. It was shown and numerically verified that CS-based RWE can accurately detect structural damage equally well with the conventional RWE case, by acquiring and processing a significantly smaller number of structural data, reduced by 90% for the sine-sweep excitation and by 80% for the white noise case in the herein numerical study.

The above results suggest that the proposed CS-based RWE is a promising tool for low-cost and energy efficient structural damage detection. It is envisioned that this will become the preferred way in practice once wireless sensors supporting this technology will become commercially available.

As a final remark, it is emphasised that the herein considered harmonic wavelet basis is not necessarily a recommended and, by no means, an optimal approach for wavelet transforming response acceleration signals for RWE-based damage detection. *It has only been used in this study as an "extreme case" of a basis with good frequency domain attributes vis-à-vis the standard dyadic discrete wavelet transform filter banks considered in the literature*. Overall, the herein numerical examples suggest that the adopted harmonic wavelet basis with constant frequency resolution across scales may be used as a reasonable approach for RWE-based damage detection where the natural frequencies of the (damaged) structure are not *a priori* known. In this case, a harmonic wavelet transform with coarser resolution than what has been employed in this study (*i.e.*, a reduced number of scales or wider bandwidth/scale) should be considered to keep the computational cost low for practical implementation, especially in the case of decentralised VSHM using wireless sensors (Yun et al. 2011).

Chapter 4
Proposed Multi-Sensor Power Spectrum Blind Sampling Approach for OMA: Theory

4.1. Preliminary Remarks

This chapter presents the mathematical framework of an alternative compressive power spectrum estimation approach for low-power WSN in OMA applications, which builds upon the *Power Spectrum Blind Sampling* (PSBS) strategy.

The main contribution herein is the theoretical development of the PSBS technique to the multi-sensor case aiming to retrieve the unknown auto/cross power spectral density matrices of structural responses to ambient excitations (wide-sense stationary stochastic processes) within WSNs, without involving signal reconstruction operations in time-domain. This is achieved by considering a deterministic non-uniform-in-time sampling, known as *multi-coset sampling pattern*, operating on wide-sense stationary stochastic processes/ random signals (in alignment with the theory of OMA). The adopted sampling scheme can measure almost all lags in a given observation window, which enables to recover the second-order statistics of structural responses directly in the compressed domain. It will be shown that, in contrast to the CS-based approaches presented in Chapter 2 (§*2. Compressive Sensing: Basic Concepts & Applications in VSHM*), the considered sampling strategy is applied to non-sparse signals of any structure, without being limited by sparsity constraints, while the undertaken spectral recovery problem mathematically defines an overdetermined system of linear equations that can be easily solved. The proposed PSBS approach can be used together with standard OMA algorithms to perform structural identification and damage detection with reduced power requirements.

The motivation of the proposed method is presented in section 4.2 (§*4.2. Related Work and Motivation*), while section 4.3 (§*4.3. Multi-Coset Sampling Pattern*) introduces the deterministic multi-coset sampling scheme. The next two sections (§*4.4. Cross-Correlation of Sub-Nyquist Measurements*, §*4.5. Power Spectral Matrix Recovery*) cover the mathematical details of the proposed multi-sensor PSBS approach. Section 4.6 (§*4.6. Design of the Multi-coset Sampling Pattern and the Weighting Matrix W*) briefly reviews the mathematics governing the design of the adopted multi-coset sampling pattern (*e.g., Tausiesakul & Gonzalez-Prelcic* (2013)), which

relies on a weighted least square criterion, being optimal in the mean square sense. Section 4.7 (§*4.7. Frequency Domain Decomposition (FDD) for Modal Estimation*) presents briefly the basic concepts of the standard FDD algorithm, which has been adopted in Chapter 5 (§*5. Proposed Multi-Sensor Power Spectrum Blind Sampling Approach for OMA: Applications*) and Chapter 6 (§*6. Assessment of the Proposed PSBS Approach vis-à-vis CS-based Approach for OMA*) for the numerical evaluation of the developed multi-sensor PSBS approach in OMA applications. Finally, section 4.8 (§*4.8. Concluding Remarks*) recapitulates the key ideas and advantages of the proposed method.

The theoretical developments in sections §4.3 – §4.6 have appeared in the following published/submitted journal papers and conference proceedings listed in section 1.5 (§1.5. List of Referred Papers): a detailed description is provided in the journal paper [J3], while a brief review is given in [J2, C4 – C7]. This mathematical framework extends a previously developed PSBS case supporting single sensor deployments, which has been presented in the conference proceedings [C2 & C3].

4.2. Related Work and Motivation

The PSBS strategy was originally developed in cognitive radio applications (*e.g., Leus & Arianandа* (2011); *D D Arianandа & Leus* (2012); *Cohen & Eldar* (2014)) to recover the power spectrum of sub-Nyquist sampled telecommunication signals observed by a *single-sensor*. Its primary aim was to efficiently detect unoccupied bands in a wide spectral range, *i.e.*, recover the frequency support of the received signal (see also *Romero et al.* (2016), *Axell et al.* (2012) and the references therein). Arguably, telecommunication signals may not have a sparse structure due to the presence of high level noise (*e.g., Axell et al.* (2012)), while their wireless transmission is limited by bandwidth constraints, requiring a prohibitively high uniform sampling at Nyquist rate which, however, is beyond the state-of-the-art of current ADCs (*e.g., Romero et al.* (2016)).

To overcome this issue, the PSBS strategy relies on deterministic non-uniform-in-time sampling schemes, known as multi-coset sampling (*e.g., Venkataramani & Bresler* (2000); *Mishali & Eldar* (2009); *D D Arianandа & Leus* (2012); *Tausiesakul & Gonzalez-Prelcic* (2013)), operating on wide-sense stationary stochastic processes (*i.e.*, random signals). The considered sampling strategy is universal/signal-agnostic since it applies to non-sparse signals of any structure, without being limited by sparsity constraints. The acquired compressed measurements are then wirelessly transmitted to the server without any on-board signal processing operation, which directly translates in reduced computational, memory and storage requirements. However, the computational intensity is transferred from the sensor to the server, where the received compressed measurements are collectively processed to recover the second-order statistics of the unknown wide-sense stationary random signals (*i.e.*, covariance and power spectrum), by-passing

the computationally demanding signal reconstruction operation in time-domain[*]. Importantly, the recovery operations undertaken by the PSBS strategy mathematically define an overdetermined system of linear equations that can be easily solved, rendering this technique a computationally efficient method for WSNs operating at sub-Nyquist sampling rates.

The above single-sensor PSBS strategy was extended to a *co-operative multi-sensor compressive power spectral estimation method* (*e.g., Arianandа & Leus* (2012); *Arianandа et al.* (2014)) with the scope to achieve stronger signal compression (*i.e.*, lower *CR*) while enhancing the wireless transmission reliability. The above aims were accomplished by considering multiple versions of the same incoming signal, transmitted and received by a network of wireless sensors. Assuming clusters of sensors operating on different multi-coset sampling patterns (but a common sampling pattern is considered within each cluster), *Arianandа et al.* (2014) managed to retrieve the power spectrum of the unknown input wide-sense stationary random signal at lower *CR*s per sensor compared to the single-sensor case by *Arianandа & Leus* (2012). The derived mathematical framework by *Arianandа et al.* (2014) relies on the assumption that the received signals from all sensors observe approximately the same second-order statistics, although this may differ in practice due to errors and uncertainties related to wireless telecommunications (*e.g.*, *Akyildiz et al.* (2011)). To alleviate this problem, an alternative co-operative WSN was introduced by *Dyonisius Dony Arianandа & Leus* (2012) capable to recover the unknown power spectrum from cross-spectral estimations computed between the acquired compressed measurements from the sensors, assuming prior knowledge on the *channel state information*. The latter can be viewed as the channel's frequency response function (or the impulse response function, *i.e.*, the Fourier pair of the frequency response function) carrying the information of the signal's propagation in wireless transmit/receive mode, including scattering, fading, and power decay with distance (*e.g.*, *Bjornson & Ottersten* (2010), *Akyildiz et al.* (2011)).

Motivated by the above technological advances (which can be particularly useful in large-scale sensor networks) and aiming to reduce the power requirements in densely instrumented structures, this study exploits the single-sensor PSBS strategy developed by *Tausiesakul & Gonzalez-Prelcic* (2013) and tests its applicability in WSNs used for OMA purposes. Similar to cognitive radio applications, OMA relies on wide-sense stationary stochastic processes due to ambient excitations, although different challenges are met. In fact, a plethora of well-established OMA algorithms require the exact recovery of the power spectrum of the unknown structural responses in terms of both frequency support and shape/amplitude to retrieve the salient features of the monitored systems (*e.g.*, modal identification). Whether the above challenges can be efficiently met within the PSBS technique is among the major objectives of this study.

[*] *The time-domain signal reconstruction operation from fewer/compressed data defines an underdetermined problem that yields a unique solution under certain constraints, e.g., signal sparsity (see also chapter 2)*

More importantly, the prime contribution herein is the extension of the theoretical background by *Tausiesakul & Gonzalez-Prelcic* (2013) to the *multi-sensor PSBS strategy* to observe datasets of structural responses with *different second-order statistics* (*i.e.*, auto/cross correlations, and auto/cross power spectral densities), obtained from various recording locations on a monitored operational structure. Assuming a centralised WSN with sensors operating on the *same multi-coset sampling scheme* along their channels, compressed structural data are acquired at sub-Nyquist rates and collectively processed to recover the auto/cross response power spectrum matrix directly in the compressed domain, without reconstructing the time-domain responses. The above theoretical developments can be further fused with standard OMA algorithms to retrieve the inherent structural modal properties (*e.g.*, the standard frequency domain decomposition (FDD) algorithm, *e.g.*, *Brincker & Ventura* (2015)) with substantial savings in energy/power requirements.

The proposed *multi-sensor PSBS* approach is free from sparsity assumptions and significantly differs from the co-operative WSN by *Dyonisius Dony Arianandа & Leus* (2012) in both the nature of the problem and the assumptions invoked. Drawing an analogy between these two approaches, the co-operative framework of *Dyonisius Dony Arianandа & Leus* (2012) in OMA terms would be interpreted as the auto-power spectrum recovery of ambient excitation forces assuming prior knowledge on the frequency response function (FRF) of the monitored system; on the contrary, the OMA goal is to infer the system's FRF assuming white-noise excitation of a sufficiently flat power spectrum that is not measured.

4.3. Multi-Coset Sampling Pattern

Let $x(t)$ be a continuous in time t real-valued wide-sense-stationary random signal (or stochastic process) characterised in the frequency domain by a power spectrum band-limited by $2\pi/T_s$. According to the multi-coset sampling strategy (*e.g.*, *Feng & Bresler* (1996); *Venkataramani & Bresler* (2000), (2001); *D D Arianandа & Leus* (2012)), an N-length Nyquist-sampled discrete-time signal $x(n\,T_s)$ is divided into K blocks of $\bar{N}$ consecutive samples (*i.e.*, $K = N / \bar{N}$) and from each block only $\bar{M} (< \bar{N})$ samples are selected. The latter is achieved by considering $\bar{M}$ different "cosets"; at the *i-th* (i= 0, 1, …, $\bar{M}-1$) coset, the discrete-time signal $x[n]= x(nT_s)$ is first shifted by s_i samples and then uniformly sampled at $1/(\bar{N}T_s)$. In this respect, an average sampling rate of $\bar{M} / (\bar{N}T_s)$ is defined, which is associated with the compression ratio (CR) given in $\bar{M} / \bar{N}$, with $0\% \leq CR \leq 100\%$, pertaining to smaller values at higher signal compression. Notably, the limiting case of CR=100% (*i.e.*, $\bar{M} = \bar{N}$) corresponds to conventional sampling at the uniform Nyquist rate. The location of the $\bar{M}$ samples within each $\bar{N}$ -length block is defined by the sampling pattern sequence

$$\mathbf{s} = [s_0, \quad s_1, \quad \cdots, \quad s_{\bar{M}-1}]^{\mathrm{T}}, \tag{4.1}$$

that applies to all K blocks, while the superscript "T" denotes matrix transposition. In the above sequence, the elements s_i, s_j are placed in ascending order and do not repeat (*i.e.*, $s_i \neq s_j \ \forall \ i \neq j$). Eq. (4.1) further defines the difference set

$$\Omega = \left\{ \left| s_i - s_j \right|, s_i, s_j \in \mathbf{s} \right\}. \tag{4.2}$$

that arises naturally in the computation of the correlation sequences of the discrete-time signals.

The above sampling strategy can be implemented by utilising $\bar{M}$ interleaved channels of ADC units, operating at a sampling rate $1/(\bar{N}T_s)$, (*i.e.*, $\bar{N}$ times slower than the Nyquist rate $1/T_s$). A discrete-time model of an ideal multi-coset sampler proposed by *Arianandа & Leus* (2012) is illustrated in Figure 4.1.

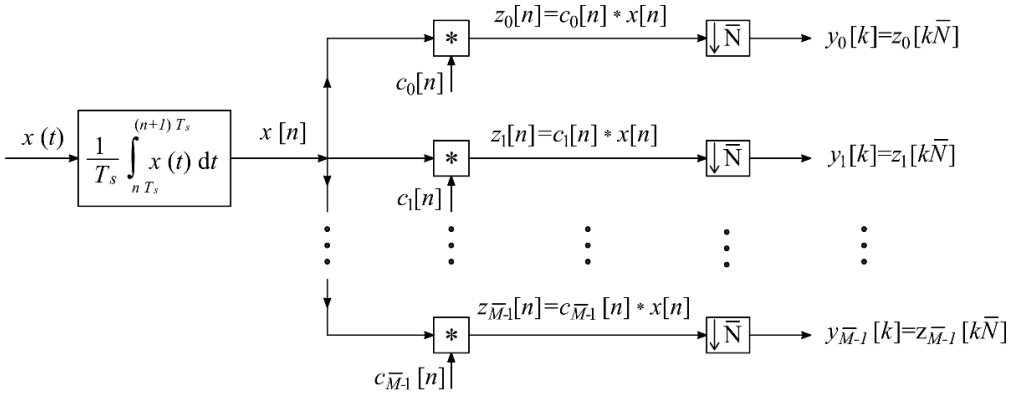

***Figure 4.1**: Discrete-time model of the considered multi-coset sampling device proposed by Arianandа & Leus* (2012)

Figure 4.1 shows that the input analog signal $x(t)$ is first discretised with an integrate-and-dump device with period T_s. Next, the generated discete-time signal $x[n]$ enters $\bar{M}$ channels and then convolved with the $\bar{N}$ -length sequence $c_i[n]$

$$c_i[n] = \begin{cases} 1, & n = s_i, \\ 0, & n \neq s_i, \end{cases}. \tag{4.3}$$

where i={0, 1, …, $\bar{M}$ -1}, and n={1- $\bar{N}$, 2- $\bar{N}$, …, 0} being in descending order. The above is expressed as

$$z_i[n] = c_i[n] * x[n] = \sum_{p=1-\bar{N}}^{0} c_i[p] \ x[n-p], \tag{4.4}$$

in which the convolution operation is denoted by *. The obtained sequence is further down-sampled by $\bar{N}$ to generate the output/ compressed measurements

$$y_i[k] = z_i[k\bar{N}], \quad k = \{0,1,\ldots,K-1\}, \tag{4.5}$$

with K being the number of compressed measurements per channel (*i.e.*, coinciding with the number of blocks). For illustration, Figure 4.2(a) depicts the multi-coset sampling strategy applied on a discrete-time sequence $x[n]$ of N=32 samples, which is divided in K=4 blocks of length $\bar{N}$ =8. The adopted sampling pattern is given in the sequence $\mathbf{s} = [0,\ 2,\ 5]^{\mathrm{T}}$, consisting of the $\bar{M}$ =3 shifting values, s_i, i={0,1,2}, shown with the circular marks in Figure 4.2(a). The considered sampling strategy can be implemented by utilising the 3-channel multi-coset sampler depicted in Figure 4.2(b). At the i-th channel, each k block of the discrete-time signal $x[n]$ (*i.e.*, $x[k\bar{N}+n]$ for $\bar{N}$ =8, k={0,1,2,3}, n={0,1,…,7}) is convolved with the filter coefficients $c_0 = [0,0,0,0,0,0,0,1]$, $c_1 = [0,0,0,0,0,1,0,0]$, and $c_2 = [0,0,1,0,0,0,0,0]$ along the three channels respectively, and down-sampled by $\bar{N}$ =8 to generate the output/ compressed measurements $y_i[k]$.

In this respect, only 12 samples are acquired from the 32-length signal $x[n]$, pertaining to a *CR* at approximately 37.5% (see also Figure 4.2). The above example confirms that the adopted multi-coset sampling is periodic with period $\bar{N}$; *non-uniform* since any subset of $\bar{M}$ samples may be selected from a total of $\bar{N}$ Nyquist-rate samples within each block; and *deterministic* since the position of the $\bar{M}$ samples on the Nyquist grid is defined *a priori* and applies to all considered blocks.

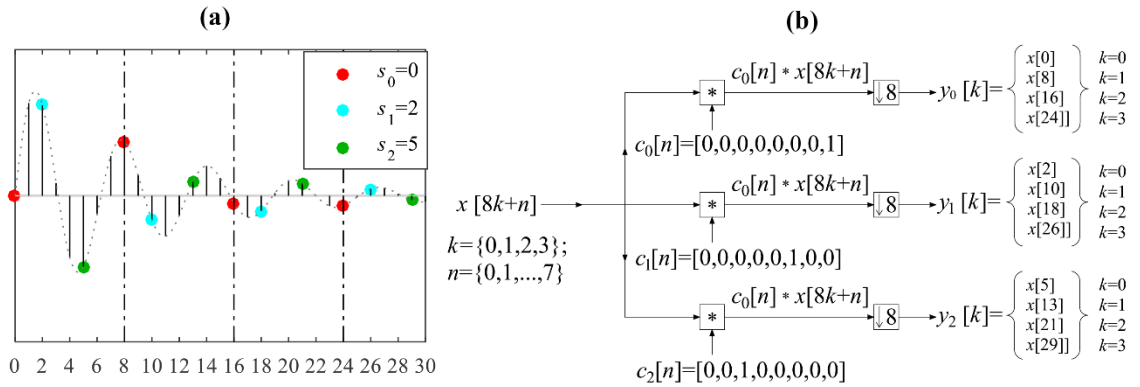

Figure 4.2: *Multi-coset sampling pattern with $\bar{M}$=3, $\bar{N}$=8, K=4, and sampling sequence $\mathbf{s}$=[0, 2, 5]^T applied on a signal of 32 samples*

Recent developments in hardware architecture has paved the way for the design of sensor prototypes that support multi-coset sampling via the use of a bank of time-interleaved ADC units (channels) (see also *Black & Hodges* (1980)). Based on the *Modulated Wideband Converter*

developed by *Mishali et al.* (*e.g.*, *Mishali et al.* (2009); *Mishali & Eldar* (2010)), a discrete-time version of a multi-coset sampler was proposed by *Arianandа & Leus* (2012) to acquire compressed measurements from a wideband non-sparse signal. A dual-rate hardware architecture was designed by *Moon et al.* (2015), comprising a pair of time-interleaved under-sampling ADCs that accommodate two different sampling patterns with a small frequency offset to iteratively acquire delayed versions of the same input signal at sub-Nyquist sampling rates. More recently, *Jingchao et al.* (2015) designed a prototype multi-coset sampler that can support up to 10 interleaved sub-Nyquist ADC sampling channels, being also capable to rectify any potential error due to channel diversity gain and/or time synchronisation among the various ADC channels. Despite the above developments, such multi-coset samplers are not commercially available yet.

4.4. Cross-Correlation of Sub-Nyquist Measurements

Consider next a network of D identical multi-coset samplers of $\bar{M}$ channels, operating on the same sampling pattern across their channels. The considered wireless sensor network is assumed to be placed along a structure, measuring D acceleration responses under ambient vibrations. Let $x^a[n]$, $x^b[n]$ ($a,b=\{1,2\ldots,D\}$) be the unknown discrete-time sequences sampled at Nyquist rate from the band-limited continuous-time acceleration response random signals (*i.e.*, stochastic processes) $x^a(t)$ and $x^b(t)$ respectively. The ultimate goal of the multi-sensor PSBS approach is the recovery of the input cross-correlations

$$r_{x^a x^b}[p] = \mathrm{E}_x\left\{x^a[n]\, x^b[n-p]\right\}, \tag{4.6}$$

computed among all input signals $x^a[n]$, $x^b[n]$ to the $a,b=\{1,2,\ldots,D\}$ devices, with $\mathrm{E}_a\{\cdot\}$ denoting the mathematical expectation operator with respect to a.

As illustrated in Figure 4.3, the above goal can be achieved through the acquisition of $\bar{M} \times D$ output/compressed sequences $y_i^a[k]$, $y_j^b[k]$ from all $i, j \in \left\{0,1,\ldots,\bar{M}-1\right\}$ channels of the $a,b=\{1,2,\ldots,D\}$ devices, using the multi-coset sampling strategy detailed in the previous sub-section.

By collectively processing the acquired compressed measurements, the output cross-correlations

$$r_{y_i^a, y_j^b}[\ell] = \mathrm{E}_y\left\{y_i^a[k]\, y_j^b[k-\ell]\right\}. \tag{4.7}$$

can be computed, which are collected further in the output cross-correlation matrix $\mathbf{r}_{y^a y^b} \in \mathbb{R}^{\bar{M}^2 \times D}$ given in

$$\mathbf{r}_{y^a y^b}[\ell] = \left[r_{y_0^a, y_0^b}[\ell] \cdots r_{y_0^a, y_{(\bar{M}-1)}^b}[\ell] \quad r_{y_1^a, y_0^b}[\ell] \cdots r_{y_{(\bar{M}-1)}^a, y_{(\bar{M}-1)}^b}[\ell] \right]^{\mathrm{T}}. \tag{4.8}$$

The following expression is then employed

$$\mathbf{r}_{y^a y^b}[\ell] = \sum_{p=0}^{1} \mathbf{R}_c[p] \; \mathbf{r}_{x^a x^b}[\ell - p], \tag{4.9}$$

which allows to relate the output cross-correlation matrix $\mathbf{r}_{y^a y^b} \in \mathbb{R}^{\bar{M}^2 \times D}$ in (4.8) with the unknown input cross-correlation matrix $\mathbf{r}_{x^a x^b} \in \mathbb{R}^{\bar{N} \times D}$ in

$$\mathbf{r}_{x^a x^b}[\ell] = \left[r_{x^a x^b}[\ell \bar{N}] \quad r_{x^a x^b}[\ell \bar{N} + 1] \cdots r_{x^a x^b}[(\ell + 1)\bar{N} - 1] \right]^{\mathrm{T}}, \tag{4.10}$$

using the pattern cross correlation matrix $\mathbf{R}_c \in \mathbb{R}^{\bar{M}^2 \times \bar{N}}$

$$\mathbf{R}_c[\ell] = \left[\mathbf{r}_{c_0, c_0}[\ell] \cdots \mathbf{r}_{c_0, c_{\bar{M}-1}}[\ell] \quad \mathbf{r}_{c_1, c_0}[\ell] \cdots \mathbf{r}_{c_{\bar{M}-1}, c_{\bar{M}-1}}[\ell] \right]^{\mathrm{T}}. \tag{4.11}$$

The latter is populated with the pattern cross-correlation functions between the sequences $c_i[n]$, $c_j[n]$ in eq. (4.3), expressed in

$$r_{c_i, c_j}[p] = \sum_{n=1-\bar{N}}^{0} c_i[n] \; c_j[n - p] = \delta[p - (s_i - s_j)]. \tag{4.12}$$

The above expression depends only on the difference set Ω given in eq. (4.2), with $\delta[\cdot]$ being the Dirac delta function (*i.e.*, $\delta[p]$=1 for p=0, and $\delta[p]$=0 for $p \neq 0$).

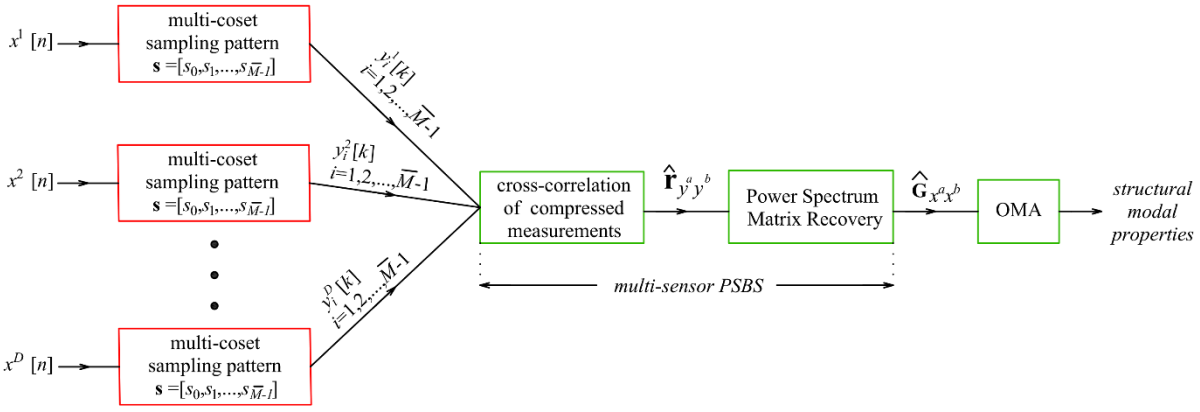

***Figure 4.3**: Workflow of the multi-sensor PSBS approach for OMA*

It is assumed further that the input cross-correlation sequences $r_{x^a x^b}[\ell \bar{N}]$ in eq. (4.10) take on negligible values outside the range $[-L\bar{N}, L\bar{N}]$ (for $\ell \in [-L, L]$), which will hold true for some L

depending on the level of damping of the monitored structural system. In this respect, the input/output relationship in eq. (4.9) can be cast in matrix form

$$\mathbf{r}_{y^a y^b} = \mathbf{R}_c \mathbf{r}_{x^a x^b}\,, \tag{4.13}$$

where the output matrix $\mathbf{r}_{y^a y^b} \in \mathbb{R}^{\bar{M}^2(2L+1)\times D}$ is defined as

$$\mathbf{r}_{y^a y^b} = \left[\mathbf{r}^{\mathrm{T}}_{y^a y^b}[0] \cdots \mathbf{r}^{\mathrm{T}}_{y^a y^b}[L] \quad \mathbf{r}^{\mathrm{T}}_{y^a y^b}[-L] \cdots \mathbf{r}^{\mathrm{T}}_{y^a y^b}[-1]\right]^{\mathrm{T}}, \tag{4.14}$$

and the input matrix $\mathbf{r}_{x^a x^b} \in \mathbb{R}^{\bar{N}(2L+1)\times D}$ is given in a similar way as above, *i.e.*,

$$\mathbf{r}_{x^a x^b} = \left[\mathbf{r}^{\mathrm{T}}_{x^a x^b}[0] \cdots \mathbf{r}^{\mathrm{T}}_{x^a x^b}[L] \quad \mathbf{r}^{\mathrm{T}}_{x^a x^b}[-L] \cdots \mathbf{r}^{\mathrm{T}}_{x^a x^b}[-1]\right]^{\mathrm{T}}. \tag{4.15}$$

Further, the pattern matrix $\mathbf{R}_c \in \mathbb{R}^{\bar{M}^2(2L+1)\times \bar{N}(2L+1)}$ supports a sparse structure as in

$$\mathbf{R}_c = \begin{bmatrix} \mathbf{R}_c[0] & \mathbf{O} & \cdots & \mathbf{O} & \mathbf{R}_c[1] \\ \mathbf{R}_c[1] & \mathbf{R}_c[0] & \mathbf{O} & \ddots & \mathbf{O} \\ \mathbf{O} & \mathbf{R}_c[1] & \mathbf{R}_c[0] & \ddots & \vdots \\ \vdots & \ddots & \ddots & \ddots & \mathbf{O} \\ \mathbf{O} & \cdots & \mathbf{O} & \mathbf{R}_c[1] & \mathbf{R}_c[0] \end{bmatrix}, \tag{4.16}$$

with $\mathbf{O}$ being the zero matrix. Notably, the assumption on the unique sampling pattern for all multi-coset samplers enables to define eq. (4.11) regardless of the sensor indices *a*, *b*, which further allows to derive the input/output cross-correlation function in eq. (4.9) as an extension of the single-sensor case (*e.g.*, *D D Ariananda & Leus* (2012); *TauSiesakul et al.* (2015)). Further, eq. (4.13) defines an overdetermined system of linear equations which can be solved for $\mathbf{r}_{y^a y^b}$ without any sparsity constraint provided that $\mathbf{R}_c$ is full column rank (*i.e.*, having at least one entry in every column). The latter condition is satisfied for $\bar{M}^2 \geq \bar{N}$.

4.5. Power Spectral Matrix Recovery

Let $G_{x^a x^b}(\omega)$ be the cross-power spectrum of $x^a[n]$, $x^b[n]$ given in

$$G_{x^a x^b}(\omega) = \sum_{p=-\infty}^{\infty} r_{x^a x^b}[p]\, \mathrm{e}^{-\mathrm{i}p\omega}, \quad 0 \leq \omega \leq 2\pi \tag{4.17}$$

Where $i = \sqrt{-1}$. The latter expression is further discretised in the frequency domain and cast in matrix form

$$\mathbf{G}_{x^a x^b} = \mathbf{F}_{(2L+1)\bar{N}} \mathbf{r}_{x^a x^b} \,. \tag{4.18}$$

where $\mathbf{F}_{(2L+1)\bar{N}} \in \mathbb{C}^{\bar{N}(2L+1)\times\bar{N}(2L+1)}$ is the standard discrete Fourier transform (DFT) matrix with properties

$$\mathbf{F}^{\mathrm{T}}_{(2L+1)\bar{N}} = \mathbf{F}_{(2L+1)\bar{N}} \tag{4.19}$$

$$\mathbf{F}^{-1}_{(2L+1)\bar{N}} = \frac{1}{2L+1}\bar{\mathbf{F}}_{(2L+1)\bar{N}}, \tag{4.20}$$

and $\mathbf{G}_{x^a x^b} \in \mathbb{C}^{\bar{N}(2L+1)\times D}$ (in eq. (4.18)) is the input power spectrum matrix computed at the discrete frequencies $\omega = \left[0,\ 2\pi/\left((2L+1)\bar{N}\right),\ \ldots,\ \left(2\pi(2L+1)\bar{N}-1\right)/\left((2L+1)\bar{N}\right)\right]$, with a frequency resolution at

$$\Delta\omega = \frac{2\pi}{(2L+1)\bar{N}} \,. \tag{4.21}$$

Given a signal compression level and the associated pair of values $(\bar{M}, \bar{N})$, it is readily observed in eq. (4.21) that the frequency resolution, $\Delta\omega$, is determined by the parameter *L*. The latter is associated with the support of the auto/cross correlation sequences in eq. (4.10), and it can be freely selected depending on the application and the damping of the monitored system (see also *D D Arianandа & Leus* (2012)). For example, consider a lightly-damped vibrating structure, pertaining to discrete-time acceleration responses whose auto/cross correlation sequences decay slowly within the range $[-L\bar{N}, L\bar{N}]$. The pertinent power spectral density estimates yield relatively sharp peaks in the frequency domain, being efficiently captured through the consideration of a relatively small $\Delta\omega$ in eq. (4.21), requiring the selection a sufficiently large *L* value.

Consider next the unbiased estimator of the output cross-correlation function $r_{y_i^a, y_j^b}[\ell]$ in eq. (4.7) given in

$$\hat{r}_{y_i^a, y_j^b}[\ell] = \frac{1}{K-|\ell|} \sum_{k=\max\{0,\ell\}}^{K-1+\min\{0,\ell\}} y_i^a[k]\, y_j^b[k-\ell], \quad -L \le \ell \le L \,. \tag{4.22}$$

The weighted least square criterion is then adopted, *i.e.*,

$$\begin{aligned}\hat{\mathbf{r}}_{x^a x^b} &= \arg\min_{\mathbf{r}_{x^a x^b}} \left\| \hat{\mathbf{r}}_{y^a y^b} - \mathbf{r}_{y^a y^b} \right\|_{\mathbf{W}}^2 \\ &= \arg\min_{\mathbf{r}_{x^a x^b}} \left\| \hat{\mathbf{r}}_{y^a y^b} - \mathbf{R}_{\mathrm{c}} \mathbf{r}_{x^a x^b} \right\|_{\mathbf{W}}^2 \\ &= \arg\min_{\mathbf{r}_{x^a x^b}} \left(\hat{\mathbf{r}}_{y^a y^b} - \mathbf{R}_{\mathrm{c}} \mathbf{r}_{x^a x^b} \right)^{\mathrm{T}} \mathbf{W} \left(\hat{\mathbf{r}}_{y^a y^b} - \mathbf{R}_{\mathrm{c}} \mathbf{r}_{x^a x^b} \right)\end{aligned}, \tag{4.23}$$

where $\|\mathbf{a}\|_{\mathbf{W}}^2 = \mathbf{a}^{\mathrm{T}}\mathbf{W}\mathbf{a}$ is the weighted version of the Euclidean norm. Note that $\mathbf{W} \in \mathbb{C}^{\bar{M}^2(2L+1)\times\bar{M}^2(2L+1)}$ is a positive-definite weighting matrix that does not depend on $\mathbf{r}_{x^a x^b}$ as detailed in §4.6. The cost function of $\mathbf{r}_{x^a x^b}$ is given in

$$f_{\mathrm{WLS}}(\mathbf{r}_{x^a x^b}) = \left(\hat{\mathbf{r}}_{y^a y^b} - \mathbf{R}_{\mathrm{c}} \mathbf{r}_{x^a x^b} \right)^{\mathrm{T}} \mathbf{W} \left(\hat{\mathbf{r}}_{y^a y^b} - \mathbf{R}_{\mathrm{c}} \mathbf{r}_{x^a x^b} \right) \tag{4.24}$$

Which represents a convex function whose critical point $\dfrac{\partial f_{\mathrm{WLS}}(\mathbf{r}_{x^a x^b})}{\partial \mathbf{r}_{x^a x^b}^*} = \mathbf{0}$ yields a minimum value when

$$\hat{\mathbf{r}}_{x^a x^b} = \left(\mathbf{R}_c^{\mathrm{T}} \mathbf{W} \mathbf{R}_c \right)^{-1} \mathbf{R}_c^{\mathrm{T}} \mathbf{W} \hat{\mathbf{r}}_{y^a y^b}, \tag{4.25}$$

Or equivalently,

$$\begin{aligned}\hat{\mathbf{G}}_{x^a x^b} &= \mathbf{F}_{(2L+1)\bar{N}} \mathbf{r}_{x^a x^b} \\ &= \mathbf{F}_{(2L+1)\bar{N}} \left(\mathbf{R}_c^{\mathrm{T}} \mathbf{W} \mathbf{R}_c \right)^{-1} \mathbf{R}_c^{\mathrm{T}} \mathbf{W} \hat{\mathbf{r}}_{y^a y^b}\end{aligned}, \tag{4.26}$$

Where the superscript "−1" denotes matrix inversion. Eq. (4.26) gives an estimate of the cross-spectrum matrix $\mathbf{G}_{x^a x^b}$ that can be efficiently computed directly from the cross-correlation estimator $\hat{\mathbf{r}}_{y^a y^b}$ of the compressed acceleration measurements from the array of *D* multi-coset samplers, by exploiting the sparse structure of $\mathbf{R}_{\mathrm{c}} \in \mathbb{R}^{\bar{M}^2(2L+1)\times\bar{N}(2L+1)}$ shown in eq. (4.16). The latter reduces the algorithmic complexity, enabling further the efficient computation of the pseudo-inverse matrix in eq. (4.26). Finally, it is noted that the above mathematical framework can be easily reduced to the single-sensor PSBS case using the convention of *a*=*b*=1 in eqs. (4.6) – (4.26).

4.6. Design of the Multi-Coset Sampling Pattern and the Weighting Matrix

This study employs the multi-coset sampling pattern derived by *Tausiesakul & Gonzalez-Prelcic* (2013) which is optimal in the mean square error sense. It is assumed that the input signal $x[n]$ is circular-symmetric complex-valued zero-mean Gaussian with second-order statistics

$$\mathrm{E}_x\left\{x[n]\,\overline{x}[m]\right\} = \sigma_x^2\ \delta_{n,m} \quad \forall n,m, \tag{4.27}$$

$$\mathrm{E}_x\left\{x[n]\,x[m]\right\} = 0 \qquad \forall n,m, \tag{4.28}$$

where, σ_{x}^2 is the variance of the input signal $x[n]$ and $\delta_{n,m}$ the Dirac delta function. A multi-coset sampling pattern sequence is designed such that the Weighted Mean Square Error (WMSE) of the power spectrum estimate of the input signal, $\hat{\mathbf{G}}_x$ (*i.e.*, for $a=b$ in (4.26)), is minimised. Note that the design of the sampling pattern is not restrictive to the temporally-white assumption for $x[n]$ (which is a limiting case pertaining to input signals with extremely low signal-to-noise ratio), and any signal waveform can be used instead.

Let $f_{\mathrm{WMSE}}(\mathbf{s})$ be the cost-function of the above WMSE criterion given by *Tausiesakul & Gonzalez-Prelcic* (2013) in

$$f_{\mathrm{WMSE}}(\mathbf{s}) = \frac{1}{\sigma_{\mathrm{x}}^4(2L+1)\bar{N}}\left(K(2L+1)-L(L+1)\right)\mathrm{E}_{\mathrm{x}}\left\{\left\|\hat{\mathbf{G}}_{\mathrm{x}}-\mathbf{G}_{\mathrm{x}}\right\|_{\mathrm{E}}^2\right\} = \sum_{n=1}^{\bar{N}}\frac{1}{\alpha_n(\mathbf{s})}, \tag{4.29}$$

where, $\alpha_n(\mathbf{s}) \in \mathbb{Z}^{1\times 1}$ is a scalar value computed for every $n=\left\{1,2,\ldots,\bar{N}\right\}$ from the expression

$$\alpha_n(\mathbf{s}) = \sum_{i=0}^{\bar{M}-1}\sum_{j=0}^{\bar{M}-1}\delta\left[-n+1-(s_i-s_j)\right]+\delta\left[\bar{N}-n+1-(s_i-s_j)\right], \tag{4.30}$$

with $\mathbf{s}$ being the sequence of $\bar{M}$ positive integers given in eq. (4.1).

Eqs. (4.29) and (4.30) suggest that the optimum design of the multi-coset sampling pattern is determined by solving the optimisation problem derived by *Tausiesakul & Gonzalez-Prelcic* (2013), *i.e.*,

$$\hat{\mathbf{s}}_{\mathrm{WMSE}} = \arg\min_{\mathbf{s}}\sum_{n=1}^{\bar{N}}\frac{1}{\alpha_n(\mathbf{s})}, \tag{4.31}$$

subject to the following constraints:

$$\begin{aligned}
&\alpha_n(\mathbf{s}) \geq 1, \quad \forall n \in \left\{2,3,\ldots,\left\lfloor \frac{1}{2}\bar{N} \right\rfloor + 1\right\},\\
&s_0 = 0,\\
&s_{\bar{M}-1} = \left\lfloor \frac{1}{2}\bar{N} \right\rfloor,\\
&s_i \in \left\{s_{i-1}+1,\ldots,\left\lfloor \frac{1}{2}\bar{N} \right\rfloor - \bar{M} + i + 1\right\}, \quad \forall i \in \{1,2,\ldots,\bar{M}-2\},
\end{aligned} \tag{4.32}$$

where $\lfloor \cdot \rfloor$ is the mathematical floor operator. This optimisation problem involves nonlinear integer programming, while the optimal sampling pattern sequence in eq. (4.1) can be obtained via exhaustive search. The weighting matrix $\mathbf{W}$ is further derived from the minimisation of mean square error (MSE) of the power spectrum estimate $\hat{\mathbf{G}}_x$, *i.e.*,

$$\hat{\mathbf{W}}_{\text{MMSE}} = \arg\min_{\mathbf{W}} \mathrm{E}_{\mathrm{x}} \left\{ \left\| \hat{\mathbf{G}}_{\mathrm{x}} - \mathrm{E}_{\mathrm{x}}\{\hat{\mathbf{G}}_{\mathrm{x}}\} \right\|_{\mathrm{E}}^2 \right\}, \tag{4.33}$$

which represents a convex function whose critical point $\frac{\partial}{\partial \mathbf{W}^*} \mathrm{E}_{\mathrm{x}} \left\{ \left\| \hat{\mathbf{G}}_{\mathrm{x}} - \mathrm{E}_{\mathrm{x}}\{\hat{\mathbf{G}}_{\mathrm{x}}\} \right\|_{\mathrm{E}}^2 \right\} = \mathbf{0}$ yields a minimum value when

$$\hat{\mathbf{W}}_{\text{MMSE}} = \mathbf{C}_{\hat{\mathbf{r}}_y}^{-1}. \tag{4.34}$$

In the above expression, $\mathbf{C}_{\hat{\mathbf{r}}_y}$ is the output covariance matrix estimator given in $\mathbf{C}_{\hat{\mathbf{r}}_y} = \mathrm{E}_x \left\{ (\hat{\mathbf{r}}_y - \mathrm{E}_x\{\hat{\mathbf{r}}_y\})(\hat{\mathbf{r}}_y - \mathrm{E}_x\{\hat{\mathbf{r}}_y\})^{\mathrm{T}} \right\}$. Under the signal assumption in eqs. (4.27) and (4.28), *Tausiesakul & Gonzalez-Prelcic* (2013) proved that eq. (4.34) can be cast in the form

$$\hat{\mathbf{W}}_{\text{MMSE}} = \frac{1}{\sigma_x^4} \left(\boldsymbol{\Lambda}^{-1}(\boldsymbol{\beta}) \otimes \boldsymbol{I}_{\bar{M}^2} \right), \tag{4.35}$$

Where $\otimes$ is the Kronecker product, and the superscript -1 denotes matrix inversion. Further, the identify matrix of size $\bar{M}^2 \times \bar{M}^2$ is denoted by $\boldsymbol{I}_{\bar{M}^2}$, and $\boldsymbol{\Lambda}(\boldsymbol{\beta})$ is a diagonal matrix of size $(2L+1)\times(2L+1)$, with the main diagonal taking the entries

$$\boldsymbol{\beta} = \left[\frac{1}{K} \quad \frac{1}{K-1} \quad \cdots \quad \frac{1}{K-L} \quad \frac{1}{K-L} \quad \cdots \quad \frac{1}{K-1} \right], \qquad \boldsymbol{\beta} \in \mathbb{R}^{(2L+1)\times 1}. \tag{4.36}$$

For the special case of $\mathbf{W} = \mathbf{I}$ (*i.e.*, the weighting matrix **W** is the identity matrix **I**), the following expression holds (see also *Tausiesakul & Gonzalez-Prelcic* (2013))

$$(\mathbf{R}_c^{\mathrm{T}}\mathbf{R}_c)^{-1}\mathbf{R}_c^{\mathrm{T}} = \begin{bmatrix} \boldsymbol{\Lambda}^{-1}(\boldsymbol{\alpha})\mathbf{R}_c^{\mathrm{T}}[0] & \boldsymbol{\Lambda}^{-1}(\boldsymbol{\alpha})\mathbf{R}_c^{\mathrm{T}}[1] & \mathbf{O} & \mathbf{O} \\ \mathbf{O} & \boldsymbol{\Lambda}^{-1}(\boldsymbol{\alpha})\mathbf{R}_c^{\mathrm{T}}[0] & \ddots & \mathbf{O} \\ \mathbf{O} & \mathbf{O} & \ddots & \vdots \\ \vdots & \ddots & \ddots & \boldsymbol{\Lambda}^{-1}(\boldsymbol{\alpha})\mathbf{R}_c^{\mathrm{T}}[1] \\ \boldsymbol{\Lambda}^{-1}(\boldsymbol{\alpha})\mathbf{R}_c^{\mathrm{T}}[1] & \cdots & \mathbf{O} & \boldsymbol{\Lambda}^{-1}(\boldsymbol{\alpha})\mathbf{R}_c^{\mathrm{T}}[0] \end{bmatrix}, \tag{4.37}$$

where, $\boldsymbol{\Lambda}(\boldsymbol{\alpha}) \in \mathbb{Z}^{\bar{N}\times\bar{N}}$ is a diagonal matrix with the diagonal $\boldsymbol{\alpha} \in \mathbb{Z}^{\bar{N}\times 1}$ given in

$$\boldsymbol{\alpha} = \begin{bmatrix} \alpha_1(\mathbf{s}) & \alpha_2(\mathbf{s}) & \cdots & \alpha_{\bar{N}}(\mathbf{s}) \end{bmatrix}^{\mathrm{T}}, \tag{4.38}$$

while the terms $\alpha_n(\mathbf{s}) \in \mathbb{Z}^{1\times 1}$ are obtained from eq. (4.30) for $n = \{1, 2, \ldots, \bar{N}\}$. The above suggests low computational cost for the recovery of the matrices in eqs. (4.25), (4.26). Further details on the design criterion of the adopted multi-coset sampling pattern and the weighted matrix $\mathbf{W}$, can be found in *Tausiesakul & Gonzalez-Prelcic* (2013).

4.7. Frequency Domain Decomposition (FDD) for Modal Estimation

Any established frequency domain algorithm for OMA can be used at this stage to retrieve the underlying structural modal properties. To this end, the standard FDD algorithm (*e.g.*, *Brincker & Ventura* (2015)) is employed herein, to extract the salient modal features (*i.e.*, natural frequencies, mode shapes) via application of the Singular Value Decomposition (SVD) to the cross-spectral matrix in eq. (4.26).

From the theory of structural dynamics, it is well-known that the response vector $\mathbf{x}(t)$ of a structural system with *R* modes of vibration, can be expressed in

$$\mathbf{x}(t) = \boldsymbol{\Phi}\,\mathbf{q}(t), \tag{4.39}$$

where $\boldsymbol{\Phi}$ is the mode shape matrix given in

$$\boldsymbol{\Phi} = \begin{bmatrix} \boldsymbol{\varphi}_1 & \boldsymbol{\varphi}_2 & \cdots & \boldsymbol{\varphi}_R \end{bmatrix}, \tag{4.40}$$

and $\mathbf{q}(t) = \begin{bmatrix} q_1(t) & q_2(t) & \cdots & q_R(t) \end{bmatrix}^{\mathrm{T}}$ is a column vector collecting the uncorrelated modal coordinates $q_r(t)$ at the $r = \{1, 2, \ldots, R\}$ modes of vibration.

It can be easily shown that the auto/cross power spectral density response matrix can be expressed in the form (see also *Brincker & Ventura* (2015))

$$\mathbf{G}_x = \mathbf{\Phi}\,\mathbf{G}_q\mathbf{\Phi}^{\mathrm{T}}, \tag{4.41}$$

where $\mathbf{G}_q$ is the diagonal and positive-valued spectrum density matrix of the modal coordinates $\boldsymbol{q}(t)$.

Consider further the SVD of the response spectrum matrix given in

$$\mathbf{G}_x = \mathbf{U}\mathbf{\Sigma}\mathbf{V}^{\mathrm{T}} \tag{4.42}$$

where $\mathbf{\Sigma}$ is a diagonal positive semi-definite matrix comprising the singular values Σ_{rr}, and $\mathbf{U}$, $\mathbf{V}$ are the unitary singular matrices holding the left and right singular vectors respectively. It is readily observed from eqs. (4.41) and (4.42), that the singular values Σ_{rr} correspond to the power spectral densities of the modal coordinate, $\mathbf{G}_q$, that carry the information of structural resonant frequencies. Likewise, the left singular vector $\mathbf{U}$ gives an estimate of the mode shapes $\mathbf{\Phi} = [\boldsymbol{\varphi}_1 \quad \boldsymbol{\varphi}_2 \quad \cdots \quad \boldsymbol{\varphi}_R]$ around the frequencies of the dominant singular values. More details on the FDD algorithm can be found in *Brincker & Ventura* (2015) and the references therein. Within the context of the proposed multi-sensor sub-Nyquist PSBS method (Figure 4.3), the dynamic structural properties can be readily obtained from eq. (4.42) using the recovered cross-spectrum matrix $\hat{\mathbf{G}}_{x^a x^b}$ in eq. (4.26). The accuracy of the extracted mode shapes is further assessed with the Modal Assurance Criterion (MAC) (*e.g.*, *Brincker & Ventura* (2015)), *i.e.*,

$$MAC(\boldsymbol{\varphi}_r, \hat{\boldsymbol{\varphi}}_r) = \frac{\left|\boldsymbol{\varphi}_r^{\mathrm{T}}\hat{\boldsymbol{\varphi}}_r\right|^2}{\left\|\boldsymbol{\varphi}_r\right\|_2^2 \left\|\hat{\boldsymbol{\varphi}}_r\right\|_2^2}, \tag{4.43}$$

which measures the level of similarity between two eigenvectors, *i.e.*, a theoretical $\boldsymbol{\varphi}_r$ and the estimated, $\hat{\boldsymbol{\varphi}}_r$. In the above expression, the ℓ_2 norm is denoted by $\|\cdot\|_2$. Note that eq. (4.43) takes a scalar value within the range of [0, 1], suggesting perfect correlation for MAC=1, and uncorrelated mode shapes when MAC=0. The criterion of MAC>0.9 is commonly used for valid mode shape estimation.

4.8. Concluding Remarks

A novel multi-sensor Power Spectrum Blind Sampling approach is developed herein for low-power wireless sensor networks used in Operational Modal Analysis applications for civil engineering structures. The proposed approach assumes centralised arrays of wireless sensors and comprises four main steps (see also Figure 1.1(c)):

(i) simultaneous signal acquisition and compression at the sensor front-end via the deterministic multi-coset sampling pattern;

(ii) wireless transmission and signal processing at the server with the scope of deriving the output cross-correlations directly from the received compressed measurements;

(iii) further signal processing for auto/cross power-spectral density estimation in the compressed domain by solving an overdetermined least-squares optimisation problem; and

(iv) fusion with standard OMA algorithms (*e.g.*, FDD algorithm) for structural modal identification.

Overall, it can be concluded that the proposed multi-sensor PSBS technique enjoys numerous advantages reflected in:

(a) the signal-agnostic nature of the adopted sampling scheme, which applies to non-sparse signals of any structure;

(b) no signal pre-processing operations is undertaken at the sensor front-end prior to wireless transmission;

(c) auto/cross power spectral estimates are obtained directly in the compressed domain, without involving signal reconstruction operations in time-domain;

(d) a computationally-efficient approach is developed, relying on relaxed optimisation algorithms that can be easily solved.

The above suggest significant energy savings in dense arrays of wireless sensors in OMA applications. Such energy savings can be of the order of 85-90% compared to conventional approaches at Nyquist rate, which is numerically verified in Chapters 6. Further, the achieved energy savings is translated directly into reduced computational, memory and storage requirements on sensor.

Chapter 5
Proposed Multi-Sensor Power Spectrum Blind Sampling Approach for OMA: Applications

5.1. Preliminary Remarks

The applicability of the proposed PSBS approach detailed in Chapter 4 (§*4. Proposed Multi-Sensor Power Spectrum Blind Sampling Approach for OMA: Theory*) within the VSHM framework is numerically attested in this chapter for the first time in the literature based on four numerical examples.

The influence of the signal compression and noise levels on the power spectral recovery performance of the developed PSBS method is first examined in section 5.2 (§*5.2. Error Assessment of the PSBS Approach (Single-Sensor Case)*). To this end, parametric analyses are performed on two case studies using simulated structural acceleration responses recorded on a single-sensor. It is shown that proposed method is practically insensitive to additive noise, while its accuracy depends strongly on the acquired number of compressed measurements, reaching up to 89% less data compared to conventional approaches at uniform sampling rates (Nyquist or above). This is verified in the second example in section 5.3 (§*5.3. Numerical Evaluation with Field-Data from an Operational Wind Turbine (Single-Sensor Case)*) for the single-sensor PSBS case using field-recorded data obtained from an operational wind turbine in Lübbenau, Germany.

The next example in section 5.4 (§*5.4. PSBS-based OMA with Computer-Generated Closely Spaced Modes of Vibration (Multi-Sensor Case)*) evaluates the efficiency of multi-sensor PSBS approach in retrieving cross-spectral matrices from sub-Nyquist sampled structural acceleration responses acquired from a network of wireless sensors/multi-coset samplers. Fused with the standard FDD algorithm, it will be shown that the proposed PSBS approach can be efficiently used in OMA applications to extract quality estimates of structural mode shapes that are susceptible to the modal coupling effect – a challenging issue within OMA. Finally, the damage detection capabilities of the developed method are examined in section 5.5 (§*5.5. PSBS-based Structural Damage Detection Using the Modal Strain Energy Index (Multi-Sensor Case)*) using the modal strain energy index (MSEI) – a well-established in the literature damage sensitive quantity. It will be demonstrated that PSBS-based MSEI can identify the location and severity of

structural damage from the acquisition of 70% less data in noisy environments without reconstructing structural responses in time-domain. Concluding remarks are summarised in section 5.6 (§*5.6. Concluding Remarks*).

It is noted that parts of this chapter have been published, or submitted for publication, in the journal papers and conference proceedings reported in section 1.5 (§1.5. List of Referred Papers). *Specifically, the Monte-Carlo simulation based framework in sub-section 5.2.1 (§5.2.1. Structural system and simulation) has been published in [C2 – C4], and parts of the wind-turbine application in §5.3 have appeared in [C7]. The numerical evaluation of section 5.4 has been submitted for publication in [J3] while the damage detection capabilities of the developed multi-sensor PSBS approach detailed in section 5.5 has been presented in [C5]. Finally, the parametric analyses undertaken in sub-section 5.2.2 (§5.2.2. Parametric analyses & results with respect to the number of compressed measurements*) *and sub-section 5.2.3 (§5.2.3. Parametric analyses & results with respect to additive measurement noise*) *have not been disseminated yet in the public domain.*

5.2. Error Assessment of the PSBS Approach (Single-Sensor Case)

Prior to the implementation of the PSBS method (§4) in VSHM applications, it was deemed essential to examine the influence of certain parameters on the performance of the proposed approach. To this end, parametric analyses are performed in a simulation-based framework assuming structural acceleration responses acquired from a single multi-coset sampler. The aim is to address the following two questions:

(1) what is the minimum number of compressed measurements, *M*, for a faithful recovery of the second-order statistics of the unknown full-length response signals?

(2) whether and to what extent is the above affected by the measurement noise?

The first issue can be addressed either through the consideration of various *CRs* for a fixed observation window, or equivalently by keeping a constant *CR* and varying the length of the observation window. The second issue considers the influence of the measurement noise at sensors level. The noise level is quantified using the signal-to-noise ratio (*SNR*), *i.e.*, $SNR = 10 \cdot \log_{10}\left(\sigma_x^2 / \sigma_\varepsilon^2\right)$, where σ_x^2 and σ_ε^2 are the signal and the noise variance, respectively. A thorough examination of the above parameters is undertaken in what follows next.

5.2.1. Structural system and simulation

Consider a viscously-damped linear Multi-Degree-of-Freedom (MDOF) structural system with *R* modes of vibration, excited by an ideal band-limited white-noise input with zero-mean and σ_w^2 variance (*i.e.*, OMA assumption), that observes, theoretically, a power spectrum density (PSD) of constant amplitude, $\mathbf{G}_w(\omega) = \sigma_w^2$, across all frequencies, ω, in the band of interest. Let $x(t)$ be the output Gaussian process, representing a real-valued time-domain acceleration response signal of the MDOF system, which, in the frequency domain, observes a maximum frequency at ω_{max}. The input-output PSD relationship is expressed in

$$\mathbf{G}_x(\omega) = \mathbf{G}_w(\omega)\left|\mathbf{H}(i\omega)\right|^2 = \sigma_w^2\left|\mathbf{H}(i\omega)\right|^2, \tag{5.1}$$

where $\mathbf{H}(i\omega)$ is the frequency response function of the MDOF system – termed as *accelerance* or *inertance* in the field of modal testing (*e.g.*, *Ewins* (2000)) for output acceleration response signals. The above expression can be cast in the form *Soong & Grigoriu* (1996)

$$\mathbf{G}_x(\omega) = \omega^4 \cdot \sum_{r,s=1}^{R}\left[A_{rs} \cdot \frac{(\omega_r{}^2 - \omega^2)\cdot(\omega_s{}^2 - \omega^2) + 4\omega^2\omega_r\omega_s\zeta_r\zeta_s}{[(\omega_r{}^2 - \omega^2)^2 + (2\omega\omega_r\zeta_r)^2]\cdot[(\omega_s{}^2 - \omega^2)^2 + (2\omega\omega_s\zeta_s)^2]}\right], \tag{5.2}$$

with ω_r (ω_s) being the resonant frequency and ζ_r (ζ_s) the damping ratio of the MDOF structural system at the *r*-th (*s*-th) mode of vibration, while the amplitude A_{rs} is a parameter associated with the structural modal deflected shapes and the modal participation factors due to the considered stationary input process (see also *Soong & Grigoriu* (1996)).

A Monte Carlo simulation-based assessment framework is introduced herein, which allows to compare the dynamic properties of MDOF system defined by eq. (5.2) with those estimated by the data-driven PSBS method fused with standard OMA algorithms. The proposed framework is illustrated Figure 5.1, which first defines an analog MDOF structural system with known modal properties (ω_r, A_r, ζ_r) attaining the PSD in eq. (5.2). This represents the "target" PSD which is sought to be captured by the developed PSBS approach as explained below.

The target PSD is replaced by a surrogate discrete-time auto-regressive moving average (ARMA) filter of order (*p*, *q*) subject to clipped white-noise excitation, $w[n]$ (*e.g.*, *Spanos & Mignolet* (1989)). Based on the ARMA process, discrete-time Nyquist-sampled signals, $x_{ARMA}[n]$, can be generated and treated as N_R realisations of an underlying stochastic process representing the acceleration responses of structural systems with known modal properties (ω_r, A_r, ζ_r). This is achieved by recursively computing each *n* sample in $x_{ARMA}[n]$ based on past observation and adding a convolution term related to the white noise input $w[n]$, *i.e.*,

$$x_{ARMA}[n] = -\sum_{k=1}^{p} b_k x_{ARMA}[n-k] + \sum_{\ell=0}^{q} c_\ell w[n-\ell]\,. \tag{5.3}$$

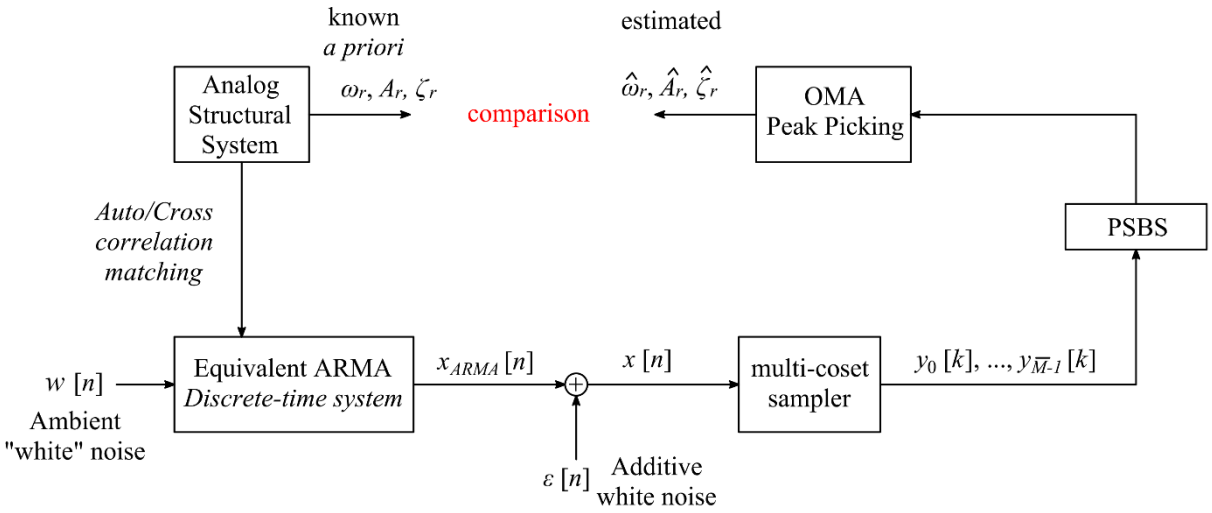

***Figure 5.1**: Adopted Monte Carlo simulation-based framework to assess the multi-coset sampling device for OMA applications*

The coefficients b_k, k=(1,2,…,p) and c_ℓ, $\ell = (0,1,...,q)$ of this ARMA filter are derived from the auto/cross-spectrum correlation matching algorithm by *Spanos & Zeldin* (1998), which is commonly used for spectrum compatible simulation (*e.g.*, *Giaralis & Spanos* (2009), (2012)). The above coefficients are obtained by solving a $(p+q)\times(p+q)$ system of linear equations such that the square modulus of the frequency response function of the ARMA filters closely trace the target PSD of the analog system in eq. (5.2), that is,

$$\mathbf{G}_x(\omega) \simeq \left|\mathbf{H}(e^{i\omega T_s})\right|^2. \tag{5.4}$$

In the above expression, T_s, is the sampling period of the discrete-time process associated with the Nyquist relation, $T_s=\pi/\omega_{max}$, and $\mathbf{H}(e^{i\omega T_s})$ is the transfer function of the ARMA filter that satisfies the equation (*e.g.*, *Spanos* (1983); *Giaralis & Spanos* (2009))

$$\mathbf{H}(e^{i\omega T_s}) = \frac{\sum_{\ell=0}^{q} c_\ell e^{-\ell i\omega T_s}}{1+\sum_{k=1}^{p} b_k e^{-ki\omega T_s}}\,. \tag{5.5}$$

For the considered stochastic process, the generated Nyquist-sampled discrete-time structural responses, $x_{ARMA}[n]$ (coloured white noise via the ARMA filter) are contaminated further with additive white noise, $\varepsilon[n]$, at various *SNRs* to simulate noisy structural responses, $x[n]$. The latter

are next treated by a single discrete-time model of the multi-coset sampling device depicted in Figure 4.2, to derive M compressed/ sub-Nyquist measurements, $y_i[k]$, in eq. (4.5) for $i=\{0,1,\ldots, \bar{M}-1\}$, $k=\{1, 2, \ldots, K\}$, and $M = K\bar{M}$. The simulated compressed data are treated by the PSBS strategy in §4, to recover the unknown power spectrum, $\hat{\mathbf{G}}_x \in \mathbb{C}^{\bar{N}(2L+1)\times 1}$ upon solving the least-squares optimisation problem in eq. (4.26) (*i.e.*, for $a=b=1$). Thus, an approximation of the target PSD in eq. (5.2) can be obtained and further processed with standard OMA algorithms (*e.g.*, the "peak picking" method detailed in *Ewins* (2000)) to retrieve the location, amplitude, and width of the recovered spectral peaks, providing approximations of the structural modal parameters, $\hat{\omega}_r, \hat{A}_r, \hat{\zeta}_r$. The accuracy of these parameters can be assessed with respect to the known modal values, ω_r, A_r, ζ_r, originally defined in the first step of the proposed framework (*i.e.*, in deriving the target PSD of the MDOF system in eq. (5.2)). The significance of the developed strategy in Figure 5.1 can be appreciated in that parametric dynamic analyses are numerically performed in MDOF systems with low computational cost, bypassing the need for linear response history analyses using standard FE software.

In this study, the simulation-based framework in Figure 5.1 is utilised to approximate a continuous MDOF structural system with $R=2$ degrees of freedom (*i.e.*, 2DOF system) and a critical damping of $\zeta_1 = \zeta_2 = 5\%$ for both modes of vibration, pertaining to the spectral coefficients $A_{11}=0.43$, $A_{22}=0.5$, $A_{12}=A_{21}=0.46$ in eq. (5.2). Note that the above coefficients can be retrieved from the PSDs of acceleration responses measured at the quarter-span of a 2DOF dynamically vibrating simply supported beam subjected to a white-noise point force applied at the 3/8 of its length (*e.g.*, Figure 5.2).

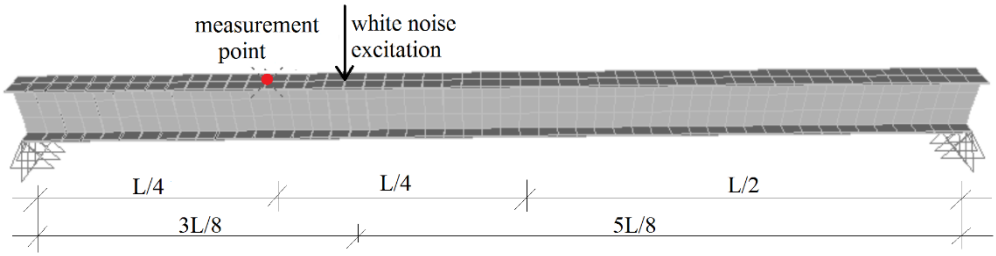

Figure 5.2: *L-length simply supported beam with two degrees of freedom and the considered location of the excitation and measurement point at the 3L/8 and L/4 respectively*

Two different case studies are examined for the above 2DOF with resonances at:

(1) $\omega_1=20$ rad/s, $\omega_2=60$ rad/s, (case of well-separated modes of vibration); and

(2) $\omega_1=20$ rad/s, $\omega_2=25$ rad/s (case of close-spaced modes of vibration).

For the above systems, their PSDs (target) are first derived from eq. (5.2). It is considered next an ARMA filter of order (200, 20) which is convolved with a clipped white-noise input assuming a sampling period at T_s=0.02s (*i.e.*, the Nyquist frequency is 157.08 rad/s). The auto/cross-spectrum correlation matching algorithm proposed by *Spanos & Zeldin* (1998) is then employed to compute the ARMA coefficients using eqs. (5.2), (5.4), and (5.5), and derive discrete-time Nyquist-sampled signals considering N_R=10 realisations of the underlying stochastic process. The generated signals represent acceleration responses of the adopted MDOFs in cases (i) and (ii) under ambient vibrations, to be treated by the proposed PSBS method in §4. For illustration, Figure 5.3 shows the above derived PSDs for the two considered cases, normalised to their peak value to facilitate comparison. It is seen that the PSD curve of the ARMA filter (broken red curves) can efficiently represent the target power spectrum (grey curve) evaluated from eq. (5.2). Figure 5.3 also presents the theoretical PSD (solid blue curve) derived from eq. (4.18) (for a=b=1) together with the autocorrelation function of the ARMA filter, $r_{xx}[p] = \mathrm{E}_x\{x[n]\,x[n-p]\}$ (see also eq. (4.6)), which is shown to closely trace the target PSD.

Further to the above, Figure 5.4 plots the recovered PSDs at CR=21%, obtained from eq. (4.26) for $\bar{M}$ =8, $\bar{N}$ =39 and $\mathbf{s}$=[0,1,3,7,9,14,18,19]$^{\mathrm{T}}$ (see also Table 5-2) for the case of well-separated (Figure 5.4(a)) and that of closely-spaced modes of vibration (Figure 5.4(b)). It is readily observed that the PSBS-recovered PSDs are capturing well the salient attributes of the systems frequency response function, such as the location of the two prominent peaks, their widths, and amplitudes, associated with the structural resonant frequencies, the damping ratio, and the modal deflected shapes, respectively, at the pertinent modes of vibration. From a qualitative point of view, the above confirms the efficiency of the proposed PSBS method in retrieving auto-spectral densities from compressed acceleration measurements acquired from a single sensor.

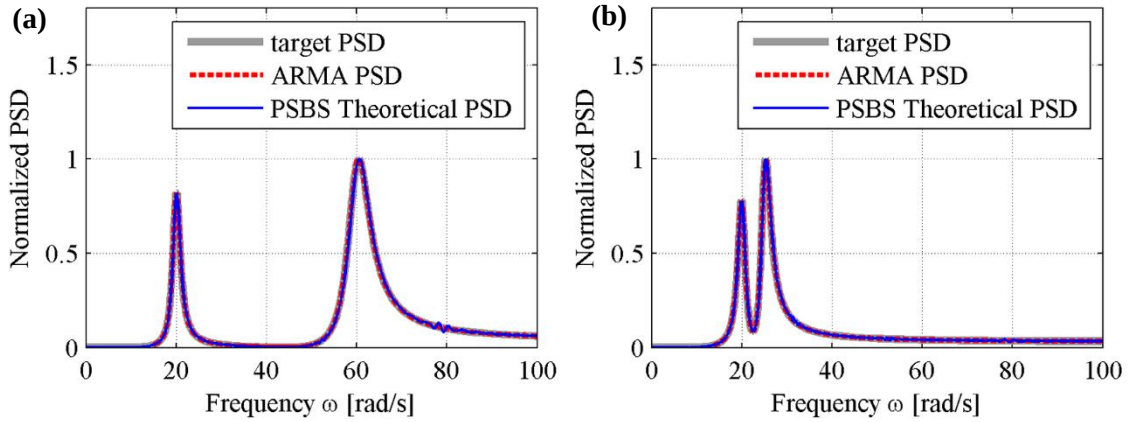

Figure 5.3: *Comparison of normalised PSD curves to maximum their amplitude, obtained from the target PSD (analytical expression in eq. (5.2)), the ARMA model, and the theoretical expression in the PSBS method for the two adopted case studies: 2DOF with (a) well-separated and (b) closely-spaced modes of vibration*

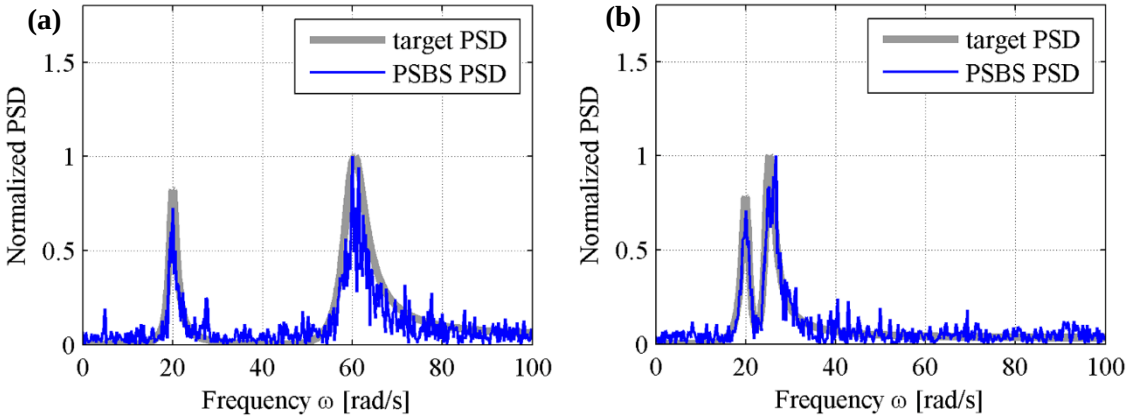

Figure 5.4: *Estimated PSDs from sub-Nyquist multi-coset sampled simulated data (K=1000,* $\bar{M}=8$, $\bar{N}=39$, *L=16) with the multi-coset sampling pattern* **s**=[0,1,3,7,9,14,18,19]^T *(blue curve) plotted against the target PSD in eq. (5.2) for the two adopted case studies: (a) 2DOF with well-separated and (b) closely-spaced modes of vibration*

An error metric is adopted to quantitatively assess the recovery performance of the PSBS method and ensure reasonable estimates of structural modal properties. In this respect, the root-mean-square error (RMSE)

$$RMSE = \sqrt{\frac{\sum_{j=0}^{n}\left(\hat{G}_x(\omega_j) - G_x(\omega_j)\right)^2}{n+1}} \tag{5.6}$$

is computed between the power spectral amplitudes derived from the PSBS-recovered PSDs, $\hat{G}_x(\omega_j)$, and those obtained from the target spectrum, $G_x(\omega_j)$, in the frequency band [ω_0, ω_n].

For the two examined 2DOF structural systems, the adopted error metric in eq. (5.6) is calculated for three different frequency bands as reported in Table 5-1, *i.e.*, one wide-band covering the frequency range of interest between [0, 100] rad/s, and two narrow-bands around the resonant frequencies of the adopted structural systems (*i.e.*, ω_1, and ω_2, respectively). For illustration, Figure 5.5 and Figure 5.6 plot with a red curve the three different spectral ranges in Table 5-1 for the two 2DOF systems analysed.

Table 5-1: Considered frequency ranges in the PSD estimates for the computation of the RMSE

	Case Study 1	**Case Study 2**
	Well-separated modes ***(ω_1=20rad/s, ω_2=60rad/s)*** **[ω_0 - ω_n]**	**Closely-spaced modes** ***(ω_1=20rad/s, ω_2=25rad/s)*** **[ω_0 - ω_n]**
Wide-band	[0 - 100] rad/s	[0 - 100] rad/s
Narrow-band around ω_1	[10 - 30] rad/s	[18.5 – 21.5] rad/s
Narrow-band around ω_2	[50 - 70] rad/s	[24 - 27] rad/s

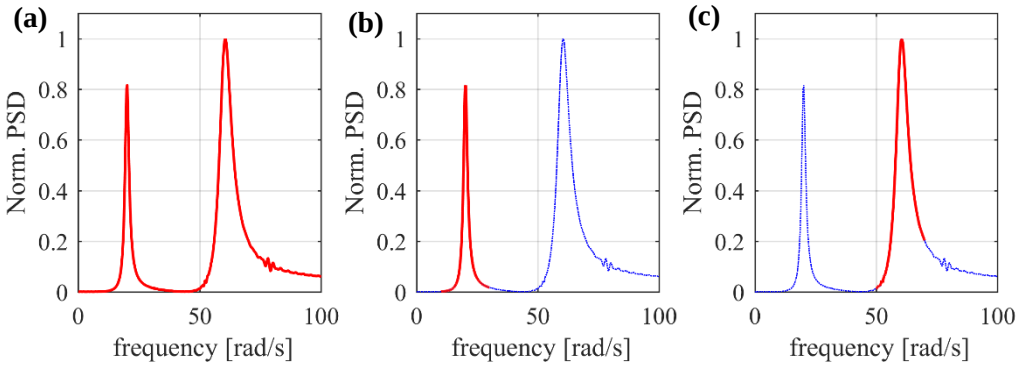

Figure 5.5: *Considered frequency bands in the computation of the RMSE between recovered PSBS-PSD and target PSD for the 1st case study: (a) wide-band; (b) narrow-band around ω_1; and (c) narrow-band around ω_2*

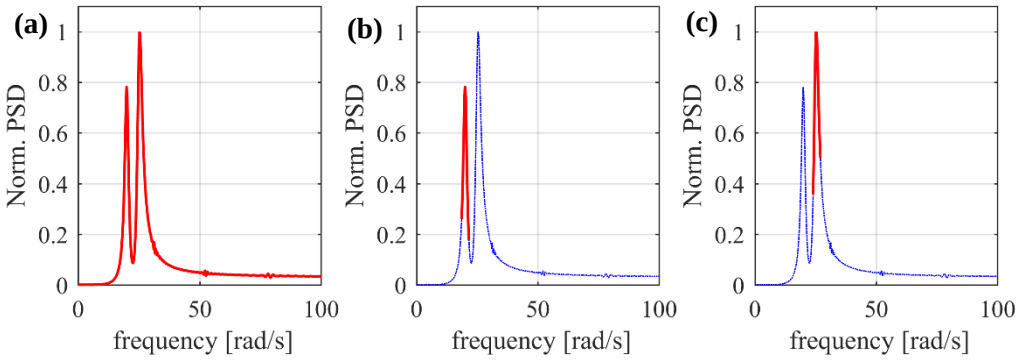

Figure 5.6: *Considered frequency bands in the computation of the RMSE between recovered PSBS-PSD and target PSD for the 2nd case study: (a) wide-band; (b) narrow-band around ω_1; and (c) narrow-band around ω_2*

5.2.2. Parametric analyses & results with respect to the number of compressed measurements

The efficiency of the PSBS method is numerically assessed herein as a function of the required number of compressed measurements, *M*. In this respect, parametric analyses are performed on both considered 2DOF systems in cases (i) and (ii) using the values listed in Table 5-2 and Table 5-3. In particular, compressed acceleration data are generated at five different *CRs* ranging between 11% and 50%. As reported in Table 5-2, the adopted *CRs* have been defined by appropriately selecting five pairs of $(\bar{M}, \bar{N})$ values. Each pair is associated with a sampling pattern sequence, **s**, which has been obtained by solving the constrained optimisation problem in eqs. (4.31), (4.32). For the five considered compression levels, Table 5-2 also reports the computed *L* values from eq. (4.21) that allow to recover the PSD estimates of the unknown full-length acceleration responses with a frequency resolution at approximately 0.005 rad/s in all *CR* cases.

It is further assumed that the observation window comprises *N* samples, with *N* ranging from 3900 to 39000. Note that the above range is approximated in the five *CR* cases listed in Table 5-3, since the value of *N* is related to both the number, *K*, and the length, $\bar{N}$, of the blocks the input signal is divided for the application of the multi-coset sampling strategy detailed in §4.2 (*i.e.*, $N = K\ \bar{N}$). The consideration of varying observation window lengths within each *CR* allows to define compressed acceleration responses of *M* samples, with *M* taking values within the ranges reported in Table 5-3.

Table 5-2: Adopted multi-coset sampling values

Compression ratio	***CR***	**11%**	**21%**	**31%**	**40%**	**50%**
Number of channels	$\bar{M}$	14	8	5	4	8
Down-sampling	$\bar{N}$	128	39	16	10	16
Sampling pattern	**s**	[0,1,2,6,8,20,29,39, 47,50,53,60,63,64]^T	[0,1,3,7,9, 14,18,19]^T	[0,1,2,5,8]^T	[0,1,2,5]^T	[0,1,2,3,4,6,7,8]^T
Design Parameter	*L*	4	16	40	64	40
Frequency resolution [rad/s]	$\Delta\omega$	5.45 10^{-3}	4.88 10^{-3}	4.85 10^{-3}	4.87 10^{-3}	4.85 10^{-3}

Table 5-3: Adopted ranges in parametric analyses

Compression ratio	***CR***	**11%**	**21%**	**31%**	**40%**	**50%**
Number of blocks	*K*	30-304	100 - 1000	243-2437	390-3900	243-2437
Nyquist samples	*N*	3888-38992	3900 - 39000	3888-38992	3900-39000	3840-38912
Sub-Nyquist samples	*M*	420-4256	800 - 8000	1215-12185	1560-15600	1944-19496
Signal-to-Noise Ratio [dB]	*SNR*	0 - 100	0 - 100	0 - 100	0 - 100	0 - 100

Considering the 1st case study (*i.e.*, the 2DOF case of well-separated modes of vibration) and the pertinent spectral ranges in Table 5-1, eq. (5.6) is employed to compute the RMSE of the PSBS-recovered PSDs at *CR*={11%, 21%, 31%, 40%, 50%} (see also Table 5-2). The obtained error values are presented in Figure 5.7 as a function of the length of the observation window, *N*. Notably, the consideration of lower *CRs* within a fixed observation window (*i.e.*, at any given *N* value in Figure 5.7) suggests the acquisition of fewer compressed/sub-Nyquist measurements, *M*.

As expected, it is seen that the RMSE decreases, in all *CRs*, as longer observation windows are considered, since larger number of compressed measurements *M* are retrieved. In fact, Figure 5.7 confirms that at higher *N* values the RMSE tends towards a constant error value (*i.e.*, roughly at 0.1 in Figure 5.7(a) and Figure 5.7(b) and 0.2 in Figure 5.7(c)) regardless of *CR*. This means

that a sufficiently large number of measurements M is obtained even for a limiting CR (*e.g.*, at 11% in this numerical example), and thus the accuracy of the recovered PSDs cannot improve further. The above also confirm that the most critical case is the consideration of short observation windows at lower *CRs*, yielding smaller M values at the cost of larger errors (*e.g.*, CR=11%). Interestingly, though, it is seen in Figure 5.7 that the recovered PSDs yield approximately the same accuracy for CR>21% in this example, as the pertinent error curves significantly overlap across N. Comparing next the RMSE amplitudes among the three panels of Figure 5.7, it can be concluded that the PSD recovery around the 2nd natural frequency (*i.e.*, Figure 5.7(c)) is a more challenging task, yielding larger error values compared to the other two cases shown in Figure 5.7(a) and Figure 5.7(b) for the wide-band spectral range and the narrow-band around ω_1.

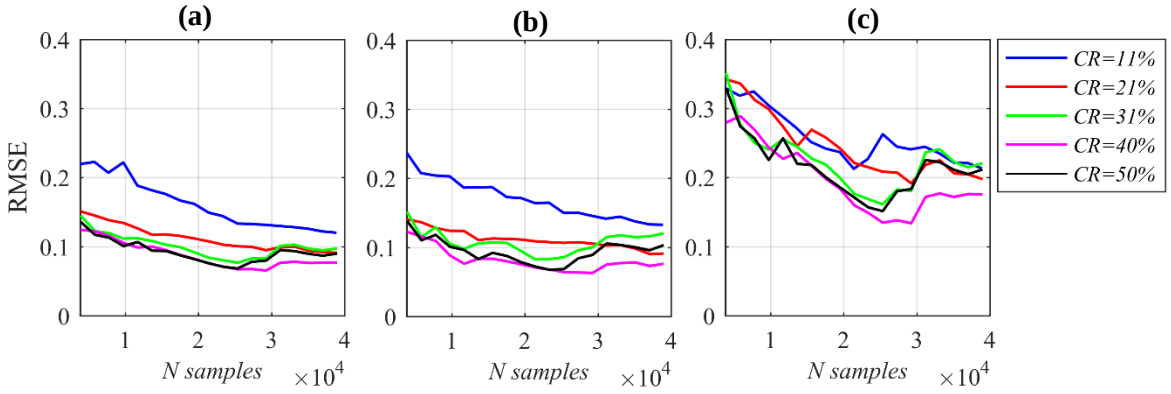

***Figure 5.7**: RMSE versus observation's window length, N, for the 1st case study with ω_1=20rad/s and ω_2=60rad/s: (a) RMSE in the wide-band range of [0-100 rad/s]; (b) RMSE in the narrow-band range of [10-30] rad/s (around ω_1); (c) RMSE in the narrow-band range of [50-60] rad/s (around ω_2)*

Based on the above results, it is recommended for practical applications to a test range of different CR (off-line) for a fixed observation window to determine the order of M for which quality PSD estimates can be obtained, while any additional increase in M yields only marginal improvements in terms of RMSE. Then, one can opt either to adopt the limiting CR value achieved in the above configuration (*i.e.*, pertaining to the fixed observation window initially defined) or to allow longer observation windows using lower sampling rates at smaller *CRs* as long as the order of M is not violated.

An alternative aspect of Figure 5.7 is shown in Figure 5.8 by plotting the computed RMSE at the five adopted *CRs* considering three fixed observation window of N=5850, N=11700 and N=21450, samples, respectively. Similarly, the three panels in Figure 5.8 pertain to the three different spectral ranges in Table 5-1, confirming the above concluding remarks.

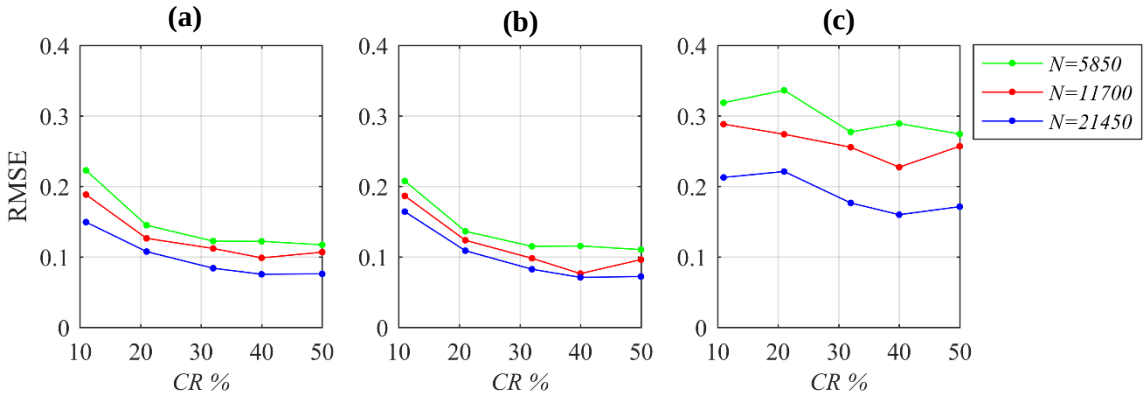

Figure 5.8: *RMSE versus CR for the 1st case study with ω_1=20rad/s and ω_2=60 rad/s: (a) RMSE in the wide-band range of [0-100 rad/s]; (b) RMSE in the narrow-band range of [10-30] rad/s (around ω_1); (c) RMSE in the narrow-band range of [50-60] rad/s (around ω_2)*

For the 2nd case study (*i.e.*, 2DOF case of closely-spaced modes of vibration), the influence of *M* on the RMSE of the PSBS-recovered PSDs is illustrated in Figure 5.9 and Figure 5.10 under the same considerations as in Figure 5.7 and Figure 5.8, respectively. Similar remarks hold as before with smaller errors observed at higher *M* values and the acquisition of larger number of compressed data. As discussed above, this is achieved by considering longer observation windows at a given *CR* (*i.e.*, Figure 5.9) and vice versa (*i.e.*, Figure 5.10). However, the need to examine the spectral recovery around the two closely-spaced natural frequencies independently, leads to very narrow frequency bands in Table 5-1. This results in larger RMSEs in the recovered PSDs around ω_1 and ω_2, as shown in Figure 5.9(b) and Figure 5.9(c), respectively, in contrast to the pertinent plots in Figure 5.7. Nonetheless, Figure 5.9 and Figure 5.10 show that the PSBS method yields almost the same level of accuracy for *CR*>21% even in this challenging case of closely-spaced modes.

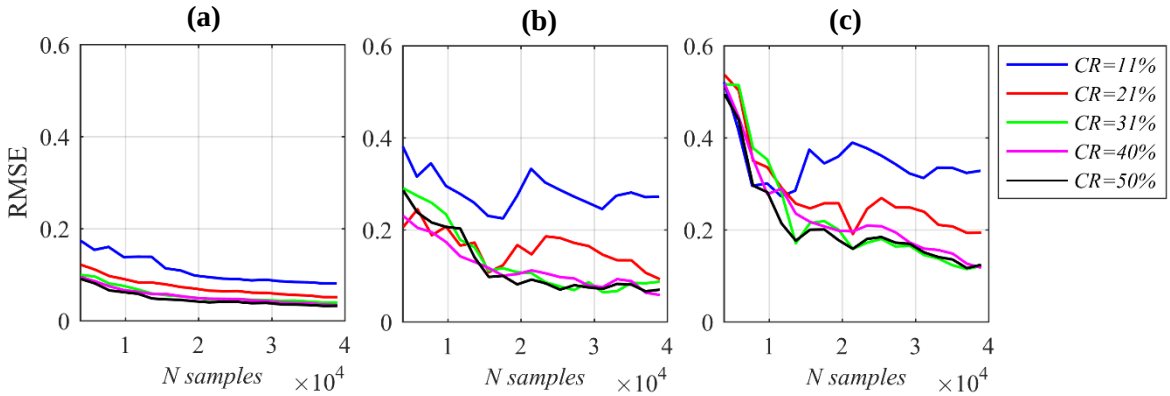

Figure 5.9: *RMSE versus observation's window length, N, for the 2nd case study with ω_1=20rad/s and ω_2=25rad/s: (a) RMSE in the wide-band range of [0-100 rad/s]; (b) RMSE in the narrow-band range of [18.5-21.5] rad/s (around ω_1); (c) RMSE in the narrow-band range of [24-27] rad/s (around ω_2)*

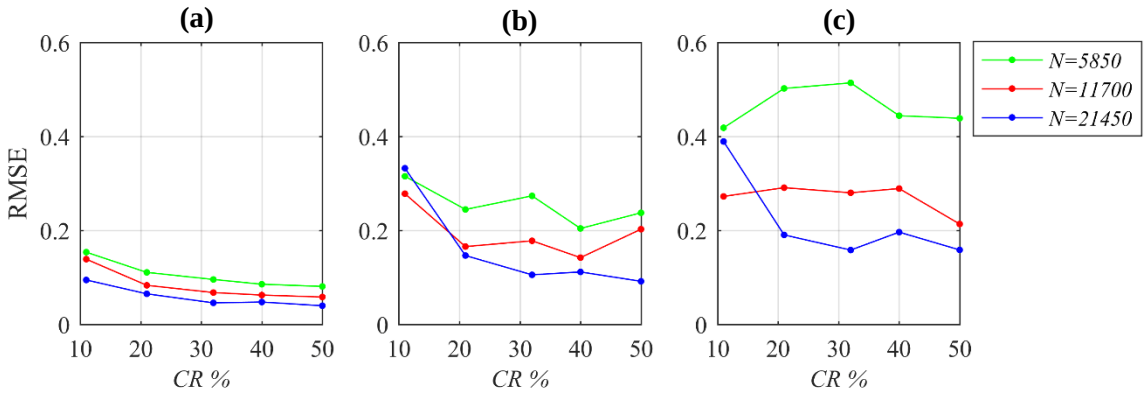

Figure 5.10: *RMSE versus CR for the 2nd case study with ω_1=20rad/s and ω_2=25rad/s: (a) RMSE in the wide-band range of [0-100 rad/s]; (b) RMSE in the narrow-band range of [18.5-21.5] rad/s (around ω_1); (c) RMSE in the narrow-band range of [24-27] rad/s (around ω_2)*

5.2.3. Parametric analyses & results with respect to additive measurement noise

This sub-section numerically assesses the influence of additive noise on the recovery performance of the PSBS method. To this end, parametric analyses are performed considering structural response signals contaminated with additive Gaussian noise at 10 different *SNR* values varying between 0dB (*i.e.*, $\sigma_e^2 \approx \sigma_x^2$, extreme noise case that may not be encountered in practical VSHM deployments) and 100dB (*i.e.*, $\sigma_e^2 \approx 10^{-10}\sigma_x^2$, relatively low-noise case) as given in Table 5-3. The noisy signals are then treated by the PSBS method using the parameters reported in Table 5-2, and the pertinent PSDs are recovered at five *CRs*. For the two considered case studies, the spectral ranges in Table 5-1 are further used to compute the RMSE in eq. (5.6) and the obtained results are presented in Figure 5.11 and Figure 5.12 as a function of *SNR* assuming fixed observation window of *N*=39000 samples.

Regarding the 2DOF case of well-separated modes of vibration (case study 1), Figure 5.11 reveals that the PSBS method is practically insensitive to additive noise for *CRs* above 21%, yielding a constant error value across the entire *SNR* range in [0, 100] dB. However, at lower *CRs* (below 21%) it is seen that the extreme noise level at *SNR*= 0 dB adversely affects the accuracy of the recovered PSDs. The latter is also confirmed in the 2nd case study in Figure 5.12 irrespective of *CR*, since spectral recovery in systems with closely-spaced modes of vibration is, inherently, a more challenging problem. Finally, it is noted that the RMSE amplitudes in Figure 5.11 and Figure 5.12 are in agreement with the values shown in Figure 5.7 and Figure 5.9, respectively, for *N*=39000.

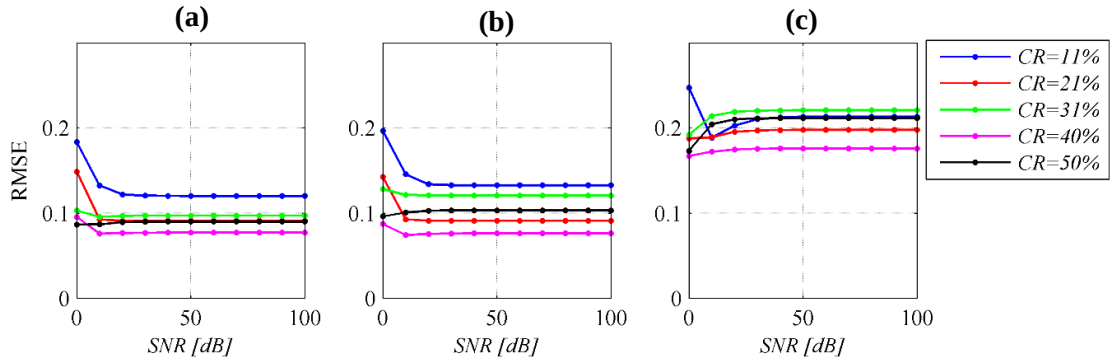

Figure 5.11: *RMSE of the PSD estimates versus SNR for the two considered CRs in the 1st case study for (a) a wide frequency band, (b) a narrow band around ω_1, and (c) around ω_2; N=39000*

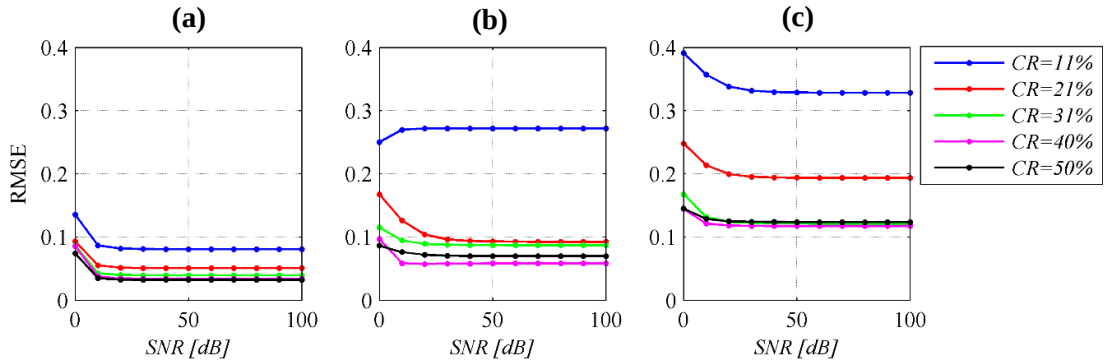

Figure 5.12: *RMSE of the PSD estimates versus SNR for the two considered CRs in the 2nd case study for (a) a wide frequency band, (b) a narrow band around ω_1, and (c) around ω_2; N=39000*

5.3. Numerical Evaluation with Field-Data from An Operational Wind Turbine (Single-Sensor Case)

The parametric analyses undertaken in the previous section confirm that the accuracy of the considered PSBS approach strongly depends on the efficiency of power spectral recovery operation applied to the acquired compressed measurements. This argument is numerically assessed herein as a function of the signal compression due to sub-Nyquist multi-coset sampling using field-recorded acceleration response data acquired from an actual monitoring campaign.

5.3.1. Structural system and response signals

The recovery performance of the PSBS-based spectral estimation approach is evaluated herein for the single-sensor case (*i.e.*, *a=b* in Chapter 4), using structural response data obtained from an operational wind turbine in Lübbenau, Germany (*e.g.*, *Chatzi & Spiridonakos* (2015); *Klis & Chatzi* (2015)). The considered structure was instrumented with wired sensors over a period of 29 days, measuring tri-axial acceleration responses for approximately 10 minutes every half an hour. The acquired datasets were conventionally sampled with a uniform rate at 200 Hz

(T_s=0.005s). Figure 5.13 shows the wind turbine and the sensors installation at 80 and 100 meters along the height of the supporting tower.

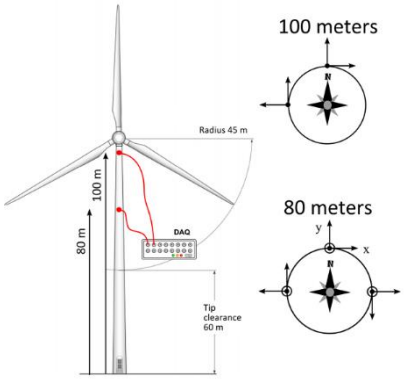

***Figure 5.13**: Wind turbine tower and location of sensors in the monitoring set-up (image reused from Chatzi & Spiridonakos* (2015)*)*

In this study, an acceleration time-series of N=172420 samples is employed recorded on the 29/12/2013 (at 15:44pm) along the northern axis (N or y-axis in Figure 5.13) from the sensor at 80m height. For illustration, Figure 5.14 presents the recorded response acceleration signal (Figure 5.14(a)) together with the velocity (Figure 5.14(b)) and displacement (Figure 5.14(c)) time-series, obtained from single and double integration, respectively. It is readily observed that unrealistically high velocity and displacement values are present within the "raw" data, which underpins the need for signal pre-processing operations prior to the implementation of the developed method. To this end, a baseline adjustment is applied to the raw data to remove the mean value and any potential low-frequency trend within the acceleration response signal. Next, a 4th-order Butterworth band-pass filter is employed within the frequency range 0.10 - 25.0 Hz. The "corrected" acceleration signal (*i.e.*, baseline adjusted and band-pass filtered) and the computed velocity and displacement time series are presented in Figure 5.15.

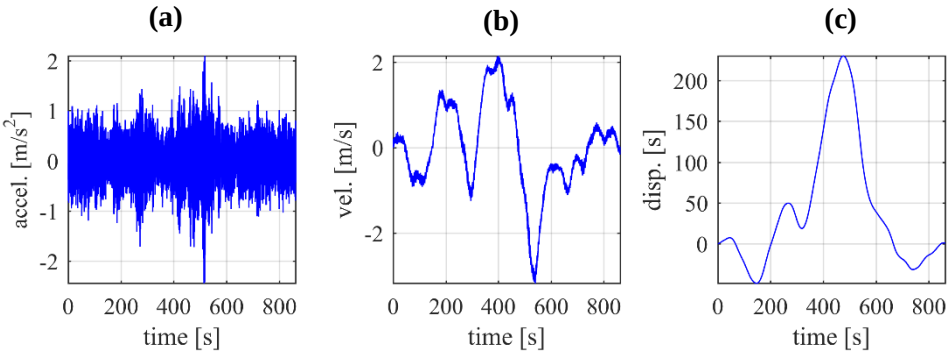

***Figure 5.14:** (a) Acceleration, (b) velocity, and (c) displacement time series acquired from sensor at 80m height (raw data)*

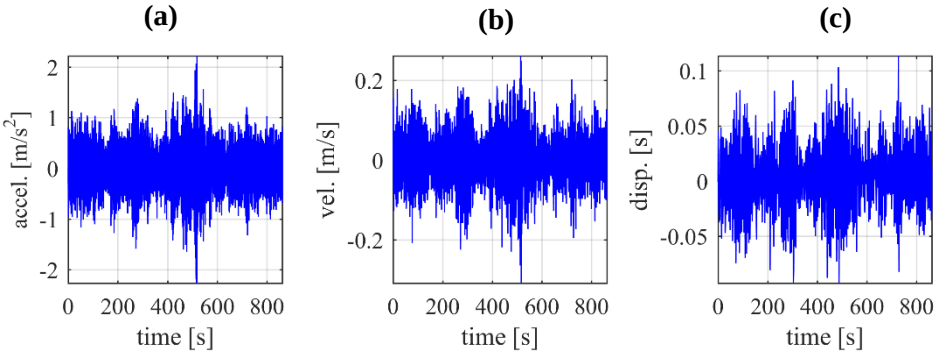

Figure 5.15: *Corrected/filtered (a) acceleration, (b) velocity, and (d) displacement time series (from sensor at 80m height) obtained from pre-processing the acceleration response in Figure 5.14*

For the above acceleration responses (before and after filtering), the standard Welch periodogram is computed for the full-length signals of 172420 samples, assuming 4096 (=2^{12}) FFT points, eight overlapping segments with 50% overlap, windowed with a Hanning function *Marple* (1987). The derived *PSD* estimates are normalised to their maximum amplitude and plotted together in logarithmic scale in Figure 5.16(a) and in linear scale in Figure 5.16(b). It is readily observed that the maximum power spectral amplitude occurs at approximately 1.4 Hz, pertaining to the dominant resonant frequency of the wind turbine. Further, it is seen that the important signal information lies in frequencies below 5 Hz, while the remaining spectral peaks (above 5 Hz) are negligible.

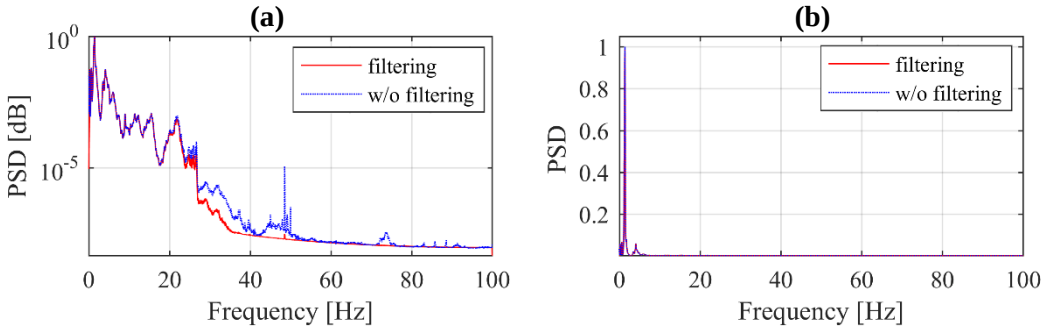

Figure 5.16*: Welch periodogram at Nyquist rate derived from the considered acceleration response signal (a) before and (b) after filtering*

Given that the PSBS-based spectral estimation approach anticipates signal stationarity, it was deemed essential to undertake a data qualification test to appraise the stationarity attributes of the recorded signals. The corrected acceleration sequence in Figure 5.15(a) is divided in 7 time-frames of 2 minutes duration and the standard non-parametric Reverse Arrangement method (*e.g.*, *Bendat & Piersol* (2010)) is used to statistically test the stationarity hypothesis. The obtained reverse arrangements are presented in Figure 5.17 showing that the stationarity hypothesis is confirmed at the 95% confidence level. The latter suggests that the recorded and pre-processed response acceleration signals from the wind turbine tower can be treated as wide-sense stationary at a high confidence level and, therefore, the PSBS approach is applicable.

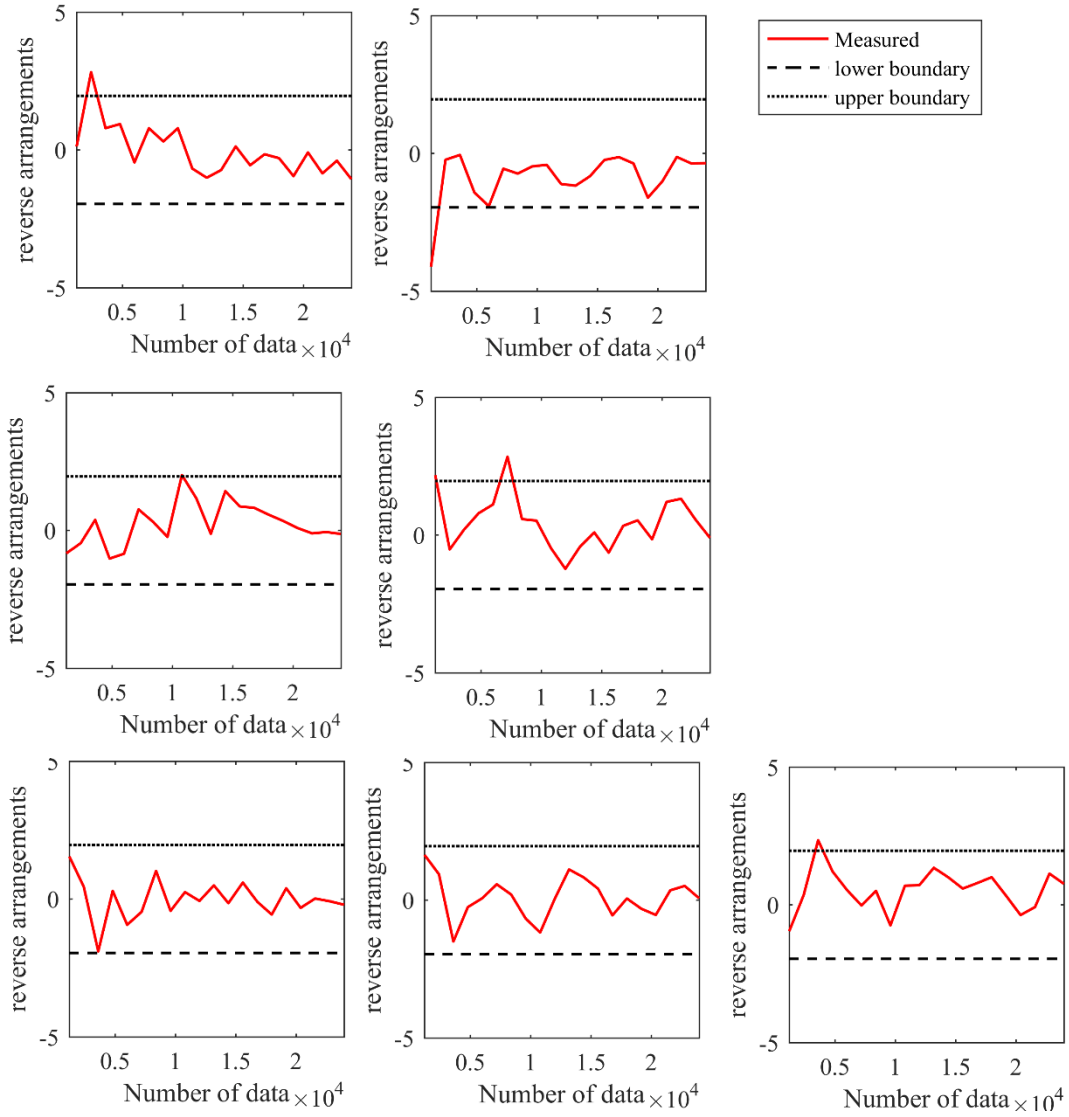

Figure 5.17: *Reverse Arrangement method applied on acceleration response signal acquired form sensor at 80m height; signal is divided in 7 segments of 2min duration*

5.3.2. PSBS application and power spectral estimation assessment

Considering next the multi-coset sampling scheme in §4.2, the corrected acceleration response signal in Figure 5.15(a) is compressed at three different *CRs* of 11%, 21% and 31%, using the ($\bar{M}$, $\bar{N}$, L) values and the sampling pattern sequences, **s**, reported in the 3rd, 4th, and 5th column of Table 5-2 for *CR*={11%, 21%, 31%}, respectively.

Specifically, for the case of *CR*= 31%, the assumed wireless sensor comprises $\bar{M}$ =5 channels that operate at a rate $\bar{N}$ =16 times slower than the uniform sampling rate at 200Hz. The sampling pattern sequence **s** = $[0, 1, 2, 5, 8]^T$ is utilised along the channels of the assumed multi-coset sampler, which has been obtained by solving the constrained optimisation problem in eqs. (4.31), (4.32) for $\bar{M}$ =5 and $\bar{N}$ =16 (*e.g.*, *Tausiesakul & Gonzalez-Prelcic* (2013)). Following the

mathematical details in chapter 4, the corrected full-length acceleration signal, $x[n]$, (of N=172420 samples) is divided in K=10776 blocks of length $\bar{N}$ =16 (*i.e.*, $K = N / \bar{N}$). From each block, only $\bar{M}$ =5 samples are selected, which are further collected in the compressed sequences $y_i[k]$ (i=0, 1,…, $\bar{M}-1$, k=1,2,…,K) in eq. (4.5), resulting in the acquisition of M=53880 compressed samples per sensor (*i.e.*, 69% fewer samples compared to $x[n]$). The unbiased estimator $\hat{r}_{y_i^a, y_j^b}[\ell]$ in eq.(4.22) is then computed for a=b=1 and $\ell \in [-40, 40]$ using the heuristically defined value of L=40 (see also Table 5-2). This enables the recovery of the unknown power spectrum $\hat{\mathbf{G}}_x \in \mathbb{C}^{1296\times 1}$ in eq.(4.26), with a frequency resolution of $\Delta\omega = 4.85 \cdot 10^{-3}$ rad/s (see also eq.(4.21)).

The above procedure also holds for the two other cases with *CR*=21% and *CR*=11%, based on the pertinent sampling parameters in Table 5-2, yielding, respectively, 79% (*i.e.*, M=35368) and 89% (*i.e.*, M=18858) fewer samples compared to the uniformly-sampled full-length signal.

Figure 5.18 - Figure 5.20 illustrate the recovered PSD estimates at *CR*={11%, 21%,31%} (solid red curves in logarithmic scale in panels (a) and in linear scale in panels (b)). These PSD estimates are normalised to their maximum amplitude to facilitate comparison and plotted against the standard Welch periodogram (dotted blue curve) in Figure 5.16 for the corrected full-length signal. From a qualitative point of view, it is observed that the PSBS-based *PSD* can closely approximate the Welch periodogram within the frequency range of interest (*i.e.*, below 5 Hz), even for *CR*=11% and the power spectral recovery from 89% fewer data samples compared to conventional approaches (*e.g.*, Figure 5.18). Note that the comparative PSD curves in Figure 5.18-Figure 5.20 observe some differences for frequencies above 5 Hz - mainly in the anti-resonance ranges- which, however, have no practical meaning given their negligible spectral amplitudes that yield almost zero values.

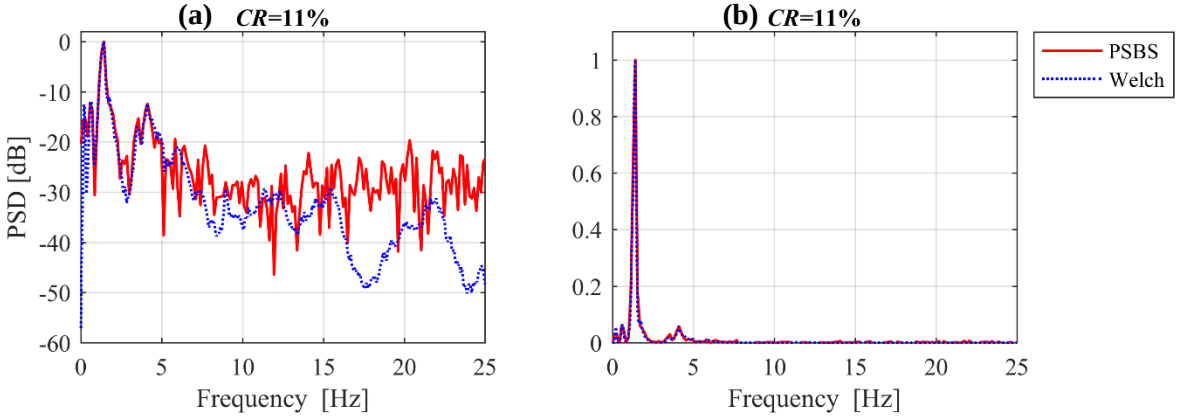

Figure 5.18: *PSD estimates: Welch periodogram at Nyquist rate compared with PSBS approach for CR=11% ($\bar{M}$=14, $\bar{N}$=128) in (a) logarithmic scale, and (b) linear scale*

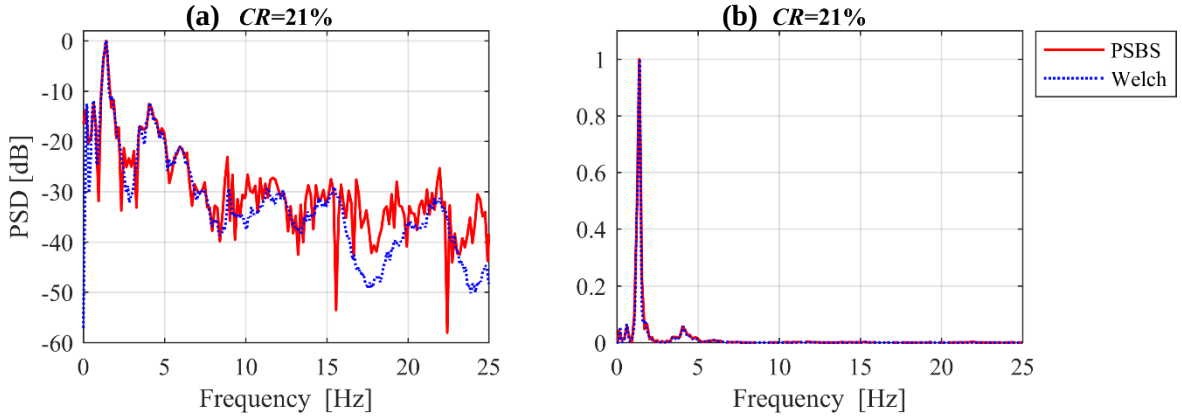

***Figure 5.19**: PSD estimates: Welch periodogram at Nyquist rate compared with PSBS approach for CR=21% ($\bar{M}$=8, $\bar{N}$=39) in (a) logarithmic scale, and (b) linear scale*

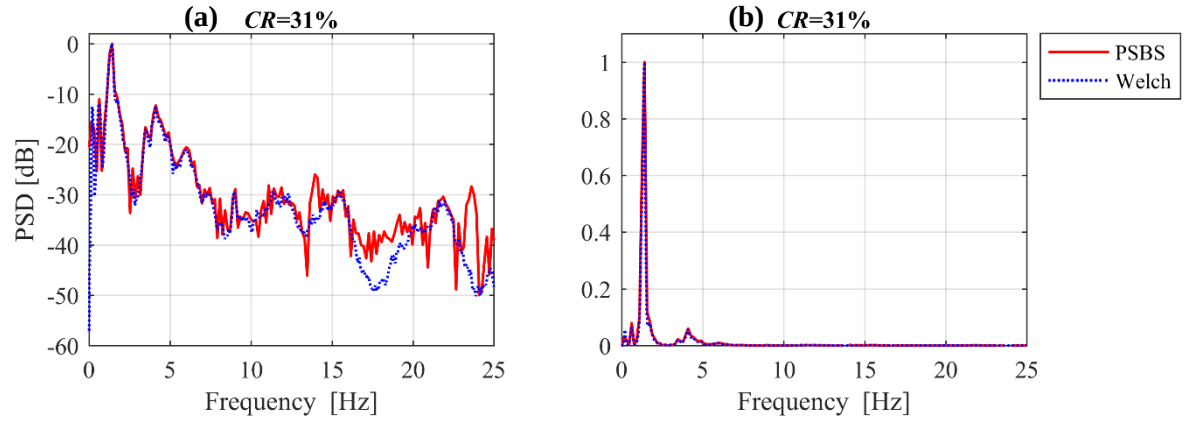

***Figure 5.20**: PSD estimates: Welch periodogram at Nyquist rate compared with PSBS approach for CR=31% ($\bar{M}$=5, $\bar{N}$=16) in (a) logarithmic scale, and (b) linear scale*

To quantify the level of accuracy of the proposed PSBS approach in the single-sensor case, Table 5-4 reports the location of the retrieved spectral peaks at *CR*={11%, 21%, 31%}, corresponding to the resonant frequencies of the considered wind turbine at the *R* excited modes of vibration.

The percentage difference error

$$\frac{df_r}{f_r} = \frac{\left|\hat{f}_{r,PSBS} - f_{r,Welch}\right|}{f_{r,Welch}} \tag{5.7}$$

is further used to measure the quality of the natural frequency estimates extracted from the PSBS approach, $\hat{f}_{r,PSBS}$, and the Welch conventional spectral estimation approach, $f_{r,Welch}$, at the *r-th* mode of vibration (where *r*=1,2,…,*R*). Overall, it can be easily noticed that the PSBS approach can accurately retrieve the 3rd natural frequency that attains the maximum spectral peak (see also Figure 5.18-Figure 5.20), yielding small percentage errors, below 1%, in all considered *CR*s. Table 5-4 further confirms that the accuracy of the proposed method is adversely affected in cases

of inadequately excited modes of vibration, which is inherently a challenging task. For example, it is shown that the 4th natural frequency cannot be detected at *CR*=21%, while the estimation of the 1st natural frequency observes large percentage errors, yielding less accurate results at lower *CRs*.

Table 5-4: Natural frequency estimates and percentage difference errors for the PSBS approach at CR={11%, 21%, 31%} and the standard welch modified periodogram applied on the full-length signal (non-compressed data with CR=100%)

	Non-compressed Welch	**PSBS**		
	***CR*=100%**	***CR*=31%**	***CR*=21%**	***CR*=11%**
f_1 [Hz]	0.195	0.159	0.156	0.285
(df_1/ f_1 [%])		(18.7%)	(20.1%)	(45.9%)
f_2 [Hz]	0.635	0.635	0.624	0.570
(df_2/ f_2 [%])		(0.0%)	(1.7%)	(10.2%)
f_3 [Hz]	1.416	1.429	1.404	1.425
(df_3/ f_3 [%])		(0.9%)	(0.8%)	(0.6%)
f_4 [Hz]	3.516	3.492	-	3.561
(df_4/ f_4 [%])		(0.7%)	-	(1.3%)
f_5 [Hz]	4.102	4.127	4.056	4.131
(df_5/ f_5 [%])		(0.6%)	(1.1%)	(0.7%)

5.4. PSBS-based OMA with Computer-Generated Closely Spaced Modes of Vibration (Multi-Sensor Case)

Having established the limits of accuracy of the PSBS approach in §4 for the single-sensor case, and verified its auto-spectral recovery performance with field-recorded data from an actual monitoring campaign, the focus is next placed on the numerical evaluation of the multi-sensor PSBS approach for cross-spectral recovery and mode shape estimation in structural systems susceptible to the modal coupling effect.

5.4.1. Structural system

Computer-simulated acceleration response data are obtained from the space truss in Figure 5.21, in which the first two modes of vibration along the vertical direction are closely spaced. Specifically, the 8-bay simply supported aluminium space truss of Figure 5.21 is simulated in a commercially available finite element (FE) software using 100 linear one-dimensional truss

elements with circular hollow cross-sections. Each bay is a cube with 707mm long side and the horizontal members in the x-y plane have 22mm diameter and 1mm wall thickness, while the vertical members in the x-z planes are 30mm in diameter and 1.5mm wall thickness. The diagonal members in the y-z plane have been purposely omitted to derive a structural system susceptible to modal coupling. Gravitational masses of 0.44kg are lumped at each of the 36 nodes of the FE model. Additional gravitational masses of 1.75kg are assigned to nodes 1,7,30, and 34, and of 2.75kg are assigned to nodes 20,26, and 32.

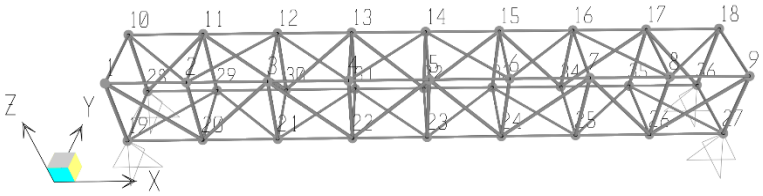

Figure 5.21: *Considered space truss model*

The considered space truss is assumed to be instrumented with an array of D=18 wireless sensors placed at nodes 1-18 in Figure 5.21, measuring vertical acceleration responses under ambient dynamic loading. The latter is approximated with a band-limited low-amplitude Gaussian white noise force of 4s duration and a time discretisation step equal to 0.001s, applied at the base of the structure along the z-axis. The considered excitation attains the power spectrum shown in Figure 5.22(a), which approximates the unit amplitude sufficiently well for the frequency range up to 500Hz. The adopted input force excites the first three bending modes of the vibrating space truss along the vertical direction, as confirmed in Figure 5.22(b), which plots together the PSD estimates of the acceleration responses measured at nodes #5 and #14 of the truss model in Figure 5.21. Assuming a critical damping ratio of 1% for all modes of vibration, linear response history analysis is conducted, generating D=18 vertical acceleration response signals, $x^d[n]$ $\left(d=\{1,2,\ldots,18\}\right)$, each consisting of 4000 uniform samples at Nyquist rate.

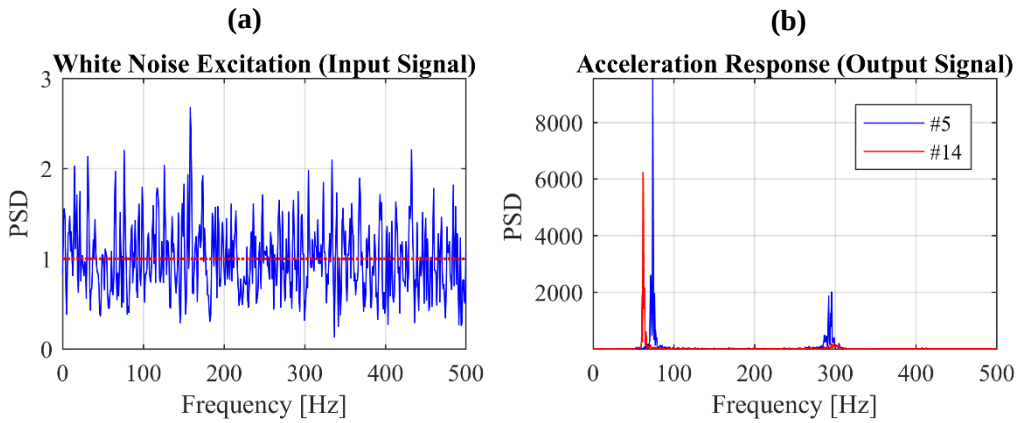

Figure 5.22*: Input/ output PSD estimates for the space truss in Figure 5.21; (a) input/white noise excitation signal; (b) output/acceleration responses measured at nodes #5 (blue curve) and #14 (red curve), respectively.*

5.4.2. Multi-sensor PSBS-based FDD application and assessment

The 18 generated acceleration responses are next sub-Nyquist sampled at three different *CRs* of approximately 31%, 21% and 11% (*i.e.*, 69%, 79% and 89% fewer samples compared to the uniformly-sampled full-length signals) using the deterministic multi-coset sampling scheme detailed in §4.2. These three different signal compression levels are achieved using the pertinent pair of $(\bar{M},\bar{N})$ values, the sampling pattern sequences, **s**, and the application-dependent parameters reported in Table 5-5.

Following the mathematical details in Chapter 4, each Nyquist-sampled acceleration response signal (of N=4000 samples) is divided in K=250 blocks of length $\bar{N}$ =16. Then, from each block, only $\bar{M}$ =5 samples are selected, resulting in the acquisition of M=1250 samples per recording location. The acquired compressed measurements from the whole array of 18 sensors are collectively processed to obtain an estimate of the output cross-correlation matrix $\hat{\mathbf{r}}_{y^a y^b} \in \mathbb{R}^{1025\times 18}$ in eq.(4.14), based on eq.(4.8) and the unbiased estimator $\hat{r}_{y_i^a,y_j^b}[\ell]$ in eq.(4.22). The latter is computed for $\ell \in [-20,20]$ (*i.e.*, L=20), which enables the recovery of the unknown power spectra with a frequency resolution at $\Delta\omega = 9.58\cdot 10^{-3}$ rad/s (or $\Delta f = 1.52\cdot 10^{-3}$ Hz) (see also eq.(4.21)). The power spectral matrix $\hat{\mathbf{G}}_{x^a x^b} \in \mathbb{C}^{656\times 18}$ is finally obtained by solving the weighted least square criterion in eq. (4.26) using the pattern correlation matrix $\mathbf{R}_c \in \mathbb{R}^{1025\times 656}$ in eq.(4.16) along with the DFT matrix $\mathbf{F}_{(2L+1)N} \in \mathbb{C}^{656\times 656}$.

The above procedure also holds for the two other cases with *CR*=21% and *CR*=11%, pertaining to sampling parameters in Table 5-5, which have been defined in a similar manner as above. Note that the value of L is judicially selected such that approximately the same frequency resolution, $\Delta\omega$, is achieved in the recovered power spectral matrices for all considered cases.

Table 5-5: Multi-coset pair ($\bar{M}$, $\bar{N}$) and pattern sampling sequence

Compression Ratio	***CR***	**31%**	**21%**	**11%**
Number of channels per sensor	$\bar{M}$	5	8	14
Down-sampling	$\bar{N}$	16	39	128
Sampling pattern	**s**	$[0,1,2,5,8]^T$	$[0,1,3,7,9,14,18,19]^T$	$[0,1,2,6,8,20,29,38,47,50,53,60,63,64]^T$
Number of blocks	K	250	102	31
Design parameter	L	20	8	2
Correlation support	$\bar{N}(2L+1)$	656	663	640
Frequency resolution	$\Delta\omega$ [rad/s]	$9.58\ 10^{-3}$	$9.48\ 10^{-3}$	$9.82\ 10^{-3}$
Nyquist sampled signals	N	4000	4000	4000
Sub-Nyquist sampled signals	M	1250	816	432

5.4.3. Modal results

For the three considered *CR* cases in Table 5-5, the standard FDD algorithm (see also *Brincker & Ventura* (2015)) is further employed to "decompose" the recovered power spectral matrix $\hat{\mathbf{G}}_{x^a x^b}$ to its singular values, $\mathbf{\Sigma}$, and singular vectors, $\mathbf{U}$, as in eq.(4.42), and extract the truss modal properties (*i.e.*, natural frequencies, $\hat{f}_r$ in Hz, and mode shapes, $\hat{\boldsymbol{\varphi}}_r$). The first singular values vectors obtained from the proposed PSBS-based FDD at *CR*={11%, 21%, 31%} are normalised to unit amplitude and plotted in Figure 5.23 within the frequency range of [0,500] Hz, in which the first three resonant frequencies of the truss in Figure 5.21 lie. For comparison, Figure 5.23 presents further the pertinent singular values vector derived the traditional FDD method at Nyquist rate (*i.e.*, at *CR*=100%). For this case, the standard Welch modified periodogram is applied to the full-length dataset of 4000 samples per signal, to estimate the response spectrum matrix, assuming that each acceleration response is divided in eight overlapping segments of 50% overlap and windowed with a Hanning function.

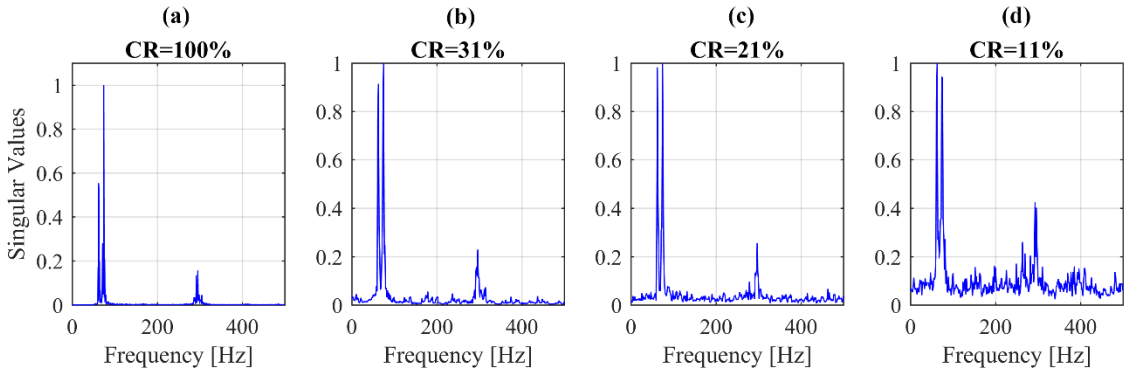

Figure 5.23: *First singular values vector of the space truss response spectrum matrix in eq. (4.26) for CR={100%, 31%, 21%, 11%}*

Notably, the first two resonances exhibit a percentage difference of approximately 15%, being clustered together in a relatively narrow frequency-band which pertains to just the 3% of the considered frequency range. It is further shown that the 3rd resonance observes a relatively low amplitude in the first singular values plot of Figure 5.23, confirming the poor/insufficient excitation of the 3rd vibrating mode of the white-noise excited FE model in Figure 5.21. Table 5-6 presents the natural frequencies extracted from the proposed multi-sensor PSBS-based FDD approach for the three adopted *CRs* (*i.e.*, 31%, 21%, and 11%), which are compared against the pertinent values obtained from the conventional FDD at Nyquist rate (*i.e.*, *CR*=100%). The accuracy of the extracted resonances is further assessed with the difference percentage error, df_r/f_r (r=1,2,3), computed between the frequency estimates at Nyquist (*i.e.*, conventional FDD) and sub-Nyquist rates (*i.e.*, PSBS-based FDD), and reported in Table 5-6. It is shown that small percentage errors are retrieved, delimited between the range of [-0.68, +1.74] %, confirming that the proposed multi-sensor PSBS method can efficiently detect the two closely-spaced natural frequencies at all considered *CRs*.

Table 5-6: Natural Frequency Estimates

	Conventional FDD at Nyquist	**PSBS-based FDD**		
	***CR*=100%**	***CR*=31%**	***CR*=21%**	***CR*=11%**
f_1 [Hz]	62.012	62.691	62.121	62.696
(df_1/f_1 [%])	-	(0.67 %)	(-0.25 %)	(-0.68 %)
f_2 [Hz]	73.643	74.924	74.242	73.668
(df_2/f_2 [%])	-	(1.74 %)	(0.81 %)	(0.03 %)
f_3 [Hz]	294.551	296.636	296.970	293.103
(df_3/f_3 [%])	-	(0.71 %)	(0.82 %)	(-0.49 %)

In all cases considered, the modal deflected shapes of the truss in Figure 5.21 are further extracted from the left singular vector **U** of the decomposed power spectral matrix $\hat{\mathbf{G}}_{x^a x^b}$ and the obtained estimates are illustrated in Figure 5.24 - Figure 5.26 for the three excited vibrating modes, respectively. In each figure, the panel (a) shows the mode shape vector extracted from the conventional FDD at Nyquist rate, while the panel (b) presents the pertinent vector retrieved from the multi-sensor PSBS-based FDD at the extreme sub-Nyquist case with *CR*=11%. The undeformed shape of the truss (grey grid) is also plotted in these figures to facilitate comparison.

The accuracy of the proposed PSBS-based FDD approach in extracting quality estimates of the truss mode shapes is assessed with the Modal Assurance Criterion (MAC) (*e.g.*, *Brincker & Ventura* (2015)). In this respect, Figure 5.24(c) - Figure 5.26(c) plot the MAC values in eq.(4.43) as a function of the three adopted *CRs* at 31%, 21%, and 11%, respectively. As expected, MAC values increase with *CR*, suggesting higher accuracy in the extracted mode shapes as more data samples are acquired. Nonetheless, the observed MAC values are above 0.9 in all cases considered, even for *CR*=11% and the acquisition of 89% fewer measurements compared to conventional approaches at Nyquist rate. More importantly, Figure 5.24 and Figure 5.25 prove the efficacy of the proposed method in separating the two closely-spaced modes of vibration regardless of the signal compression level. Finally, Figure 5.26 reveals the multi-sensor PSBS-based FDD approach can efficiently detect the less excited 3rd mode of vibration, yielding MAC values well above threshold of 0.9.

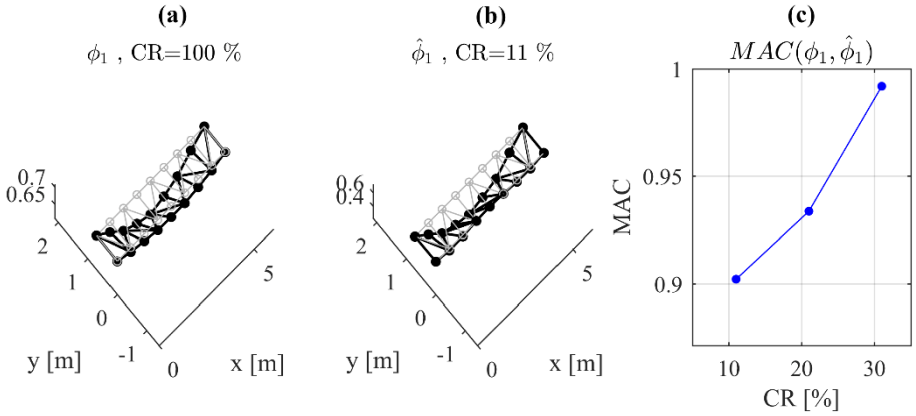

Figure 5.24: *Estimation of the 1st bending mode shape of the space truss; (a) conventional FDD at CR=100%; (b) PSBS-based FDD at* CR*=11%; and (c) MAC values versus CR*

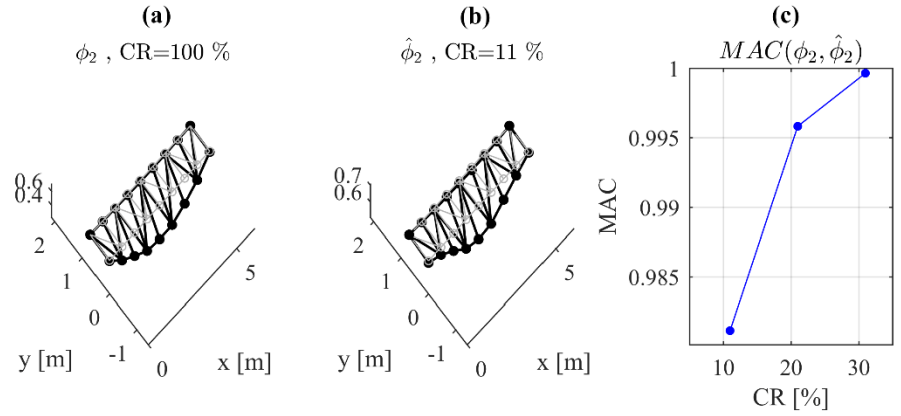

Figure 5.25: *Estimation of the 2nd bending mode shape of the space truss; (a) conventional FDD at CR=100%; (b) PSBS-based FDD at* CR*=11%; and (c) MAC values versus CR*

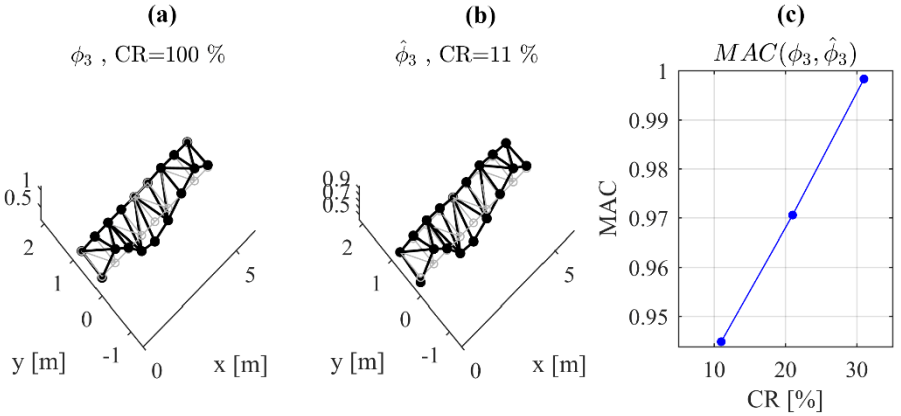

Figure 5.26: *Estimation of the 3rd bending mode shape of the space truss; (a) conventional FDD at CR=100%; (b) PSBS-based FDD at* CR*=11%; and (c) MAC values versus CR*

5.5. PSBS-based Structural Damage Detection Using the Modal Strain Energy Index (Multi-Sensor Case)

In the previous numerical example, it was shown that the developed PSBS approach is strictly a spectral estimation method, capable to extract structural modal properties directly from the acquired compressed data, yielding computationally efficient OMA. By adopting a damage-sensitive index that measures changes in modal quantities, the efficacy of the proposed PSBS-based approach in detecting structural damage without retrieving the time-domain signal information is numerically assessed herein.

5.5.1. Structural systems and PSBS-based OMA application

To this end, computer-simulated acceleration data are obtained from finite element (FE) models of a simply supported IPE300-profiled steel beam at one healthy (*DS*0) and three different damage states (*DS*1- *DS*3). The considered beam, shown in Figure 5.27, has length λ=5m and

flexural rigidity $\mathcal{E}I$=16.78·10^3 kNm^2 (*i.e.*, elastic modulus $\mathcal{E}$=210 GPa, moment of inertia around the z-axis I=7.99·10^{-5} m^4). It is modelled in the commercial FE software SAP2000 using 100 Euler-Bernoulli beam elements of equal length with mass lumped at the nodes of the FE grid acting along the gravitational z-axis. It is assumed that the beam is instrumented with an array of 15 sensors distributed along the beam's length with locations marked by an "x" in Figure 5.27 and Figure 5.28. Three structural damage states of increasing severity are defined by locally reducing the stiffness of certain beam elements close to the mid-span. As illustrated in Figure 5.28, the 1st damage state (*DS1*) is associated with 50% local stiffness reduction within a 0.1m width, the 2nd damage state (*DS2*) pertains to 50% reduced stiffness within a 0.2m width, and the 3rd damage state (*DS3)* yields 80% local stiffness reduction within a 0.2m width.

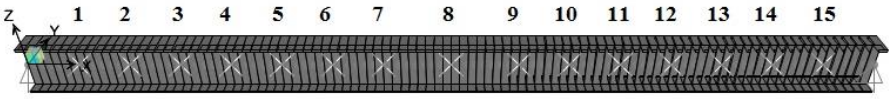

Figure 5.27: *Simply supported steel beam instrumented with 15 sampling devices measuring vertical acceleration response signals.*

Linear response history analysis is undertaken for the FE models in Figure 5.28 (*i.e.*, for *DS0* – *DS*3), subjected to a low-amplitude bandlimited Gaussian white noise base-excitation acting along the gravitational axis. The adopted excitation is observed for 4s with a time discretisation step at 0.0005s, corresponding to a Nyquist frequency of 1000Hz. A critical damping ratio of 1% for all modes of vibration is assumed in the analysis, and the vertical acceleration response signals are recorded at a sampling rate of 2000Hz (*i.e.*, 8000 "Nyquist measurements" per signal) at the 15 points of the FE grid where the sampling devices of the considered array of sensors are deployed. The considered excitation is assumed to simulate ambient noise input under operational conditions. It excites the first three bending modes of vibration along the gravitational direction of the different states of the simply supported beam. Consequently, the obtained response acceleration signals are treated as typical noise-free vibration/acceleration data for OMA.

Next, the above signals are contaminated with additive Gaussian white noise at 3 different signal-to-noise ratios (*SNRs*): 10^{20}dB (*i.e.*, practically noise-free case), 20dB, and 10dB (extreme noise case). The noisy acceleration response signals $x^a[n]$, $x^b[n]$, (a, b=1, 2, …, 15), are multi-coset sampled, assumed to have the same specifications for all D=15 wireless sensors: number of channels $\bar{M}$ =5 and down-sampling parameter $\bar{N}$=16, achieving a compression ratio of $CR \simeq$ 31%. The adopted sampling pattern is given by the sequence $\mathbf{s}$=[0, 1, 2, 5, 8]^T. In this respect, every single channel of each sensor measures only K=500 compressed data in $y_i^a[k]$, $y_j^b[k]$ (k = {0, 1, …, K-1}, i, j = {0,1,…, $\bar{M}-1$}) out of the 8000 Nyquist samples per signal (*i.e.*, 2500 sub-

Nyquist samples are acquired per sensor). By collectively processing the compressed data from all sensors, the unbiased estimator $\hat{r}_{y_i^a,y_j^b}[\ell]$ in eq.(4.22) is computed in the range of $-L \le \ell \le L$, assuming an L value equal to 20. An estimate of the cross-spectrum matrix, $\hat{\mathbf{G}}_{x^a x^b}$, is obtained for all considered structural states (*DS0-DS3*) at a frequency resolution of $\Delta\omega = 9.58 \cdot 10^{-3}$ rad/s (see also eqs. (4.26) and (4.21)).

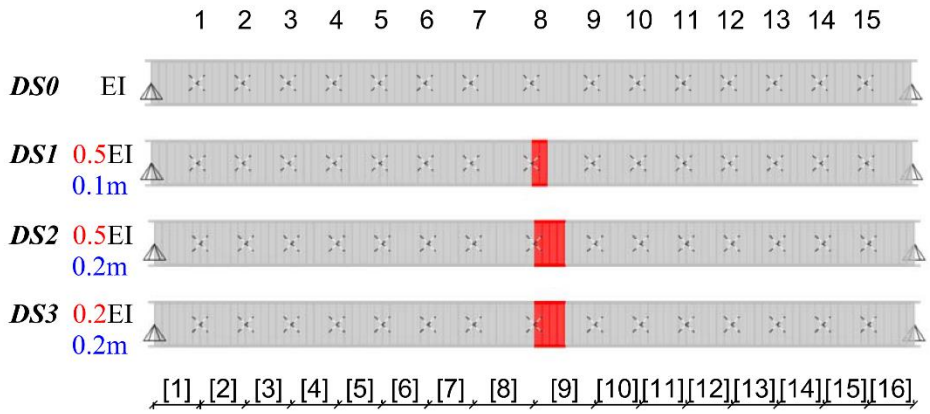

Figure 5.28: *Damage states;* DS0*: intact/healthy structure;* DS1*: 50% stiffness reduction over 0.1m beam length;* DS2*: 50% stiffness reduction over 0.2m beam length;* DS3*: 80% stiffness reduction over 0.2m beam length*

5.5.2. OMA results

The FDD algorithm (§4.6) is then applied to the recovered cross-spectrum matrix, $\hat{\mathbf{G}}_{x^a x^b}$, to extract the modal properties of the FE models in Figure 5.28 (at *DS0-DS3)* for the three adopted *SNRs* at 10^{20}dB, 20dB, and 10dB. Eq. (4.42) returns the singular values, $\mathbf{\Sigma}$, and singular vectors, $\mathbf{U}$, of the "decomposed" matrix $\hat{\mathbf{G}}_{x^a x^b}$, carrying the structural modal information at the excited modes of vibration. For all considered structural states of the adopted beam, the first three natural frequencies (f_1 to f_3) retrieved from the largest singular values in eq.(4.42) are reported in Table 5-7 and Table 5-8 for the noiseless (*SNR*=10^{20}dB) and extreme noisy (*SNR*=10dB) cases, respectively. In both tables, estimates of the natural frequencies obtained from the Nyquist measurements using conventional cross-spectral estimation and the FDD algorithm are also reported.

Table 5-7: Nyquist FDD versus PSBS-based FDD for natural frequency estimation at *DS0-DS3* for *SNR*=10^{20}dB

	f_1 [Hz]		f_2 [Hz]		f_3 [Hz]	
	Nyquist FDD (8000 samples)	*PSBS-based FDD (2500 samples)*	*Nyquist FDD (8000 samples)*	*PSBS-based FDD (2500 samples)*	*Nyquist FDD (8000 samples)*	*PSBS-based FDD (2500 samples)*
DS0	40.04	39.76	310.55	311.93	717.77	718.65
DS1	39.06	39.76	310.55	311.93	716.80	712.54
DS2	38.09	39.76	302.73	305.81	704.10	712.54
DS3	35.16	33.64	288.09	287.46	676.76	678.90

Table 5-8: Nyquist FDD versus PSBS-based FDD for natural frequency estimation at *DS0-DS3* for *SNR*=10dB

	f_1 [Hz]		f_2 [Hz]		f_3 [Hz]	
	Nyquist FDD (8000 samples)	*PSBS-based FDD (2500 samples)*	*Nyquist FDD (8000 samples)*	*PSBS-based FDD (2500 samples)*	*Nyquist FDD (8000 samples)*	*PSBS-based FDD (2500 samples)*
DS0	40.04	39.76	310.55	311.93	717.77	718.65
DS1	39.06	39.76	310.55	311.93	704.10	712.54
DS2	38.09	39.76	302.73	305.81	704.10	712.54
DS3	35.16	33.64	288.09	287.46	676.76	678.90

It is seen in the above tables that the noise level does not significantly affect the natural frequency estimation in this numerical example. More importantly, the estimated natural frequencies extracted directly from the sub-Nyquist measurements by means of the proposed OMA approach lie very close to the estimates obtained from the Nyquist measurements (maximum observed error is 4.4%). As expected, the value of the natural frequencies decreases with increasing damage severity, with the higher modes of vibration being more sensitive to such changes.

To visualise the changes to the modal deflected shapes due to localised structural damage, Figure 5.29 illustrates the first three vertical mode shapes of the beam at *DS*0-*DS*3, retrieved from the left singular vector **U** of the recovered cross-spectrum matrix, $\hat{\mathbf{G}}_{x^a x^b}$, for the noisy case at *SNR*=10dB. For the *DS*0, Figure 5.30 plots together the pertinent mode shapes derived from both the Nyquist FDD (8000 measurements/sensor) and PSBS-based FDD (2500 measurements/sensor) for *SNR*=10dB. It is readily observed that the estimated modes retrieved

from about 70% less measurements in the PSBS-based FDD approach are visually close to the estimated ones from the conventional FDD method at Nyquist rate.

To quantify the level of accuracy for the extracted mode shapes, the modal assurance criterion (*MAC*) in eq.(4.43) is considered. Table 5-9 and Table 5-10 report the MAC values computed for the first three modes of vibration for all structural states of the beam considered (*DS0-DS3*) and for *SNR*=10^{20} dB and *SNR*=10dB noise levels, respectively. Most of the MAC values in Table 5-9 and Table 5-10 are close to unity, demonstrating a high level of correlation between the estimated mode shapes $\hat{\boldsymbol{\varphi}}$ and $\boldsymbol{\varphi}$, confirming the good accuracy of the proposed PSBS-based OMA approach. In fact, MAC drops below 0.9 only in the case of the third mode shape of the *DS1*. Finally, a comparison between Table 5-9 and Table 5-10 confirms that the obtained mode shape estimates from sub-Nyquist measurements are not sensitive to additive Gaussian white noise.

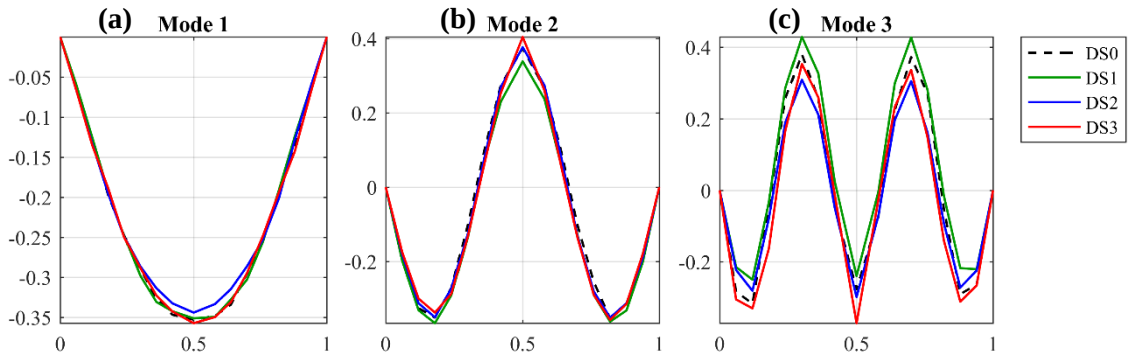

Figure 5.29: *PSBS-based FDD at CR=31% for mode shape estimation at DS0-DS3 for SNR=10dB (the horizontal axis gives the relative distance from the left support of the beam normalised with its length)*

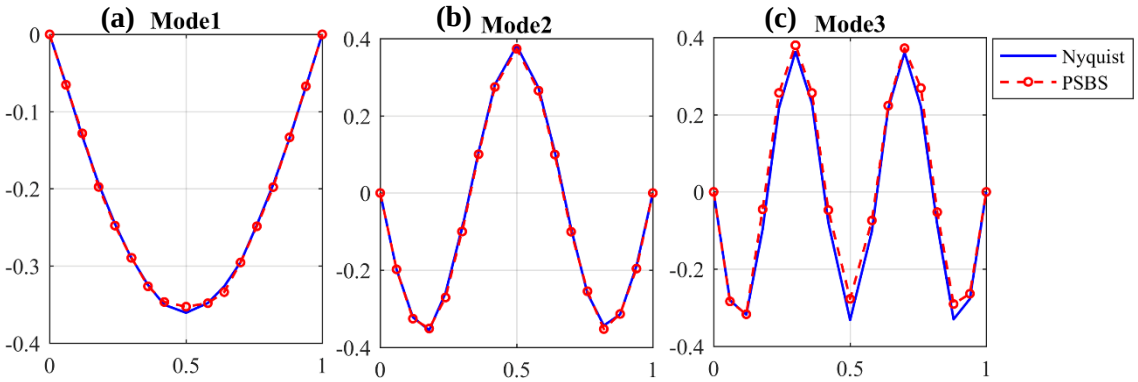

Figure 5.30: *Nyquist FDD versus PSBS-based FDD at CR=31% for mode shape estimation at DS0 for SNR=10dB (the horizontal axis gives the relative distance from the left support of the beam normalised with its length)*

Table 5-9: Modal Assurance Criterion (PSBS-based FDD versus Nyquist FDD) on the estimated mode shapes at *DS0-DS3* for $SNR=10^{20}$ dB

	MAC 1st mode	***MAC 2nd mode***	***MAC 3rd mode***
	PSBS/Nyquist	*PSBS/Nyquist*	*PSBS/Nyquist*
DS0	1.000	0.999	0.987
DS1	0.999	0.999	0.888
DS2	0.998	0.996	0.988
DS3	0.999	0.999	0.995

Table 5-10: Modal Assurance Criterion (PSBS-based FDD versus Nyquist FDD) on the estimated mode shapes at *DS0-DS3* for *SNR*=10 dB

	MAC 1st mode	***MAC 2nd mode***	***MAC 3rd mode***
	PSBS/Nyquist	*PSBS/Nyquist*	*PSBS/Nyquist*
DS0	1.000	0.999	0.984
DS1	0.999	0.999	0.852
DS2	0.997	0.995	0.990
DS3	0.999	0.999	0.991

5.5.3. PSBS-based modal strain energy index (MSEI) assessment & results

Upon retrieval of the structural mode shapes, a further step is herein pursued towards vibration-based structural health monitoring of civil engineering structures directly from sub-Nyquist/compressed acceleration measurements acquired under operational conditions. To this aim, the modal strain energy index (MSEI) (*e.g., Kim & Stubbs* (1995)) is adopted to achieve structural damage localisation by relying on the mode shapes of a reference (healthy) state and of a potentially damaged state of a given structure derived from sub-Nyquist acceleration data as discussed in the previous sub-section. Focusing on rigid-jointed frame structures, the computation of the MSEI requires the division of each structural member into Z number of segments along the local longitudinal axis u defined by the $[u_z, u_{z+1}]$ intervals with $z=1,2,\ldots,Z$ and $u_1=0$, $u_{Z+1}=\lambda$, with λ being the length of the structural member. Under the assumption that at the damaged state, damage is localised within a few segments and, therefore, (i) the flexural rigidity of structural members of the healthy structure $\mathcal{E}I$ is almost equal to the flexural rigidity of structural members of the damaged structure $\mathcal{E}I^*$, and (ii) the strain energy stored due to modal deformation for each mode shape is also equal between the healthy and the damaged states, the MSEI is defined by the ratio (see also *Kim & Stubbs* (1995); *Humar et al.* (2006))

$$\beta_z = \frac{1+\sum_{r=1}^{R}\left[\int_{u_z}^{u_{z+1}}\left(\frac{\partial^2 \boldsymbol{\varphi}_r^*}{\partial u^2}\right)^2 du \Big/ \int_0^{\lambda}\left(\frac{\partial^2 \boldsymbol{\varphi}_r^*}{\partial u^2}\right)^2 du\right]}{1+\sum_{r=1}^{R}\left[\int_{u_z}^{u_{z+1}}\left(\frac{\partial^2 \boldsymbol{\varphi}_r}{\partial u^2}\right)^2 du \Big/ \int_0^{\lambda}\left(\frac{\partial^2 \boldsymbol{\varphi}_r}{\partial u^2}\right)^2 du\right]}. \tag{5.8}$$

The above index achieves damage localization by detecting local changes to the flexural rigidity within each segment between the healthy and the damaged states. The flexural rigidities are computed from the modal curvatures (*i.e.*, second derivative of the mode shapes) of the first R excited modes denoted by $\boldsymbol{\varphi}_r$ and $\boldsymbol{\varphi}^*_r$, r=1,2,…,R for the healthy and the damaged structure, respectively. Therefore, the MSEI quantifies potential local stiffness reduction inferring damage in small segments of structures based on the differences of the first R modal curvatures or, equivalently, mode shapes. In the ensuing numerical work, the following normalized version of the MSEI is reported

$$\bar{\beta}_z = \frac{\beta_z - \mu_\beta}{\sigma_\beta}, \tag{5.9}$$

where μ_β is the mean, and σ_β the standard deviation of the MSEI computed across all considered segments. The damage index in (5.9) yields positives values at the damaged locations of the considered structure and negative values elsewhere. Overall, the MSEI is suitable when only incomplete modal information is available (*e.g.* only few mode shapes are excited) *Kim & Stubbs* (1995), while there is no requirement on the normalisation (mass, displacement, etc.) of the considered mode shapes (*e.g.*, *Cornwell et al.* (1999)). Although it may overestimate damage severity (see also *Kim & Stubbs* (1995)), *Humar et al.* (2006) showed that it is a quite reliable damage index, especially in case of noisy data (see also *Alvandi & Cremona* (2006)).

The potential of using the MSEI for damage localisation from mode shapes estimated directly from sub-Nyquist measurements is numerically illustrated. The normalised damage index $\bar{\beta}_z$ in eq.(5.9) is computed from the estimated mode shapes, $\boldsymbol{\varphi}_{DS0}$,$\boldsymbol{\varphi}^*_{DS1}$, $\boldsymbol{\varphi}^*_{DS2}$, $\boldsymbol{\varphi}^*_{DS3}$ corresponding to the healthy (*DS0*) and damaged states (*DS1-DS3*) respectively, upon dividing the beam in Figure 5.27 in Z=16 segments. The second derivatives appearing in eq.(5.8) are numerically approximated with the standard finite difference method. The location of damage is inferred by the positive amplitudes of the normalised damage index $\bar{\beta}_z$ plotted in Figure 5.31, Figure 5.32, and Figure 5.33 for SNR=10^{20} dB, SNR=20dB and SNR=10dB, respectively obtained from both Nyquist measurements (panels (a)) and sub-Nyquist measurements (panels (b)). It is seen that for the *DS2* and *DS3* states, the MSEI computed from the sub-Nyquist measurements can unambiguously identify the damage location (mid-span) and even discern the damage severity for *SNR* as low as

10dB. In fact, the MSEI derived from sub-Nyquist measurements performs equally well with the MSEI from Nyquist measurements, although 70% fewer measurements are used in mode shape estimation. In the case of the least severe damaged state herein considered, *DS1*, the MSEI computed by the proposed approach performs relatively well in locating damage for the noise-less case. For noisy sub-Nyquist measurements, discriminating damage location becomes challenging (see also Figure 5.32(b)) for *SNR*=20dB and practically not possible for *SNR*= 10dB (*e.g.*, Figure 5.33(b)). Note, however, that this is pretty much the case for the MSEI obtained for Nyquist sampled measurements and, therefore, the fact that the MSEI cannot accurately and unambiguously locate the damage from noisy signals for the *DS1* case is a matter of the effectiveness of the particular damage index to locate relatively small and well-localised damage in noisy environments, rather than damage information loss due to sub-Nyquist signal sampling.

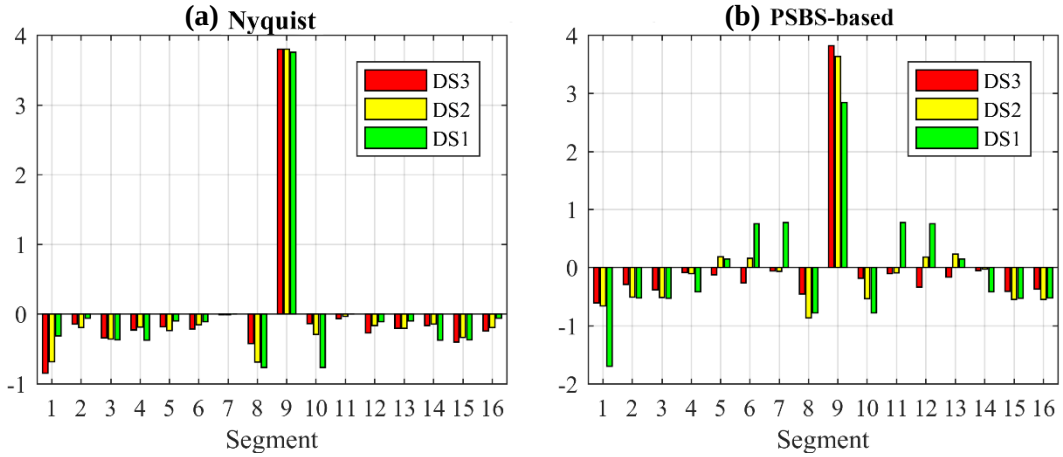

Figure 5.31: *(a) Nyquist and (b) PSBS-based normalised modal strain energy index for DS0-DS3 and* SNR=10^{20}*dB.*

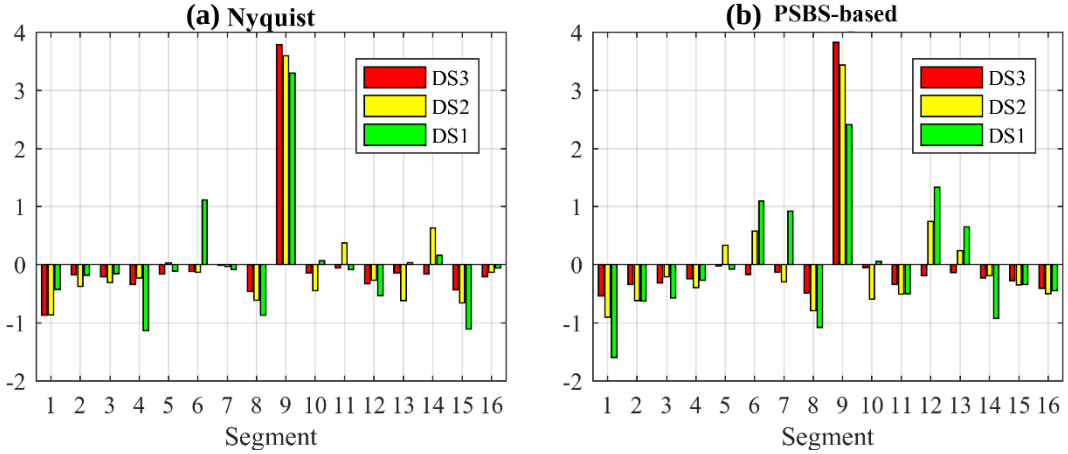

Figure 5.32: *(a) Nyquist and (b) PSBS-based normalised modal strain energy index for DS0-DS3 and SNR=20dB*

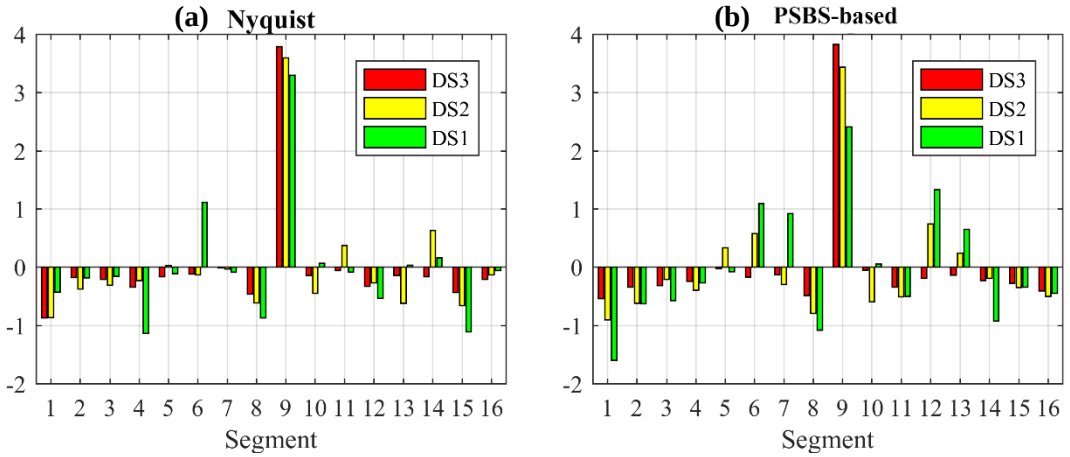

Figure 5.33: *(a) Nyquist and (b) PSBS-based normalised modal strain energy index for DS0-DS3 and SNR=10dB*

5.6. Concluding Remarks

This chapter presents four different applications aiming to assess the effectiveness of the proposed PSBS method in §4 for VSHM. Considering first the PSBS approach in the (simplified) single-sensor case, parametric analyses are performed in §5.2 using two different structural systems, aiming to: (1) define the required number of compressed measurements, *M*, for a faithful recovery of the second-order statistics of the unknown full-length response signals; and (2) examine the sensitivity of the developed method to measurement noise. The obtained results confirmed that the PSBS method can efficiently recover power spectral densities directly from sub-Nyquist-sampled acceleration data even in structural systems with closely-spaced modes of vibration. Further, it was demonstrated that the performance of PSBS method depends strongly on the acquired number of compressed measurements, *M*, which may differ in various applications, and it was proved to be practically insensitive to additive noise for *SNRs* as low as 10dB.

Considering next field-recorded data acquired from an operational wind turbine in Lübbenau, Germany, the recovery performance of the proposed PSBS approach was numerically evaluated in §5.3 at three different *CR* of 11%, 21% and 31%. The developed method was proved capable to retrieve quality auto-spectral density estimates within the frequency range of interest, even for the lowest adopted *CR* value at 11% (*i.e.*, 89% fewer data compared to conventional sampling schemes), but it was shown to be adversely affected in cases of poorly excited modes of vibration.

Using the same three *CR* values as above (i.e., *CR*={11%, 21%, 31%}), the OMA capabilities of the proposed multi-sensor PSBS method was numerically assessed in §5.4. Based on cross-spectral matrices recovered directly from compressed measurements, the standard FDD algorithm was employed to extract the underlying modal properties (natural frequencies, mode shapes) of a FE truss model with 2 closely-spaced modes of vibration. The reported numerical results

confirmed the efficacy of the proposed approach in accurately identifying the closely-spaced mode shapes in all considered *CRs*, yielding MAC values well-above 0.9 and natural frequency estimates with very small percentage errors delimited in range [-0.68, +1.74] %. Finally, the damage detection capabilities of the PSBS approach in chapter §4 were numerically verified in §5.5 by adopting the well-established modal strain energy index (MSEI). The latter was applied to mode shapes derived from approximately 70% fewer measurements, achieving equal level/quality of damage localisation compared to conventional sampling schemes at Nyquist rate for all damaged states and *SNRs* considered.

Overall, the numerical results demonstrate that the proposed multi-sensor PSBS technique coupled with standard OMA and damage detection approaches can achieve effective VSHM in noisy environments from significantly fewer acceleration measurements, without returning the monitored signals deterministically in time domain.

Chapter 6
Assessment of the Proposed PSBS Approach vis-à-vis CS-Based Approach for OMA

6.1. Preliminary Remarks

In this chapter, the effectiveness of the proposed Power Spectrum Blind Sampling (PSBS) method in Chapter 4 (§*4. Proposed Multi-Sensor Power Spectrum Blind Sampling Approach for OMA: Theory*), is numerically assessed vis-à-vis the Compressive Sensing (CS) based approach developed by *O'Connor et al.* (2014) and detailed in Chapter 2 (§*2. Compressive Sensing: Basic Concepts & Applications in VSHM*) for Operational Modal Analysis (OMA) in vibrating structures under operational conditions. Recalling from the pertinent chapters that the two considered approaches rely on different low-rate (sub-Nyquist) non-uniform in time sampling schemes, and the main aim of the comparison is to appraise, for the first time in the literature, the potential advantages of using deterministic multi-coset sampling vis-à-vis random CS-based sampling in undertaking OMA.

The above aim is facilitated by the fact that both approaches utilise the same frequency-domain OMA algorithm (*i.e.*, FDD). Therefore, any differences to the quality of mode shapes achieved by the competing methods can be attributed to the different low-rate sampling schemes, and to the limitations posed by the associated post-processing methods applied on the compressed measurements, rather than to the adopted OMA algorithm. Furthermore, the fairness of the comparison in relation to up-front and/or operational monitoring costs is safeguarded by the fact that neither of the approaches consider on-sensor data processing before transmission, while no prior knowledge on the properties (*i.e.*, the sparsity) of the acquired signals is assumed available. The latter would theoretically benefit the CS-based approach but would require either the use of an additional complementary network of wired sensors (*e.g.*, *Klis & Chatzi* (2015)) incurring additional monitoring costs, or increased energy demands due to fast (conventional) uniform-in-time sampling and heavy data post-processing on the wireless sensors (*e.g.*, *Bao et al.* (2013); *Zou et al.* (2015); *Huang et al.* (2016); *Klis & Chatzi* (2017)). Instead, this study assumes the availability of sensors that acquire and transmit signals directly in the compressed domain supporting low-power WNSs. It is expected that the gains achieved by sub-Nyquist spectral

estimation approaches would reflect analogously to energy savings in WSNs, mainly due to reduced sampling requirements and wireless transmission payloads compared to conventional approaches at Nyquist sampling rates or above. Thus, it was deemed essential to provide estimates for the anticipated energy savings achieved by the proposed approach in Chapter 4 (§*4. Proposed Multi-Sensor Power Spectrum Blind Sampling Approach for OMA: Theory*), assuming that a battery-operated wireless multi-coset sampler is available.

The above comparative assessment is numerically undertaken in section 6.3 (§*6.3. Numerical Assessment for Simulated Signals of Different Sparsity Level*) and section 6.4 (§*6.4. Numerical Assessment for Field-Recorded Signals*), using two different sets of acceleration response signals sub-sampled at compression rates between 11% and 31%. Specifically, the first numerical example in section 6.3 relies on computer-generated response acceleration signals corrupted by additive Gaussian white noise, yielding different sparsity levels on the DFT domain. The second comparative numerical evaluation in section 6.4 employs field-recorded response acceleration time-histories from an overpass in Zürich, Switzerland monitored under operational conditions *Chatzi E.N. & Spiridonakos M.D.* (2015); *Spiridonakos et al.* (2016). The daily energy requirements of this bridge monitoring system are further presented in section 6.5 (§*6.5. Energy Consumption and Battery Life Savings*), showcasing the benefits of the proposed PSBS approach at *CR*={11%, 21%, 31%} over conventional approaches at uniform sampling rates. Finally, section 6.6 (§*6.6. Concluding Remarks*) summarised concluding remarks.

The comparative numerical results of sections 6.3 and 6.4 have been published in [J2], while the energy estimates presented in section 6.5 have been submitted for publication in [J3] (see also list of publications in section 1.5 (§1.5. List of Referred Papers)).

6.2. Overview of the Comparative Approaches for Frequency Domain OMA Using Sub-Nyquist Sampled Measurements

A comprehensive overview of the two considered sub-Nyquist spectral estimation approaches is provided in Figure 6.1 by illustrating in parallel the pertinent flowcharts that consist of three distinct stages (I to III).

The left flowchart of Figure 6.1 depicts the CS-based OMA approach proposed by *O'Connor et al.* (2014), in which CS-based data sampling and sparse recovery steps are applied to an array of D identical CS-based sensors. In particular, Stage I involves random non-uniform in time sampling of D structural acceleration response signals, $x^d[n]$, $d=\{1,2,\ldots,D\}$, that attain some level of sparsity on the DFT basis (see also Chapter §2). The acquired compressed measurements $y^d[m]$ are wirelessly transmitted to a server, where they are treated (stage II) by the CoSaMP sparse signal recovery algorithm developed by *Needell & Tropp* (2009), to derive D estimates of the S_T-sparse DFT coefficients, $\hat{u}^d[n]$, of the response acceleration signals on the uniform Nyquist grid.

This is a computationally demanding step relying on a heuristically defined target sparsity level, S_T, in the reconstructed signals. In stage III, the estimated S_T DFT coefficients from all sensors are used to construct the response acceleration power spectral density (PSD) matrix (*e.g.*, *Marple* (1987)). Lastly, the PSD matrix is fed to the FDD algorithm to estimate the structural modal properties (natural frequencies and mode shapes).

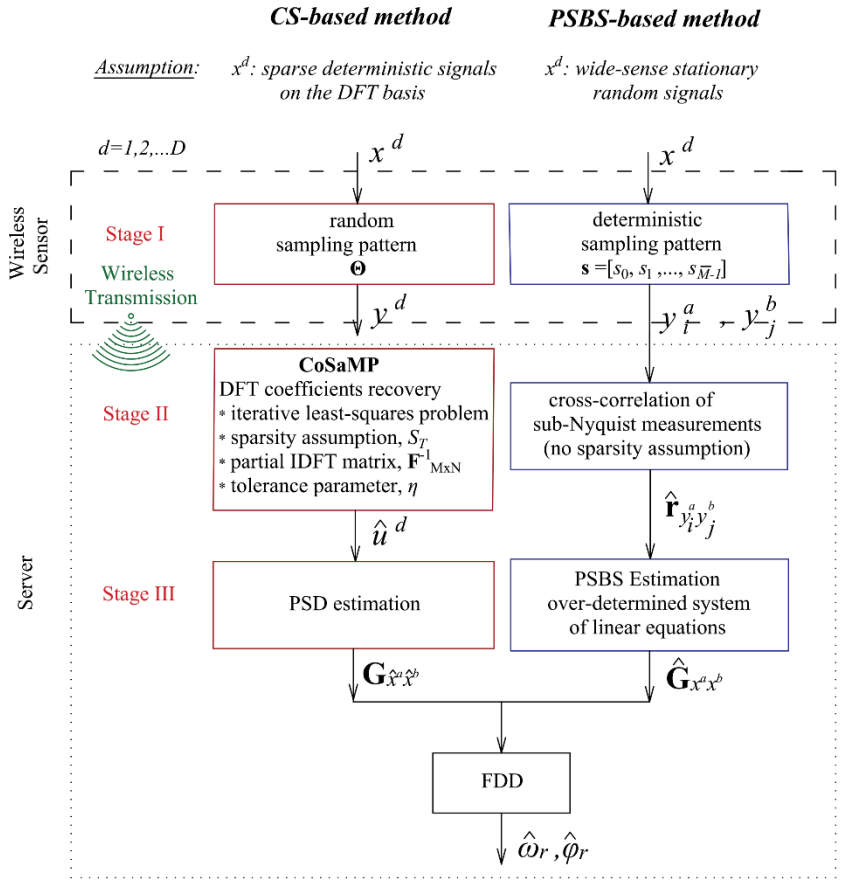

Figure 6.1: *Flowcharts of the two different sub-Nyquist sampling and spectral estimation approaches under comparison for frequency domain OMA*

The right flowchart of Figure 6.1 presents the proposed PSBS-based FDD method detailed in chapter §4 that comprises one of the major contributions of this PhD thesis. This alternative OMA approach supports sub-Nyquist data acquisition rates, without imposing any sparsity conditions to the acquired signals (*i.e.*, is signal agnostic). Similar to the approaches of *O'Connor et al.* (2014) and *Park et al.* (2014), the considered PSBS approach derives directly the mode shapes in the frequency domain and, therefore, bypasses the need to retrieve the time-histories of the acquired signals. Further, it treats the structural response acceleration signals as wide-sense stationary random processes, in alignment with the theory of OMA. Specifically, the adopted PSBS approach comprises three stages delineated in the right flowchart of Figure 6.1. The first stage involves a low-rate (sub-Nyquist) deterministic periodic non-uniform-in-time multi-coset sampling scheme developed by *Tausiesakul & Gonzalez-Prelcic* (2013). In the next stage, the

acquired compressed measurements from all sensor nodes of the WSN are wirelessly transmitted to the server and collectively processed to obtain their cross-correlation vectors. The latter vectors are used in Stage III to estimate the response acceleration PSD matrix by solving an overdetermined system of linear equations without invoking any signal sparsity assumption (see also *Arianandа & Leus* (2012); *Tausiesakul & Gonzalez-Prelcic* (2013)). Lastly, the FDD algorithm is used to obtain natural frequencies and mode shapes.

The performance of the two comparative methods is quantified in terms of the modal assurance criterion (MAC) (*e.g.*, *Brincker & Ventura* (2015)) of mode shapes derived from a fixed number of compressed measurements. Focus is given on quantifying the sparsity requirements of the CS-based approach and on numerically verifying that the accuracy of the PSBS-based approach is insensitive to signal sparsity. Emphasis is also placed on the level of signal compression that can be reached by the different compressive sampling schemes utilised in the two approaches, while achieving accurate mode shapes with MAC>0.9.

6.3. Numerical Assessment for Simulated Signals of Different Sparsity Level

6.3.1. Computer-simulated acceleration response signals

In this section, the effectiveness of the two sub-Nyquist spectral estimation approaches in Figure 6.1 for OMA is assessed by considering simulated noisy structural acceleration response signals obtained from the finite element (FE) model in Figure 5.27 (*i.e.*, the IPE300-profiled simply supported steel beam at healthy state, DS0). As detailed in §5.5.1, the adopted structure is assumed to be instrumented with a dense array of D=15 sensors measuring vertical accelerations along its length.

Following the same analyses steps as in §5.5.1, the considered FE model is base-excited by a band-limited low-amplitude Gaussian white noise force, observing a sufficiently flat spectrum in the frequency range up to 1000Hz. The considered excitation is applied along the gravitational axis of the beam, having a duration of 4s and a time discretization step equal to 0.0005s. Linear response history analyses are then conducted, assuming a critical damping ratio of 1% for all modes of vibration which is a reasonable value for a bare steel structure (*e.g.*, *Ji et al.* (2013)). Thus, vertical response acceleration time-series are recorded at the 15 locations shown in Figure 5.27, with Nyquist sampling rate at 2000Hz (*i.e.*, 8000 “Nyquist samples” per signal). The acquired acceleration responses are further contaminated with additive Gaussian white noise expressed by the signal-to-noise ratio $SNR = 10 \cdot \log_{10}\left(\sigma_x^2 / \sigma_\varepsilon^2\right)$, where σ_x^2 is the variance of the response acceleration signal and σ_ε^2 is the noise variance. Two limiting *SNR* values are considered

to simulate response datasets associated with different sparsity levels: (i) a practically noiseless case with SNR=10^{20}dB (*i.e.*, the noise variance σ_ε^2 takes on a very small value close to zero), yielding "high-sparse" signals on the DFT basis; and (ii) a noisy case with SNR=10dB (*i.e.*, the noise variance σ_ε^2 equals the 10% of the signal variance σ_x^2) yielding "low-sparse" signals. It is noted that the additive noise to the signal $x[n]$ *does* influence the signal's sparsity attributes and cannot be rectified during CS sparse recovery *Davenport et al.* (2012), since the noise term $\boldsymbol{\varepsilon}$ cannot be separated by the signal coefficients $u[n]$ in eq.(2.9) (see also Chapter §2).

For illustration, Figure 6.2 plots a typical noisy acceleration response signal with SNR=10dB in time (Figure 6.2(a)), its single-sided magnitude Fourier spectrum normalised to its peak value (Figure 6.2(b)), as well as the normalised magnitude Fourier coefficients sorted in descending order (Figure 6.2(c)).

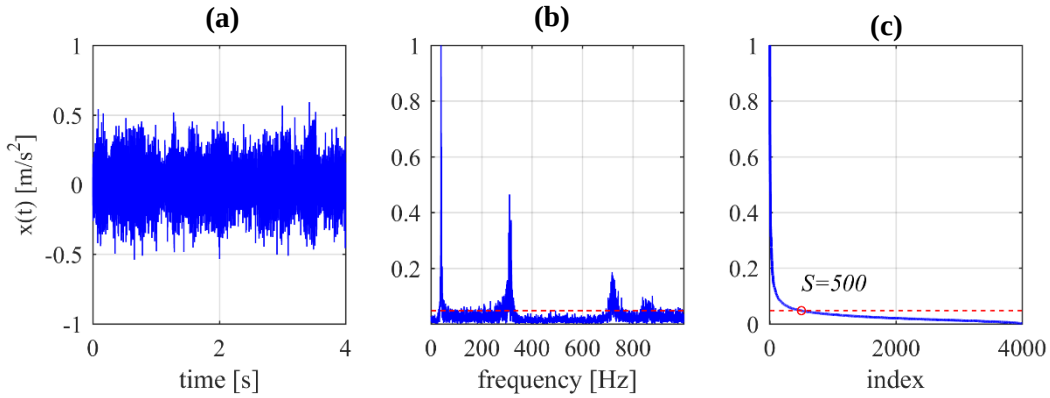

Figure 6.2: *Typical noisy acceleration response signal with SNR=10dB; (a) time history; (b): normalised single-sided Fourier spectrum magnitude; (c): Normalised magnitude Fourier coefficients in descending order. The red broken line signifies an arbitrary threshold at normalized Fourier magnitude of 0.05*

From Figure 6.2(b), it is readily observed that three dominant harmonics are included in the signal on top of broadband noise, corresponding to the three first flexural mode shapes of the beam. By inspection, a threshold is set in Figure 6.2(c) (red broken line) to indicate that the significant signal energy is captured from about 500 Fourier coefficients and thus, a sparsity level of approximately S=500 may be assumed for the considered noisy signals (see also *O'Connor et al.* (2014)). It is emphasised that this threshold can only be heuristically defined and is related to the concept of approximating an S-sparse signal by an S-compressible signal provided that the coefficients of the latter on a given basis function decay rapidly when sorted by magnitude. It is also important to clarify that the considered CS-based spectral estimation approach assumes no prior knowledge on the actual sparsity level S, but this is only reported here to facilitate the interpretation of the comparative results presented in sub-section §6.3.3.

6.3.2. Sub-Nyquist sampling and power spectral estimation

The acceleration response signals generated as detailed above are next compressively sampled at two different *CRs* of approximately 31% and 11% (*i.e.*, 69% and 89% fewer samples compared to the Nyquist samples) using the random CS-based sampling scheme of chapter §2 and the deterministic multi-coset sampling scheme of chapter §4. The adopted sampling parameters are collected in Table 6-1. Specifically, a *CR*= 31% is achieved by multi-coset samplers comprising $\bar{M}$ =5 channels, where each channel samples uniformly in time with a rate $\bar{N}$ =16 times slower than the Nyquist rate. The adopted sampling pattern is $\mathbf{s} = [0, 1, 2, 5, 8]^T$, and a target frequency resolution is set at approximately $\Delta\omega \simeq 5 \cdot 10^{-3} rad/s$, which is derived from (4.21) for *L*=40. In this respect, each sensor acquires only *M*=2500 compressed samples out of the *N*=8000 Nyquist samples. This exact pair of *M, N* values (*i.e.*, *M*=2500, *N*=8000) is further used to define the partial IDFT matrix $\mathbf{F}_{M\times N}^{-1} \in \mathbb{C}^{2500\times 8000}$ in eq.(2.8) for the CS-based approach (see also chapter §2). The effectiveness of the CS-based approach is assessed for various assumed (target) sparsity levels S_T ($\leq \max(M/3, S)$) in the range of [50, 500]. For the case of *CR*=11%, the pertinent parameters are defined in a similar manner as above, such that the same number of compressed measurements are acquired and transmitted by each sensor node for both the CS and the multi-coset sampling schemes, while approximately the same frequency resolution is achieved for the PSBS approach at both *CRs*.

Table 6-1: Considered parameters for the CS-based and the PSBS-based approaches for OMA of the structure in Figure 5.27 for two different compression ratios

	Compression ratio	***CR***	**31%**	**11%**
Common parameters for both approaches	Number of samples uniformly acquired in time	N	8000	8000
	Sub-Nyquist Sampling Rate*		69%	89%
	Number of Sub-Nyquist/Compressed samples	M	2500	875
CS-based approach	Target Sparsity Level	S_T	50-500	50-290
PSBS-based approach	Number of channels	$\bar{M}$	5	14
	Down-sampling	$\bar{N}$	16	128
	Design Parameter	L	40	4
	Frequency resolution [rad/s]	$\Delta\omega$	$4.85\ 10^{-3}$	$5.45\ 10^{-3}$
	Sampling pattern	$\mathbf{s}$	$[0,1,2,5,8]^T$	$[0,1,2,6,8,20,29, 38,47,50,53,60,63,64]^T$

** Assumed Nyquist sampling rate at 2000Hz*

Next, power spectral density matrices collecting estimates of the auto- and cross- power spectra of the acceleration signals from the D=15 sensors are obtained using the two considered spectral estimation methods in Figure 6.1. Specifically, for the CS-based approach, the power spectral density functions are derived in three stages: (i) compressive sensing using the matrix $\mathbf{A}=\mathbf{\Theta\Psi}$ in eq.(2.9); (ii) recovery of DFT coefficients using the CoSaMP algorithm in eq.(2.11) with an assumed target sparsity S_T and stopping criteria determined by tolerance $\eta=10^{-8}$ and predefined maximum number of iterations set at 50; and finally (iii) power spectrum estimation using the standard Welch's modified periodogram (*e.g.*, *Marple* (1987)). The latter is applied to time-domain reconstructed acceleration responses, $\hat{x}[n]$, obtained by application of the IDFT to the recovered signal coefficients, $\hat{u}[n]$, using eq.(2.1). To this end, the "cpsd" built-in function in MATLAB® is adopted herein, in which the reconstructed signals are divided in eight segments with 50% overlap and windowed with a Hanning function.

For illustration, Figure 6.3(a) evaluates the recovery performance of the CoSaMP algorithm by plotting the CS reconstruction error, $\|\hat{u}[n]-u[n]\|_2/\|u[n]\|_2$, as a function of the target sparsity, S_T, for both the examined *CRs* (*i.e.*, 31% and 11%), at the two limiting *SNRs* values (*i.e.*, 10^{20}dB, 10dB). For the case of CR=31%, smaller reconstruction errors are observed at higher S_T values, suggesting more accurate estimates as the number of recovered measurements increases. This can be visualised in Figure 6.3(b, c) (for the high-sparsity case at SNR=10dB), where the reconstructed DFT coefficients, $\hat{u}[n]$, are plotted against the pertinent uncompressed values, $u[n]$, by considering two target sparsity levels at $S_T=\{100, 290\}$. However, the above observation is not confirmed for CR=11%, in which case the reconstruction error increases with S_T. This rather poor reconstruction performance is because an overly high compression level was assumed for which the relatively small number of sub-Nyquist measurements $y[m]$ in eq.(2.2) do not retain sufficient information of the structural response signals. Adopting, for example, the heuristic value of S=500 in Figure 6.2 (for the low-sparse signals with SNR=10dB), the required M value should be of the order of $S\cdot\log(N)= 500\cdot\log(8000)\approx1950$ (*e.g.*, *O'Connor et al.* (2014)); however, only M=875 sub-Nyquist samples are acquired at CR=11%, which are evidently too few. Along these lines, Figure 6.3(d, e) confirm that the assumption of higher S_T values closer to the upper bound of $M/3\approx290$ cannot compensate for the insufficient number of compressed measurements, yielding spurious large amplitudes in the recovered DFT coefficients that increase the reconstruction error and adversely affect the accuracy of the obtained modal estimates, which will be presented in the next sub-section. Similar conclusions have also been reported by *O'Connor et al.* (2013), (2014).

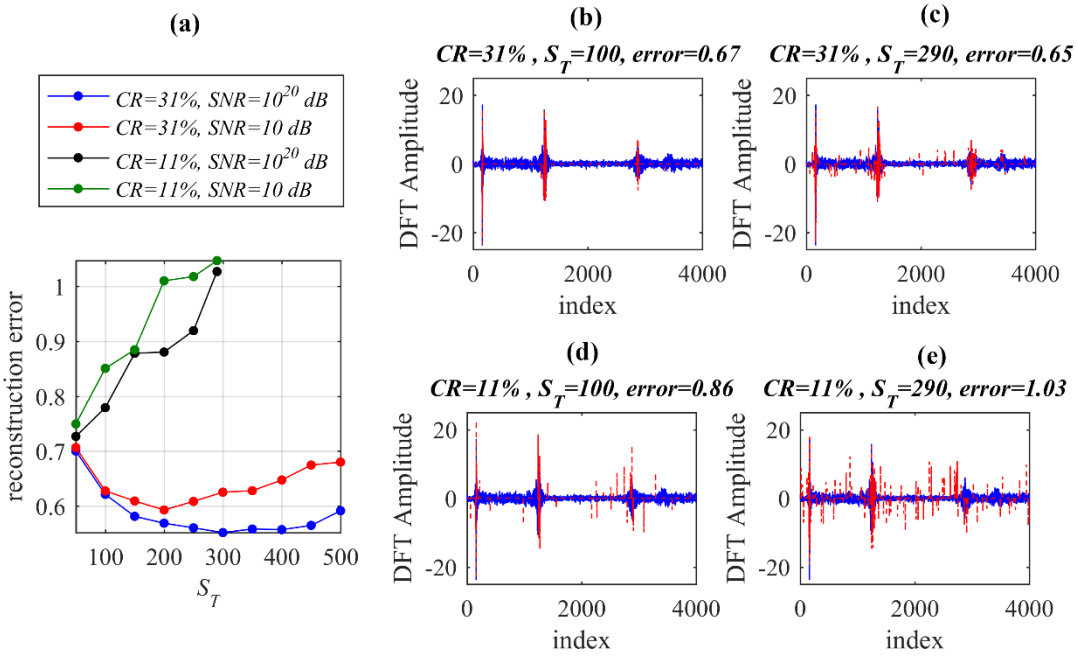

Figure 6.3: *(a) Signal reconstruction error of CoSaMP algorithm versus the target sparsity level S_T; (b-e) original and reconstructed DFT coefficients at CR={31%,11%}, S_T={100, 290} for SNR=10 dB*

Moving to the PSBS-based approach, the PSD matrix is estimated through the following three stages: (i) multi-coset sampling based on the sampling pattern in Table 6-1; (ii) cross-correlation estimation applied to the compressed measurements as in eq.(4.22); and (iii) power spectrum estimation using eq.(4.26). The recovered PSD estimates are illustrated in Figure 6.4 (red curve) for the two adopted *CRs* at 31% (Figure 6.4(a)) and 11% (Figure 6.4(b)), respectively, considering the low-sparse dataset. For comparison, Figure 6.4 also plots the pertinent PSD curves obtained from the standard Welch's modified periodogram at Nyquist rate (black curve), and reports the mean square error (MSE) of the two comparative PSDs. It is readily observed that more ripples are found for lower *CRs* (Figure 6.4(b)), which increases the MSE value. Nonetheless, the spectral peaks are well captured from the PSBS approach in both amplitude and shape even for *CR*=11%, which is essential for accurate modal identification.

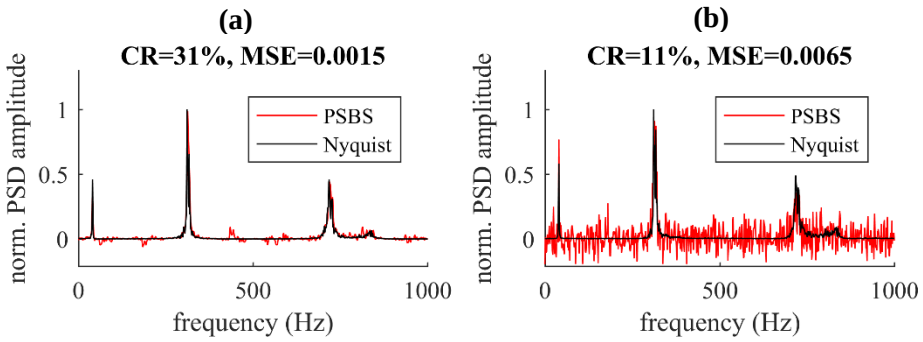

Figure 6.4: *PSBS spectral recovery and MSE for the low-sparse response accelerations (SNR=10 dB) at (a) CR=31% and (b) CR=11%.*

6.3.3. Mode shape estimation

The FDD algorithm is lastly applied to the PSD matrices obtained as detailed above to extract the modal properties of the beam in Figure 5.27. For illustration, Figure 6.5 presents all three excited mode shapes derived from the noisy (*i.e.*, lower-sparsity) measurements, as extracted from the two different approaches (CS-based for S_T=290 and PSBS-based) for *CR*=31%. In Figure 6.6 only the first two mode shapes are shown for *CR*=11% and for *SNR*=10dB since the third mode is not detectable at this low *CR*. For comparison, Figure 6.5 and Figure 6.6 plot further the mode shapes obtained by application of the FDD to the conventionally (Nyquist) sampled measurements, considering the Welch periodogram (*e.g.*, *Marple* (1987)) with the same settings as detailed in the previous sub-section. From a qualitative viewpoint, it is observed that both sub-Nyquist approaches perform well for *CR*=31% in capturing the shape and relative amplitude of the modal deflected shapes compared to the conventional approach, with the PSBS-based method being slightly more accurate. For higher signal compression at *CR*=11%, the PSBS-based method clearly outperforms the CS-based method.

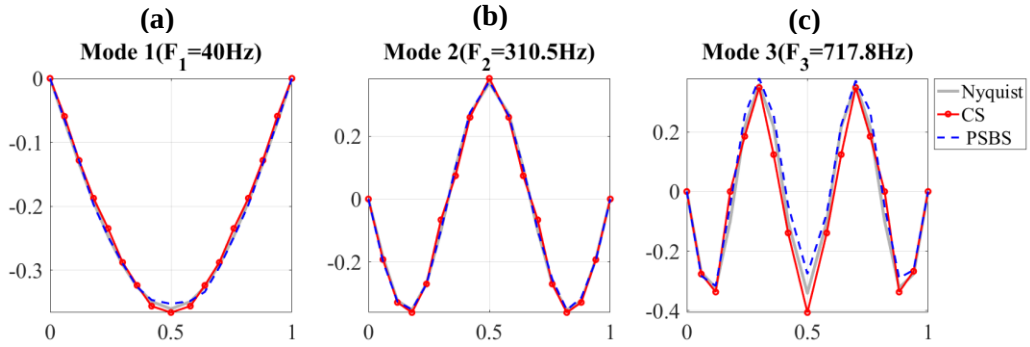

Figure 6.5: *Mode shape estimation for CR=31%, SNR=10dB (low-sparse signals) and target reconstruction sparsity S_T=290 for the CS-based approach*

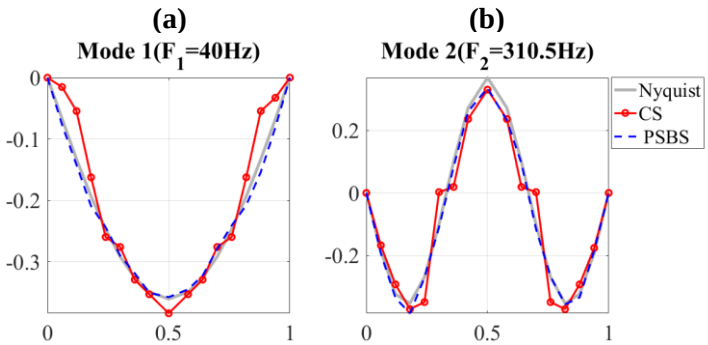

Figure 6.6: *Mode shape estimation for CR=11%, SNR=10dB (low-sparse signals) and highest possible target reconstruction sparsity S_T=290 in the CS-based approach*

The accuracy for the extracted mode shapes is quantified with the modal assurance criterion (MAC) in eq. (4.43) (*e.g.*, *Brincker & Ventura* (2015)), measuring the correlation between the modes shapes, $\hat{\boldsymbol{\varphi}}_r$ and $\boldsymbol{\varphi}_r$, estimated by means of the FDD algorithm from compressed (sub-Nyquist) and Nyquist samples, respectively. Figure 6.7 and Figure 6.8 plot the computed MAC

values with respect to the assumed target sparsity S_T for both the relatively high-sparse (SNR= 10^{20} dB) and low-sparse (SNR=10dB) signals for *CRs* at 31% and 11%, respectively.

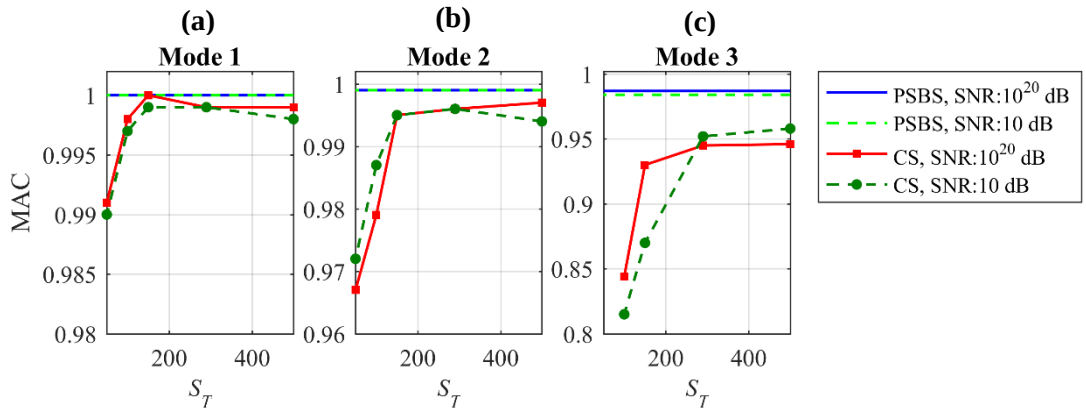

Figure 6.7: *MAC versus reconstruction sparsity level* S_T*, obtained from the two considered approaches, PSBS-based and CS-based FDD, for CR= 31% and SNR={10^{20},10}dB*

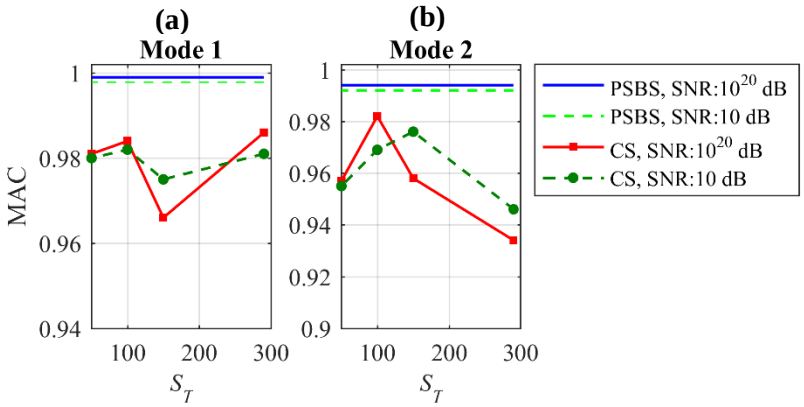

Figure 6.8: *MAC versus reconstruction sparsity level* S_T*, obtained from the two considered approaches, PSBS-based and CS-based FDD, for CR= 11% and SNR={10^{20},10}dB*

The above figures show that for both sparsity levels, the PSBS-based approach outperforms the CS-based approach for the same number of acquired (and wirelessly transmitted) sub-Nyquist measurements regardless of the adopted target sparsity S_T value. Specifically, the PSBS-approach can accurately retrieve the modal deflected shapes yielding MAC values close to unity. Notably, the PSBS method does not rely on sparsity assumptions, and therefore the obtained MAC values are not functions of S_T. Still, Figure 6.7 shows that the CS-based approach does perform quite well at least for *CR*=31%, though its performance depends heavily on the assumed S_T value. Importantly, for *CR*=31% higher accuracy is achieved for higher S_T values (note also the decreasing trend in the reconstruction error curve in Figure 6.3), but this comes at the cost of higher computational cost in the signal reconstruction step.

However, this is not the case for *CR*=11% and for the second and less excited mode shape in Figure 6.8, where the accuracy deteriorates yielding lower MAC values with increasing S_T. This rather unfavourable condition can be explained through Figure 6.3, where it is numerically shown

that higher CS reconstruction errors occurs at larger S_T values for *CR*=11%, having a profound impact on the accuracy of the obtained CS modal results. In this case, if a *priori* knowledge of the signal sparsity was known (*e.g.*, *Bao et al.* (2013); *Klis & Chatzi* (2015), (2017); *Zou et al.* (2015); *Huang et al.* (2016)), then one should normally opt to increase the average random sampling rate (*i.e.*, obtain a larger number of measurements, *M*, within the same time-window). Nevertheless, the signal agnostic PSBS approach is capable to extract structural mode shapes associated with the local peaks of the spectrum even for *CR*=11% and signals with lower sparsity (at *SNR*=10dB) as long as they are not completely "buried" in noise. For instance, Figure 6.4 (b) reveals that the recovered PSBS-PSD at *CR*=11% and *SNR*=10dB attains relatively large amplitudes close to the 3rd spectral peak, which hinders the extraction of the associated vibrating mode of the beam in Figure 5.27.

As a final remark, it is noted that both the adopted sub-Nyquist methods yield fairly accurate natural frequency estimates in all considered cases (error is less than 1% compared to the conventional approach at Nyquist rate).

6.4. Numerical Assessment for Field-Recorded Signals

6.4.1. The Bärenbohlstrasse bridge case-study and pre-processing of recorded data

Further to the previous comparison and along similar lines, the effectiveness of the two considered spectral estimation approaches of Figure 6.1 is herein assessed against field recorded data from an existing bridge, namely the Bärenbohlstrasse overpass in Zürich, Switzerland (*e.g.*, *Chatzi E.N. & Spiridonakos M.D.* (2015); *Spiridonakos et al.* (2016)), vibrating under operational loading. The bridge is 30.90m long, having a deck of variable width, while it is almost symmetric along the longitudinal direction. It consists of a solid prestressed-slab with two equal-length spans of 14.75m each. The deck is supported, via steel bearings, in all directions at mid-span and in one of the abutments. The second abutment supports the deck only in the vertical and transverse directions. The bottom face of the deck was permanently instrumented for the 12-month period of 12th July 2013 to 26th July 2014 by a network of 18 tethered sensors of the *Gantner Q-series DAQ* type, equipped with an anti-aliasing filter at the cut-off frequency of 50Hz (see also *Spiridonakos et al.* (2016)). The adopted network of sensors was acquiring 18 vertical acceleration response signals with a sampling rate at 200Hz (T_s=0.005s) for approximately 10min per hour using a conventional uniform sampling scheme. A photo of the bridge and a sketch of the sensors layout is shown in Figure 6.9, including the relative distances in both horizontal dimensions. Further details regarding the bridge, the sensors installation and data acquisition can be found in *Chatzi E.N. & Spiridonakos M.D.* (2015); *Spiridonakos et al.* (2016).

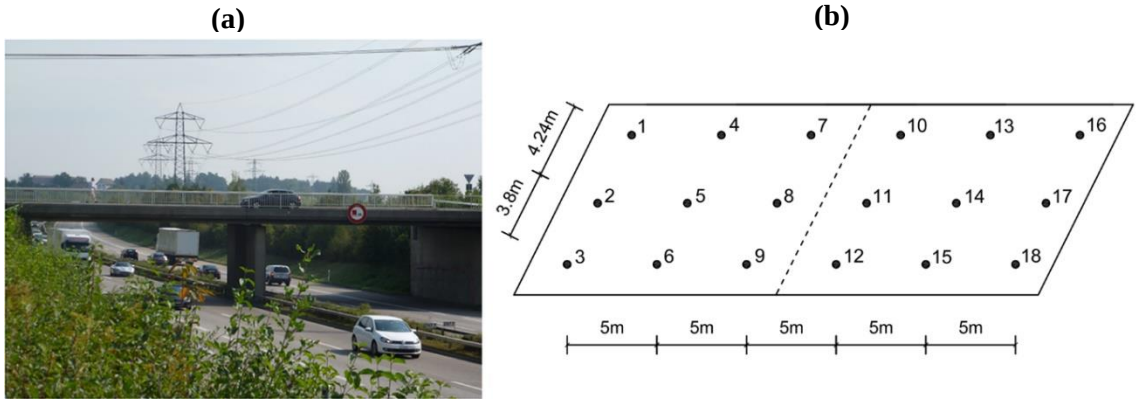

***Figure 6.9**: (a) Bärenbohlstrasse bridge in Zurich, Switzerland (image reused from Spiridonakos et al.* (2016)*) and (b) layout of the 18 sensors recording vertical acceleration responses under ambient excitation*

In this study, a dataset of 18 vertical acceleration response signals is used, recorded on 19/06/2014 between 15:08:54 and 15:17:51, comprising 107460 samples per sensing location, being conventionally (*i.e.*, uniformly) sampled at 200Hz. The considered dataset pertains to ambient wind and traffic dynamic loads that sufficiently excite the first few modes of the monitored bridge. For illustration, Figure 6.10 presents a typical acceleration response signal recorded at sensor #13 (Figure 6.10(a)), along with the computed velocity (Figure 6.10(b)) and displacement (Figure 6.10(c)) time-series, obtained from application of single and double integration, respectively. From this figure, it is readily observed that unrealistically high velocity and displacement values are present within the raw data, which underlines the need for signal pre-processing operations prior to the implementation of the developed method. To this end, a baseline adjustment is applied to the raw data to remove the mean value and any potential low-frequency trend within each acceleration response signal. Next, a 4th-order Butterworth band-pass filter is employed within the frequency range [0.15, 50] in Hz. Notably, the upper cut-off frequency at 50Hz is determined by the sensors' anti-aliasing filter which defines a Nyquist sampling frequency at F_{NYQ}=100Hz.

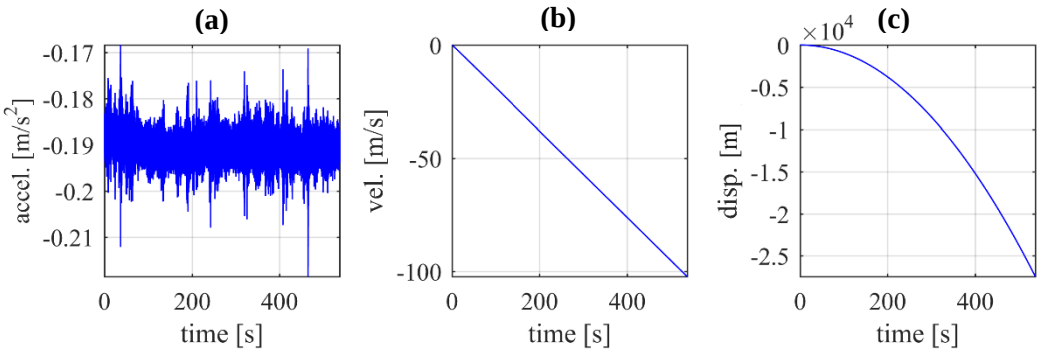

***Figure 6.10**: Typical acceleration-velocity-displacement time series recorded at sensor #13 pertaining to the raw data*

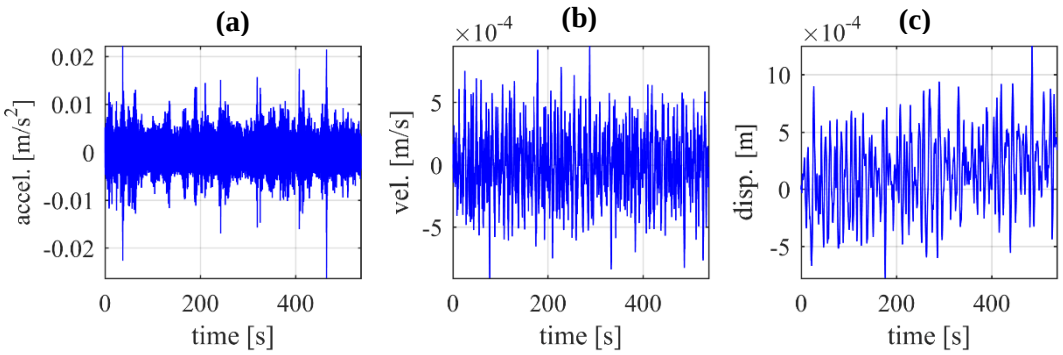

***Figure 6.11**: (a) Typical acceleration, (b) velocity, and (c) displacement time series recorded at sensor #13 pertaining to the corrected responses*

The "corrected" signal (*i.e.*, baseline adjusted and band-pass filtered) are presented in Figure 6.11 for the sensor #13. Figure 6.12(a) shows further the magnitude Fourier spectrum of the corrected acceleration in Figure 6.11(a), normalised to its peak value and plotted within the frequency range [0, 20] Hz, in which the first four modes of the vibrating bridge lie (*e.g.*, *Chatzi E.N. & Spiridonakos M.D.* (2015); *Spiridonakos et al.* (2016)). Lastly, Figure 6.12(b) plots the normalised magnitude Fourier coefficients sorted in descending order. On the last plot, a heuristically selected threshold at 5% of the peak Fourier spectrum magnitude (red broken line) is shown indicating that the significant signal energy is captured from approximately 10000 Fourier coefficients. Thus, the actual sparsity level of the considered field recorded signals is roughly $S \approx 10000$. As previously discussed, though, no such information would be available from the low-rate data acquisition using the two sub-Nyquist spectral estimation approaches of Figure 6.1, but it is only reported to inform the comparison of the OMA results discussed in the following sub-section.

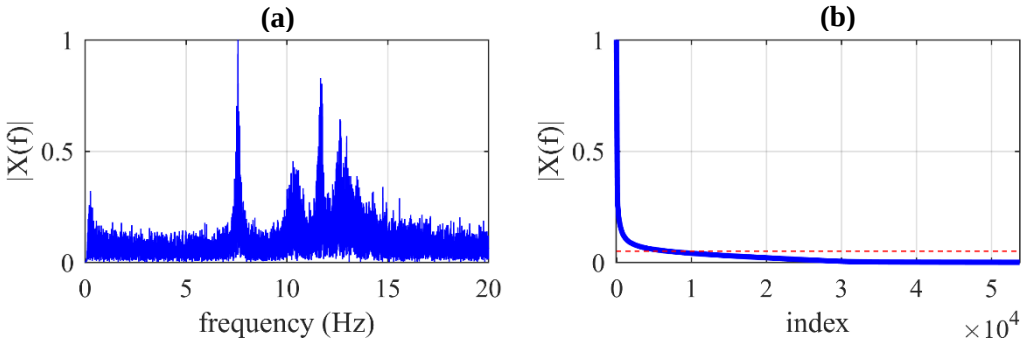

***Figure 6.12:** (a) Normalised Fourier spectrum magnitude of the acceleration response signal measured at sensor #13, plotted within the frequency range of [0, 20] Hz; and (b) normalised magnitude Fourier coefficients sorted in descending order. The red broken line signifies an arbitrary threshold at normalized Fourier spectrum of 0.05.*

Given that the PSBS-based spectral estimation approach anticipates signal stationarity, it was deemed essential to undertake a data qualification test to appraise the stationarity attributes of the recorded signals. To this end, the corrected acceleration sequence in Figure 6.11(a) is divided in 8 time-windows of one minute duration, and the standard non-parametric Reverse Arrangement

method (*e.g., Bendat & Piersol* (2010)) is used to statistically test the stationarity hypothesis. The obtained Reverse Arrangement results are presented in Figure 6.13, showing that the stationarity hypothesis is confirmed at the 95% confidence level. It is concluded that the recorded and pre-processed response acceleration signals from the Bärenbohlstrasse bridge can be treated as wide-sense stationary at a high confidence level and, therefore, the PSBS approach is applicable.

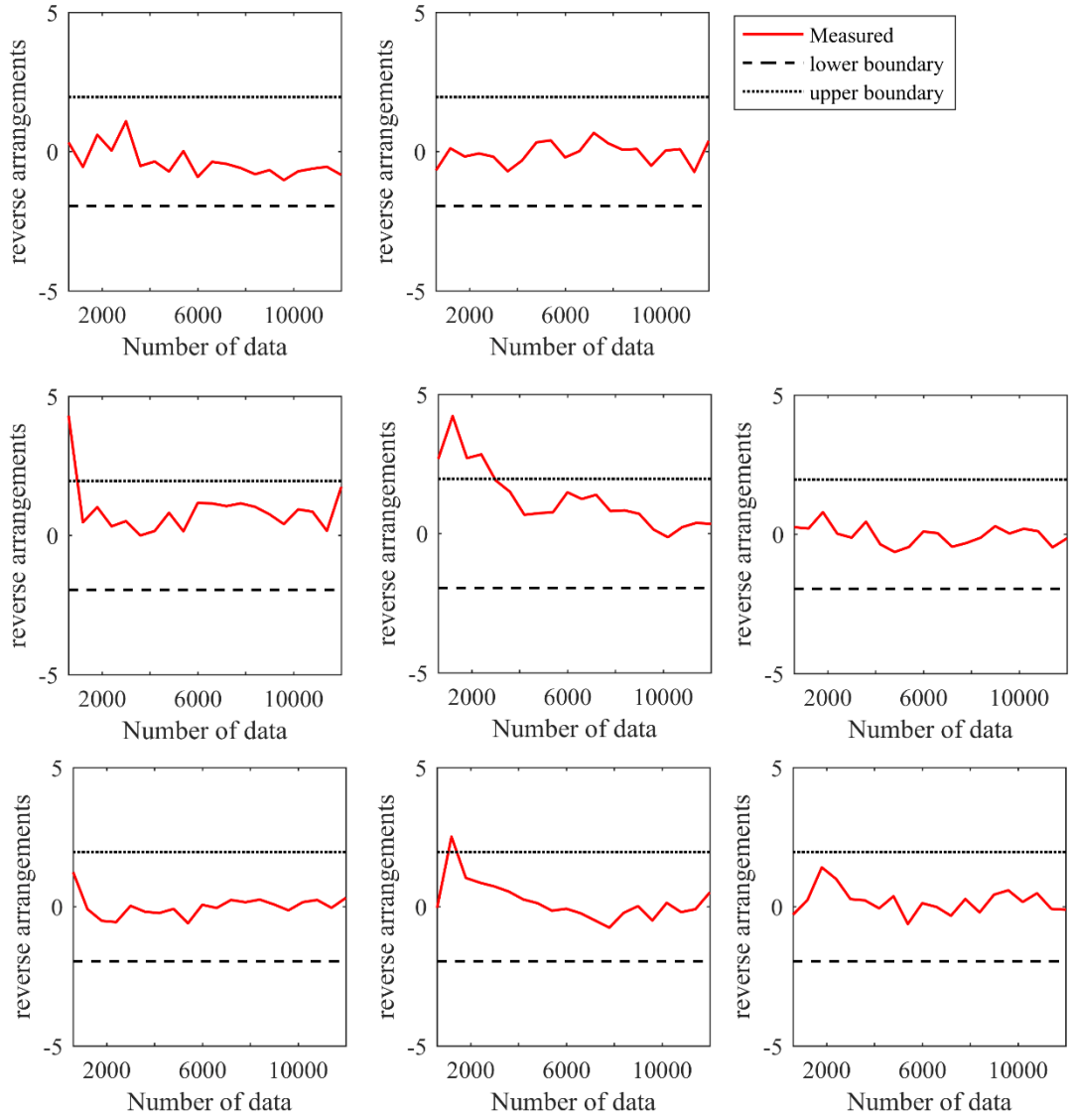

Figure 6.13: *Reverse Arrangement method applied on acceleration response signal measured at sensor #13; signal is divided in 8 segments of 1min duration.*

6.4.2. Mode shapes estimation of the Bärenbohlstrasse bridge

The same steps detailed in sub-sections §6.3.2 and 6.3.3 (see also Figure 6.1) are herein taken to estimate the mode shapes of the Bärenbohlstrasse bridge from the 18 corrected (*i.e.*, baseline-adjusted and band-pass filtered) field recorded acceleration responses. Table 6-2 collects the parameters adopted for the random CS-based and the deterministic multi-coset sampling at three

CRs in the range between 11% and 31%. Table 6-2 also reports the sub-Nyquist sampling rates achieved by the adopted *CRs* based on the maximum cut-off frequency of the filtering operation at 50Hz, which pertains to an assumed Nyquist sampling rate at 100Hz.

Table 6-2: Considered parameters for the CS-based and the PSBS-based approaches for OMA of the structure in Figure 6.9 for two different compression ratios.

	Compression ratio	***CR***	**31%**	**21%**	**11%**
Common parameters for both approaches	Number of samples uniformly acquired in time	N	107460	107460	107460
	Sub-Nyquist Sampling Rate *		62.5%	41%	21.9%
	Number of Sub-Nyquist/Compressed samples	M	33581	22040	11753
CS-based approach	Target Sparsity Level	S_T	1200-11160	1200-7320	1200-3840
PSBS-based approach	Number of channels	$\bar{M}$	5	8	14
	Down-sampling	$\bar{N}$	16	39	128
	Sampling pattern	**s**	$[0,1,2,5,8]^T$	$[0,1,3,7,9,14,18,19]^T$	$[0,1,2,6,8,20,29,38,47,50,53,60,63,64]^T$
	Design Parameter	L	40	16	4
	Frequency resolution [rad/s]	$\Delta\omega$	$4.85\ 10^{-3}$	$4.88\ 10^{-3}$	$5.45\ 10^{-3}$

**Assumed Nyquist sampling rate at 100Hz*

Further, Table 6-2 presents the range of different S_T values ($<M/3$) considered in the CS-based approach, which are directly related to the algorithmic trade-off between accuracy and complexity. The latter reflects on the required running time of the CS signal reconstruction algorithm for various S_T values. As an example, Figure 6.14 plots the off-line computational time required by the CoSaMP algorithm to recover the 18 bridge acceleration responses from the acquired compressed measurements at *CR*=31%, 21%, and 11% (Figure 6.14 (a) - (c), respectively). From this figure, it is readily observed that the CS computational cost exponentially increases with S_T. For comparison, Figure 6.14 also depicts the running time of the PSBS-based approach (broken line) associated with the 18x18 spectral matrix estimation in eq.(4.26). All reported numerical work was performed on a quadcore Intel Core i7-6700HD with 16GB RAM.

For the CS-based approach at the three considered *CRs*, Figure 6.15(a)-Figure 6.17(a) illustrate the randomly acquired compressed measurements, $y[m]$, against the full-length bridge acceleration response, $x[n]$, for a time-window of 2sec. The latter are also superimposed onto the reconstructed signals, $\hat{x}[n]$ (Figure 6.15(b)-Figure 6.17(b)), obtained from the CoSaMP algorithm in eq.(2.11) using the maximum target sparsity value S_T in Table 6-2 for each *CR*. From a qualitative point of view, it is observed that the reconstructed signal at *CR*=31% can faithfully approximate the original uncompressed signal at the expense of longer running time during reconstruction (e.g., Figure 6.14). In fact, based on the assumption that *S*=10000 for all signals considered in the dataset (see also Figure 6.12(b)), the number of compressed measurements that provides reasonably accurate signal recovery results should be in the order of $M \approx S \cdot \log(N) \approx 10000 \cdot \log(107460) \approx 50000$ (see also *O'Connor et al.* (2013), (2014)). Thus, the case of *CR*=31% corresponds to the acquisition of *M*=33581 compressed measurements which is close to the above requirement. On the contrary, the reconstruction performance considerably degrades at lower *CRs*, and especially in the limiting *CR* value of 11% (Figure 6.17) due to the acquisition of only *M*=11753 compressed data which is well below the required order of $M \approx 50000$.

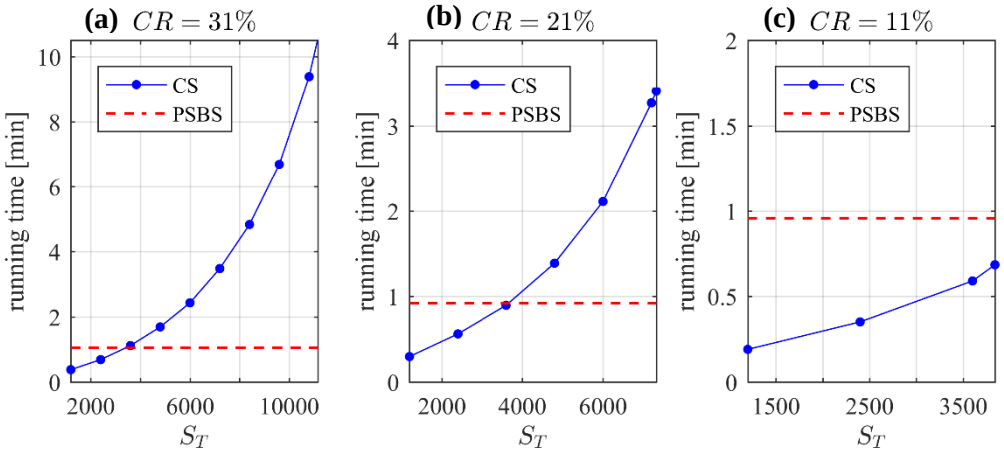

Figure 6.14: *Total running time for off-line signal and power spectral recovery required by the CS-based and the PSBS-based approach, respectively, versus reconstruction sparsity level for (a) CR=31%, (b) CR=21%, and (c) CR=11%.*

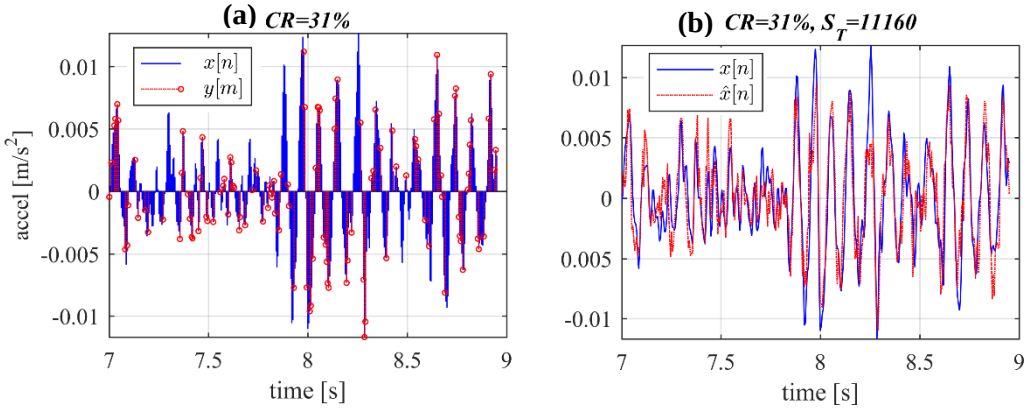

***Figure 6.15**: (a) Compressive sensing at CR=31% and the acquisition of M=125 samples within a time-window of 2sec duration with N=400 Nyquist samples and (b) CoSaMP-based signal reconstruction of acceleration response signal at sensor #13 for S_T=11160.*

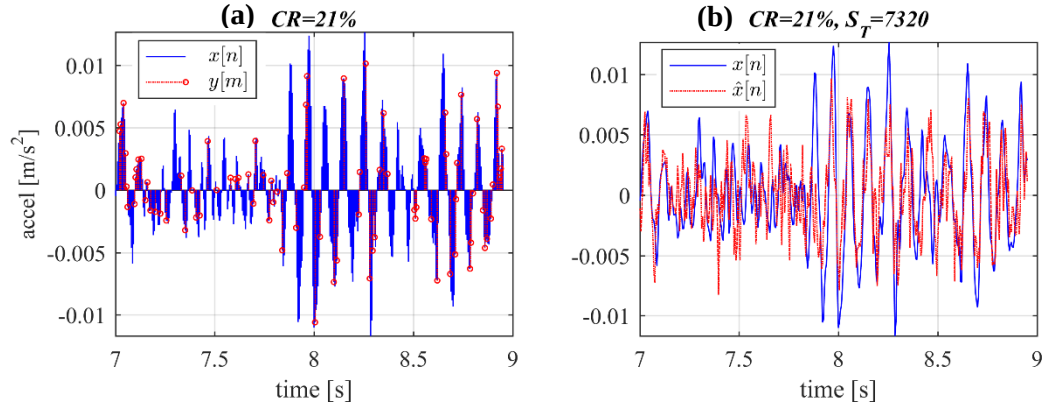

***Figure 6.16**: (a) Compressive sensing at CR=21% and the acquisition of M=82 samples within a time-window of 2sec duration with N=400 Nyquist samples and (b) CoSaMP-based signal reconstruction of acceleration response signal at sensor #13 for S_T=7320.*

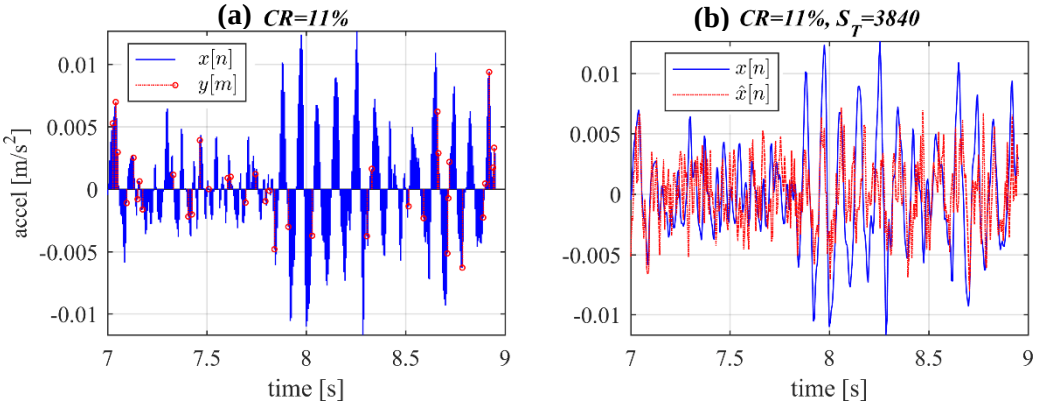

***Figure 6.17**: (a) Compressive sensing at CR=11% and the acquisition of M=44 samples within a time-window of 2sec duration with N=400 Nyquist samples and (b) CoSaMP-based signal reconstruction of acceleration response signal at sensor #13 for S_T=3840.*

As a final step, the standard FDD algorithm is applied to the PSD matrices estimated by the CS-based method (*i.e.*, standard Welch's modified periodogram (*e.g.*, *Marple* (1987)) applied on the reconstructed signals $\hat{x}[n]$), and the PSBS-based spectral estimation approach (*i.e.*, eq.(4.26)

using the unbiased estimator in eq.(4.22) for the compressed measurements in eq.(4.5)), to extract the bridge mode shapes (see also chapter 2, 4 and sub-section §6.3.2).

For the two considered approaches, Figure 6.18 plots the derived first singular values vector at the three considered signal compression levels in Table 6-2, normalised to the maximum amplitude and plotted against the conventional/non-compressive FDD at uniform sampling rate (at *CR*=100%). From this figure, it is readily observed that the highest singular values amplitudes occur at 7.617 Hz and 11.719 Hz, pertaining to the 1st and 3rd resonant frequencies of the monitored bridge, respectively, while relatively smaller amplitudes occur at 10.352 Hz and 12.598 Hz, associated with the bridge natural frequencies at the less excited 2nd and 4th vibrating modes.

Table 6-3 and Table 6-4 report the natural frequency estimates obtained from the two comparative approaches in Figure 6.1, respectively, at the three adopted *CRs* (*i.e.*, 11%, 21%, 31%), which are compared against the pertinent values extracted from the non-compressive FDD at uniform sampling rate (at *CR*=100%). In the latter case, the PSD response matrix has been computed for the full-length dataset using the standard Welch modified periodogram as detailed in §6.3.2. The difference percentage error, df_r/f_r (for r=1,2,3,4) is further used to quantify the accuracy of the proposed approach in detecting the bridge natural frequencies at the four excited modes of vibration, and the computed errors values are listed in Table 6-3 and Table 6-4. Commenting first on the multi-sensor PSBS-based FDD, small percentage errors (below ±1.6%) are observed in Table 6-3, confirming the efficiency of this method in retrieving the first four bridge resonant frequencies without being significantly affected by the signal compression at the considered *CRs*. Next, Table 6-4 reveals that the underlying bridge natural frequencies are extracted with high accuracy from the CS-based approach that relies on the same spectral estimation method as the non-compressive FDD (*i.e.*, the Welch modified periodogram).

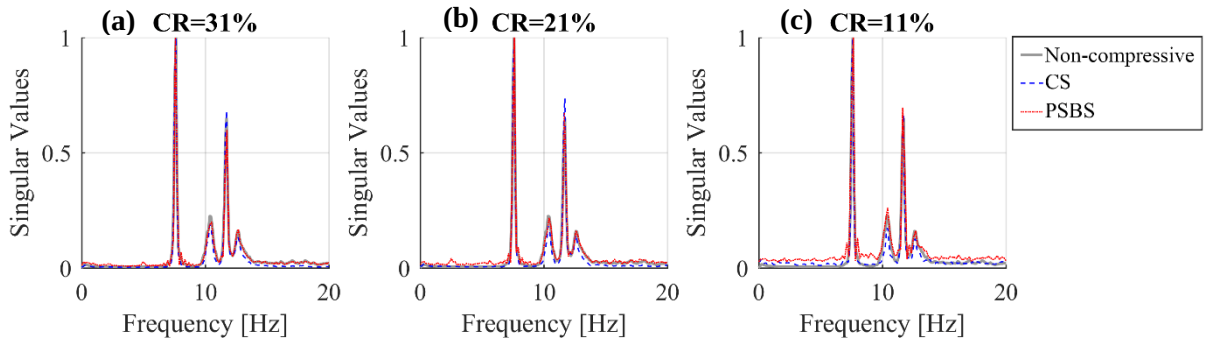

***Figure 6.18**: First singular values vector of the bridge response spectrum matrix for CR={100%, 31%,21%, 11%}*

Table 6-3: Natural Frequency Estimates from PSBS-based approach.

	Non-compressive FDD	***PSBS-based FDD***		
	***CR*=100%**	***CR*=31%**	***CR*=21%**	***CR*=11%**
f_1 [Hz]	7.617	7.573	7.632	7.652
(df_1/ f_1 [%])	-	(-0.57 %)	(+0.20 %)	(+0.46%)
f_2 [Hz]	10.352	10.510	10.436	10.435
(df_2/ f_2 [%])	-	(+1.53 %)	(+0.82 %)	(+0.80 %)
f_3 [Hz]	11.719	11.747	11.682	11.652
(df_3/ f_3 [%])	-	(+0.24 %)	(-0.31 %)	(-0.57 %)
f_4 [Hz]	12.598	12.674	12.617	12.696
(df_4/ f_4 [%])	-	(+0.61%)	(+0.15 %)	(+0.78 %)

Table 6-4: Natural Frequency Estimates from CS-based approach.

	Non-compressive FDD	***CS-based FDD S_T=3600***		
	***CR*=100%**	***CR*=31%**	***CR*=21%**	***CR*=11%**
f_1 [Hz]	7.617	7.617	7.617	7.617
(df_1/ f_1 [%])	-	(0.00%)	(0.00%)	(0.00%)
f_2 [Hz]	10.352	10.352	10.352	10.352
(df_2/ f_2 [%])	-	(0.00%)	(0.00%)	(0.00%)
f_3 [Hz]	11.719	11.719	11.719	11.719
(df_3/ f_3 [%])	-	(0.00%)	(0.00%)	(0.00%)
f_4 [Hz]	12.598	12.598	12.598	12.598
(df_4/ f_4 [%])	-	(0.00%)	(0.00%)	(0.00%)

For illustration, Figure 6.19-Figure 6.22 plot the first four mode shapes of the considered bridge corresponding to two bending (modes 1 and 2) and two rotational (modes 3 and 4) vibrating modes. They are obtained from the standard FDD method using: (i) the 18 conventionally acquired signals, each comprising N=107460 samples (panels (a)); (ii) the PSBS-based approach for CR=11% (panels (b)); and (iii) the CS-based approach for CR=11% and S_T=3840 (panels (c)).

From a qualitative inspection of these mode shapes, it can be deduced that both the sub-Nyquist methods can adequately capture the shapes of the modal responses as estimated from the uniformly sampled dataset. However, non-negligible differences are observed between the conventional FDD and the CS-based approach, especially for the 2nd and the 4th vibrating modes.

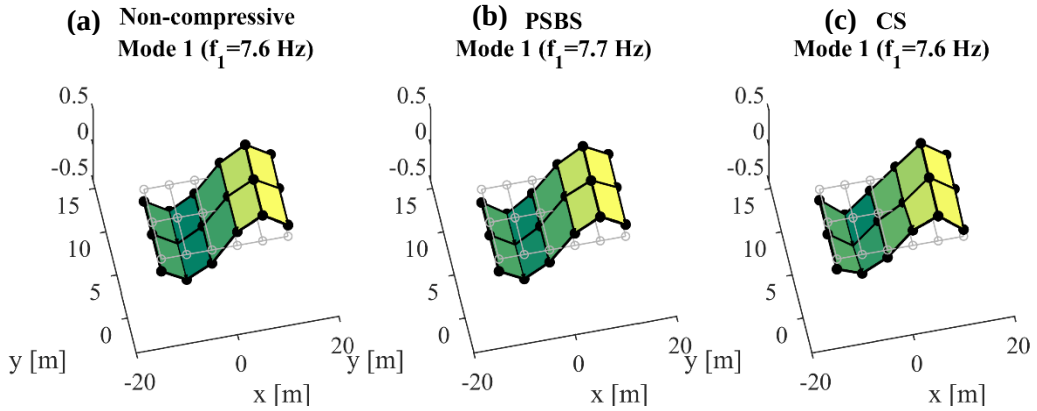

***Figure 6.19**: Estimation of the 1st mode shape (bending) of the Bärenbohlstrasse bridge; (a) conventional/non-compressive FDD; (b) PSBS-based FDD at CR=11%; and (c) the CS-based approach for CR=11% and target reconstruction sparsity S_T=3840.*

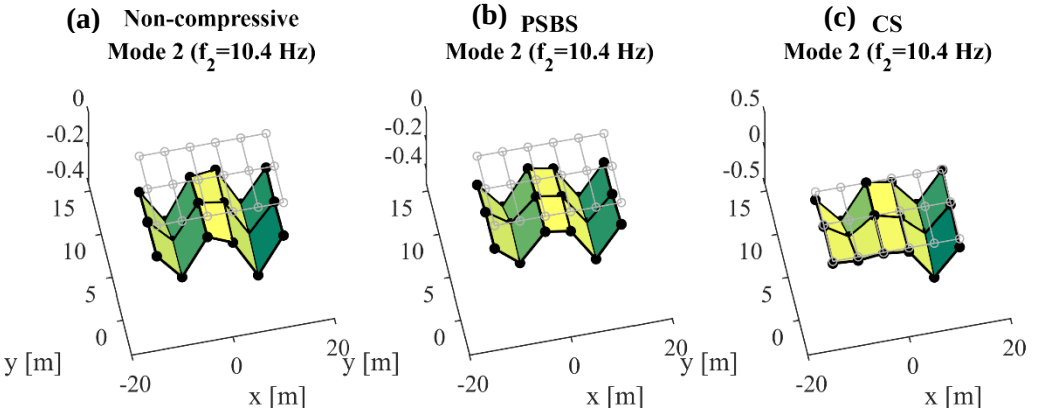

***Figure 6.20**: Estimation of the 2nd mode shape (bending) of the Bärenbohlstrasse bridge;(a) conventional/non-compressive FDD; (b) PSBS-based FDD at CR=11%; and (c) the CS-based approach for CR=11% and target reconstruction sparsity S_T=3840.*

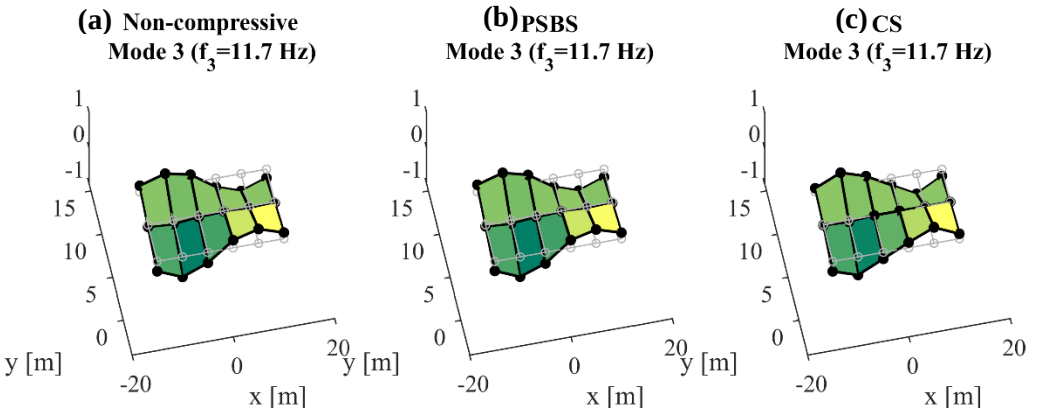

***Figure 6.21**: Estimation of the 3rd mode shape (rotational) of the Bärenbohlstrasse bridge; (a) conventional/non-compressive FDD; (b) PSBS-based FDD at CR=11%; and (c) the CS-based approach for CR=11% and target reconstruction sparsity S_T=3840.*

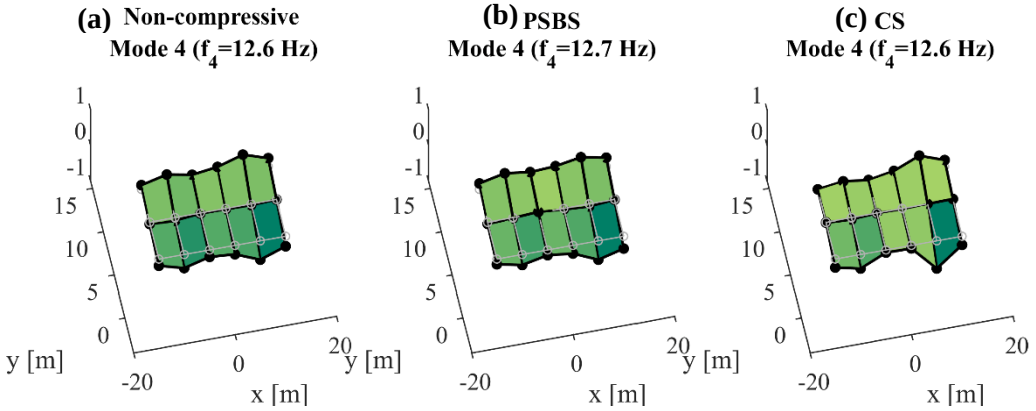

***Figure 6.22**: Estimation of the 4th mode shape (rotational) of the Bärenbohlstrasse bridge; (a) conventional/non-compressive FDD; (b) PSBS-based FDD at CR=11%; and (c) the CS-based approach for CR=11% and target reconstruction sparsity S_T=3840.*

To quantify the level of similarity between mode shapes obtained from the conventionally sampled dataset and from the sub-Nyquist sampled acceleration responses, the MAC in eq.(4.43) is plotted in Figure 6.23, Figure 6.24 and Figure 6.25 for the three considered *CR*s, respectively, as a function of the assumed target sparsity S_T . In these figures, the computed MAC values from the CS-based approach are shown with blue circular marks, while the pertinent values obtained from the PSBS-based approach are depicted with red broken lines of constant amplitude. The influence of the signal compression level to the derived MAC values is further assessed in Figure 6.26 for the two considered approaches, based on the maximum target sparsity S_T value at the limiting *CR* case of 11%.

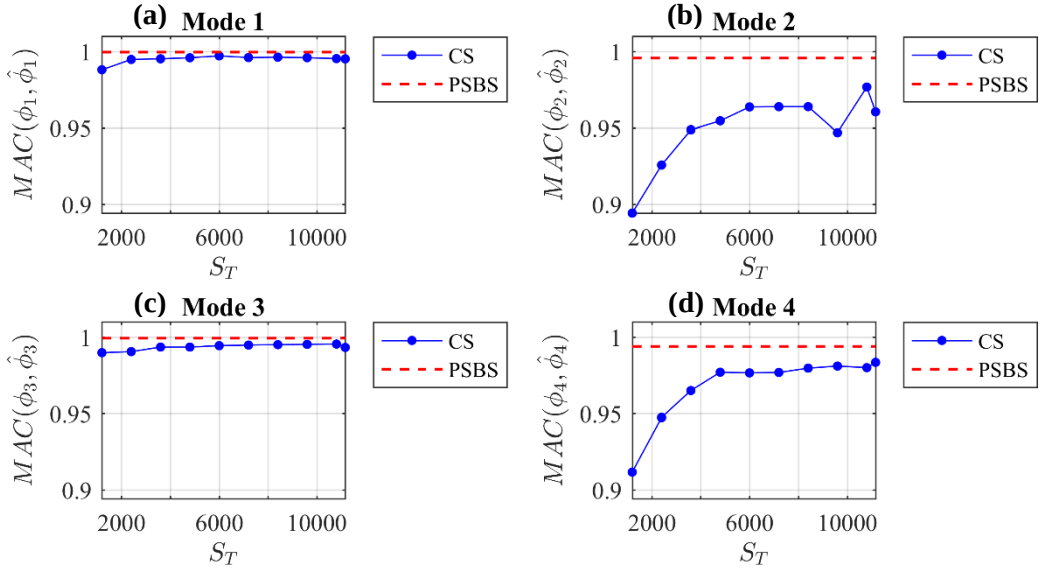

***Figure 6.23:** MAC versus reconstruction sparsity level S_T, obtained from the two considered approaches (i.e., PSBS-based and CS-based FDD) for CR= 31%*

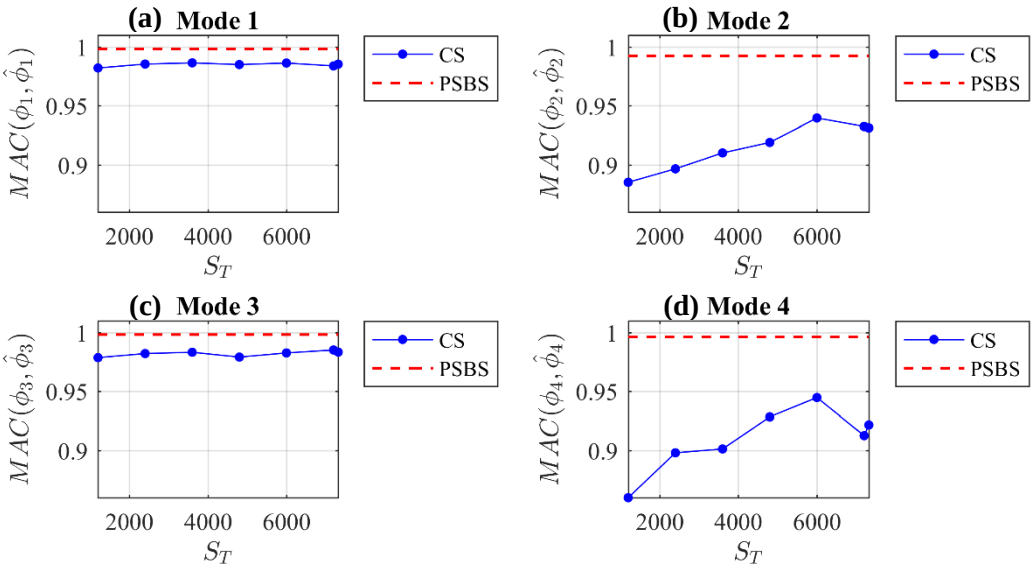

***Figure 6.24**: MAC versus reconstruction sparsity level S_T, obtained from the two considered approaches (i.e., PSBS-based and CS-based FDD) for CR= 21%*

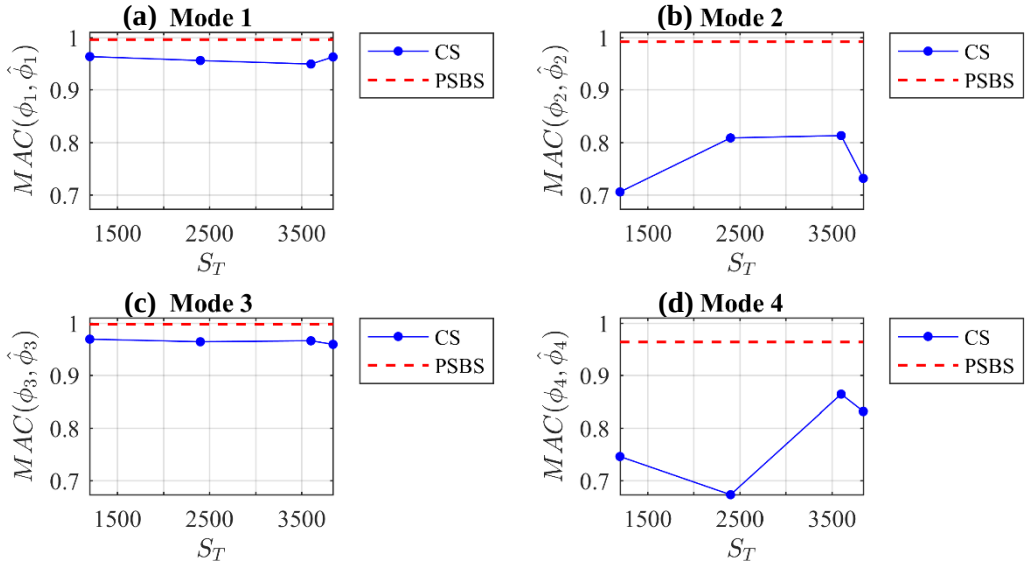

***Figure 6.25:** MAC versus reconstruction sparsity level S_T, obtained from the two considered approaches (i.e., PSBS-based and CS-based FDD) for CR= 11%.*

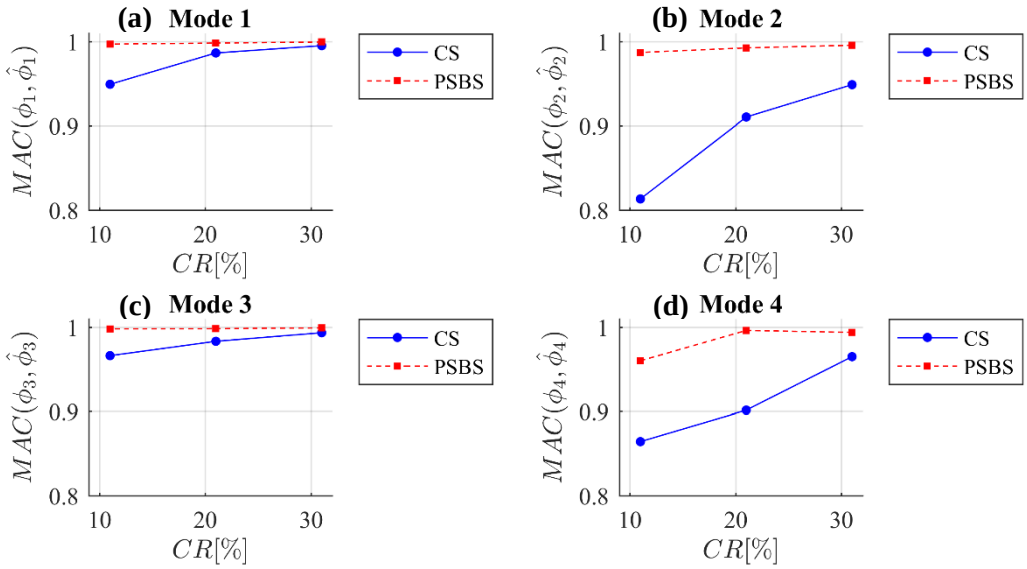

Figure 6.26: *MAC with respect to CR; PSBS-based approach compared against CS-based approach for S_T=3600*

The above figures confirm that the PSBS-based method outperforms in accuracy the CS-based approach, yielding higher MAC values in most of the cases considered. More importantly, the PSBS-based approach provides mode shapes exhibiting nearly unit MACs, even in the case of *CR*=11% without the need to assume a target sparsity level. On the antipode, the CS-based approach is considerably affected by the assumed S_T values. In fact, for the smaller compression level considered (*CR*=31%), better accuracy is achieved for larger S_T values for all mode shapes, at the expense of higher computational cost during the sparse recovery step (see Figure 6.14). However, such monotonic trends of MAC with S_T are not confirmed for all the mode shapes for the case of *CR*=11% in Figure 6.25, while the 2nd and 4th modes are not satisfactorily estimated regardless of the S_T value (*i.e.*, MAC values lying below 0.9 are commonly used as a practical criterion for rejecting mode shapes as inaccurate). As discussed before, this poor performance of the CS-based approach is related to the underlying level of sparsity of the acquired signals with respect to the number of compressed measurements, *M*, which is approximately 4 time smaller from the required value of *M* (*i.e.*, $M \approx S \cdot \log(N)$) for faithful reconstruction of the compressed datasets (see also the discussion above).

Remarkably, it appears that the performance of the PSBS approach in terms of MAC values is almost insensitive to *CR* observing a constant value close to unity in all cases of Figure 6.26, with the exception of the 4th mode at *CR*=11%. Nevertheless, it was deemed prudent not to consider lower *CR* values in this numerical assessment, since this would require a large number of cosets ($\bar{M}$ >14) or parallel channels (e.g., Figure 4.1) to satisfy the theoretical constraint of $\bar{M}^2 > \bar{N}$, as discussed in chapter 4. In fact, one may note that even the consideration of $\bar{M}$ =14 channels may be unrealistic in practice. However, this is a setting that has been used before in

pertinent theoretical studies (*e.g.*, *Ariananda & Leus* (2012); *Jingchao et al.* (2015); *TauSiesakul et al.* (2015); *Gkoktsi et al.* (2016)), while recent advancements in the hardware implementation of multi-coset samplers provide *CR*s independently of the number of interleaved ADCs (*e.g.*, *Moon et al.* (2015)).

As a final remark, it is expected that the gains to the *CR* achieved by the PSBS approach compared to the CS-based approach in accomplishing quality OMA estimates, as those reported above, would reflect analogously to energy savings in WSNs (*e.g.*, *Lynch et al.* (2003); *O'Connor et al.* (2014)). This is because wireless data transmission is by far the most power-hungry operation in wireless sensors, being directly related to the amount of data, *M*, transmitted from each sensor in the considered setting. This issue is addressed in the next section.

6.5. Energy Consumption and Battery Life Savings

This numerical example showcases the daily energy savings of the bridge monitoring system in section §6.4, based on the sampling rate reductions achieved by the proposed multi-sensor PSBS approach. To this end, a star network topology of equidistant wireless sensors is assumed, measuring bridge acceleration responses of approximately 10min every hour (*i.e.*, a dataset of Q=24 acceleration time-series are collected per wireless sensor within a day).

Table 6-5: Wireless Sensor WiseNode_v4 technical specifications

Mode	Current Drawn	Power Consumption
Idle	27 μA	81 μW
Sampling	variable	E_s/T_s (E_s=55.3 μJ)
ADC	0.72 mA	2.16 mW
Transmit	34.6 mA	103.8 mW

Energy consumption estimates are then computed for the three case studies in Table 6-2, considering a battery-operated wireless multi-coset sampler of $\bar{M}$ interleaved channels that operates at the sub-Nyquist sampling rates reported in Table 6-2. In active mode, the channels sampling activity is assumed to run concurrently with the analog-to-digital conversion (ADC), followed by the wireless data transmission operation. Table 6-5 reports the power requirements of the considered wireless sensor in idle and active modes, which have been adopted from a commercially available wireless sensor, *i.e.*, the WiseNode_v4, developed by *Novakovic et al.* (2009). Table 6-5 reports further the current drawn in each functionality mode assuming a supply voltage at 3V. It can be seen in Table 6-5 that the wireless transmit mode is the most power-consuming operation of the considered sensor, while the channel sampling activity has increased power demands at faster sampling rates, T_s.

It is assumed further that the sensor's power supply consists of two Energizer L91 AA-size lithium batteries with a nominal voltage of V=1.5V and a capacity of C=3000 mAh, providing a total energy of E_b=64800 J (*i.e.*, E_b= $(2C)\cdot(2V)\cdot 60^2$). A continuous discharge current is assumed to occur across the lifetime of the battery, pertaining to an annual battery energy loss due to leakage expressed in the percentage ratio of ξ=1%. In this respect, the following expression can be used

$$T_b = \frac{E_b}{E_{tot} + \xi \cdot E_b}, \tag{6.1}$$

to estimate the remaining battery life of the adopted wireless multi-coset sampler under various sampling rates, with E_{tot} being the total energy requirements of the sensor in all considered functionality modes.

Table 6-6 reports the daily energy demands and the required time in each functionality mode of the adopted multi-coset sampler for the three considered *CR* cases (*i.e.*, 31%, 21% and 11%). Specifically, for the case of *CR*=11%, the considered multi-coset sampler comprises $\bar{M}$ =14 channels, each operating at a sampling rate of $T_{s,CR}$=0.64 s, which is $\bar{N}$ =128 times slower than the conventional sampling, T_s=0.005 s, reported in sub-section §6.4.1. The above parameters define the power consumption due to sampling in $P_{s,CR} = \bar{M} \cdot (E_s / T_{s,CR}) = 1.21$ mW, with E_s given in Table 6-5. In this respect, the daily acquisition and discretisation of Q=24 compressed acceleration responses of M=11746 samples each requires 3.58 hours ($=Q\cdot M\cdot T_{s,CR}/\bar{M}$) of the sensor's sampling activity, consuming $E_{s,ADC}$= 43.45 Joules of energy per day. Assuming next that each ADC has a resolution of 16 bits (*i.e.*, 2 bytes), $I_{FWD}\approx$23507 bytes of data package information are generated per compressed acceleration sequence, which are wirelessly transmitted to the server within a time interval of $t_T = (I_{FWD} / I_{T1}) \cdot t_{T1} \approx 68.13s$, where I_{T1}=7 bytes is the information carried within one data package and t_{T1}= 0.02s is the time required for its wireless transmission (*e.g., Novakovic et al.* (2009)). Thus, 0.45 hours are required for the daily transmission of the considered dataset (*i.e.*, 24 compressed acceleration responses), consuming $E_T = 169.73$ $(= P_T \cdot t_T)$ Joules of energy per day. The adopted wireless sensor is assumed to be in the idle mode for the remaining $t_z = 19.96$ hours of the day, using $E_z = 5.82$ J $(= P_z \cdot t_z)$ of energy. Table 6-6 reports further the total energy requirements, E_{tot}, of the sensor per day, obtained from the superposition of the pertinent values in all considered functionality modes. Eq. (6.1) is used next to estimate the charging capacity of the battery source, which is presented in the last row of Table 6-6. The above PSBS-based energy consumption and battery life estimates are compared in Table 6-6 against the conventional approach at uniform sampling rate (*i.e.*, Figure 1.1(c) versus Figure 1.1(a)), assuming two different types of wireless sensors, *i.e.*, one that performs off-line lossless signal compression using the Huffman coding at *CR*=77.6% (*e.g.*,

Lynch et al. (2003)) and a second one that treats full-length datasets (*i.e.*, *CR*=100%) being in alignment with relevant studies in the literature (*e.g.*, *O'Connor et al.* (2013), (2014); *Klis & Chatzi* (2017)).

Table 6-6: Daily energy consumption and remaining battery life for various *CRs*

	Conventional				***PSBS***					
Mode	***CR*=100%***		***CR*=77.6%****		***CR*=31%**		***CR*=21%**		***CR*=11%**	
	Time [h]	Energy [J]	Time [h]	Energy [J]	Time [h]	Energy [J]	Time [h]	Energy [J]	Time [h]	Energy [J]
Idle	16.27	4.74	17.20	5.01	19.12	5.58	19.57	5.71	19.96	5.82
Sampling& ADC	3.58	170.48	3.58	170.48	3.58	72.42	3.58	57.11	3.58	43.45
Transmit	4.15	1551.85	3.22	1204.23	1.30	484.95	0.85	318.33	0.45	169.73
E_{tot} [J]	-	**1727.06**	-	**1379.72**	-	**562.95**	-	**381.14**	-	**219.01**
T_b [months]	-	**1.25**	-	**1.56**	-	**3.82**	-	**5.64**	-	**9.78**

**Non-compressive; **Off-line lossless compression*

The above table shows that the concurrent sampling and discretisation of a fixed time-window (*i.e.*, 10 mins per hour) of the observed bridge acceleration responses requires 3.58 hours regardless of signal compression. However, the benefits of the lower sampling rates are reflected to the reduced power consumption due to sampling, given its inverse proportionality to the sampling time T_s (see also Table 6-5), which, for the case of *CR*=11%, yields up to 4 times lower energy requirements compared to the conventional approaches. More importantly, significant energy gains are obtained at lower *CRs* due to the wireless transmission of a considerably smaller number of measurements. In this respect, substantial energy reduction is achieved in transmit mode, being directly proportional to the number of transmitted data. For the proposed multi-sensor PSBS approach with *CR*=11%, this energy reduction is of the order of 85-90% compared to conventional approaches at uniform sampling (*i.e.*, 86% compared to the conventional sampling scheme with off-line lossless compression and 89% for the non-compressive case). On the antipode, the decrease in the transmit time results in the prolongation of the idle state of the sensor and the associated energy consumption, which, however, is negligible compared to the power demands in the other modes, contributing very little to the total energy consumption reported in Table 6-6.

For illustration, Figure 6.27(a) plots the total energy consumption, E_{tot}, of the sensor per day as a function of *CR*, which decreases linearly at higher signal compression levels. The reduced energy consumption has a positive effect on the elongation of battery lifetime as shown in Figure 6.27(b). In fact, the battery life expectancy increases exponentially with lower *CRs*, leading to a

more sustainable bridge monitoring system with reduced costs associated with labour expenses and/or interruption of the normal operation of the monitored bridge.

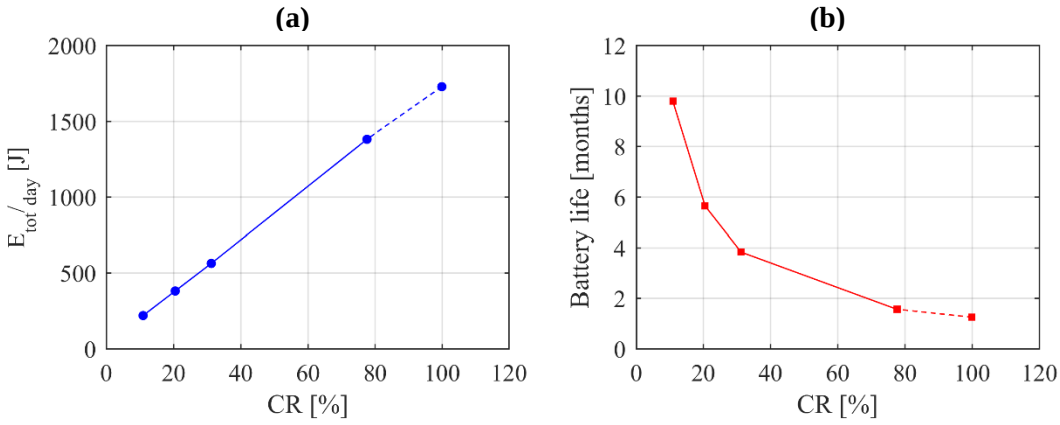

Figure 6.27: *Estimates of (a) the total energy requirements and (b) the battery life with respect to CR for the bridge case study*

The adopted sampling considerations also affect the distribution of the energy demands among the various sensor activities, expressed as the percentage ratio of the total energy consumption in each case. For example, Figure 6.28 illustrates the energy distribution for two different sampling schemes, *i.e.*, the conventional with off-line compression at *CR*=77.6%, and multi-coset sampling with *CR*=11%. It is readily observed in Figure 6.28 that the energy requirements in the wireless transmit mode dominate the performance of the wireless sensor, yielding a significantly higher percentage compared to all other functionality modes (*i.e.*, 87% and 77% for two sampling schemes, respectively). Comparing the two panels in Figure 6.28, it is seen that the slower sampling rate (Figure 6.28(b)) observes an increase in the contribution of the concurrent sensing and ADC operation to the total energy demands (e.g., from 12% to 20% in Figure 6.28). A similar increase occurs in the percentage energy consumption during the idle mode, which however remains negligible for this case study (*i.e.*, 1% and 3% in the two panels of Figure 6.28, respectively).

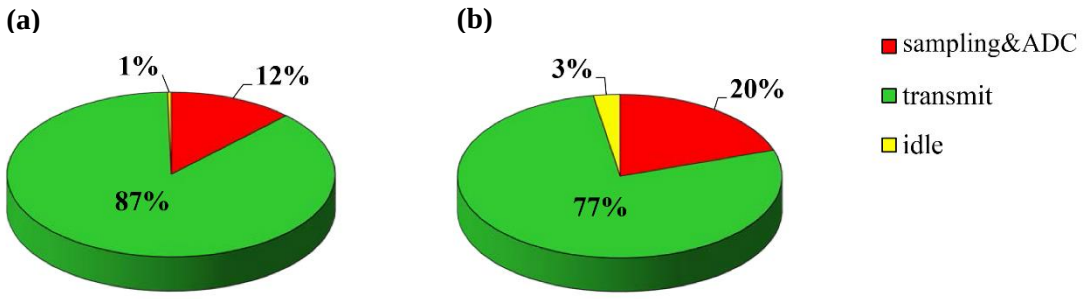

Figure 6.28: *Energy distribution in the various sensor activities for (a) the conventional sampling with CR=77.6% off-line lossless compression and (b) the multi-coset sampling scheme with CR=11% for the bridge case study*

It is noting in passing that the above energy and battery estimates have computed for the sensors activity during data acquisition and transmission, without considering the on-board off-line computational demands during lossless signal compression for the conventional approach. Further, any information related to the communication reliability (*i.e.*, communication protocol, loss of information due to packet error, multi-path fading, etc.) as well as external parameters that can adversely affect the operationality of the monitoring system (e.g. harsh environmental conditions, power shutdown at server, network failure etc.) were beyond the scope of this numerical evaluation. Finally, the network size has not been considered herein but a simplified case was employed pertaining to the power demands of a single wireless sensor operating under various sensing schemes. This simplified approach can be regarded as a rather conservative treatment since higher energy savings can be observed at larger WSNs, as reported by *Novakovic et al.* (2009); *O'Connor et al.* (2014).

6.6. Concluding Remarks

The performance of the novel PSBS-based spectral estimation approach proposed in §4 is numerically assessed vis-à-vis a recently developed in the literature CS-based approach in undertaking OMA. Both the approaches aim to reduce data transmission payloads facilitating reliable and cost-efficient long-term OMA via WSNs operating on different sub-Nyquist sampling schemes, *i.e.*, deterministic multi-coset (PSBS-based) versus random sub-Nyquist sampling (CS-based). The above is accomplished by considering compressed structural acceleration responses acquired at sub-Nyquist rates of *CRs* up to 31%, (*i.e.*, 31% below the conventional uniform sampling rate at Nyquist or above), and wirelessly transmitted to a base station without any local on-sensor data processing. The adopted approaches estimate the PSD matrix of the acceleration signals by processing sub-Nyquist/compressed measurements at the base station. Then, the standard FDD algorithm for OMA is applied to the estimated PSD matrix to extract the inherent modal properties of the monitored structures. The percentage difference error and the MAC have been used as error metrics to quantify the accuracy of the extracted natural frequencies and mode shapes, respectively, at the excited modes of vibration. These error metrics have been computed with respect to the modal quantities retrieved from Nyquist sampled acceleration signals.

Two sets of acceleration signals have been considered. The first set was generated through linear response history analysis of a simply supported steel beam excited by white-noise. Additive white Gaussian noise was considered at SNR=10dB to produce a suite of relatively low-sparse acceleration signals in the frequency domain, aiming to gauge the influence of signal sparsity to the performance of the considered approaches vis-à-vis the high-sparse noiseless signals. The second set of signals was acquired from an array of 18 tethered sensors deployed onto a particular

overpass in Zürich, Switzerland open to the traffic. Pertinent post-processing and statistical stationarity tests were applied to the field recorded data prior to compressive sampling.

It has been numerically shown and theoretically justified, that, for a given sub-Nyquist sampling rate, the capability of the CS-based approach to extract faithful estimates of the mode shapes depends heavily on the target sparsity level, S_T, which needs to be assumed in the CS signal reconstruction step. It has also been demonstrated that the accuracy of the CS-based approach improves at larger S_T values at the cost of higher computational effort reflected on the increased required runtime of the adopted CS sparse signal recovery algorithm. However, no increase to the assumed S_T value can compensate for the acquisition of an excessively small number of compressed measurements which is the case for CR=11% for all the sets of acceleration signals considered in this work. In this regard, it is concluded that conservative compression ratios should be adopted in using the CS-based approach to ensure acceptable quality of modes shapes, especially in the case where no prior knowledge on the acceleration signal sparsity is available.

On the antipode, it was numerically shown that the PSBS-based approach, which treats response acceleration signals as wide-sense stationary stochastic processes without imposing any signal sparsity conditions, performs equally well and consistently better than the CS-based approach in extracting mode shapes for all the herein considered sets of compressively sampled acceleration signals. In fact, the PSBS-based approach yields MAC>0.96 even for the low-sparse signals contaminated with white noise at SNR=10dB and for low sampling rates at CR=11% (*i.e.*, 89% below the Nyquist rate). It was further confirmed that significant energy gains can be achieved by the proposed method at such low *CRs* in battery-operated wireless sensors. This was numerically verified based on the power requirements of a commercially available wireless sensor in idle and active (*i.e.*, sampling, transmit) mode. The estimated energy savings were evaluated against two conventional approaches at uniform sampling rates – one that involves off-line lossless signal compression on-board at an assumed *CR* of approximately 77.6%, and a second one applied on full-length signals (*i.e.*, no compressive case).

Overall, the herein numerical data demonstrate that the inherent signal agnostic attributes of the PSBS-based approach render this method more advantageous compared to the CS-based approach in cases where high signal compression levels are desired to address sensor power consumption and wireless bandwidth transmission limitations. Still, further research is warranted to assess the potential of the considered PSBS-based spectral estimation approach in actual field deployments. Such an assessment necessitates the development of custom-made wireless sensors featuring either multi-coset samplers at the hardware level or, alternatively, efficient algorithms for off-line on-sensor multi-coset sampling. These aspects are an open area of research in the sensors community.

Chapter 7
A Novel MUSIC-Based Approach for Structural Damage Detection from Sub-Nyquist Measurements

7.1. Preliminary Remarks

In this chapter, a *sub-Nyquist pseudo-spectral estimation method* is proposed as a viable alternative for low-cost and power efficient wireless sensors in monitoring heavily instrumented structures (see also Figure 1.1(d)). This approach couples the deterministic sub-Nyquist *co-prime sampling* scheme proposed by *Vaidyanathan & Pal* (2011) with the *multiple signal classification* (MUSIC) algorithm for spectral estimation (*e.g.*, *Marple* (1987)) – a fusion that was originally developed in radar applications to address the bandwidth limitations in wireless communications and detect unoccupied bands in telecommunication signals buried in noise (see also *Vaidyanathan & Pal* (2011)).

Similar to the multi-coset PSBS method of Chapter 4 (§*4. Proposed Multi-Sensor Power Spectrum Blind Sampling Approach for OMA: Theory*), the herein adopted co-prime MUSIC strategy does not rely on any signal sparsity condition while it treats the acquired signals as wide-sense stationary stochastic processes (random signals), being consistent with the OMA framework that assumes stochastic input excitation and linear structural responses (*e.g.*, *Brincker & Ventura* (2015)). Further, it is a signal reconstruction-free compressive power spectral estimation approach that utilises the *spatial smoothing technique* developed by *Pal & Vaidyanathan* (2011) to retrieve auto-correlation functions of stochastic structural response processes directly from noisy compressed measurements without undertaking any pre-processing operation to remove noise.

Despite the above similarities, the co-prime sampling scheme is fundamentally different from the multi-coset sampling, as it considers two sensors per acceleration channel operating at different sub-Nyquist rates and accumulating collectively in time a much smaller number of measurements than a single sensor operating at Nyquist rate. Moreover, the adopted MUSIC algorithm is a "super resolution" pseudo-spectral estimator (*i.e.*, not a true PSD estimator) that relies on the eigenvalue decomposition of autocorrelation matrices, yielding a spectrum-like

shape with very sharp peaks at the frequency components of the analysed signals. As opposed to the PSBS-based approach in Chapter 4, the co-prime MUSIC algorithm does not return cross-spectral estimates between structural responses, but it is particularly useful in estimating closely-spaced natural frequencies from compressed structural responses contaminated with high level noise.

The advantages offered by the co-prime MUSIC algorithm are exploited in the current research study for the first time to address the modal coupling effect in OMA applications in the presence of noise. To this end, parametric analyses are undertaken using computer-simulated acceleration structural responses derived from a multi-degree-of-freedom system with two closely-spaced modes of vibration. The focus is primarily placed on the performance assessment of the sub-Nyquist pseudo-spectral estimator in resolving the two closely-spaced resonances under various signal compression and noise levels.

Motivated further by recent OMA-based studies for rapid condition assessment of instrumented structures in the aftermath of earthquake events *Jiang & Adeli* (2007); *Rainieri et al.* (2012); *Foti et al.* (2014), a novel damage detection strategy is proposed herein aiming to infer structural damage due to low-intensity earthquake excitations by monitoring small shifts to the resonant frequencies directly from compressed response acceleration measurements without involving time-domain signal reconstruction operations and without imposing signal sparsity constraints. The effectiveness and applicability of the proposed approach is numerically assessed by considering simulated acceleration response signals corrupted by different levels of additive white noise, originating from a low-amplitude white-noise excited 3-storey reinforced concrete frame building before and after being exposed to a particular ground motion, pertaining to a healthy and to a potentially damaged state, respectively. Two earthquake intensities are considered through scaling of the input ground motion, yielding different levels of structural damage. Special attention is given in modelling the different levels of earthquake-induced damage, based on localised stiffness degradation at the formed plastic hinge zones, as this is captured by the well-known Takeda hysteretic model in conducting non-linear response history analysis.

It is noted in passing that the MUSIC algorithm has also been considered in the past for earthquake-induced damage detection in building structures (*e.g.*, *Jiang & Adeli* (2007)), using conventional sensors to acquire structural acceleration signals at Nyquist rate. Furthermore, this pseudo-spectrum technique has found to outperform conventional FFT-based spectral estimators for VSHM applications (*e.g.*, *Amezquita-Sanchez et al.* (2012); *Camarena-Martinez et al.* (2014)). The latter is attributed to the high resolution achieved by the MUSIC spectral estimator, which is capable to capture very small changes in resonant frequencies of linear structural response acceleration (random) signals between healthy and damaged structural states.

Thus, it is envisioned that the consideration of the proposed sub-Nyquist MUSIC-based damage detection approach will facilitate the widespread installation of VSHM systems in civil engineering structures located in seismically prone areas (*e.g., Gattulli et al.* (2014)). This will lead to reduced installation, operational and maintenance cost of the monitoring systems, paving the way towards more resilient communities against the seismic hazard.

The next section of this chapter (§*7.2. Theoretical Background*) outlines the theory of the adopted co-prime sampling method along with the spatial smoothing technique for auto-correlation function estimation, and reviews the mathematical details of the MUSIC algorithm. Section 7.3 (§*7.3. Performance Assessment of the Sub-Nyquist MUSIC Algorithm with Simulated Closely-Spaced Modes of Vibration in Noisy Environments*) appraises the usefulness of the adopted sub-Nyquist pseudo-spectral estimation method in OMA applications and numerically attests its efficiency in separating two closely-spaced natural frequencies from compressed data contaminated with noise. Section 7.4 (§*7.4. Sub-Nyquist MUSIC for Earthquake Damage Detection*) showcases the damage detection capabilities of this method and furnish novel numerical results originating from noise-corrupted response acceleration signals recorded on a 3-storey frame building subjected to seismic excitations of increased intensity. Finally, section 7.5 (§*7.5. Concluding Remarks*) summarises concluding remarks.

The mathematical details of the co-prime sampling and the MUSIC algorithm given in §7.2 along with the novel post-earthquake damage detection results of section 7.4 have been published in the conference proceedings in [C8] (see also section 1.5 (§1.5. List of Referred Papers)). It is further noted that the numerical assessment in §7.3 has not been disseminated yet in the public domain.

7.2. Theoretical Background

7.2.1. Co-prime sampling and auto-correlation estimation of stationary stochastic processes

Let $x(t)$ be a real-valued wide-sense stationary band-limited stochastic process (or random signal), expressed as a superposition of R sinusoidal functions with frequencies f_r, real amplitudes B_r, and uncorrelated random phases θ_r uniformly distributed in the interval $[0, 2\pi]$, where $r=1,2,\ldots,R$. That is,

$$x(t) = \sum_{r=1}^{R} B_r \cos(2\pi f_r t + \theta_r), \tag{7.1}$$

where $j = \sqrt{-1}$. Co-prime sampling (*e.g., Pal & Vaidyanathan* (2011); *Vaidyanathan & Pal* (2011)) assumes that the signal $x(t)$ is simultaneously acquired by two sampling devices, operating

at different (sub-Nyquist) sampling rates, $1/(N_1T_s)$ and $1/(N_2T_s)$, where N_1, N_2 are co-prime numbers ($N_1 < N_2$), and $1/T_s = 2f_{\max}$ is the Nyquist sampling rate with $f_{\max}$ being the highest frequency component in (7.1). The signal $x(t)$ is then divided in time blocks of $(2N_1\text{-}1)N_2T_s$ duration and, within each such block, only $2N_1+N_2\text{-}1$ samples are retained from a total number of $floor\{2(N_1+N_2)\text{-}1\text{-}N_2/N_1\}$ acquired measurements. The thus retained samples of $x(t)$ from the two different samplers are

$$\begin{aligned} x_1[k] &= x\left(kN_1T\right) = \sum_{r=1}^{R} B_r \cos(2\pi f_r kN_1T_s + \theta_r) + \varepsilon_1[k], \quad k \in \{0,\ldots,N_2-1\} \\ x_2[\ell] &= x\left(\ell N_2T\right) = \sum_{r=1}^{R} B_r \cos(2\pi f_r \ell N_2T + \theta_r) + \varepsilon_2[\ell], \quad \ell \in \{1,\ldots,2N_1-1\} \end{aligned}, \tag{7.2}$$

where $\varepsilon_1[k]$ and $\varepsilon_2[\ell]$ are zero-mean Gaussian white noise sequences, assumed to have the same power, σ_ε^2. Notably, the noise sequences $\varepsilon_1[k]$ and $\varepsilon_2[\ell]$ in eq.(7.2) are added at the output of the two sampling devices and assumed to be uncorrelated with the signals and from each other. In this manner, N_2 samples are obtained from the first device, which operates at sampling rate $1/(N_1T_s)$. Similarly, $(2N_1-1)$ samples are retrieved from the second device with sampling rate $1/(N_2T_s)$. This choice is not arbitrary; it was shown by *Vaidyanathan & Pal* (2011) that the cross-difference set of numbers $\Omega = \{N_2\ell - N_1k,\ k \in \{0,\ldots,N_2-1\},\ \ell \in \{1,\ldots,2N_1-1\}\}$ contains all possible integers within the range $[-N_1N_2,\ N_1N_2]$. Thus, the cross-correlation function of the sequences $x_1[k]$, $x_2[\ell]$, whose support involves all the time-lags included in the set Ω, can be continuously estimated in the above range of interest. To this aim, the sequences in eq.(7.2) are first stacked in a vector $\mathbf{y}_n \in \mathbb{R}^{(2N_1+N_2-1)}$ as in

$$\begin{aligned} \mathbf{y}_n &= \left[x_1^{\mathrm{T}}\left[2N_2n+k\right] \quad x_2^{\mathrm{T}}\left[2N_1n+\ell\right] \right]^{\mathrm{T}} \\ &= \sum_{r=1}^{R} B_r\ \mathbf{e}(f_r)\ \cos(2\pi f_r N_1N_2nT_s + \theta_r) + \boldsymbol{\varepsilon}_n \end{aligned}, \tag{7.3}$$

where the superscript "T" denotes vector/matrix transposition, $\boldsymbol{\varepsilon}_n \in \mathbb{R}^{(2N_1+N_2-1)}$ is the vector collecting the noise terms, and $\mathbf{e}(f_r) \in \mathbb{R}^{(2N_1+N_2-1)}$ is given by

$$\begin{aligned} \mathbf{e}(f_r) = \big[& 1 \quad \cos(2\pi f_r\ N_1T_s) \quad \cdots \quad \cos(2\pi f_r (N_2-1)N_1T_s) \\ & \cos(2\pi f_r\ N_2T_s) \quad \cdots \quad \cos(2\pi f_r (2N_1-1)N_2T_s) \big]^{\mathrm{T}} \end{aligned}. \tag{7.4}$$

Notably, in eq.(7.3), the inclusion of the non-negative integer index $n \in \mathbb{Z}^*$ allows for arbitrarily placing the co-prime sampling block in time (*e.g.*, for n=0 the time block starts at t=0 and corresponds to the block considered in eq.(7.2)). Therefore, an arbitrary large number of

blocks (and corresponding vectors $\mathbf{y}_n$) can be used for co-prime sampling a theoretically infinitely long random signal $x(t)$. The position of each block in time depends on the adopted values of n. The autocorrelation matrix of $\mathbf{y}_n$ is given as (see also *Pal & Vaidyanathan* (2011))

$$\mathbf{R}_{\mathbf{yy}} = \mathrm{E}\left\{\mathbf{y}_n\ \mathbf{y}_n^{\mathrm{T}}\right\} = \sum_{r=1}^{R} B_r^2\ \mathbf{e}(f_r)\ \mathbf{e}^{\mathrm{T}}(f_r) + \sigma_\varepsilon^2 \mathbf{I}\,, \tag{7.5}$$

in which $\mathbf{I} \in \mathbb{R}^{(2N_1+N_2-1)\times(2N_1+N_2-1)}$ is the identity matrix, while the mathematical expectation operator $\mathrm{E}\{\cdot\}$ averages over n. In other words, the matrix $\mathbf{R}_{\mathbf{yy}}$ in eq.(7.5) is computed by averaging over all the time blocks considered in sampling, within a Monte Carlo-based context.

Next, following the spatial smoothing technique by *Pal & Vaidyanathan* (2011), the autocorrelation matrix in eq.(7.5) is first stacked in a column vector, $\mathbf{r}_{\mathbf{y}} = \mathrm{vec}\left(\mathbf{R}_{\mathbf{yy}}\right)$, with $\mathbf{r}_{\mathbf{y}} \in \mathbb{R}^{(2N_1+N_2-1)^2\times 1}$. Then, the elements of $\mathbf{r}_{\mathbf{y}}$ are sorted and truncated within the range [$-N_1N_2$, N_1N_2], while the repeated terms are eliminated, so that the integer indices of the exponential terms in eq.(7.4) are given in increasing order with no repetition. The thus generated reduced autocorrelation vector $\hat{\mathbf{r}}_{\mathbf{y}}$ (*i.e.* sorted and truncated), is subsequently divided into i={ 1,2,…, N_1N_2+1 } overlapping subarrays, $\hat{\mathbf{r}}_{\mathbf{y}_i}$, each consisting of ($N_1N_2$+1) elements, which are averaged as in

$$\mathbf{R}_{ss} = \frac{1}{N_1N_2+1} \sum_{i=1}^{N_1N_2+1} \hat{\mathbf{r}}_{\mathbf{y}_i} \hat{\mathbf{r}}_{\mathbf{y}_i}^{\mathrm{T}}\,, \tag{7.6}$$

to generate the spatially smoothed matrix $\mathbf{R}_{ss} \in \mathbb{R}^{(N_1N_2+1)\times(N_1N_2+1)}$. In the following section, this matrix is used as input to a specific super-resolution spectral estimator to detect the R frequencies f_r, (r= 1,2,…,R), of the considered stochastic process $x(t)$.

7.2.2. Multiple signal classification (MUSIC) algorithm for resonant frequencies estimation

The Multiple Signal Classification (MUSIC) algorithm (*e.g.*, *Marple* (1987)) is a super-resolution pseudo-spectrum estimation method, which relies on the eigenvalue decomposition of autocorrelation matrices estimated by field measurements. For the purposes of this study, the MUSIC algorithm is applied to the autocorrelation matrix $\mathbf{R}_{ss}$ in eq.(7.6), which is decomposed as in

$$\mathbf{R}_{ss} = \sum_{i=1}^{R} (\lambda_i + \sigma_\varepsilon^2)\mathbf{v}_i\,\mathbf{v}_i^{\mathrm{T}} + \sum_{i=R+1}^{N_1N_2+1} \sigma_\varepsilon^2 \mathbf{v}_i\,\mathbf{v}_i^{\mathrm{T}}\,, \tag{7.7}$$

where the eigenvectors $\mathbf{v}_i$ are orthonormal, *i.e.* $\mathbf{v}_i \mathbf{v}_j^{\mathrm{T}} = 0$ for $i \neq j$. The first term in eq.(7.7) represents the signal sub-space with R eigenvalues $(\lambda_i + \sigma_\varepsilon^2)$, i=1,…,R, and R principal eigenvectors spanning the same subspace with the signal vector in eq.(7.4). Likewise, the second term corresponds to the noise sub-space with (N_1N_2-R) identical eigenvalues σ_ε^2, and (N_1N_2-R) eigenvectors.

The cost function of the unbiased MUSIC estimator is then given as

$$G_{MUSIC}(f) = \frac{1}{\mathbf{e}^{\mathrm{T}}(f) \cdot \left(\sum_{i=R+1}^{N_1N_2+1} \mathbf{v}_i \mathbf{v}_i^{\mathrm{T}} \right) \cdot \mathbf{e}(f)}, \tag{7.8}$$

The above estimator (pseudo-spectrum) relies on the orthogonality condition between the signal vectors and the noise sub-space, that is,

$$\mathbf{e}^{\mathrm{T}}(f_r) \cdot \left(\sum_{i=R+1}^{N_1N_2+1} \mathbf{v}_i \right) = 0, \quad \text{for } r = \{1,...,R\}, \tag{7.9}$$

which attains, theoretically, infinite values at the locations on the frequency axis where the natural frequencies of the considered system lie, *i.e.* at f=f_r in eq.(7.8). In practical numerical applications, though, involving errors in solving the eigenvalue problem and other estimation errors, eq.(7.8) takes finite values observing sharp peaks at each f_r and resulting in a spectrum-like shape. Limitations of the MUSIC algorithm are the *a priori* knowledge on the number of R signal components required, as well as the increased computational demands of the eigenvalue decomposition in eq.(7.7). Nonetheless, the significance of utilising the MUSIC algorithm together with the co-prime sampling strategy and the spatial smoothing technique lies on its capability to capture up to $R \leq N_1N_2$ natural frequencies in noisy signals, at the high frequency resolution of $1/(N_1N_2T_s)$ (in Hz), outperforming conventional approaches at Nyquist rate that can only retrieve up to ($2N_1$+N_2-2) frequencies (see also *Pal & Vaidyanathan* (2011)).

7.3. Performance Assessment of the Sub-Nyquist MUSIC Algorithm with Simulated Closely-Spaced Modes of Vibration in Noisy Environments

7.3.1. Structural system and simulated noisy acceleration responses

In this section, the potential of the MUSIC algorithm to resolve closely-spaced natural frequencies from co-prime sampled response acceleration signals contaminated with high level noise is numerically assessed. To this end, the simulation-based framework presented in §5.2 is adopted herein to generate discrete-time Nyquist-sampled acceleration responses of white-noise

excited MDOF structural dynamical systems with R vibrating modes and PSDs given by eq.(5.2). Recall from chapter 5 that the above is accomplished by considering the steady-state response of several different white-noise excited discrete-time auto-regressive moving average (ARMA) filters. The coefficients of these ARMA filters are defined via the *auto/cross correlation matching algorithm* by *Spanos & Zeldin* (1998) using eqs. (5.2), (5.4), and (5.5).

Note that this approach of obtaining response acceleration signals enables the consideration of a range of different MDOF structural systems (*i.e.*, with different dynamic/modal properties) which are conveniently defined in terms of their natural frequencies, ω_r, damping ratios, ζ_r, and mode shapes at the R vibrating modes (r=1, 2, …, R). Note that any information related to the modal deflected shapes can be efficiently captured by the weighting factors A_{rs} in the R^2 contributing terms of eq.(5.2) (see also §5.2). Therefore, the requirement for defining explicitly a mass, a damping, and a stiffness matrix for each system is by-passed. This consideration facilitates significantly the following comprehensive parametric analyses where two different structural systems are utilised with heuristically defined natural frequencies and relative spectral peak amplitudes.

Specifically, a continuous MDOF structural system with R=3 degrees of freedom (*i.e.*, 3DOF system) is assumed with two equally-excited closely-spaced modes of vibration and a third less excited mode of relatively low spectral amplitude. The above system is approximated via the simulation-based framework in §5.2, considering a critical damping of ζ_r =5% (r=1,2,3) in all vibrating modes along with the spectral (weighting) coefficients A_{11}= A_{13}= A_{31}=A_{22}= A_{23}= A_{32}=1, A_{12}=A_{21}=2, A_{33}=0.25 in eq.(5.2). Two different case studies are examined for the above 3DOF system with natural frequencies:

(1) f_1=67 Hz, f_2=70 Hz, and f_3=120 Hz (*i.e.*, the percentage difference between f_1 and f_2 is df/f=4.5%); and

(2) f_1=66 Hz, f_2=70 Hz, and f_3=120 Hz (*i.e.*, the percentage difference between f_1 and f_2 is df/f=6%).

For the two adopted systems, Figure 7.1 illustrates the PSDs derived from eq.(5.2), representing the "target" spectra that are sought to be captured by the proposed sub-Nyquist pseudo-spectral estimation method (*i.e.*, MUSIC algorithm fused with co-prime sampling techniques). In this respect, each target PSD is first replaced by a surrogate discrete-time ARMA filter of order (120, 12) subject to a clipped white-noise excitation of 20s duration, sampled at a Nyquist rate of F_s=1/T_s=500Hz (*i.e.*, T_s=0.002s). The *auto/cross correlation matching* algorithm by *Spanos & Zeldin* (1998) is then employed to compute the ARMA coefficients using eqs. (5.2), (5.4), and (5.5), and derive (noiseless) discrete-time acceleration response signals at Nyquist, treated as realisations of an underlying stochastic process.

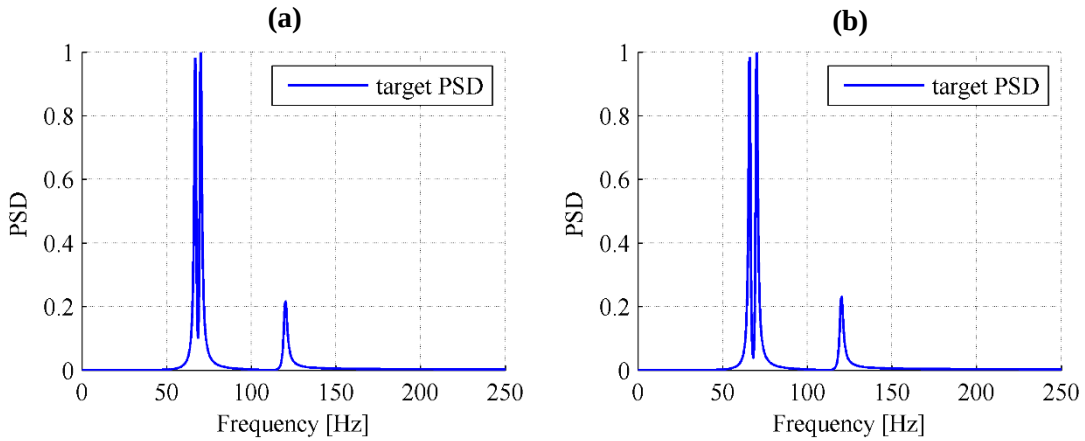

***Figure 7.1**: Normalised target PSD curves to their maximum amplitude (derived from eq. (5.2)) for the two adopted 3DOF system with closely-spaced natural frequencies pertaining to (a) df/f=5% (f_1=67Hz, f_2=70Hz) and (b) df/f=6% (f_1=66Hz, f_2=70Hz).*

To assess the efficacy of the proposed sub-Nyquist pseudo-spectral estimation method at various noise levels, the above generated discrete-time acceleration responses are then corrupted with additive white noise at five *SNRs* (*i.e.*, $SNR = 10 \cdot \log_{10}\left(\sigma_x^2 / \sigma_\varepsilon^2\right)$, with σ_x^2 and σ_ε^2 denoting the signal and noise variance, respectively) between 0 dB and 20 dB to simulate structural responses buried in high level noise. Note that the limiting case of *SNR*=0 dB corresponds to equal power in signal and noise components (*i.e.*, extreme noise case with $\sigma_e^2 \approx \sigma_x^2$), while the case of *SNR*=20 dB pertains to a relatively lower noise level with $\sigma_e^2 \approx 0.01 \cdot \sigma_x^2$.

7.3.2. Sub-Nyquist pseudo-spectral estimation

The obtained noisy acceleration responses are sub-Nyquist sampled (compressed) at 4 different levels, using the co-prime sampling strategy reviewed in sub-section §7.2.1 with the sampling parameters reported in Table 7-1. In particular, 4 different pairs of co-prime numbers, (N_1, N_2), are considered, pertaining to different average sub-Nyquist sampling rates, $1/(N_1T_s) + 1/(N_2T_s)$, spectral resolutions, $1/(N_1N_2T_s)$, and other sampling features as listed in Table 7-1 (*e.g.*, cross-difference set Ω, number of non-overlapping time-blocks the signal is divided, number of Nyquist and compressed samples per block, size of spatially smoothed autocorrelation matrix, etc.).

For example, consider the sub-Nyquist sampling case with co-prime N_1=7 and N_2=11. The underlying assumption is that two samplers are deployed per recording location to acquire uniform samples of the same acceleration response signal (in time), with sampling rates equal to $1/(7T_s)$ and $1/(11T_s)$, respectively. Therefore, the two co-prime samplers accumulate measurements at an average rate of $1/(7T_s) + 1/(11T_s)$ samples per second, which is about 76.6% lower than the Nyquist rate. Further, the assumed co-prime numbers define the cross-difference

set $\Omega = \{11\ell - 7k,\ k \in [0,10], \ell \in [1,13]\}$, which includes all discrete time lags within the support [-77, 77] of the cross-correlation function between the measurements of the two sensors (see also section §7.2.1). It is further assumed that the measured acceleration signal is divided in K=69 non-overlapping time-blocks that are further used for the computation of the autocorrelation matrix in eq.(7.5). Each block contains $(2N_1\text{-}1)\times N_2$=143 Nyquist samples from which only $2N_1+N_2\text{-}1$= 24 samples are taken to populate the $\mathbf{R}_{yy} \in \mathbb{R}^{24\times 24}$ matrix in eq.(7.5). Next, the spatially smoothing technique by *Pal & Vaidyanathan* (2011) is employed to generate the semi-positive correlation matrix $\mathbf{R}_{ss} \in \mathbb{R}^{78\times 78}$ in eq.(7.6) directly from the coprime-sampled (compressed) measurements. Finally, the MUSIC algorithm reviewed in sub-section §7.2.2 is applied, by first considering the eigenvalue decomposition of the spatially smoothed matrix $\mathbf{R}_{ss}$ in eq.(7.7). Finally, the MUSIC estimator in eq.(7.8) is evaluated, based on the assumption of R=3 degrees of freedom being present in the measured acceleration response signals. For the other sub-Nyquist sampling cases in Table 7-1 the pertinent co-prime parameters are defined in a similar manner as above.

Table 7-1: Adopted co-prime sampling values

Co-prime Numbers	**(N_1, N_2)**	**(3,7)**	**(5,7)**	**(7,11)**	**(7, 13)**
Average sampling rate [Hz] (below Nyquist rate)	$\frac{1}{N_1T_s}+\frac{1}{N_2T_s}$	238.10 (52.4%)	171.43 (65.7%)	116.88 (76.6%)	109.89 (78.0%)
Frequency Resolution [Hz]	$\frac{1}{N_1N_2T_s}$	23.81	14.29	6.49	5.49
cross-difference set	Ω	$\{7\ell-3k\}$ $\ell\in[1,7]$ $k\in[0,6]$	$\{7\ell-5k\}$ $\ell\in[1,9]$ $k\in[0,6]$	$\{11\ell-7k\}$ $\ell\in[1,13]$ $k\in[0,10]$	$\{13\ell-7k\}$ $\ell\in[1,13]$ $k\in[0,12]$
Co-prime Numbers	**(N_1, N_2)**	**(3,7)**	**(5,7)**	**(7,11)**	**(7, 13)**
Size of spatially smoothed autocorrelation matrix	$(N_1N_2+1)\times(N_1N_2+1)$	22×22	36×36	78×78	92×92
Number of blocks	K	285	144	69	59
Nyquist samples / block	$(2N_1\text{-}1)\times N_2$	35	63	143	169
Sub-Nyquist samples / block	$2N_1+N_2\text{-}1$	12	16	24	26

7.3.3. Identification of closely-spaced structural resonances from noisy data

Further to the above, Figure 7.2 and Figure 7.3 illustrate the obtained pseudo-spectra for the two 3DOF structural systems, respectively. In each figure, the four co-prime cases of Table 7-1

are presented in different panels which present in three-dimensional plots the five PSD curves derived from co-prime sampled noisy acceleration responses at the five adopted *SNR* values in the range [0, 20] dB. The derived PSDs are normalised to unity amplitude to facilitate comparison and plotted with different colours along a horizontal axis labelled after the pertinent *SNRs*.It is readily observed from Figure 7.2 and Figure 7.3 that the efficacy of the adopted sub-Nyquist MUSIC algorithm in extracting two closely-spaced natural frequencies depends strongly on the frequency resolution supported by the considered co-prime sampling scheme.

For instance, consider the 1st case study in Figure 7.1(a), in which the first two natural frequencies are located very close to each other, yielding a percentage difference of approximately df/f=4.5%. For this case, Figure 7.2 (a) reveals that the co-prime MUSIC algorithm associated with a low frequency resolution at 23.81Hz (for N_1=3, N_2=7) cannot separate the closely-spaced frequencies; instead, it merges together the two underling resonances, yielding a unique spectral peak at an average frequency value. Notably, the third and less excited natural frequency can be efficiently retrieved from the resolved spectral peak at 120Hz. Nonetheless, the combination of low resolution and high noise level (below 10dB) can lead to false frequency estimation since spurious spectral peaks are observed at higher frequencies which lie beyond the range of interest. Similar remarks hold for the co-prime sampling case in Figure 7.2 (b) for N_1=5, N_2=7, pertaining to a relatively coarse frequency resolution (at 14.29 Hz) for the problem at hand. On the antipode, at a higher resolution of 6.49 Hz, Figure 7.2 (c) confirms that the co-prime MUSIC algorithm yields sharper spectral peaks, capable to isolate the two closely-spaced natural frequencies and retrieve the poorly excited mode of vibration with high accuracy. It is further observed that the adopted pseudo-spectral estimator is practically immune to noise, yielding exactly the same performance for *SNRs* as low as 5dB. More importantly, the proposed sub-Nyquist MUSIC algorithm attains higher resolution as larger co-prime numbers are employed (*i.e.*, N_1=7, N_2=11) which are associated with slower sampling rates (*i.e.*, 76.6%) and stronger signal compression (see also Table 7-1). Interestingly, Figure 7.2 (d) suggests that the obtained results do not improve any further at higher spectral resolution (*e.g.*, 5.49 Hz for N_1=7, N_2=13) in this particular study.

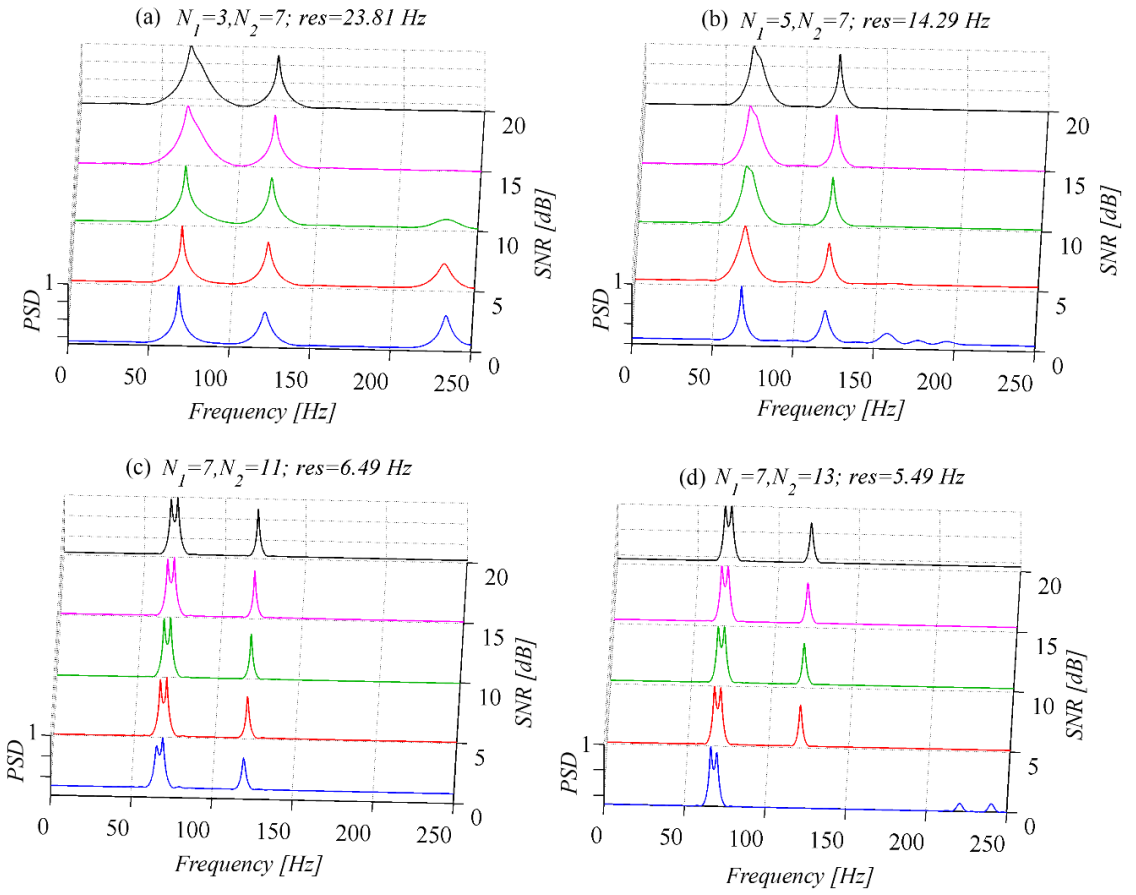

Figure 7.2: *Parametric analysis with respect to SNR for the MUSIC and co-prime method for df/f=5% (f_1=67Hz, f_2=70Hz); (a) N_1=3, N_2=7, resolution 23.81Hz (b) N_1=5, N_2=7, resolution 14.29Hz (c) N_1=7, N_2=11, resolution 6.49Hz (b) N_1=7, N_2=13, resolution 5.49Hz*

The above observations are also confirmed in Figure 7.3 for the 2nd case study, which yields a larger percentage difference of approximately 6% between the first two resonances of the adopted structural system. The latter suggests that the modal coupling effect is less severe in this case compared to the previous one, which explains the slightly improved performance of the low-resolution pseudo-spectral estimators of Figure 7.3 (a, b) in approximating the three underlying spectral peaks from compressed measurements.

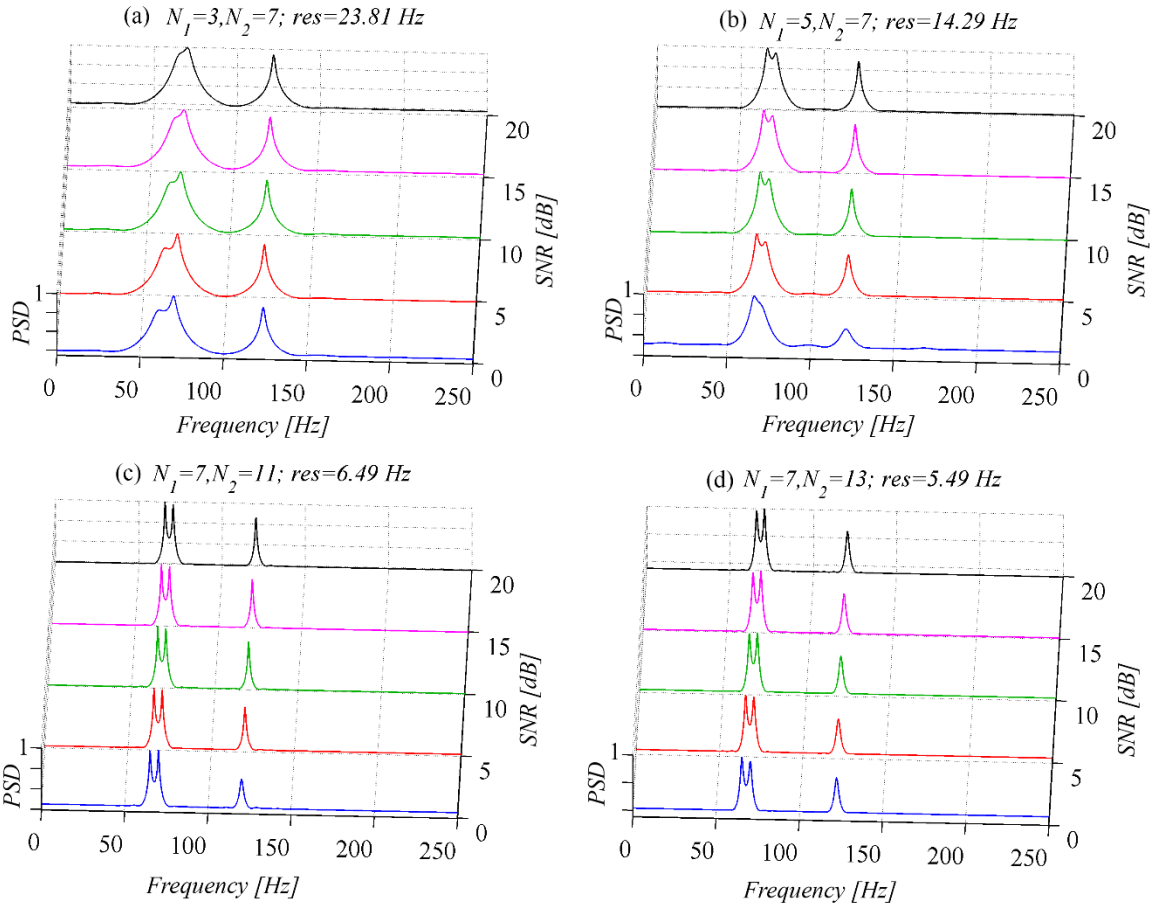

Figure 7.3: *Parametric analysis with respect to SNR for the MUSIC and co-prime method for df/f=6% (f_1=66Hz, f_2=70Hz); (a) N_1=3, N_2=7, resolution 23.81Hz (b) N_1=5, N_2=7, resolution 14.29Hz (c) N_1=7, N_2=11, resolution 6.49Hz (b) N_1=7, N_2=13, resolution 5.49Hz*

7.4. Sub-Nyquist MUSIC for Earthquake Damage Detection

Having proved the efficiency of the sub-Nyquist MUSIC algorithm in resolving closely-spaced natural frequencies, this numerical example illustrates its usefulness for OMA and structural damage detection in low-intensity earthquake excitations by measuring small changes in resonances between healthy and damaged structural states.

7.4.1. Adopted structure and seismic action

In this numerical example, a planar 3-storey single-bay reinforced concrete frame is considered. Figure 7.4 illustrates the adopted structure and provides further the geometrical properties of the frame along with the longitudinal and transverse reinforcement of its beams and columns. The nominal concrete strength is taken equal to 20MPa, while the characteristic steel yielding strength is f_{yk}=400MPa for both the longitudinal and transverse reinforcement and the

steel hardening ratio is taken as f_{uk}/f_{yk}=1.15. In computing the axial forces carried by the columns, a gravitational uniform distributed load along the beams equal to 35 kN/m is assumed.

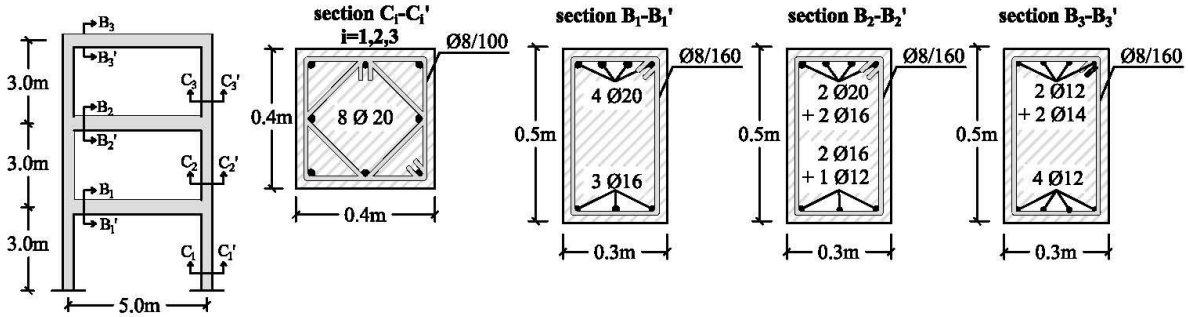

Figure 7.4: *Configuration details of the adopted reinforced concrete frame*

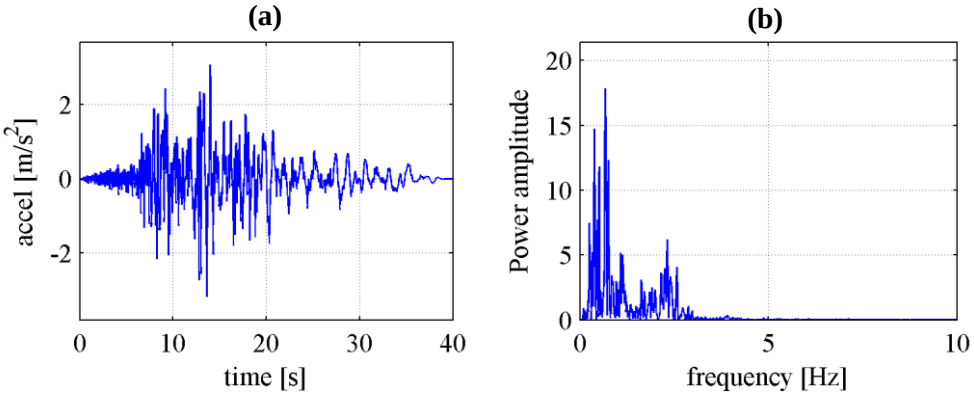

Figure 7.5: *Considered Chuetsu-oki (Japan, 2007) horizontal ground motion component: (a) Time-history, (b) Squared amplitude of Fourier spectrum*

The structure in Figure 7.4 is then exposed to the horizontal ground motion shown in Figure 7.5 and to a scaled version of this ground motion by a factor of 0.5, leading to two different levels of structural damage. Notably, the considered (unscaled) ground motion of Figure 7.5 was recorded from the "*Sanjo Shinbori*" station during the M_w=6.8 *Chuetsu-oki* earthquake (16.7.2007) that occurred in Japan (see also *Ancheta et al.* (2014)). It has a peak ground acceleration (PGA) equal to 3.17m/s^2 and is characterised by high energy in a wide range of frequencies. The two different damaged states of the structure in Figure 7.4 are modelled in a finite element (FE) software, as detailed in the following sub-section.

7.4.2. Finite element modelling of earthquake-induced damage

Non-linear response history analysis is undertaken using the *Ruaumoko* FE software to quantify the structural damage induced to the structure in Figure 7.4 due to the earthquake excitation in Figure 7.5 scaled by a factor of 0.5 (damaged state 1) and its unscaled version (damaged state 2). To this aim, a non-linear lumped-plasticity FE model is developed, based on

the material properties, geometry, and detailing of the considered structure given in the previous sub-section. This is accomplished by first conducting a section analysis to determine the values of the moment capacity- curvature pairs at yielding, M_y-φ_y, and at collapse, M_u-φ_u, at the critical (energy dissipation) zones of all the frame members (*i.e.*, ends of all beams and columns in Figure 7.4). Then, the secant flexural rigidity at yielding, $\mathcal{E}I_y=M_y/\varphi_y$, corresponding to cracked reinforced concrete sections at all the critical zones are obtained. In this respect, Table 7-2 reports the average $\mathcal{E}I_y$ values of the two ends at each frame member. Next, the plastic hinge length of all critical zones is estimated by the empirical formula (*e.g.*, *Priestley et al.* (2007))

$$L_{pl} = \max\begin{Bmatrix} \min\left(0.2(\frac{f_{uk}}{f_{yk}}-1)L_o, 0.08\right) + 0.022\, f_{yk} d_{bl} \\ 0.044\, f_{yk} d_{bl} \end{Bmatrix}, \quad (7.10)$$

where L_o is the shear span taken herein as half the structural member length, d_{bl} is the diameter of the longitudinal reinforcement, and f_{yk}, f_{uk}/f_{uk} are the steel strength and strain hardening ratio, respectively, given in the previous sub-section. In this study, eq. (7.10) yields the value L_{pl}=0.352m for the critical zones in all beams and columns with the exception of the beam at the 3rd storey exhibiting plastic zones with L_{pl}=0.246m at both ends.

Table 7-2: Average secant flexural rigidity at yielding, $\mathcal{E}I_y$, at the ends of the frame structural members of Figure 7.4

	Beams			Columns		
	1st storey	2nd storey	3rd storey	1st storey	2nd storey	3rd storey
$\mathcal{E}I_y$ [kNm^2]	23531	20719	16219	19709	18237	16573

Having obtained the moment capacity-curvature pairs at yielding, M_y-φ_y, and at collapse, M_u-φ_u, as detailed above, non-linear rotational springs with moment-curvature curves, M-φ, governed by the Takeda hysteretic model (*e.g.*, *Takeda et al.* (1970)), are used to capture the behavior of the plastic hinges that may develop at the critical zones of the considered frame under seismic excitation. The sections of beams and columns in between the critical zones are modelled as linear-elastic with flexural rigidity equal to $\mathcal{E}I_y$, that is, equal to the secant values at yielding given in Table 7-2.

Non-linear response history analysis is applied to the developed non-linear FE model for the ground motion of Figure 7.5 scaled-down by a factor of 0.5 and for the original ground motion (unscaled). For both considered ground motion intensities, it is observed that all beam members yield, while columns remain elastic. In this regard, the inelastic behaviour of the considered

structure represents well the case of a properly detailed reinforced concrete frame structure for earthquake resistance. To further illustrate this point and to demonstrate the impact of scaling-down the considered ground motion by 0.5 in terms of non-linear response behavior, Figure 7.6 plots the moment-curvature curves at the left plastic hinge on the beam of the 1st storey, for the two damaged states considered. Notably, the maximum curvature ductility in Figure 7.6(a) is close to unity (*i.e.*, μ_φ=1.45) associated with a very small structural damage near yield. From Figure 7.6, it is readily observed that maximum stiffness degradation occurs at the maximum curvature ductility characterised by an effective flexural rigidity, $\mathcal{E}I_{eff}$ (slope of red dashed lines in Figure 7.6), smaller than the secant flexural rigidity at yielding, $\mathcal{E}I_y$ (slope of green dashed lines in Figure 7.6, also reported in Table 7-2). In this regard, the average ratio $\mathcal{E}I_{eff}/\mathcal{E}I_y$ (flexural stiffness reduction factor) at the critical zones is herein considered to represent local earthquake-induced damage related to stiffness degradation as captured by the Takeda hysteretic model (which, however, does not take into account the strength deterioration and pinching effects due to cyclic loading). Table 7-3 presents the thus defined stiffness reduction factors for the two considered damaged states, which yield smaller values within the second case pertaining to a seismic event of increased intensity. As expected, the increased severity of the second damage state reflects on lower values of stiffness reduction factors for the beams, while columns remain practically linear.

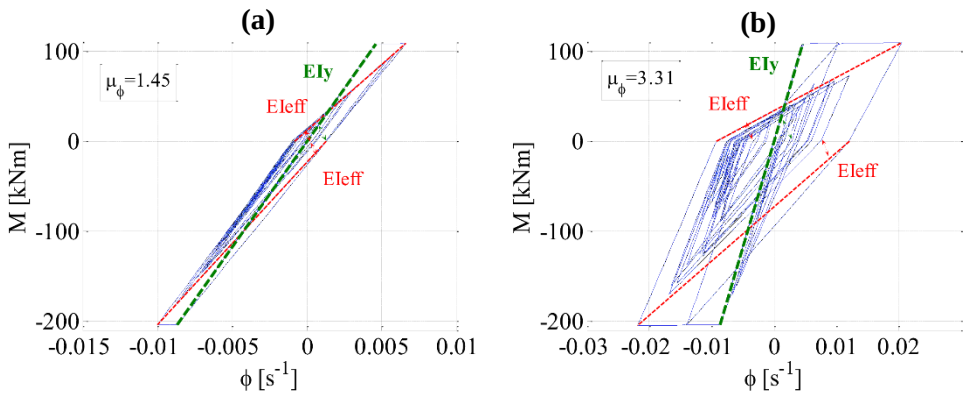

Figure 7.6: *Moment-curvature (*M-φ*) hysteretic curves at the left plastic hinge of the 1st storey beam for (a) damage state 1 and (b) damage state 2.*

Table 7-3: Flexural rigidity reduction factor ($\mathcal{E}I_{eff}/\mathcal{E}I_y$) at critical member zones of the structure in Figure 7.4 for the two different damage states considered due to different seismic intensity excitation

	Beams			**Columns**		
	1st storey	**2nd storey**	**3rd storey**	**1st storey**	**2nd storey**	**3rd storey**
Damaged state 1	0.71	0.53	0.46	1.00	1.00	1.00
Damaged state 2	0.21	0.15	0.17	1.00	1.00	1.00

The reduction factors of Table 7-3, obtained from Non-linear response history analysis as detailed above, are used to model earthquake-induced structural damage to the structure of Figure 7.4 due to the two different levels of seismic excitation adopted. Specifically, two equivalent linear FE models are defined, corresponding to the two different damage states, in which the earthquake-induced damage is represented by means of the flexural stiffness reduction factors of Table 7-3. In particular, the latter are assigned to linear beam elements of length L_{pl} at the considered plastic hinge zones, while the remaining non-critical frame members exhibit the flexural rigidities in Table 7-2. Notably, this modelling of local structural damage is deemed more realistic compared to the arbitrary reductions of floor stiffness (*i.e.,* along the whole length of structural members), commonly considered in the relevant literature (*e.g., Humar et al.* (2006); *Yan et al.* (2010); *Loh et al.* (2016)). Further, it is assumed that the pre-damage/"healthy" state of the considered structure (before the seismic event) is available and is modelled by a linear FE model with the secant flexural rigidities at yield presented in Table 7-2, which are assigned to the full length of structural members. Moreover, it is assumed that environmental conditions (*e.g.*, temperature, humidity, etc.), whose fluctuations may influence the structural dynamic properties extracted from standard OMA techniques, are the same before and after the seismic event. Thus, in this particular study, any potential change to the modal properties of the considered structure is only associated with the seismic action. The latter assumption is reasonable given the small duration of a typical earthquake and the fact that a power-efficient VSHM system is installed to the structure supported by sensors sampling at a sub-Nyquist rate, allowing for more frequent data acquisition and processing.

7.4.3. System identification and damage detection using co-prime sampling and the MUSIC spectrum

Linear response history analyses are undertaken for the three FE models defined in the previous sub-section (healthy plus two damaged states), which are subjected to the same low amplitude white noise base excitation of 80s duration. A time discretization step of T_s=0.01s is taken corresponding to a Nyquist frequency of 50Hz. The considered excitation models ambient wide-band noise input under operational conditions. A critical damping ratio of 5% for all modes of vibration is assumed in the analysis. Horizontal response acceleration signals at all floor levels are recorded at the Nyquist rate F_s=1/T_s= 100Hz (*i.e.,* 8000 Nyquist measurements per signal) and stored. They are treated as noise-free structural response acceleration time-histories due to ambient noise, field-recorded by sensors located at each floor. Further, these response signals are contaminated with additive Gaussian white noise at three different signal-to-noise ratios (*SNRs*): 10^{20}dB (practically noise-free case), 30dB, and 10dB.

The obtained discrete-time noisy response acceleration signals from the healthy and the two damaged states are compressively sensed using the co-prime sampling strategy reviewed in sub-section §7.2.1. Considering the optimal performance of the the adopted pseudo-spectral estimator shown in §7.3.3, it was deemed reasonable to select herein the co-prime numbers N_1=7 and N_2=11 along with the pertinent sampling values reported in Table 7-1. Thus, two co-prime samplers are assumed per recording location that operate on uniform sampling rates N_1=7 and N_2=11 times slower than Nyquist, respectively, yielding an average rate which is about 76.6% lower than Nyquist. In this numerical evaluation, the autocorrelation matrix in eq.(7.5) is computed from 492 time-blocks. Each block contains 143 Nyquist samples from which only 24 samples are taken to populate the $\mathbf{R}_{yy} \in \mathbb{R}^{24\times24}$ matrix. It is noted that a certain level of overlapping between the considered time blocks occurs, given that the structural response acceleration signals are only 8000 Nyquist samples long. However, under the wide-sense stationary assumption and implied ergodicity in the data, this overlapping does not affect the obtained numerical results. Following the same lines as in §7.3.2, the coprime-sampled (compressed) measurements are next used to derive the spatially smoothed correlation matrix $\mathbf{R}_{ss} \in \mathbb{R}^{78\times78}$ in eq.(7.6). The latter is further treated by the MUSIC algorithm in §7.2.2 to compute the pseudo-spectral estimator in eq.(7.8), assuming R=3 degrees of freedom in the measured response acceleration signals.

Compared to traditional Discrete Fourier Transform (DFT) based spectral estimators, the MUSIC algorithm yields a pseudo-spectrum with sharp peaks corresponding to the natural frequencies of the white-noise excited 3-storey frame (following standard OMA and linear random vibrations considerations), while filtering out additive broadband noise. As an example, aiming at system identification, Figure 7.7 plots the conventional periodograms (DFT-based spectral estimators) of Nyquist-sampled noisy response acceleration signals (at SNR=10dB), recorded at all floors of the healthy 3-storey white-noise excited structure. Figure 7.7 also superimposes the MUSIC pseudo-spectra, obtained from both Nyquist-sampled signals (red broken line) and co-prime sampled signals (solid blue line) using the approach detailed in section §7.1. All spectra are normalised to their peak amplitude to facilitate comparison. It is seen that it is not possible to extract the natural frequencies of the structure from the periodogram of the considered noisy signals sampled at the Nyquist rate (*e.g.* the 3rd natural frequency is masked by noise). However, the MUSIC pseudo-spectrum estimated directly from the co-prime sampled signals (using less than 76% measurements from the sub-Nyquist rate) can be readily used to detect the resonant frequencies of the structure with high resolution, even for this extreme noise level. More importantly, it is found that the MUSIC pseudo-spectrum derived from the Nyquist and the sub-Nyquist sampled signals practically coincide in this case. Thus, the signal information pertaining to the natural frequencies of the system is not lost due to a more than 76% signal compression at acquisition (sub-Nyquist sampling).

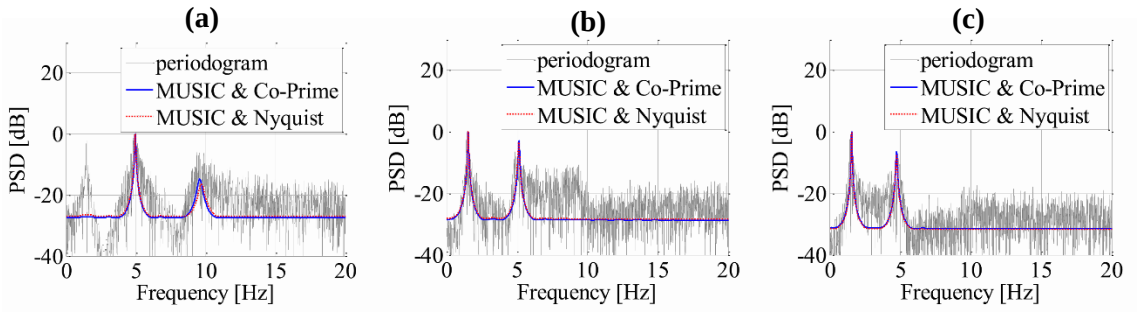

Figure 7.7: *Spectrum estimation from noisy acceleration response signals with SNR=10dB at the (a) first, (b) second, and (c) third floor of the structure in Figure 7.4 (healthy state) subject to 80s duration white noise base excitation*

Having demonstrated numerically the capability of the MUSIC spectrum to identify structural resonant frequencies from the compressively sensed signals buried in noise, structural damage detection is next pursued based on the shifts of the natural frequencies between the healthy state of the structure in Figure 7.4, and the two damaged states due to different levels of ground motion excitation, as detailed in previous sub-sections. For illustration, Figure 7.8 and Figure 7.9 plot the MUSIC spectra obtained by co-prime sampled measurements for damaged states 1 and 2, respectively, at all three floors (recording locations). The MUSIC spectra of co-prime sampled measurements from the healthy state are superimposed in all panels of Figure 7.8 and Figure 7.9. In all plots, a shift of the natural frequencies towards smaller values (more flexible structure) is evident indicating structural damage. Apparently, these shifts are relatively much smaller for the damage state 1 (*i.e.*, lighter damage near yield pertaining to the scaled-down input ground motion), rendering the damage detection problem as a more challenging task. It is further important to note that in each panel of Figure 7.8 and Figure 7.9 only two out of the expected three structural natural frequencies are detected. Specifically, the MUSIC spectra at the first floor do not capture the first (fundamental) natural frequency, while the spectra at the 2nd and the 3rd floor do not capture the highest (third) natural frequency. In this regard, the three natural frequencies, for each of the three different FE models considered, are estimated by averaging the natural frequency values obtained from the MUSIC spectra across all three floors. Table 7-4 and Table 7-5 report the thus estimated three natural frequencies (*i.e.*, averaged over the three floors) for the different FE models and for three different *SNR* levels *i.e.* 10^{20}dB (practically noise-free case), 30dB, and 10dB. The "exact" natural frequencies obtained from standard modal analysis in *Ruaumoko* are also reported. It is seen that the MUSIC algorithm coupled with co-prime sampling can retrieve the underlying resonant frequencies of the adopted frame in the three considered structural states (*i.e.*, one healthy and two damage states, respectively), with a small error of 1-5% with respect to the exact solution. Table 7-4 and Table 7-5 further report the percentage differences computed between the natural frequencies of the healthy and the damaged states in all cases considered – a quantity that is used as an indicator of structural damage. Notably,

the reported percentages derived from the co-prime MUSIC spectra yield almost the same values within the entire *SNR* range, and closely approximate the percentage differences retrieved from the exact modal values (*i.e.*, from the standard modal analysis in *Ruaumoko*). Thus, the numerical results show that the proposed methodology is capable to infer structural damage even in low-intensity earthquake excitations by capturing small changes to the natural frequencies while being practically insensitive to noise.

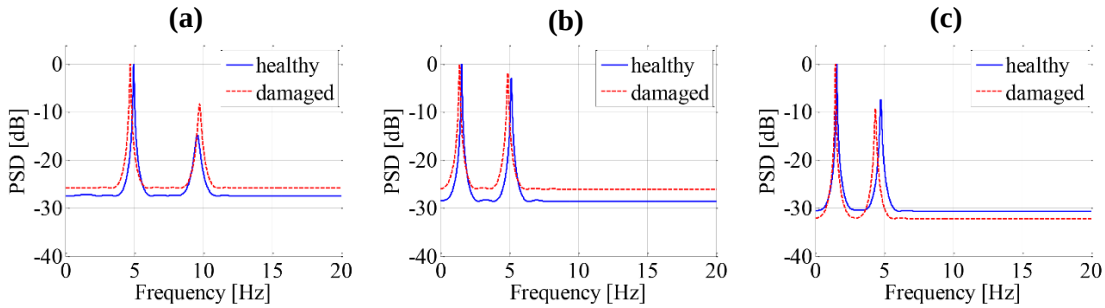

Figure 7.8: *MUSIC pseudo-spectra with co-prime sampling of noisy acceleration response signals with SNR=10dB at the (a) first, (b) second, and (c) third floor for the healthy and the damaged state 1 structure in Figure 7.4*

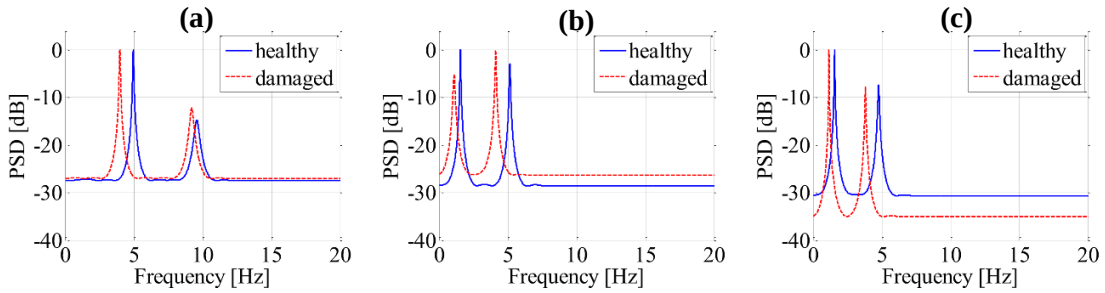

Figure 7.9: *MUSIC pseudo-spectra with co-prime sampling of noisy acceleration response signals with SNR=10dB at the (a) first, (b) second, and (c) third floor for the healthy and the damaged state 2 structure in Figure 7.4*

Table 7-4: Assessment of MUSIC spectra from co-prime sampled noisy measurements for damage detection based on structural natural frequency shifts: damage state 1

SNR		f_1 [Hz]		df_1/f_1	f_2 [Hz]		df_2/f_2	f_3 [Hz]		df_3/f_3
[dB]	State*	H	D	[%]	H	D	[%]	H	D	[%]
∞	exact	1.51	1.40	7%	4.96	4.62	7%	9.68	9.46	2%
10^{20}	MUSIC	1.56	1.44	8%	4.97	4.67	6%	9.69	9.76	1%
30		1.56	1.43	8%	4.97	4.67	6%	9.68	9.75	1%
10		1.56	1.43	8%	4.96	4.66	6%	9.58	9.74	2%

**H: healthy; D: damaged*

Table 7-5: Assessment of MUSIC spectra from co-prime sampled noisy measurements for damage detection based on structural natural frequency shifts: damage state 2

SNR		f_1 [Hz]		df_1/f_1	f_2 [Hz]		df_2/f_2	f_3 [Hz]		df_3/f_3
[dB]	State*	H	D	[%]	H	D	[%]	H	D	[%]
∞	exact	1.51	1.07	29%	4.96	3.97	20%	9.68	9.09	6%
10^{20}	MUSIC	1.56	1.13	27%	4.97	3.98	20%	9.69	9.38	3%
30		1.56	1.13	28%	4.97	3.98	20%	9.68	9.36	3%
10		1.56	1.13	28%	4.96	3.97	20%	9.58	9.21	4%

**H: healthy; D: damaged*

7.5. Concluding Remarks

This chapter explored the potential of a recently established *sub-Nyquist pseudo-spectral estimation* method for VSHM in civil engineering structures instrumented with wireless sensors of reduced power demands. The adopted approach relies on a deterministic sub-Nyquist sensing technique – termed *co-prime sampling* – to acquire compressed structural data at a much lower average sampling rate than Nyquist. The acquired measurements are treated as stationary stochastic processes free from sparsity requirements. Further, the considered method exploits the *MUSIC* super-resolution pseudo-spectrum estimator to identify structural natural frequencies by processing noise-corrupted compressed data. This involves signal processing operations directly in the compressed domain, without requiring any filtering and/or computationally expensive signal reconstruction operations in time-domain.

It was shown that the adopted co-prime MUSIC-based strategy is a potent tool for OMA, capable to efficiently address the structural modal coupling effect even by treating response signals buried in noise. This was numerically verified within a simulation-based framework using accelerations responses originating from a white-noise excited structural system with 2 closely-spaced modes of vibration carrying the same amount of energy, and a 3rd less excited vibrating mode under the considered forcing case. Parametric analyses were conducted using noise-corrupted compressed data at five *SNRs* between 0 and 20 dB, by employing four different pairs of co-prime numbers associated with different sub-Nyquist rates and spectral resolutions. It was shown that higher resolution is achieved at stronger signal compression levels (*i.e.*, larger co-prime numbers), which further allows the separation of very closely-spaced structural resonant frequencies (with a percentage difference of roughly 4.5%) from a significantly reduced number of noisy measurements at *SNRs* as low as 5dB.

Further to the above, a novel structural damage detection approach was proposed, based on small changes to the structural natural frequencies, before and after a seismic event of low-intensity. These resonant frequencies are extracted from sub-Nyquist sampled acceleration

response signals within an operational modal analysis framework. It is assumed that within this short time interval (*i.e.*, pre- and post- earthquake), the environmental conditions remain the same and thus any (likely to be slight) change to the natural frequencies is caused by the input seismic action to the structure. The effectiveness and applicability of the proposed approach was numerically evaluated using a white-noise excited linear reinforced concrete 3-storey frame in a healthy and two damaged states caused by two ground motions of increased intensity. The damaged models were simulated with locally reduced effective flexural rigidities (*i.e.*, along the plastic hinge zones), computed by non-linear response history analysis and the Takeda hysteretic model. The numerical results demonstrate that the considered approach is capable to detect very small structural damage directly from the compressed measurements even for high noise levels at SNR=10dB. It was further shown that any additive broadband noise during data acquisition does not affect the damage detection capabilities of the proposed approach (at least for the noise levels encountered in practical applications) as such kind of noise is filtered out by application of the MUSIC spectral estimator.

The above results suggest that the adopted approach makes a dependable noise-immune structural damage detection technique that can be potentially embedded within arrays of wireless sensors for cost-efficient (in terms of data sampling and wireless transmission rates) VSHM in seismically prone regions.

Chapter 8
Conclusions

This thesis has focused on novel algorithmic approaches supporting sub-Nyquist data acquisition and processing techniques to reduce the power consumption in wireless sensor networks used for operational modal analysis and data-driven damage detection in civil engineering structures. By exploiting recent theoretical and technological advances, the proposed methods achieve simultaneous data acquisition and compression at the sensor front-end, eliminating the need for local on-sensor data processing. The latter consideration directly translates into minimum sensor complexity with reduced computational, power, and memory requirements, enabling low-cost and power-efficient monitoring deployments in densely instrumented structures. This final section summarises the milestones reached in each chapter and highlights the main contributions of this research, concluding with recommendations for future work.

8.1. Summary and Main Contributions

The latest advances in sub-Nyquist data acquisition strategies for low-power and reliable wireless VSHM in civil engineering structures have been reviewed in *Chapter 2* (§*2. Compressive Sensing: Basic Concepts & Applications in VSHM*). These strategies rely on random sampling schemes and signal reconstruction operations, originating from the theory of compressive sensing (CS). In this respect, *Chapter 2* explained the basic principles of the CS theory followed by an extensive literature survey on the state-of-the-art CS-based VSHM approaches and discussed their limitations which are summarised as follows.

- *Limitation 1: Time-domain signal reconstruction, sparsity constraints and computational cost*

The aim of CS signal reconstruction operations is to retrieve time-domain response data at Nyquist rate (or above) from a considerably reduced number of measurements. This is an underdetermined problem with increased computational demands that yields a unique solution when subjected to signal's sparsity constraints.

Limitation 2: Sparsity requirements on a pre-defined vector basis

The signal compression level for which quality CS-based signal reconstruction can be achieved is limited by the sparsity level of the monitored response acceleration signals on a pre-defined vector basis. It was observed that the widely-used discrete Fourier transform (DFT) basis does not provide significantly sparse representations of structural responses due to detrimental noise folding and spectral leakage, while the consideration of alternative expansion bases, such as the discrete *Haar* wavelet basis, does not significantly improve the underlying signal sparsity. It was recognised that generalised harmonic wavelet bases or over-complete dictionaries may enhance the signals' sparsity attributes, although such practices depend strongly on the application at hand.

- *Limitation 3: Unknown signal sparsity and noise influence in practical applications*

In practice, field-recorded structural response signals are not strictly sparse on a given domain (*i.e.*, compressible signals) but they can be adequately approximated as sparse representations. Further, the actual sparsity/compressibility level of real-time monitored signals is not known in advance while it is adversely affected by environmental noise. Notably, information on the sparse signal structure can only be retrieved from signal processing operations at the expense of increased computational, power, and memory demands. In the absence of such information, a target sparsity level should be assumed in the CS sparse signal recovery step, the selection of which is not trivial since it is associated with a trade-off between reconstruction accuracy and computation complexity.

Aiming to address *Limitation 2* and improve the efficiency of CS-based VSHM approaches, *Chapter 3* (§*3. CS-based Damage Detection Using the Relative Wavelet Entropy*) examined the "sparsest" representation of structural acceleration responses on the wavelet transform domain using four energy-preserving wavelet analysis filter banks (*i.e.*, Haar, smooth Daubechies, Meyer, Harmonic) with different frequency domain attributes. The suitability of the adopted wavelet bases was numerically assessed in terms of data-driven structural damage identification results (*i.e.*, damage detection and localisation) considering the relative wavelet entropy (RWE) index – a damage-sensitive quantity that has been efficiently embedded on wireless sensors for VSHM deployments. This comprehensive numerical study was mainly driven by the signal sparsity requirements of the CS theory and motivated by the lack of comparative studies and practical recommendations for the computation of the RWE.

Thus, the conventional RWE approach was numerically tested on full-length response acceleration datasets obtained from a healthy and a damaged state of a benchmark structure subject to broadband excitations, and RWE values were reported vis-à-vis for the four different wavelet filter banks. The reported numerical data confirmed that frequency selectivity and resolution across the scales of the wavelet analysis filter bank are the key for achieving enhanced

RWE-based stationary damage detection/localisation drawing information about damage from multiple mode shapes. It was shown that the widely-used Haar wavelets in conjunction with the standard dyadic discrete wavelet transform suffer from significant energy leakage across scales and may not be able to detect damage based on information carried at relatively high frequencies. It was further confirmed that wavelet filter banks with enhanced frequency selectivity among scales reduce spectral leakage, enabling the detection of damage in the vicinity of structural resonances at the excited modes of vibration. Thus, it was verified that the harmonic wavelets are the most effective for RWE-based stationary damage detection as they are not limited by the dyadic discrete wavelet transform discretisation and can achieve any level of frequency resolution.

An important contribution of *Chapter 3* was the development of a novel data-driven damage detection approach that couples the CS theory with the RWE damage index using sparse signal representations on the harmonic wavelet transform. Based on random sub-Nyquist sampling schemes, the proposed method can significantly reduce the number of acquired and wirelessly transmitted measurements. Considering a "partial" harmonic wavelet basis matrix saved at the server, standard CS-reconstruction algorithms (*e.g.*, CoSaMP) can be used to retrieve the underlying harmonic wavelet coefficients and derive the CS-based RWE damage index directly from the received compressed data without recovering the full-length acceleration response signals in time-domain. It was shown that this novel approach yields highly sparse structural response signals on the harmonic wavelet transform, being capable to detect structural damage equally well with the conventional RWE method while drastically reducing the required number of data samples by 80%-90% compared to traditional uniform-in-time sampling schemes. The numerical results suggest that the proposed CS-based RWE is a potent tool for inexpensive data-driven damage detection implementations in civil structures instrumented with wireless sensors of low energy demands.

Chapter 4 (§ *4. Proposed Multi-Sensor Power Spectrum Blind Sampling Approach for OMA: Theory*) provided the theoretical development of a multi-sensor power spectrum blind sampling (PSBS) approach capable to circumvent the CS limitations detailed above. This innovative approach extends a previously considered PSBS technique supporting single sensor deployments and it was proposed herein, for the first time, as a viable alternative for low-power WSNs used for operational modal analysis (OMA) and data-drive damage detection in civil structures. This is a fundamentally different approach that enjoys numerous advantages over the current CS-based approaches, in that:

- It relies on a common deterministic multi-coset sampling pattern among sensors, capable to acquire signals at sub-Nyquist rates (*i.e.*, compression) without imposing sparsity conditions;

- It is genuinely signal agnostic, theoretically and numerically, and, therefore, it does not require any *a priori* knowledge of the signal structure (*e.g.*, sparsity);
- It only requires that signals be wide-sense stationary which is in alignment with OMA theory;
- It retrieves auto/cross power-spectral density estimates directly from compressed data by solving a least-squares optimisation problem while by-passing signal reconstruction operations in time-domain;
- It attains a computationally efficient and relatively fast algorithm that mathematically relies on overdetermined systems of linear equations that can be easily solved;
- It can be fused with standard OMA algorithms (*e.g.*, FDD algorithm) for structural natural frequency and mode shape estimation, and combined further with data-driven damage detection strategies based on the extracted modal information (*e.g.*, the modal strain energy damage index).

The efficacy of the developed PSBS approach was numerically assessed in *Chapter 5* (§5. *Proposed Multi-Sensor Power Spectrum Blind Sampling Approach for OMA: Applications*) while its superiority over a recently proposed CS-based approach (*e.g.*, *O'Connor et al.* (2014)) was numerically verified in *Chapter 6* (§6. *Assessment of the Proposed PSBS Approach vis-à-vis CS-based Approach for OMA*). The numerical evaluation was performed with wide-sense stationary acceleration response signals measured on structures under low-amplitude ambient excitations. The considered datasets involved both synthetic (computer-simulated) data – generated either by linear analyses in white-noise excited finite element models or by white-noise sequences coloured via ARMA filters – and field-recorded acceleration responses originating from actual monitoring campaigns (*i.e.*, an operational wind turbine in Lübbenau, Germany, and an overpass in Zurich, Switzerland). By adopting an optimal multi-coset sampling scheme in the mean square error sense, simulated compressed acceleration data were derived at various compression ratios (*CRs*) ranging between 11% and 50% (*i.e.*, 89% and 50% fewer measurements compared to conventional uniform-in-time sampling schemes).

In this study, the primary focus was on extracting quality modal estimates (natural frequencies and mode shapes) from a significantly reduced number of measurements with special attention drawn on identifying closely-spaced and poorly excited modes of vibration in noisy environments pertaining to signal-to-noise-ratios (*SNRs*) as low as zero decibel (*i.e.*, 0 dB – extreme noise case yielding equal power in signal and noise components). The identification of local structural damage has also been addressed within the OMA context, using sub-Nyquist noisy acceleration response datasets at various structural states (*i.e.*, reference/healthy and damaged states).

It was observed that the accuracy of the proposed method depends on the power spectral recovery performance of the PSBS strategy. The latter was found to be a function of the acquired number of compressed measurements, controlled by the adopted *CR* value in a fixed observation time-window. It was further confirmed that the PSBS method can efficiently recover power spectral densities (PSDs) directly from sub-Nyquist-sampled acceleration data even in cases of closely-spaced structural vibrating modes whose resonant frequencies are spaced less than 1 Hz apart (*i.e.*, 20rad/s and 25rad/s). This novel spectral estimation method was shown to be practically insensitive to additive noise for *SNRs* as low as 10dB. At higher noise levels, though, of the order of 0 dB, larger errors were observed on the recovered PSDs estimates. However, such extreme noise cases may not be encountered in practical VSHM deployments.

Overall, it was confirmed that multi-sensor PSBS approach can retrieve quality modal estimates even for the lowest considered *CR* value at 11% pertaining to 89% fewer data compared to conventional uniform-in-time sampling schemes (at Nyquist rate or above), yielding natural frequency estimates with small errors of the order of 1-5% (depending on the application), and modal deflected shapes with MAC values well above 0.9 (*i.e.*, the established modal assurance criterion for accurate mode shape extraction).

The damage detection capabilities of the PSBS method were tested for *CR*=31% and a wide range of *SNR* values. The numerical results demonstrated that the proposed multi-sensor PSBS technique coupled with standard OMA and damage detection approaches can identify the location of light structural damage of equal quality compared to conventional approaches at Nyquist rate, using less than 69% of data samples buried in high level noise with *SNR* at 10 dB. Thus, it was confirmed that the PSBS approach can infer structural damage directly from the recovered PSDs in the compressed domain without returning the monitored signals deterministically in time domain.

The comparison against the CS-based approach by *O'Connor et al.* (2014) revealed that the inherent signal agnostic attributes of the proposed multi-sensor PSBS-based approach renders the latter method more advantageous in cases where high signal compression levels are desired to address sensor power consumption and wireless bandwidth transmission limitations. In fact, it has been numerically shown and theoretically justified, that, for a given sub-Nyquist sampling rate, the capability of the CS-based approach to extract faithful estimates of the mode shapes depends heavily on the target sparsity level, S_T, which needs to be assumed in the CS signal reconstruction step. It has also been demonstrated that the accuracy of the CS-based approach improves at larger S_T values at the cost of higher computational effort reflected on the increased required runtime of the adopted CS sparse signal recovery algorithm. However, no increase to the assumed S_T value can compensate for the acquisition of an excessively small number of compressed measurements which is the case for *CR*=11% for all the sets of acceleration signals considered in this work. In this regard, it is concluded that conservative compression ratios should

be adopted in using the CS-based approach to ensure acceptable quality of modes shapes, especially in the case where no prior knowledge on the acceleration signal sparsity is available.

On the antipode, it was numerically shown that the signal-agnostic PSBS-based approach performs equally well and consistently better than the CS-based approach in extracting mode shapes from compressively sampled acceleration signals. In fact, the PSBS-based approach yields MAC>0.96 even for the low-sparse signals contaminated with white noise at *SNR*=10dB and for low sampling rates at *CR*=11% (*i.e.*, 89% below the Nyquist rate). It was further confirmed that significant energy gains can be achieved by the proposed method at such low *CRs* using battery-operated wireless sensors, leading to drastic reductions on individual sensor power consumption and, therefore, to considerable increase of battery life expectancy which enables the sustainability of OMA monitoring systems.

Finally, a novel structural damage detection approach was developed in *Chapter 7* (§*7. A Novel MUSIC-Based Approach for Structural Damage Detection from Sub-Nyquist Measurements*), capable to capture small shifts in structural natural frequencies before and after a seismic event of low intensity using compressed acceleration data contaminated with broadband noise. This novel approach relies on a recently established sub-Nyquist pseudo-spectral estimation method which combines the deterministic co-prime sensing technique with the MUSIC super-resolution pseudo-spectrum estimator. The latter shares certain common features with the PSBS technique, given the signal-agnostic nature of the co-prime sampling scheme which applies to wide-sense stationary signals without being limited by sparsity constraints. Despite these similarities, these two strategies are fundamentally different, in that:

- the co-prime sampling scheme relies on two sensors per acceleration channel operating at different sub-Nyquist rates and accumulating collectively in time a much smaller number of measurements than a single sensor operating at Nyquist rate;
- the MUSIC algorithm is not a true PSD estimator, yielding a spectrum-like shape with very sharp peaks at the frequency components of the monitored accelerations responses (*i.e.*, structural resonances) based on *a priori* knowledge of the number of the excited structural vibrating modes;
- the sub-Nyquist MUSIC-based approach retrieves only auto power-spectral estimates directly from compressed measurements using a spatially smoothing technique, by-passing signal reconstruction operations in time-domain;
- it solely identifies structural natural frequencies but it does not retrieve any information related to the modal deflected shapes of the monitored structure.

The numerical results confirmed that the considered sub-Nyquist pseudo-spectral estimation approach can efficiently address, with high resolution, the modal coupling effect in extreme noise

environments with *SNRs* as low as 5dB. In fact, it was verified that higher spectral resolution is achieved at stronger signal compression levels (*i.e.*, larger co-prime numbers) which are associated with lower average sub-Nyquist sampling rates. The damage detection capabilities of the proposed approach were also verified even in cases of very small structural damage using compressed data corrupted with high noise levels (of *SNRs* up to 10dB). Thus, it was concluded that the proposed method supports a dependable noise-immune structural damage detection technique that can be potentially embedded within arrays of wireless sensors for cost-efficient (in terms of data sampling and wireless transmission rates) VSHM in seismically prone regions.

8.2. Recommendations for Future Research

The development of this thesis sets an agenda for further research in structural health monitoring algorithms supporting the use of low-energy wireless sensors.

One potential line for future research lies on the consideration of advanced wavelet analysis tools to improve further the CS-based RWE damage index. Among others, the wavelet packet transform is a potent tool, which relaxes the strict dyadic discretisation of the discrete wavelet transform to "zoom-in" specific frequency bands of interest while it is applicable to any energy-preserving wavelet family. Thus, the wavelet packet transform can be used in to "target" natural frequencies of a given structure and, therefore, to capture changes to the wavelet energy distribution of response signals associated with structural damage (*e.g.*, *Yen & Lin* (2000); *Sun & Chang* (2004)). Another recommendation is the utilisation of a harmonic wavelet transform spanning frequency bins of non-constant width (*e.g.*, *Giaralis & Spanos* (2009)) to achieve enhanced frequency resolution in the vicinity of the known natural frequencies and, therefore, to yield more efficient CS-based RWE damage detection.

Within this context, it is recognised that the sparsest signal representation can be achieved in basis functions that are as close as possible to the analysed structural vibrating responses. In this respect, the derivation of customised wavelet basis that closely trace the shape of time-varying structural signals may be a promising tool for stronger signal compression and more efficient signal reconstruction based on standard CS algorithms. A stepping-stone in this line of research could be the customised wavelet bases derived from single-degree-of-freedom under-damped linear oscillators (see also *Dick et al.* (2012)), in which the impulse response signals of civil engineering structures are expected to be sufficiently sparse.

The distributed compressive processing framework (*e.g.*, *Baron et al.* (2009)) can be cast as another field for future research in CS-based VSHM applications with the scope of reducing further the power and computational demands in wireless sensor network (WSN) deployments. This can be achieved by exploiting the inherent temporal, spatial and joint sparsity attributes of structural dynamic signals recorded at different locations on the monitored structure. Thus, a

minimum number of encoded (compressed) measurements can be acquired by each sensor and directly transmitted to the server, eliminating the communication among sensors. The encoded measurements can be collectively processed to jointly recover multiple response signals, thus, providing a viable tool for fast and power efficient VSHM implementations, especially in densely instrumented structures.

The above idea of distributed processing in the compressed domain may also be applicable within the multi-sensor PSBS strategy developed in this thesis. This interesting extension can be investigated under the consideration of multiple wireless sensors operating on different multi-coset sampling patterns to achieve higher signal compression at lower sub-Nyquist sampling rates per sensor, yielding significant gains in energy. The proposed research may be facilitated by recent findings of *Arianandа et al.* (2014) focused on cooperative compressive power spectrum estimation of a single input signal entering multiple multi-coset samplers that operate on different sampling patterns.

The multi-sensor PSBS approach and the mathematical framework in *Chapter 4* could be possibly extended to non-stationary structural response data, observing time-dependent amplitude and frequency content (*e.g.*, structural responses subject to nonlinear phenomena). Such theoretical developments may be facilitated by the recent study of *Lim & Wakin* (2016), expected to be particularly useful into VSHM applications under extreme events and actions by providing important information about the onset of structural damage and/or changes in dynamic characteristics in real-time.

Another aspect that sets the scene for promising future research is the consideration of the PSBS strategy to rectify the problem of data loss in WSNs for VSHM applications, which, to the best of the author's knowledge, has yet to be addressed in the literature. Thus, the potential applicability of the proposed method should be explored in cases when random or continuous data packet loss occurs. In such cases, special attention should be given on assessing the efficiency of the power spectral recovery from incomplete measurements using the deterministic multi-coset sampling technique which relies on pre-defined sample delays (*i.e.*, the entries of the sampling pattern sequence).

Further, it is envisioned that the developed multi-sensor PSBS strategy fused with multi-coset sampling will open new directions within the research field of optimal sensor placement (*e.g.*, *Papadimitriou* (2004)) by exploiting the spatial attributes of structural responses to achieve compression in space-domain (*i.e.*, spatial compression). For example, in structural modal identification applications, the number and location of sensors required to capture a given number of significant modes of vibration would coincide with the number of cosets and the delay values in the adopted sampling pattern sequence, respectively. If successful, this can pave the way towards concurrent compression in both time and space domains (*i.e.*, spatio-temporal compression), leading towards optimal VSHM applications using the minimum information and

effort required for quality structural condition assessment. Within this context, the co-prime sampling scheme could also be advantageous, since it has proved efficient in both temporal and spatial compression to address the direction-of-arrival estimation problem in telecommunication signals (see also *Pal & Vaidyanathan* (2011); *Vaidyanathan & Pal* (2011)).

As a final note, new insights will be gained regarding the feasibility of the novel algorithmic approaches discussed in this thesis through experimental testing in actual field deployments, which is warranted for future work. Currently, this remains a challenging task due to the lack of commercially available sensing units with embedded compressive sampling schemes. The latter may be facilitated by the rapid technological advances in efficient design of compressive sensor prototypes, but such aspects are an open area of research in the sensors community.

It is aspired that the benefits gained from the multidisciplinary approaches presented in this thesis and the novel directions suggested for future research will enable cost-efficient VSHM deployments in terms of power, computational, and monetary cost, paving the way towards more resilient civil engineering structures.

Bibliography

Akyildiz, I.F., Lo, B.F. & Balakrishnan, R., 2011. Cooperative spectrum sensing in cognitive radio networks: A survey. *Physical Communication*, 4(1), pp.40–62.

Amezquita-Sanchez, J.P. & Adeli, H., 2016. Signal Processing Techniques for Vibration-Based Health Monitoring of Smart Structures. *Archives of Computational Methods in Engineering*, 23(1), pp.1–15.

Amezquita-Sanchez, J.P. et al., 2012. High-resolution spectral-analysis for identifying the natural modes of a truss-type structure by means of vibrations. *Journal of Vibration and Control*, 19(16), pp.2347–2356.

Ancheta, T.D., Darragh, R.B. & Stewart, J.P., 2014. Pacific Earthquake Engineering PEER NGA-West2 Database.

Ariananda, D.D. & Leus, G., 2012. Compressive Wideband Power Spectrum Estimation. *Signal Processing, IEEE Transactions on*, 60(9), pp.4775–4789.

Ariananda, D.D. & Leus, G., 2012. Cooperative compressive wideband power spectrum sensing. In *2012 Conference Record of the Forty Sixth Asilomar Conference on Signals, Systems and Computers (ASILOMAR)*. IEEE, pp. 303–307.

Ariananda, D.D., Romero, D. & Leus, G., 2014. Cooperative compressive power spectrum estimation. In *2014 IEEE 8th Sensor Array and Multichannel Signal Processing Workshop (SAM)*. IEEE, pp. 97–100.

Axell, E., Leus, G., Larsson, E. & Poor, H., 2012. Spectrum Sensing for Cognitive Radio : State-of-the-Art and Recent Advances. *IEEE Signal Processing Magazine*, 29(3), pp.101–116.

Bajwa, W.U., Haupt, J.D., Raz, G.M., Wright, S. J., & Nowak, R.D., 2007. Toeplitz-Structured Compressed Sensing Matrices. In *2007 IEEE/SP 14th Workshop on Statistical Signal Processing*. IEEE, pp. 294–298.

Bao, Y. Li, H., Sun, X., Yu, Y. & Ou, J., 2013. Compressive sampling-based data loss recovery for wireless sensor networks used in civil structural health monitoring. *Structural Health Monitoring*, 12(1), pp.78–95.

Bao, Y., Beck, J.L. & Li, H., 2011. Compressive sampling for accelerometer signals in structural health monitoring. *Structural Health Monitoring*, 10(3), pp.235–246.

Bao, Y., Li, H. & Ou, J., 2014. Emerging data technology in structural health monitoring: Compressive sensing technology. *Journal of Civil Structural Health Monitoring*, 4(2), pp.77–90.

Bao, Y., Shi, Z., Wang, X. & Li, H., 2017. Compressive sensing of wireless sensors based on group sparse optimization for structural health monitoring. *Structural Health Monitoring: An International Journal*, p.147592171772145.

Baraniuk, R. Davenport, M., Duarte, M. F. & Hegde, C., 2011. An Introduction to Compressive Sensing. *Connexions, Rice University, Houston,Texas*, p.118.

Baraniuk, R., 2007. Compressive Sensing [Lecture Notes]. *IEEE Signal Processing Magazine*, 24(4), pp.118–121.

Baron, D., Duarte, M.F., Wakin, M.B., Sarvotham, S. & Baraniuk, R.G., 2009. Distributed Compressive Sensing. *arXiv:0901.3403v1*.

Becker, S.R., 2011. *Practical compressed sensing : modern data acquisition and signal processing*. Ph.D thesis in California Institute of Technology Pasadena, California.

Bendat, J.S. & Piersol, A.G., 2010. *Random Data: Analysis and Measurement Procedures* 4th ed., Hoboken, New Jersey: John Wiley & Sons, Inc.

Bjornson, E. & Ottersten, B., 2010. A Framework for Training-Based Estimation in Arbitrarily Correlated Rician MIMO Channels With Rician Disturbance. *IEEE Transactions on Signal Processing*, 58(3), pp.1807–1820.

Black, W.C. & Hodges, D.A., 1980. Time Interleaved Converter Arrays. *IEEE Journal of Solid-State Circuits*, 15(6), pp.1022–1029.

Blanco, S., Figliola, A., Quian Quiroga, R., Rosso, O. A. & Serrano, E., 1998. Time-frequency analysis of electroencephalogram series. III. Wavelet packets and information cost function. *Physical Review E - Statistical Physics, Plasmas, Fluids, and Related Interdisciplinary Topics*, 57(1), pp.932–940.

Brincker, R. & Ventura, C.E., 2015. *Introduction to Operational Modal Analysis*, Chichester, UK: John Wiley & Sons, Ltd.

Brown, J.C., 1991. Calculation of a constant Q spectral transform. *The Journal of the Acoustical Society of America*, 89(1), p.425.

Brownjohn, J.M.W., 2007. Structural health monitoring of civil infrastructure. *Philosophical Transactions of the Royal Society A: Mathematical, Physical and Engineering Sciences*, 365(1851), pp.589–622.

Bruckstein, A.M., Donoho, D.L. & Elad, M., 2009. From Sparse Solutions of Systems of Equations to Sparse Modeling of Signals and Images. *SIAM Review*, 51(1), pp.34–81.

Camarena-Martinez, D., Amezquita-sanchez, J. P., Valtierra-rodriguez, M., Romero-troncoso, R. J., Osornio-rios, R. A. & Garcia-perez, A., 2014. EEMD-MUSIC-Based Analysis for Natural Frequencies Excitations. *The Scientific World Journal*, 2014, pp.1–12.

Candès, E., 2006. Compressive sampling. *Proceedings of the International Congress of Mathematicians: Madrid*, pp.1433–1452.

Candès, E.J., 2008. The restricted isometry property and its implications for compressed sensing. *Comptes Rendus Mathematique*, 346(9–10), pp.589–592.

Candès, E.J., Romberg, J. & Tao, T., 2006. Robust uncertainty principles: Exact signal reconstruction from highly incomplete frequency information. *IEEE Transactions on Information Theory*, 52(2), pp.489–509.

Chatzi E.N. & Spiridonakos M.D., 2015. Incorporating Uncertainty in Vibration-Based Monitoring and Simulation. In *Fourth International Conference on Soft Computing Technology in Civil, Structural and Environmental Engineering (CIVIL-SOFT-COMP 2015)*. Prague, Czech Republic.

Chatzi, E.N. & Spiridonakos, M.D., 2015. Structural Identification and Monitoring based on Uncertain/Limited Information. In *MATEC Web of Conferences, EVACES'15, 6th International Conference on Experimental Vibration Analysis for Civil Engineering Structures*.

Cohen, D. & Eldar, Y., 2014. Sub-Nyquist Sampling for Power Spectrum Sensing in Cognitive Radios: A Unified Approach. *IEEE Transactions on Signal Processing*, 62(15), pp.3897–3910.

Cohen, L., 1995. *Time-frequency analysis*, Prentice Hall PTR.

Comerford, L., Kougioumtzoglou, I.A. & Beer, M., 2015. Compressive sensing based stochastic process power spectrum estimation subject to missing data. *Probabilistic Engineering Mechanics*, 44, pp.66–76.

Cornwell, P., Doebling, S.W. & Farrar, C.R., 1999. Application of the Strain Energy Damage Detection Method To Plate-Like Structures. *Journal of Sound and Vibration*, 224(2), pp.359–374.

Daubechies, I., 1992. *Ten lectures on wavelets*, Society for Industrial and Applied Mathematics (SIAM, 3600 Market Street, Floor 6, Philadelphia, PA 19104).

Davenport, M.A. & Wakin, M.B., 2012. Compressive sensing of analog signals using Discrete Prolate Spheroidal Sequences. *Applied and Computational Harmonic Analysis*, 33(3), pp.438–472.

Davenport, M.A., Boufounos, P.T., Wakin, M.B. & Baraniuk, R.G., 2010. Signal Processing With Compressive Measurements. *Selected Topics in Signal Processing, IEEE Journal of*, 4(2), pp.445–460.

Davenport, M.A., Laska, J.N., Treichler, J.R. & Baraniuk, R.G., 2012. The Pros and Cons of Compressive Sensing for Wideband Signal Acquisition: Noise Folding versus Dynamic Range. *IEEE Transactions on Signal Processing*, 60(9), pp.4628–4642.

Dick, A.J., Phan, Q.M., Foley, J.R. & Spanos, P.D., 2012. Calculating scaling function coefficients from system response data for new discrete wavelet families. *Mechanical Systems and Signal Processing*, 27, pp.362–369.

Doebling, S.W., Farrar, C.R. & Prime, M.B., 1988. A summary Review of Vibration-Based Damage ldentification Methods. *The Shock and Vibration Digest*, 30(2), pp.91–105.

Donoho, D.L., 2006. Compressed sensing. *IEEE Transactions on Information Theory*, 52(4), pp.1289–1306.

Duarte, M.F. & Baraniuk, R.G., 2013. Spectral compressive sensing. *Applied and Computational Harmonic Analysis*, 35(1), pp.111–129.

Duarte, M.F., Shen, G., Ortega, A. & Baraniuk, R. G., 2012. Signal compression in wireless sensor networks. *Philosophical transactions. Series A, Mathematical, physical, and engineering sciences*, 370(1958), pp.118–35.

Ewins, D.J., 2000. *Modal testing: Theory practice and application*, 2nd ed., Research Studies Press. Baldock.

Feng, P. & Bresler, Y., 1996. Spectrum-blind minimum-rate sampling and reconstruction of multiband signals. *Proceedings of 3rd IEEE International Conference on Image Processing*, 1, pp.1688–1691.

Foti, D., Gattulli, V. & Potenza, F., 2014. Output-Only Identification and Model Updating by Dynamic Testing in Unfavorable Conditions of a Seismically Damaged Building. *Computer-Aided Civil and Infrastructure Engineering*, 29(9), pp.659–675.

Ganesan, V., Das, T., Rahnavard, N. & Kauffman, J. L., 2017. Vibration-based monitoring and diagnostics using compressive sensing. *Journal of Sound and Vibration*, 394, pp.612–630.

Gattulli, V., Potenza, F., Graziosi, F., Federici, F., Colarieti, A. & Faccio, M., 2014. Distributed Structural Monitoring for a Smart City in a Seismic Area. *Key Engineering Materials*, 628, pp.123–135.

Giaralis, A. & Spanos, P.D., 2009. Wavelet-based response spectrum compatible synthesis of accelerograms—Eurocode application (EC8). *Soil Dynamics and Earthquake Engineering*, 29(1), pp.219–235.

Giaralis, A. & Spanos, P.D., 2012. Derivation of response spectrum compatible non-stationary stochastic processes relying on Monte Carlo-based peak factor estimation. *Earthquakes and Structures*, 3(5), pp.581–609.

Gkoktsi, K. & Giaralis, A., 2014. On the influence of frequency selectivity of wavelet bases for relative wavelet entropy-based structural damage localization. In *6th World Conference on Structural Control and Monitoring (6WCSCM)*. pp. 1366–1378.

Gkoktsi, K. & Giaralis, A., 2015. Effect of frequency domain attributes of wavelet analysis filter banks for structural damage localization using the relative wavelet entropy index. *International Journal of Sustainable Materials and Structural Systems (IJSMSS)*, 2(1/2), pp.134–160.

Gkoktsi, K. & Giaralis, A., 2016. Assessment of sub-Nyquist deterministic and random data sampling techniques for operational modal analysis. In *8th European Workshop On Structural Health Monitoring (EWSHM 2016)*. Bilbao, Spain.

Gkoktsi, K. & Giaralis, A., 2017. A multi-sensor sub-Nyquist power spectrum blind sampling approach for low-power wireless sensors in operational modal analysis applications. *Mech. Syst. Signal Process.* (under review, submitted September 2017).

Gkoktsi, K. & Giaralis, A., 2017. Assessment of sub-Nyquist deterministic and random data sampling techniques for operational modal analysis. *Structural Health Monitoring: An International Journal*, 16(5), pp.630–646.

Gkoktsi, K., Giaralis, A. & TauSiesakul, B., 2016. Sub-Nyquist signal-reconstruction-free operational modal analysis and damage detection in the presence of noise. In J. P. Lynch, ed. *SPIE Smart Structures and Materials + Nondestructive Evaluation and Health Monitoring*. International Society for Optics and Photonics, p. 980312.

Gkoktsi, K., Giaralis, A. & Tausiesakul, B., 2017. A reconstruction-free sub-Nyquist sensing approach for earthquake damage detection using the MUSIC algorithm. In *16th World Conference on Earthquake Engineering*.

Gkoktsi, K., Giaralis, A., Klis, R.P., Dertimanis, V. & Chatzi E., 2017. Vibration-based structural performance assessment via output-only sub-Nyquist / compressive wireless sensor data. In *4th International Conference on Smart Monitoring, Assessment and Rehabilitation of Civil Structures (SMAR)*.

Gkoktsi, K., TauSiesakul, B. & Giaralis, A., 2015. Multi-channel sub-Nyquist cross-Spectral Estimation for Modal Analysis of Vibrating Structures. In *International Conference on Systems, Signals and Image Processing (IWSSIP 2015)*.

Gkoktsi, K., TauSiesakul, B. & Giaralis, A., 2015. Multi-channel sub-Nyquist cross-Spectral Estimation for Modal Analysis of Vibrating Structures. In *International Conference on Systems, Signals and Image Processing (IWSSIP 2015)*.

Goswami, J.C. & Chan, A.K., 1999. *Fundamentals of Wavelets: Theory, algorithms, and applications*, New York, USA: John Wiley & Sons, Inc.

Huang, Y., Beck, J. L., Wu, S. & Li, H., 2016. Bayesian compressive sensing for approximately sparse signals and application to structural health monitoring signals for data loss recovery. *Probabilistic Engineering Mechanics*, 46, pp.62–79.

Humar, J., Bagchi, A. & Xu, H., 2006. Performance of Vibration-based Techniques for the Identification of Structural Damage. *Structural Health Monitoring*, 5(3), pp.215–241.

Jayawardhana, M. ,Zhu, X., Liyanapathirana, R. & Gunawardana, U., 2017. Compressive sensing for efficient health monitoring and effective damage detection of structures. *Mechanical Systems and Signal Processing*, 84, pp.414–430.

Jerri, A.J., 1977. The Shannon sampling theorem-Its various extensions and applications: A tutorial review. *Proceedings of the IEEE*, 65(11), pp.1565–1596.

Ji, X., Hikino, T., Kasai, K. & Nakashima, M., 2013. Damping identification of a full-scale passively controlled five-story steel building structure. *Earthquake Engineering & Structural Dynamics*, 42(2), pp.277–295.

Jiang, X. & Adeli, H., 2007. Pseudospectra, MUSIC, and dynamic wavelet neural network for damage detection of highrise buildings. *International Journal for Numerical Methods in Engineering*, 71(5), pp.606–629.

Jingchao, Z., Peizhuo, L., Ning, F. & Xiyuan, P., 2015. Prototype design of multicoset sampling based on compressed sensing. In *2015 IEEE 12th International Conference on Electronic Measurement & Instruments (ICEMI'2015)*. Qingdao, Shandong, China., pp. 1303–1308.

Kim, J.-T. & Stubbs, N., 1995. Damage Detection In Offshore Jacket Structures From Limited Modal Information. *International Journal of Offshore and Polar Engineering*, 5(1).

Klis, R. & Chatzi, E., 2015. Data recovery via Hybrid Sensor Networks for Vibration Monitoring of Civil Structures. *Int. J. Sustainable Materials and Structural Systems*, 2(1/2), pp.161–184.

Klis, R. & Chatzi, E.N., 2017. Vibration monitoring via spectro-temporal compressive sensing for wireless sensor networks. *Structure and Infrastructure Engineering*, 13(1), pp.195–209.

Lee, S.G., Yun, G.J. & Shang, S., 2014. Reference-free damage detection for truss bridge structures by continuous relative wavelet entropy method. *Structural Health Monitoring*, 13(3), pp.307–320.

Leus, G. & Arianandа, D.D., 2011. Power Spectrum Blind Sampling. *Signal Processing Letters, IEEE*, 18(8), pp.443–446.

Lim, C.W. & Wakin, M.B., 2016. Reconstruction of Frequency Hopping Signals From Multi-Coset Samples. *arXiv:1603.06886v1*, (Mc), pp.1–13.

Loh, C.-H., Chan, C.-K. & Lee, C.-H., 2016. Application of time series based damage detection and localization algorithms to structures under ambient excitations. In J. P. Lynch, ed. *SPIE Smart Structures and Materials + Nondestructive Evaluation and Health Monitoring*. International Society for Optics and Photonics, p. 98031Q.

Lynch, J.P. & Loh, K.J., 2006. A Summary Review of Wireless Sensors and Sensor Networks for Structural Health Monitoring. *The Shock and Vibration Digest*, 38(2), pp.91–128.

Lynch, J.P., 2007. An overview of wireless structural health monitoring for civil structures. *Philosophical Transactions of the Royal Society A: Mathematical, Physical and Engineering Sciences*, 365(1851), pp.345–372.

Lynch, J.P., Sundararajan, A., Law, K.H., Kiremidjian, A.S. & Carryer E., 2003. Power-efficient data management for a wireless structural monitoring system. In F.-K. Chang, ed. *From Diagnostics and Prognostics to Structural Health Management - Proceedings of the 4th International Workshop on Structural Health Monitoring, IWSHM 2003*. Stanford University; United States: DEStech Publications, pp. 1177–1184.

Marple, S.L., 1987. *Digital spectral analysis*, Englewood Cliffs, London: Prentice-Hall.

Mascarenas, D., Cattaneo, A., Theiler, J. & Farrar, C., 2013. Compressed sensing techniques for detecting damage in structures. *Structural Health Monitoring*, 12(4), pp.325–338.

Mishali, M. & Eldar, Y.C., 2009. Blind Multiband Signal Reconstruction: Compressed Sensing for Analog Signals. *IEEE Transactions on Signal Processing*, 57(3), pp.993–1009.

Mishali, M. & Eldar, Y.C., 2010. From Theory to Practice : Sub-Nyquist Sampling of Sparse Wideband Analog Signals. *IEEE Journal of Selected Topics in Signal Processing, the special issue on Compressed Sensing*, 4(2), pp.375–391.

Mishali, M., Eldar, Y.C., Dounaevsky, O. & Shoshan, E., 2009. Xampling : Analog to Digital at Sub Nyquist Rates. *Elect. Eng. Dept., Technion, Haifa, Isreal, CCIT Rep. no. 751, arXiv.org 0912.2495*

Misiti, M., Misiti, Y., Oppenheim, G. & Poggi J.-M., 1997. Wavelet Toolbox™ 4 User's Guide Product enhancement suggestions Wavelet Toolbox™ User's Guide.

Moon, T. et al., 2015. Wideband Sparse Signal Acquisition with Dual-rate Time-Interleaved Undersampling Hardware and Multicoset Signal Reconstruction Algorithms. *IEEE Transactions on Signal Processing*, 63(24), pp.6486–6497.

Nagarajaiah, S. & Yang, Y., 2017. Modeling and harnessing sparse and low-rank data structure: a new paradigm for structural dynamics, identification, damage detection, and health monitoring. *Structural Control and Health Monitoring*, 24(1), p.e1851.

Nagayama, T. & Spencer, B.F.J., 2007. Structural health monitoring using smart sensors. *Report No NSEL-001 Newmark Structural Engineering Laboratory University of Illinois at Urbana-Champaign*, p.186.

Nagayama, T., Sim, S.H., Miyamori, Y. & Spencer, B.F., 2007. Issues in structural health monitoring employing smart sensors. In *Smart Structures and Systems*. pp. 299–329.

Needell, D. & Tropp, J.A., 2009. CoSaMP: Iterative signal recovery from incomplete and inaccurate samples. *Applied and Computational Harmonic Analysis*, 26(3), pp.301–321.

Needell, D. & Tropp, J.A., 2010. CoSaMP: Iterative signal recovery from incomplete and inaccurate samples. *Communications of the ACM*, 53(12), p.93.

Newland, D.E., 1994. Harmonic and Musical Wavelets. *Proceedings of the Royal Society of London A: Mathematical, Physical and Engineering Sciences*, 444(1922), pp.605–620.

Newland, D.E., 1999. Ridge and phase identification in the frequency analysis of transient signals by harmonic wavelets. *Journal of Vibration and Acoustics, Transactions of the ASME*, 121(2), pp.149–155.

Novakovic, A., Meyer, J., Bischoff, R., Feltrin, G., Motavalli, M., El-Hoiydi, A., Restrepo, A. & Decotignie, J.-D., 2009. *Low power wireless sensor network for monitoring civil infrastructure*, Technical report, Empa, Swiss Federal Laboratories for Materials Testing and Research. CSEM, Swiss Center for Electronics and Microtechnology.

O'Connor, S.M., Lynch, J.P. & Gilbert, A.C., 2013. Implementation of a compressive sampling scheme for wireless sensors to achieve energy efficiency in a structural health monitoring system. In T. Y. Yu et al., eds. *Proceedings of SPIE - The International Society for Optical Engineering*. p. 86941L.

O'Connor, S.M., Lynch, J.P. & Gilbert, A.C., 2014. Compressed sensing embedded in an operational wireless sensor network to achieve energy efficiency in long-term monitoring applications. *Smart Materials and Structures*, 23(8), p.85014.

Pal, P. & Vaidyanathan, P.P., 2011. Coprime sampling and the music algorithm. *2011 Digital Signal Processing and Signal Processing Education Meeting, DSP/SPE 2011 - Proceedings*, 0(1), pp.289–294.

Papadimitriou, C., 2004. Optimal sensor placement methodology for parametric identification of structural systems. *Journal of Sound and Vibration*, 278(4–5), pp.923–947.

Park, J.Y.., Wakin, M.B.. & Gilbert, A.C.., 2014. Modal analysis with compressive measurements. *IEEE Transactions on Signal Processing*, 62(7), pp.1655–1670.

Priestley, M.J.N., Calvi, G.M. & Kowalsky, M.J., 2007. *Displacement-based seismic design of structures*, IUSS Press.

Qaisar, S., Bilal, R.M., Iqbal, W., Naureen, M. & Lee, S., 2013. Compressive sensing: From theory to applications, a survey. *Journal of Communications and Networks*, 15(5), pp.443–456.

Rainieri, C., Fabbrocino, G., Manfredi, G. & Dolce, M., 2012. Robust output-only modal identification and monitoring of buildings in the presence of dynamic interactions for rapid post-earthquake emergency management. *Engineering Structures*, 34, pp.436–446.

Ren, W.-X. & Sun, Z.-S., 2008. Structural damage identification by using wavelet entropy. *Engineering Structures*, 30(10), pp.2840–2849.

Reynders, E., 2012. System Identification Methods for (Operational) Modal Analysis: Review and Comparison. *Archives of Computational Methods in Engineering*, 19(1), pp.51–124.

Romero, D., Arianandа, D.D., Tian, Z. & Leus, G., 2016. Compressive Covariance Sensing: Structure-based compressive sensing beyond sparsity. *IEEE Signal Processing Magazine*, 33(1), pp.78–93.

Rosso, O.A., Martin, M.T., Figliola, A., Keller, K. & Plastino, A, 2006. EEG analysis using wavelet-based information tools. *Journal of Neuroscience Methods*, 153(2), pp.163–182.

Rubinstein, R., Bruckstein, A.M. & Elad, M., 2010. Dictionaries for Sparse Representation Modeling. *Proceedings of the IEEE*, 98(6), pp.1045–1057.

Rudelson, M. & Vershynin, R., 2008. On sparse reconstruction from {Gaussian} and {Fourier} measurements. *Comm. Pure Appl. Math.*, 61, pp.1025–1045.

Slavinsky, J.P. et al., 2011. The compressive multiplexer for multi-channel compressive sensing. In *2011 IEEE International Conference on Acoustics, Speech and Signal Processing (ICASSP)*. IEEE, pp. 3980–3983.

Sohn, H. & Farrar, C.R., 2001. Damage diagnosis using time series analysis of vibration signals. *Smart Materials and Structures*, 10, pp.446–451.

Soong, T.T. & Grigoriu, M., 1996. *Random Vibration of Mechanical and Structural Systems*, Prentice Hall PTR.

Spanos, P.D. & Mignolet, M.P., 1989. Arma Monte Carlo Simulation in Probabilistic Structural Analysis. *The Shock and Vibration Digest*, 21(11), pp.3–14.

Spanos, P.D. & Zeldin, B.A., 1998. Monte Carlo Treatment of Random Fields: A Broad Perspective. *Applied Mechanics Reviews*, 51(3), pp.219–237.

Spanos, P.D. et al., 2007. Numerical Treatment of Seismic Accelerograms and of Inelastic Seismic Structural Responses Using Harmonic Wavelets. *Computer-Aided Civil and Infrastructure Engineering*, 22(4), pp.254–264.

Spanos, P.-T.D., 1983. ARMA Algorithms for Ocean Wave Modeling. *Journal of Energy Resources Technology*, 105, pp.300–309.

Spencer, B.F. & Yun, C., 2010. Wireless Sensor Advances and Applications for Civil Infrastructure Monitoring. *Report No NSEL-024 Newmark Structural Engineering Laboratory University of Illinois at Urbana-Champaign*.

Spiridonakos, M.D., Chatzi, E.N. & Sudret, B., 2016. Polynomial Chaos Expansion Models for the Monitoring of Structures under Operational Variability. *ASCE-ASME Journal of Risk and Uncertainty in Engineering Systems, Part A: Civil Engineering*, 2(3), p.B4016003.

Sun, Z. & Chang, C.C., 2004. Statistical wavelet-based method for structural health monitoring. *Journal of Structural Engineering*, 130(7), pp.1055–1062.

Taha, M.M.R., 2006. Wavelet Transform for Structural Health Monitoring: A Compendium of Uses and Features. *Structural Health Monitoring*, 5(3), pp.267–295.

Takeda, Sozen & Nielsen, 1970. Reinforced Concrete Response to Simulated Earthquakes. *Journal of the Structural Division*, 96(12), pp.2557–2573.

Tausiesakul, B. & Gonzalez-Prelcic, N., 2013. Power Spectrum Blind Sampling Using Minimum Mean Square Error and Weighted Least Squares. In *47th Asilomar Conference Signals, Systems and Computers (ACSSC)*. pp. 153–157.

Tausiesakul, B., Gkoktsi, K. & Giaralis, A., 2014. Compressive Sensing Spectral Estimation For Output-Only Structural System Identidication. In *7th International Conference on Computational Stochastic Mechanics*. pp. 1–12.

TauSiesakul, B., Gkoktsi, K. & Giaralis, A., 2015. Compressive power spectrum sensing for vibration-based output-only system identification of structural systems in the presence of noise. In *SPIE Sensing Technology + Applications*.

Tropp, J.A., Laska, J. N., Duarte, M. F., Romberg, J. K. & Baraniuk, R. G., 2010. Beyond Nyquist: Efficient Sampling of Sparse Bandlimited Signals. *IEEE Transactions on Information Theory*, 56(1), pp.520–544.

Tropp, J.A., Wakin, M.B., Duarte, M.F., Baron, D. & Baraniuk, R.G., 2006. Random Filters for Compressive Sampling and Reconstruction. In *2006 IEEE International Conference on Acoustics Speed and Signal Processing Proceedings*. IEEE, p. III-872-III-875.

Vaidyanathan, P.P. & Pal, P., 2011. Sparse Sensing With Co-Prime Samplers and Arrays. *IEEE Transactions on Signal Processing*, 59(2), pp.573–586.

Vaidyanathan, P.P. & Pal, P., 2011. Sparse Sensing With Co-Prime Samplers and Arrays. *IEEE Transactions on Signal Processing*, 59(2), pp.573–586.

Vaswani, N. & Zhan, J., 2016. Recursive Recovery of Sparse Signal Sequences from Compressive Measurements: A Review. *IEEE Transactions on Signal Processing*, 64(13), pp.3523–3549.

Venkataramani, R. & Bresler, Y., 2000. Perfect reconstruction formulas and bounds on aliasing error in sub-Nyquist nonuniform sampling of multiband signals. *IEEE Transactions on Information Theory*, 46(6), pp.2173–2183.

Venkataramani, R. & Bresler, Y., 2001. Optimal sub-Nyquist nonuniform sampling and reconstruction for multiband signals. *IEEE Transactions on Signal Processing*, 49(10), pp.2301–2313.

Vetterli, M. & Herley, C., 1992. Wavelets and filter banks: theory and design. *IEEE Transactions on Signal Processing*, 40(9), pp.2207–2232.

Wang, Y. & Hao, H., 2015. Damage Identification Scheme Based on Compressive Sensing. *Journal of Computing in Civil Engineering*, 29(2), p.4014037.

Worden, K., Farrar, C.R., Manson, G. & Park, G., 2007. The fundamental axioms of structural health monitoring. *Proceedings of the Royal Society A: Mathematical, Physical and Engineering Sciences*, 463(2082), pp.1639–1664.

Yan, G., Duan, Z., Ou, J. & De Stefano, A., 2010. Structural damage detection using residual forces based on wavelet transform. *Mechanical Systems and Signal Processing*, 24(1), pp.224–239.

Yang, Y. & Nagarajaiah, S., 2014. Structural damage identification via a combination of blind feature extraction and sparse representation classification. *Mechanical Systems and Signal Processing*, 45(1), pp.1–23.

Yang, Y. & Nagarajaiah, S., 2015. Output-only modal identification by compressed sensing: Non-uniform low-rate random sampling. *Mechanical Systems and Signal Processing*, 56–57, pp.15–34.

Yao, R., Pakzad, S.N. & Venkitasubramaniam, P., 2016. Compressive sensing based structural damage detection and localization using theoretical and metaheuristic statistics. *Structural Control and Health Monitoring*, 24(4), pp.1–14.

Yen, G.G. & Lin, K., 2000. Wavelet Packet Feature Extraction for Vibration Monitoring. *IEEE Transactions on Industrial Electronics*, 47(3), pp.650–667.

Yun, G.J., Lee, S.-G., Carletta, J. & Nagayama, T., 2011. Decentralized damage identification using wavelet signal analysis embedded on wireless smart sensors. *Engineering Structures*, 33(7), pp.2162–2172.

Zhang, L., Brincker, R. & Andersen, P., 2005. An Overview of Operational Modal Analysis : Major Development and Issues. *1st International Operational Modal Analysis Conference*, (1).

Zou, Z., Bao, Y., Li, H., Spencer, B.F. & Ou, J., 2015. Embedding compressive sensing-based data loss recovery algorithm into wireless smart sensors for structural health monitoring. *IEEE Sensors Journal*, 15(2), pp.797–808.